Structural Effects of Plasma Instabilities on the JET Tokamak

Marco BUZIO

PhD Thesis

Imperial College of Science, Technology and Medicine, London, UK
Mechanical Engineering Department

BIBL
LONDON
UNIV.

ABSTRACT

The subject of this work is a novel approach to the analysis of the mechanical response of the main structural components of the JET Tokamak to the **J**×**B** forces generated by MHD plasma instabilities. The proposed method is based on the creation of simplified lumped-parameter models representing the essential mechanical and electromagnetic characteristics of the interacting components and consists basically in fitting their output to experimental measurements in order to infer information on induced currents and related forces by means of statistical parameter estimation techniques.

First of all, the general time history and space distribution of disruption loads are described and the path of the reaction forces throughout the machine is analysed in detail, with particular reference to the recently observed non-axisymmetric cases. For this purpose, a magneto-static model of the interaction between a kinked plasma and the coil system has been developed. This is based on semi-analytical integration of Biot-Savart's law and makes use of a representation of the conductors in terms of Bèzier curves. The method implemented, which permits efficient and detailed calculation of magnetic load distributions in complex geometries, is used to analyse non-axisymmetric events and to point out the most critical components under this kind of loading.

The attention is focused next on lumped-parameter models which have been created to represent the basic response modes of the Vessel. These models are represented by a combination of concentrated masses, springs and dampers and include additional parameters describing the magnetic loads. The output of these models is fitted to experimental measurements of displacements and support forces in order to obtain estimates for the magnitude, position and timing of induced currents and related forces .

A general procedure for model-based maximum likelihood parameters estimation has been implemented as an interactive PC-Windows program in order to solve this problem. This procedure is an adaptation and an improvement of the well-known Levenberg-Marquardt algorithm for non-linear multi-dimensional minimisation.

The results obtained are used to derive peak stresses and displacements of the structure for observed as well as extrapolated events. The ultimate aim of this work is to guarantee safe machine operation at higher performance and to derive design guidelines for the next generation of fusion devices.

Keywords: tokamak disruptions, toroidal asymmetries, halo currents, parameter estimation, prior knowledge, Levenberg-Marquardt method, Biot-Savart method, Bèzier curves, lumped-parameter mechanical modelling, transient force estimation.

ACKNOWLEDGEMENTS

This work has been carried out with the essential support of many people who helped me with their knowledge, their time and their friendship. It is my pleasure to express first my gratitude to:

my supervisor at Imperial College Dr. Simon P. Walker, who inspired and directed my work with constant encouragement and patience;

my supervisors at JET Giulio Sannazzaro, Tullio Raimondi and Stamos Papastergiou, who guided me and shared their experience with me during my wonderful experience in this laboratory;

the former Head of the Magnet & Power Supplies Division and Chief Engineer of JET, Enzo Bertolini, who made my work at JET possible at all and who has been a constant reference point with his experience and suggestions.

I also want to thank the following friends and colleagues for many fruitful discussions, their suggestions and their criticism:

Philip Andrew, Pietro Barabaschi, Tiziano Businaro, Susana Clement, Massimo Garribba, David Gray, Hans Hemmerich, Mike Johnson, John Last, Morten Lennholm, Vito Marchese, Federico Milani, Andy Miller, Roma Mohanti, Peter Noll, Pierre Presle, Stefano Puppin, Krishan Purahoo, Valeria Riccardo, Fernanda Rimini, Adriana Rossi, Gabriella Saibene, Ettore Salpietro, Luigi Scibile, Lars Sonnerup, David Starkey, John Tait, Christiane Van Der Goot, Mario Verrecchia

A very, very special thanks to my wife Adriana and to the *terzo incomodo* Ciuffo, who have patiently endured a long separation; and to my parents, who encouraged and supported me when I took the big step and came to JET.

This work has been funded by a JET Fellowship grant awarded in 1994 by the European Commission in the Framework of the IVth fusion programme.

TABLE OF CONTENTS

ABSTRACT **2**

ACKNOWLEDGEMENTS **3**

TABLE OF CONTENTS **4**

PREFACE **8**

Subject of the work *8*
Overview of the thesis *8*
Summary of the principal features *10*

LIST OF SYMBOLS **12**

Units and symbols *12*
Abbreviations and subscripts *13*

LIST OF FIGURES **14**

LIST OF TABLES **17**

1 INTRODUCTION **18**

1.1 OVERVIEW OF JET 19
1.1.1 Structural components of the JET Tokamak *19*
1.1.1.1 Poloidal Field (PF) and Divertor coils 20
1.1.1.2 Toroidal Field (TF) Coils 20
1.1.1.3 Mechanical Structure and Iron Core 22
1.1.1.4 Vacuum vessel 23
1.1.2 Mechanical vessel diagnostics *28*
1.1.2.1 Reliability of mechanical measurements 28
1.1.3 Magnetic vessel diagnostics *30*
1.2 ELECTROMECHANICAL MODELLING OF PLASMA INSTABILITIES 32
1.2.1 Axisymmetric VDEs *32*
1.2.1.1 Sequence of events during a VDE 32
1.2.1.2 Halo currents 34
1.2.2 Non-axisymmetric VDEs *35*
1.2.3 Global VDE model *36*
1.3 STRUCTURAL EFFECTS OF PLASMA INSTABILITIES 40
1.3.1 Axisymmetric VDE effects *41*
1.3.1.1 Rolling motion 41
1.3.1.2 Radial motion 42
1.3.1.3 Vertical motion 42
1.3.2 Non-axisymmetric effects *43*
1.3.2.1 Sideways motion 43
1.3.2.2 Non-axisymmetric rolling motion 44
1.3.3 Vessel stress assessment *45*
1.3.4 Mechanical effects in other Tokamaks *47*

2 TOKAMAK LOAD PATHS DURING DISRUPTIONS **48**

2.1 BÈZIER CURVE-BASED MAGNETIC COIL MODELLING 49
2.1.1 Modelling of coil geometry via Bèzier curves *49*
2.1.2 Semi-analytical integration of Biot-Savart's law *52*
2.1.2.1 Field integration over rectangular bricks 53
2.1.2.2 Errors in single-brick modelling of arc-shaped coil segments 55

2.1.2.3 Errors in multi-brick coil modelling 61
2.1.2.4 Adaptive coil discretization 63
2.1.3 Numerical integration of magnetic forces *67*
2.2 LOAD PATHS IN THE TOKAMAK 69
2.2.1 Axisymmetric force balance *69*
2.2.2 Non-axisymmetric force balance *71*
2.2.2.1 Vessel eddy currents due to plasma kink 71
2.2.2.2 Plasma kink for a vertically symmetric configuration 74
2.2.2.3 Plasma kink case II: JET pulse 34078 78
2.2.2.4 Qualitative analysis of the path of sideways loads 79

3 ELECTRO-MECHANICAL VACUUM VESSEL MODELLING 83

3.1 MODELS FOR AXISYMMETRIC MOTIONS 85
3.1.1 Rolling motion model *85*
3.1.1.1 Experimental evidence 86
3.1.1.2 Finite Element analysis 87
3.1.1.3 Model formulation 88
3.1.1.4 Non-linear hydraulic damping 91
3.1.1.5 Transient plasma force model 92
3.1.1.6 Support forces 93
3.1.2 Vertical motion model *94*
3.1.3 Radial motion model *94*
3.1.4 Global axisymmetric motion model *94*
3.1.5 Inductive coupling model *95*
3.1.5.1 Toroidal vessel eddy currents 96
3.1.5.2 Vessel force balance 97
3.1.5.3 Halo current estimate 97
3.2 MODEL FOR SIDEWAYS MOTION 99
3.2.1.1 Experimental evidence 99
3.2.1.2 Finite Element model of ½ vessel 100
3.2.1.3 Model formulation 101
3.2.1.4 Transient plasma force model 101
3.2.1.5 Friction mechanism 104
3.2.1.6 Magnetic damping 106
3.3 MODEL FOR GENERAL NON-AXISYMMETRIC MOTIONS 108

4 MODEL-BASED PARAMETER ESTIMATION 109

4.1 USING MECHANICAL MODELS AS DIAGNOSTICS 111
4.1.1 Inferring information via parameter estimation *111*
4.1.2 Alternative inference method: input reversal *114*
4.1.2.1 Input reversal on Finite Element models 116
4.1.3 Literature survey *117*
4.2 REVIEW OF PARAMETER ESTIMATION THEORY 119
4.2.1 Maximum-likelihood parameter estimation *119*
4.2.1.1 Parametric dynamic models 119
4.2.1.2 Statistical assumptions 120
4.2.1.3 Likelihood maximisation 120
4.2.2 Inclusion of prior knowledge *122*
4.2.2.1 Bayesian inference 123
4.2.2.2 Maximum a-posteriori (MAP) estimation 124
4.2.3 Levenberg-Marquardt minimisation method *125*
4.2.3.1 Formulation of the problem 125
4.2.3.2 Steepest descent method 125
4.2.3.3 Inverse Hessian method 126
4.2.3.4 Levenberg-Marquardt (LM) method 126
4.2.3.5 Alternative minimisation methods 128
4.2.4 Statistical measure of the goodness-of-fit *128*
4.2.5 Variance of the estimated parameters *129*
4.2.5.1 Variance matrix 129
4.2.5.2 Confidence intervals for the estimated parameters 130
4.3 PRELIMINARY ANALYSIS 132

4.3.1 Global minimum search *132*
4.3.2 Measurement analysis *133*
4.3.2.1 Frequency 133
4.3.2.2 Damping ratio 135
4.3.2.3 Force pulse start time 135
4.3.2.4 Analysis by sub-modelling 136
4.3.3 Noise analysis and removal *138*
4.3.3.1 Noise modelling 138
4.3.3.2 Data smoothing 139
4.4 IMPLEMENTATION OF THE ITERATIVE LEVENBERG-MARQUARDT MINIMISATION ALGORITHM 142
4.4.1 Numerical calculation of the derivatives *143*
4.4.1.1 Parameter increments for first-order forward differences 143
4.4.1.2 Centred differences 145
4.4.1.3 Inclusion of the second-order derivatives 146
4.4.1.4 Parameter increments for second-order differentiation 146
4.4.1.5 Alternative differentiation strategies 147
4.4.2 Damping-undamping stagnation loops *149*
4.4.2.1 Mono-dimensional stagnation loops 149
4.4.2.2 Stagnation loop stability 151
4.4.2.3 Multi-dimensional stagnation loops 152
4.4.3 Adaptive damping-undamping strategy *153*
4.4.3.1 Choice of boost and drop factors 153
4.4.3.2 Effect of the local topology of the Hessian 155
4.4.3.3 Bounds on damping parameter 156
4.4.4 Robust solution of the linearized equations *157*
4.4.4.1 Model identification issues 157
4.4.4.2 SVD solution of the linearized system 158
4.4.4.3 Null singular value detection 159
4.4.5 Termination criteria *160*
4.5 INCORPORATION OF PRIOR KNOWLEDGE 162
4.5.1 Weighting of measurements and prior knowledge *162*
4.5.2 Parameter constraints *164*
4.5.3 Parameter cluster estimation *165*
4.5.4 Multi-stage estimation *166*
4.5.4.1 Combination of prior distributions 167
4.5.4.2 Parameter estimate updating 168
4.5.4.3 Progressive modelling 168

5 ANALYSIS OF AXISYMMETRIC DISRUPTIONS 169

5.1 ANALYSIS OF PRE-DIVERTOR EVENTS 170
5.1.1 JET Pulse 16297 ..... *170*
5.1.2 JET Pulse 20802 ..... *173*
5.1.3 Summary of results *174*
5.2 ANALYSIS OF MKII DIVERTOR EVENTS 175
5.2.1 JET Pulse 37628 ..... *175*
5.2.2 JET Pulse 38690 ..... *180*
5.2.3 Summary of results *183*

6 ANALYSIS OF NON-AXISYMMETRIC DISRUPTIONS 184

6.1 ANALYSIS OF SIDEWAYS EVENTS 185
6.1.1 JET Pulse 34078 ..... *185*
6.1.2 JET Pulse 38705 ..... *189*
6.2 ANALYSIS OF GENERAL NON-AXISYMMETRIC EVENTS 192

7 RESULTS 193

7.1 TOKAMAK DISRUPTION LOAD PATHS 194
7.1.1 Magnetic coil force integration *194*
7.1.2 Non-axisymmetric disruption load paths *194*
7.2 ESTIMATES OF MECHANICAL AND FORCE PARAMETERS 196
7.2.1 Application of the parameter estimation procedure *196*

7.2.2 Results for the axisymmetric models *200*
7.2.2.1 Vertical vessel force 200
7.2.2.2 Coefficients for the Main Vertical Port dampers 200
7.2.2.3 Model limitations and possible improvements 201
7.2.3 Results for the sideways model *202*
7.2.3.1 Sideways vessel force 202
7.2.3.2 Magnetic damping and stiffness 202
7.2.3.3 Neutral Beam Injectors forces 202
7.2.3.4 Model limitations and possible improvements 203
7.3 IMPACT ON JET OPERATIONS 204
7.3.1 On-line stress assessment *204*
7.3.2 Predictive use of the models *205*
7.3.2.1 Extrapolation to future plasma configurations 205
7.3.2.2 Support design optimisation 206
7.4 DESIGN SUGGESTIONS 207
7.5 FURTHER WORK 208

APPENDICES 209

REFERENCES 222

PREFACE

Subject of the work

Magnetic confinement devices such as the Joint European Torus (JET) Tokamak are, to date, the most widely pursued and promising route towards the exploitation of thermonuclear fusion as an energy source for the next millennium. One of the biggest technological problems to overcome is represented by plasma instabilities and disruptions, generating huge $\mathbf{J}\times\mathbf{B}$ forces which affect heavily the design and the operation of these machines.

The subject of this thesis is a novel approach to the analysis of the mechanical response of the main structural components of JET to these forces. The problem is first approached on a global level, investigating the general 3D pattern of forces and reactions during a generic, non axisymmetric event, identifying thus the more critical mechanical components on which to focus the attention. A specific, more detailed analysis is then made on the Vacuum Vessel, based on the creation of simplified electro-mechanical lumped-parameter models and on the comparison of their the output to experimental measurements in order to estimate the models' parameters.

The process of matching simulations to observations, carried out by means of suitably adapted statistical parameter estimation techniques based on the maximum likelihood principle, allows one to infer information in a backwards fashion on some of the mechanical properties of the machine, the J×B forces generated by induced currents and other features of the disrupting plasma. This approach can be considered complementary to the direct procedure consisting in simulating MHD evolution first, calculating forces next and then feeding them into mechanical models. Although approximate, the proposed method has the advantage that many uncertainties inherent in the plasma and structural modelling, affecting adversely predictive simulations, can be bypassed altogether. The results obtained in terms of magnitude of forces and induced currents have a strong credibility because the models are fitted to fundamental mechanical quantities such as displacements and support forces, which can be measured with a high degree of reliability.

This new method can therefore be seen as an alternative, general kind of plasma diagnostic tool. The information gained can be confidently used to contribute to guarantee safe machine operation and to derive design guidelines for the next generation of fusion devices.

Overview of the thesis

The thesis is structured so as to proceed from the general to the particular, attempting a logical progression from the global framework of plasma instabilities to the parameter estimation techniques, and to the details of the models representing JET-specific behaviour. Mathematical and coding details, where cluttering the exposition, have been moved to the appendices at the end of the text.

First of all, the Introduction is devoted to a brief exposition of the necessary background information on JET structures, measurement apparatus and general behaviour during plasma instabilities. The reader is assumed to be familiar with the general functioning of tokamak devices, but pointers to introductory references are provided and those aspects which are peculiar of JET are illustrated in more detail.

The second chapter provides (it is believed for the first time) a global picture of the electromechanical forces and corresponding reactions throughout the machine in the case of non-axisymmetric events. In fact, Tokamak plasmas have always been thought to be axisymmetric to a high degree of approximation, even during disruptions. In JET, in particular, some non-symmetric features in the mechanical response had always been ascribed purely to non uniformity in the distribution of structural mass and restraints. More recently, sideways movements of the vessel as a whole have been clearly observed, implying the presence of a net horizontal force and prompting intense research effort in this area. The currently accepted model includes a vertical plasma displacement superimposed to a n=1, m=1 or m=2 kink mode (approximately represented by a tilt of the plasma ring plus a shift along the tilt axis). The analysis presented here proceeds from the assumption that the magnetic interaction between the displaced plasma ring and the coil system is the key to understand the pattern of forces exchanged between the components. The method devised to carry out the analysis of the force distribution, based upon an optimised, adaptive implementation of Biot-Savart's formula, is also explained. The results obtained permit to identify the most heavily loaded structures, to assess their stresses and, in general, to understand better the balance of forces and reaction throughout the machine during one of these events.

In the remainder of the work the focus is shifted onto the Vacuum vessel, identified as the most critical component and the one for which disruption effects are most evident and dangerous. Chapter three includes the descriptions of the electro-mechanical models which have been created to describe the basic response modes of the Vessel, providing a link between the characteristics of the magnetic force (such as magnitude, position and timing) and observations. Two basic types of movement are considered: oscillations of the Vessel in the poloidal plane (toroidally uniform or otherwise) and sideways motion in the horizontal plane. The rationale for this choice is explained on the basis of observations and detailed Finite Element (FE) analyses of typical events.

In chapter four the parameter estimation procedure, which is basically an improved adaptation of the familiar least-squares fitting method applied to dynamic models, is explained in full detail. After a brief review of the existing state-of-the-art, the emphasis is put on a practical approach to the problem (which is after all of applied engineering rather than pure mathematics !). In fact, the incorporation in the algorithm of a considerable amount of prior knowledge about the physics and the mechanical behaviour of the system has proven to be the key to a rapid and efficient solution. Such prior knowledge can be taken into account on more than one level: for instance, to fix the initial parameter variances; to select a reasonable starting guess for the iterative minimisation procedure, possibly on the basis of previous analyses; and to establish constraints limiting the zones of parameter space where a meaningful solution can be found.

The following chapters give a detailed exposition of the results obtained from the application of the parameter estimation procedure to JET disruption data. Chapter five is concerned with the averaged axisymmetric component of the response, while chapter six deals with the recently discovered non-axisymmetric components. For each of the models described in chapter three the preliminary stage of the

procedure, involving estimation of the geometrical and mechanical properties, leads initially to the validation of the model itself. The procedure is then applied more specifically to the parameters describing induced currents and magnetic forces, which are ultimately the physical quantities of interest. Several examples relative to major disruptions are given and the quality and reliability (in the statistical sense) of the results are discussed.

Finally, chapter seven gives a summary of the results inferred from the models, emphasising practical relevance to JET operations. Vacuum vessel stresses are reviewed on the basis of the new knowledge and are found to be lower than previously estimated. On the other hand, the danger represented by non-axisymmetric forces is clearly assessed and quantified. Design recommendations are derived on the best way to contain these new structural effects, with reference to possible JET upgrades and to future machines. In the end, directions for improvements of the methods presented and suggestions for more detailed models are given.

Summary of the principal features

This work includes some features which, to the best of the author's knowledge, are believed to be original. They are summarised in the following list:

I. ***Bèzier curve-based magnetic coil modelling with semi-analytical integration of Biot-Savart's law (section 2.1)***

The JET magnetic system (including toroidal field, poloidal field and divertor coils) has been modelled with of a novel numerical procedure representing the coil geometry by means of Bèzier curves. The magnetic field is obtained by integrating symbolically Biot-Savart's law over brick-shaped subdomains, the size and location of which is determined adaptively in order to reach a target accuracy with the least computational effort; the total field, as well as the distributed and integrated forces and moments are then integrated numerically. The procedure has been implemented within a general-purpose interactive program for the Microsoft Windows platform, able to compute efficiently field, forces and other quantities of practical interest internally or externally to a coil.

II. ***Analysis of 3D non-axisymmetric Tokamak load paths during disruptions (section 2.2)***

The problem of the distribution of disruption forces and of the corresponding reactions within a Tokamak is addressed for the first time in full detail in the case of a generic VDE plus an n=1, m=1 kink plasma instability giving rise to the kind of non-axisymmetric Vessel movements recently observed in JET. The detailed distribution of non-symmetric forces exerted on the TF coils by the tilted and shifted plasma ring, calculated with the method described in (I), has been used as the primary input to this analysis. Simple mechanical and MHD equilibrium considerations have then been employed to follow the path of the reactions throughout the machine, taking also into account the dynamic nature of the phenomena and making appropriate corrections for inertia and inductive effects.

III. ***Improvement and adaptation of model-based maximum-likelihood parameter estimation techniques to Tokamak disruptions (chapter 4)***

Simplified lumped-parameter models representing the response of JET vacuum vessel to disruptions have been created. These include parameters such as masses, spring constants, friction and damping coefficients (representing the mechanical behaviour) as well as magnitude, position and timing of induced currents and **J**×**B** forces (describing the inductive coupling). The maximum likelihood parameter estimation method has been adapted to the problem of fitting the output of these multiply coupled models to the available mechanical measurements. The Levenberg-Marquardt non-linear minimisation algorithm has been numerically optimised for this class of problems and has been modified so as to incorporate to the maximum possible extent prior knowledge on the phenomena under investigation. The resulting algorithm has been formulated in a generalised way and has been implemented in the form of an interactive program for the Microsoft Windows operating system, giving the user the possibility to define, edit and experiment with new models and parameters.

IV. ***Electro-mechanical modelling of axisymmetric disruption effects (chapter 5)***

Lumped-parameter models have been created to represent the various components of the axisymmetric deformation of JET Vacuum vessel (namely rolling motion, radial motion and vertical motion) and to link them to the magnetic forces and to the behaviour of the plasma during a disruption (section 3.1). The consistency of these with detailed Finite Element calculations and with observations has been discussed first, then the procedure (III) has been applied to fully validate them and to get precise estimate of their parameters.

The combination of mechanical modelling and parameter estimation technique has proven to be a very useful technique to analyse disruptions and to infer information on the currents and forces generated by an unstable plasma. In particular, the lumped-parameter approach has been found to be an extremely flexible and efficient tool, allowing experimentation with alternative methods for calculating the structural response on the basis of measurements and for extrapolating it to future experiments or modified configurations.

V. ***Electro-mechanical modelling of non-axisymmetric disruption effects (chapter 6)***

An additional lumped-parameter model has been created to analyse non-axisymmetric phenomena. This model includes a 2 degrees of freedom system representing the averaged sideways motion of the vessel along an horizontal axis. The parameter estimation procedure has been used to fit the model to the mechanical measurements, providing detailed information, *inter alia*, on the magnitude of the non-symmetric forces and on the relative weight of magnetic damping effects in restraining Vessel movements.

LIST OF SYMBOLS

Units and symbols

The International System of units (metric system) is used throughout the work. Vectors and arrays are indicated with bold typeface (**B**) or, in component form, by curly braces ($\{p_j\}$). Matrices are indicated with square brackets ([H]).

Most symbols used in the text have been formed by a combination of the variables listed in the following table with the subscripts and/or superscripts listed in the next section:

Symbol	*Quantity*
Φ	Magnetic flux
ε	non-dimensional error
ε	mechanical strain
σ	mechanical stress
ρ	resistivity
ρ	radius
μ	magnetic permeability
ν	kinematic viscosity
A	Area
B	Magnetic field
b	damping coefficient (force/velocity ratio)
F	force
I	Electric current
J	Current density
k	stiffness
l	length
L	inductance
m	mass
P,Q,R, r	position
R	electrical resistance
u	1st local coordinate
v	2nd local coordinate
t	3rd local coordinate
t	time
v	velocity

Abbreviations and subscripts

1D, 2D, 3D	one-, two- or three-dimensional
ADC	Analogue-Digital Converter
ALU	Arithmetic-Logic Unit
avg.	average
CPU	Central Processing Unit
d.o.f.	degree(s) of freedom
e.m.	electromagnetic
e.m.f.	electro-motive force
FE	Finite Element
FFT	Fast Fourier Transform
FLOPs	FLoating-Point Operations per second
GUI	Graphical User Interface
H	Halo
IVP	Intermediate Vertical Port
JPF	JET Pulse File
JPN	JET Pulse Number
l.h.s.	left-hand side
LM	Levenberg-Marquardt
LPF	Low-Pass Filter
LVR	Linear Variable Resistor
MAP	Maximum A-Posteriori
MBPE	Model-Based Parameter Estimation
MHD	MagnetoHydroDynamic
MHP	Main Horizontal Port
MS	Mechanical Structure
MVP	Main Vertical Port
NBI	Neutral Beam Injectors
norm.	normalised
ODE	Ordinary Differential Equation
PLA	Plasma
POL	poloidal
PPCC	Plasma Position and Current Control system
R, RAD	radial
r.h.s.	right-hand side
S/N	Signal-to-Noise ratio
SDE	Sideways Displacement Event
SOL	Scrape-off layer
SVD	Singular Value Decomposition
SW	sideways
T, TANG	tangential
TOR	Toroidal
VDE	Vertical Displacement Event
VV	Vacuum Vessel

LIST OF FIGURES

FIG. 1.1 - THE JET TOKAMAK 18

FIG. 1.2 - CROSS-SECTION OF THE JET MACHINE 19

FIG. 1.3 - POLOIDAL AND TOROIDAL FIELD COIL SYSTEMS..... 21

FIG. 1.4 - ASSEMBLY OF A JET OCTANT SHOWING THE VACUUM VESSEL, FOUR TF COILS AND PART OF THE MS SHELL..... 21

FIG. 1.5 - MECHANICAL STRUCTURE SCHEMATICS (SHELL, CYLINDER AND COLLAR)..... 22

FIG. 1.6 - IRON CORE LIMBS 22

FIG. 1.7 - SPACERS MOUNTED ACROSS THE BELLOWS..... 24

FIG. 1.8 - INTERNAL VIEW OF THE VV IN THE 1998 CONFIGURATION..... 25

FIG. 1.9 - EXTERNAL VIEW OF A VESSEL OCTANT BEFORE ASSEMBLY. 26

FIG. 1.10 - VESSEL RESTRAINTS AT THE EQUATORIAL PLANE (TOP VIEW). 27

FIG. 1.11 - VACUUM VESSEL SUPPORT SYSTEM IN THE 1997 CONFIGURATION 27

FIG. 1.12 - MAIN MECHANICAL MEASUREMENTS ON JET VACUUM VESSEL..... 29

FIG. 1.13 - MAGNETIC FIELD AND CURRENT SENSORS (ISOMETRIC VIEW)..... 30

FIG. 1.14 - MAGNETIC FIELD/CURRENT SENSORS IN THE VV CROSS-SECTION 31

FIG. 1.15 - TRAJECTORY OF THE PLASMA IN THE VESSEL DURING PULSE 34078 (AVERAGED TOROIDALLY)33

FIG. 1.16 - N=1, M=1 PLASMA KINK MODE 35

FIG. 1.17 - GLOBAL VDE MODEL (SQUARE BOXES REPRESENT EQUATIONS, ROUND BOXES DATA)..... 39

FIG. 1.18 - AXISYMMETRIC MOVEMENTS OF THE VACUUM VESSEL: RIGID-BODY ROLLING AND RADIAL MOTION IN THE POLOIDAL PLANES. 41

FIG. 1.19 - VERTICAL VESSEL DEFORMATION..... 42

FIG. 1.20 - NON-AXISYMMETRIC MOVEMENTS OF THE VACUUM VESSEL. 43

FIG. 1.21 - STRESS CONCENTRATION AT THE BASE OF A MAIN VERTICAL PORT (INBOARD) OBTAINED..... 45

WITH THE NON-LINEAR FE ABAQUS LOCAL MODEL 45

FIG. 2.1 - A BÉZIER CURVE..... 50

FIG. 2.2 - GEOMETRY OF A COIL SEGMENT 51

FIG. 2.3 - A TF COIL REPRESENTED BY A CHAIN OF STRAIGHT AND CURVED BÉZIER SEGMENTS..... 51

FIG. 2.4 - RECTANGULAR BRICK GEOMETRY..... 53

FIG. 2.5 - GEOMETRY FOR THE ERROR STUDY ON THE SINGLE-BRICK APPROXIMATION OF AN ARC-SHAPED COIL SEGMENT 55

FIG. 2.6 - 2D NORMALISED ERROR PLOTS FOR $\Delta\vartheta$=5° AND 45° @ Z=0, W/R=H/R=0.2 (COLOR MAP). 58

FIG. 2.7 - NORMALISED ERROR PLOTS FOR $\Delta\vartheta$=20° @ Z=0, W/R=H/R=0.2..... 59

FIG. 2.8 - PEAK ERROR AS A FUNCTION OF COIL ARC GEOMETRY..... 59

FIG. 2.9 - GEOMETRY TO DETERMINE ERROR BOUNDS ON THE SINGLE-BRICK APPROXIMATION..... 60

FIG. 2.10 - 2D NORMALISED ERROR PLOT IN CASE OF 10-BRICKS DISCRETISATION FOR $\Delta\vartheta$=45° @ Z=0, W/R=H/R=0.2 62

FIG. 2.11 - MAXIMUM ERROR AS A FUNCTION OF THE NUMBER OF BRICKS USED..... 62

FIG. 2.12 - COIL DECOMPOSITION FOR MAGNETIC FORCE INTEGRATION 68
FIG. 2.13 - QUALITATIVE VERTICAL FORCE BALANCE DURING AN AXISYMMETRIC VDE (ONLY MAGNETIC FORCES ARE CONSIDERED) 70
FIG. 2.14 - QUALITATIVE PATTERN OF NON-AXISYMMETRIC TOROIDAL EDDY CURRENTS IN THE VESSEL DUE TO A PLASMA TILT + SHIFT. THE STABILISING FORCES ARISING ON THE VESSEL ARE ALSO INDICATED.73
FIG. 2.15 - COMET MODEL OF THE JET TF AND PF COIL SYSTEM 74
FIG. 2.16 - DISTRIBUTED LOAD ON TF COIL 1 DUE TO PLASMA KINK 74
FIG. 2.17 - RESULTANT LOADS ON ALL 32 TF COILS DUE TO PLASMA KINK (TOTAL = 1 MN) 75
FIG. 2.18 - SIDEWAYS FORCE ON THE PLASMA (TOP AND ISOMETRIC VIEWS) 78
TABLE 2.5 - FORCES ON KINKED PLASMA IN JET PULSE 34078. 78
FIG. 2.19A - FORCE BALANCE THROUGHOUT TOKAMAK COMPONENTS DURING A SIDEWAYS EVENT (PHASE I - MAXIMUM ACCELERATION). 80
FIG. 2.19B: PHASE II) - MAXIMUM VELOCITY 81
FIG. 2.19C: PHASE III) - MAXIMUM ELONGATION 82
FIG. 3.1 - SCHEME OF THE AXISYMMETRIC ROLLING MOTION MODEL 85
FIG. 3.2 - FOURIER SPECTRA OF THE AXISYMMETRIC RESPONSE SIGNALS FOR JET PULSE 38690 86
FIG. 3.3 - NASTRAN FINITE ELEMENT MODEL OF HALF-OCTANT OF THE VACUUM VESSEL, SHOWING THE ROLLING MOTION EIGENMODE SUPERIMPOSED TO THE UNDEFORMED SHAPE 87
FIG. 3.4 - HYDRAULIC DAMPER AT THE MAIN VERTICAL PORTS 91
FIG. 3.5 - QUALITATIVE HISTORY OF THE VESSEL VERTICAL FORCE DURING A VDE 92
FIG. 3.6 - SIMPLIFIED MODEL OF THE ELECTRODYNAMIC INTERACTION BETWEEN PLASMA, PF/DIVERTOR CURRENTS AND ETH TOROIDAL EDDY CURRENTS IN THE VESSEL 95
FIG. 3.7 - HALO CURRENT FORCE MODEL 98
FIG. 3.8 - FOURIER SPECTRUM OF THE MEASUREMENTS SIDEWAYS RESPONSE OF JET PULSE 34078 99
FIG. 3.9 - DEFORMED SHAPE OF THE VESSEL DUE TO SIDEWAYS LOAD 102
FIG. 3.10 - LUMPED-PARAMETER MODEL FOR THE SIDEWAYS MOTION OF JET VACUUM VESSEL 102
FIG. 3.11 - PERSISTENCE OF THE OFFSET IN THE SIDEWAYS DISPLACEMENT SIGNAL BETWEEN SUBSEQUENT JET PULSES 106
FIG. 3.12 - QUALITATIVE SCHEME FOR THE MAGNETIC DAMPING EFFECT 106
FIG. 3.13 - FINITE ELEMENT MODEL FOR THE NON-AXISYMMETRIC ROLLING MOTION 108
FIGURE 4.3 - DE-SPIKING ALGORITHM 141
FIGURE 4.4 - OCCURRENCE AND STABILITY OF LOOPS IN LEVENBERG-MARQUARDT ALGORITHM 150
FIG. 4.1 - PATHOLOGICAL TEST FUNCTION FOR LEVENBERG-MARQUARDT STAGNATION LOOPS 152
FIG. 4.2 - TEST WAVEFORM FOR LM DAMPING STRATEGY STUDY 154
FIG. 4.3 - MINIMISATION PATHS CORRESPONDING TO THE RUNS WITH BOOST AND DROP FACTORS EQUAL TO (6.3, 3.5) AND (2, 6.3). 155
FIG. 5.1 - ROLLING MOTION OF PULSE 16297 171
FIG. 5.2 - EFFECT OF DE-SPIKING ON THE FITTING PROCEDURE, EXEMPLIFIED BY THE PROFILE OF χ^2 AS A FUNCTION OF THE PARAMETER β_{VV} CLOSE TO THE MINIMUM. 172
FIG. 5.3 - ROLLING MOTION OF PULSE 20802 173
FIG. 5.4 - ROLLING MOTION OF PULSE 37628 177

FIG. 5.5 - VERTICAL MVP SUPPORT FORCE PULSE 37628 177
FIG. 5.6 - MECHANICAL AND MAGNETIC MEASUREMENTS FOR PULSE 37628 178
FIG. 5.7 - AVERAGE MVP DAMPER RADIAL FORCE FOR PULSE 37628 179
FIG. 5.8 - AVERAGE TOTAL MVP RADIAL FORCE FOR PULSE 37628 179
FIG. 5.9 - ROLLING MOTION OF PULSE 38690 181
FIG. 5.10 - VERTICAL MVP SUPPORT FORCE PULSE 38690 181
FIG. 5.11 - VERTICAL IVP MOTION PULSE 38690 182
FIG. 5.12 - VERTICAL VESSEL FORCE PULSE 38690 182
FIG. 6.13 - SIDEWAYS MOTION OF PULSE 34078 186
FIG. 6.14 - MVP SIDEWAYS SUPPORT FORCE IN PULSE 34078 187
FIG. 6.15 - SIDEWAYS FORCE IN PULSE 34078 187
FIG. 6.16 - SIDEWAYS MOTION OF PULSE 38705 190
FIG. 6.17 - MVP SIDEWAYS SUPPORT FORCE IN PULSE 38705 190
FIG. 6.18 - SIDEWAYS FORCE IN PULSE 38705 191
FIG. 6.19 - EFFECT OF MHP SUPPORTS AND MAGNETIC DAMPING IN PULSE 38705 191
FIG. 6.20 - DEVIATIONS FROM THE AXISYMMETRY OF ROLLING MOTION AND VERTICAL SUPPORT FORCE IN PULSE 34078 192
FIG. 7.1 - EFFECT OF INCREASING SIDEWAYS FORCE UP TO THE MAXIMUM EXPECTED AT 4T, 6MA (F_{SW}=4 TO 7 MN × 38 MS) 205
FIG. 7.2 - EXTRAPOLATED EFFECT OF ADDITIONAL HORIZONTAL VESSEL RESTRAINT (K_{SW}=20 TO 2000 MN/M) 206
FIG. A.1 - COMET SCREENSHOT SHOWING THE MAIN FIELD VISUALISATION METHODS: ARROW PLOT, COLOR MAP AND FIELD LINES 209
FIG. A.2- TEMPEST SCREENSHOT SHOWING THE MAIN WINDOW AND THE DIALOG BOX TO ENTER PARAMETERS VALUES 213
FIG A.3- POSSIBLE SERIES CONNECTIONS OF A MASS/SPRING/DAMPER SYSTEM 219
FIG. A.4 - RESPONSE OF SERIES SPRING/DAMPER SYSTEMS TO A 1 KN× 1S RECTANGULAR FORCE PULSE 221

LIST OF TABLES

TABLE 1.1 - EVOLUTION OF JET VV SUPPORT & RESTRAINT SYSTEM 24
TABLE 1.2 - MECHANICAL DIAGNOSTICS ON JET VV 29
TABLE 1.3 - MAGNETIC DIAGNOSTICS ON JET VV 31
(N° INDICATES THE NUMBER OF INSTRUMENTED OCTANTS TIMES THE NUMBER OF SENSORS PER OCTANT) 31
TABLE 2.1 - DATA FOR TF/KINKED PLASMA FORCE CALCULATION..... 74
TABLE 2.2 - FORCES BETWEEN TF COILS AND TILTED/SHIFTED PLASMA. 75
TABLE 2.3 - FORCES BETWEEN PF AND DIVERTOR COILS AND TILTED/SHIFTED PLASMA..... 76
TABLE 3.1 - PEAK-TO-PEAK ERROR WITH REDUCED NUMBER OF MODES 88
TABLE 3.2 - PARAMETERS FOR THE ROLLING MOTION MODEL. 90
TABLE 3.3 - PARAMETERS FOR 2 D.O.F. SIDEWAYS MOTION MODEL..... 103
TABLE 4.1 - N_{LM} VS. BOOST AND DROP FACTORS FOR THE IDEAL TEST. 154
TABLE 5.1 - ESTIMATED MECHANICAL/FORCE PARAMETERS FROM PRE-DIVERTOR ROLLING MOTION EVENTS
. 174
TABLE 5.2 - ESTIMATED FORCE PARAMETERS FROM MKII ROLLING MOTION EVENTS..... 183
TABLE 6.3 - ESTIMATED FORCE PARAMETERS FOR SDE 34078..... 188
TABLE 6.4 - ESTIMATED PARAMETERS FOR SDE 38705 189

1
INTRODUCTION

This chapter provides the background necessary to understand the terms of the problem and the purpose of the models described in the next chapters. A brief overview of JET hardware is given first in section 1.1, including all the essential details on the mechanical and magnetic diagnostic systems used in the analysis. The conventional "forward" approach employed so far to study disruptions and plasma instabilities, consisting of predictive calculations based on first principles, is outlined in section 1.2. The shortcomings of this approach and the role that the proposed parameter estimation procedure may have in circumventing them are highlighted. Finally, in section 1.3 the range of observed mechanical effects is described including axisymmetric and non-axisymmetric movements of the JET vacuum vessel.

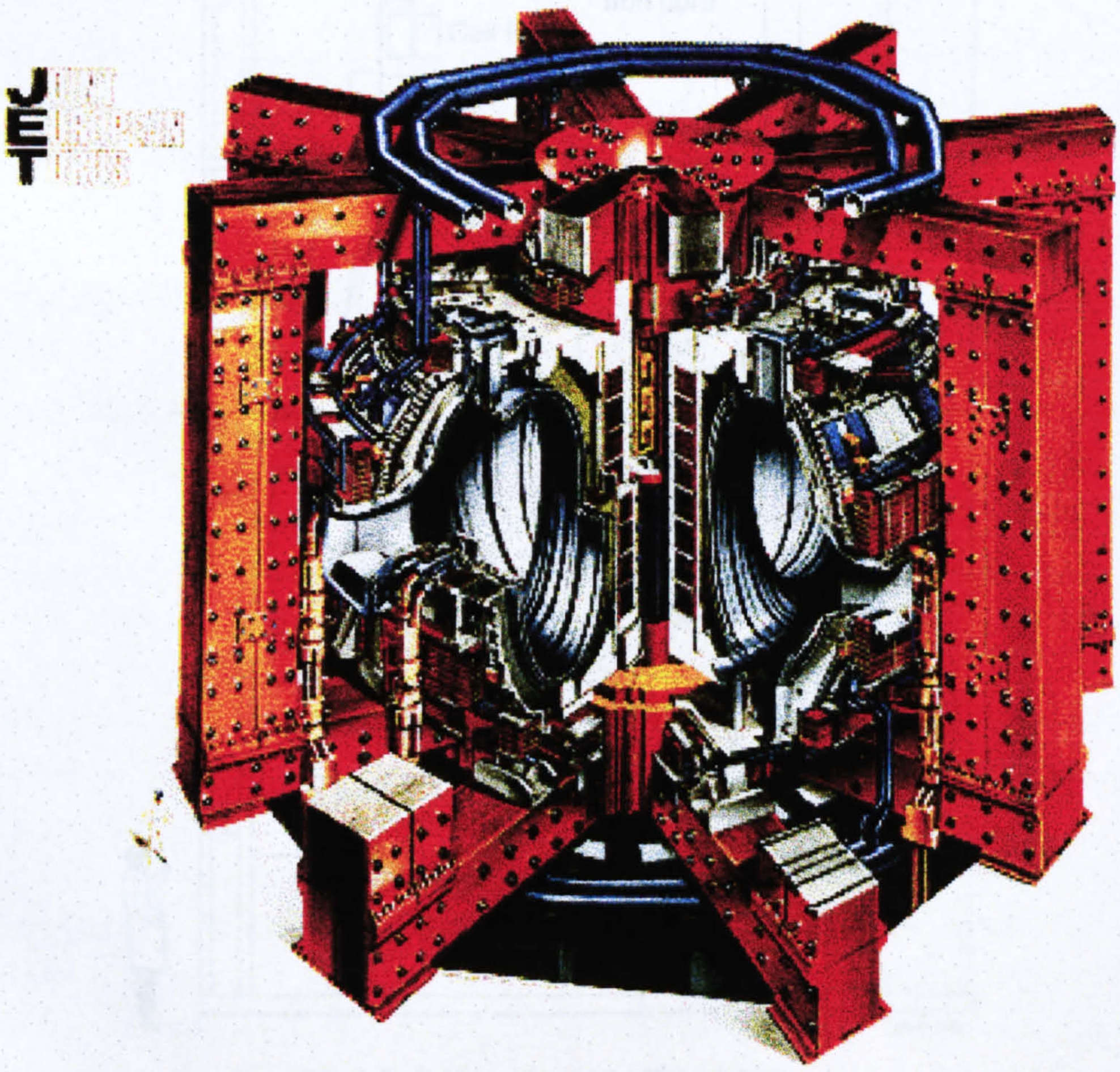


Fig. 1.1 - The JET Tokamak

1.1 Overview of JET

This section gives the background information strictly needed to understand the hardware details of the models presented in chapter 3. For a more general introduction to JET and to the technology of magnetic confinement fusion see for example [1, 2, 3, 6].

1.1.1 Structural components of the JET Tokamak

This section provides an short overview of JET hardware, schematically represented in Fig. 1.2. This includes the main structural components (subdivided in 8 octants), the magnetic circuit and the arrangement of connections and ground supports. More information on the design of JET structure can be found in [5,7].

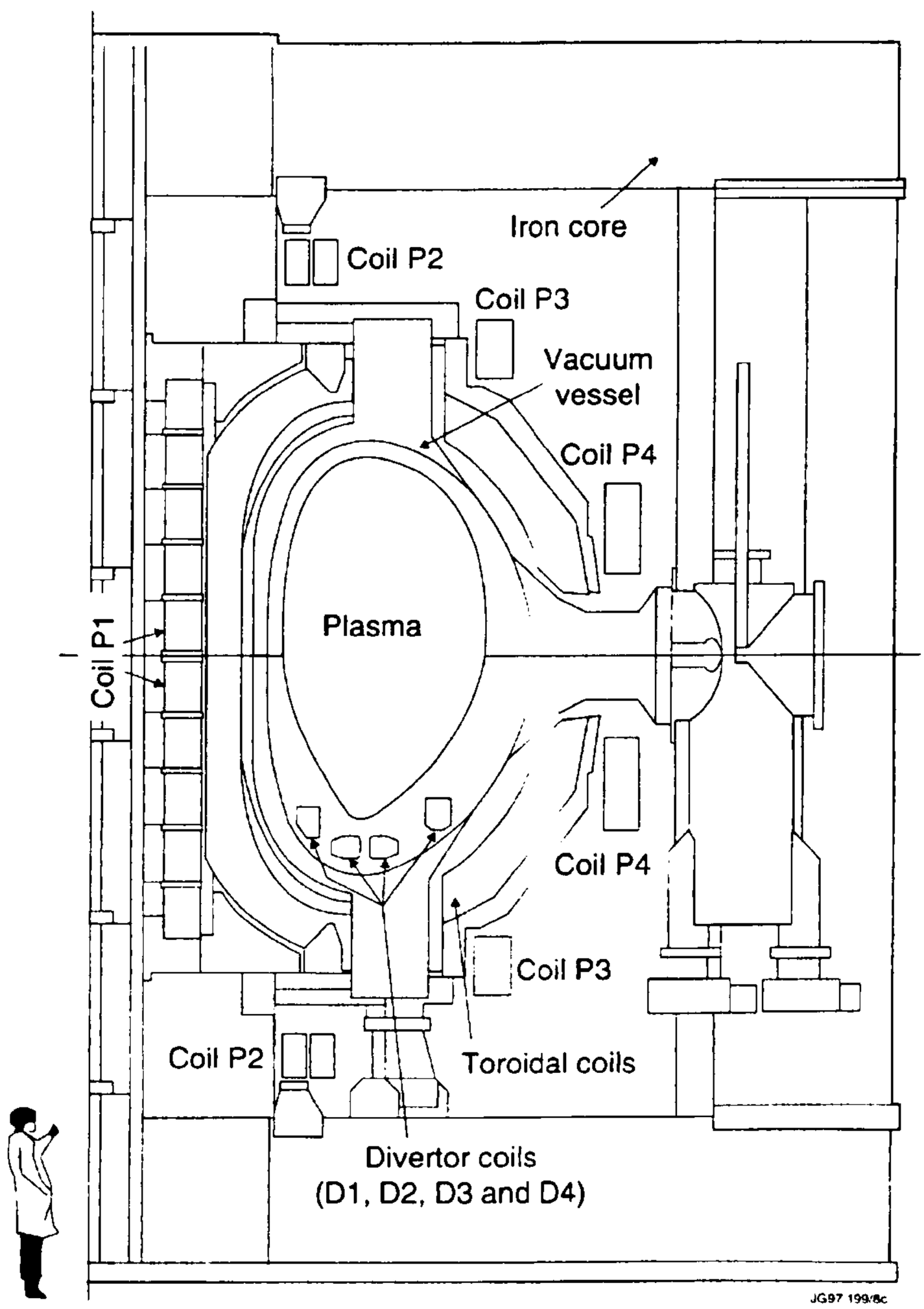


Fig. 1.2 - Cross-section of the JET machine

1.1.1.1 Poloidal Field (PF) and Divertor coils

The poloidal field system includes a total of 11 coils made of freon-cooled copper turns, insulated with an epoxy/fibreglass compound and enclosed by an Inconel casing (Fig. 1.2 and 1.3). Seven PF coils are placed externally to the Mechanical Structure, symmetrically respect to the equatorial plane. PF coil turns are connected in series, with flexible configurations and polarities, to the following four independent circuits (the signs have to be compared with the plasma polarity, i.e. $I_{PLA}>0$ if clockwise):

1) *Magnetisation* (+P1): the primary of the transformer
2) *Radial field* (+P2U,+P3U, +P2L,+P3L): a dipole field used to control the plasma vertically
3) *Shaping field* (–P2U, +P3U, –P2L, +P3L): a quadrupole field that gives the plasma its distinctive triangular shape by respectively pulling with the P2 and pushing with the P3.
4) *Vertical field* (+P4U,+P4L): equilibrates the plasma current against hoop tension.

Four additional coils (D1 to D4), installed inside the vessel in 1993, generate an X-point magnetic configuration which diverts scrape-off layer (SOL) fluxes and impurities towards a suitable target structure (the divertor).

From the mechanical viewpoint, all these coils are subject to large hoop forces resisted by their own stiffness. Vertical loads on the PF and TF coils and are supported by the mechanical structure, while vertical loads on the divertor coils are transferred directly to the vessel.

1.1.1.2 Toroidal Field (TF) Coils

The toroidal field system (Fig. 1.3 b) is made by 32 freon-cooled copper coils with a distinctive Princeton-D shape, characterised by a curvature radius increasing with the distance from the vertical axis of the machine. This is necessary to produce a state of pure hoop stress when the coil is immersed in a toroidal field, provided that the straight vertical part is uniformly supported. Each coil carries a nominal current of 1.6 MA (corresponding $B_{T0}=3.45$ at $r_0=2.96$ m). The current is scheduled to be upgraded in early 1999 to 1.72 MA so as to get a nominal field $B_{T0}=4.0$ T.

The shape of the coils is, in reality, slightly different from a true Princeton-D as each turn was formed from a straight bar by bending around 6 circular forms of different radii (this is exploited in 2.1.1 to get a compact geometrical representation of the coils).

From the viewpoint of the loads, the toroidal geometry of the field implies that each TF coil is subject to a nominal net centripetal force of ~18 MN. The total compressive load is taken by the PF1 coil via the Inner Cylinder of the mechanical structure (see below). Interaction with the plasma current and the PF coils generates out-of-plane forces, roughly top-bottom symmetric in the current operational configuration, which tend to tilt each TF coil around the equatorial plane with a torque of the order of 6~7 MNm. These forces are supported by a number of teeth and pads in the mechanical structure, into which the coils are fitted as shown in Fig. 1.4.

Unfortunately, some of these teeth support only a fraction of the width and thus apply concentrated loads up to ~500 kN. Since the TF coils have no steel casing (for reasons of compactness), this loads generate very high peak stresses in the inter-turn insulation, which is a relatively brittle epoxy-fibreglass composite. For these and other reasons, the TF coils are an extremely critical component that needs a very detailed stress assessment prior to be operated in the upgraded configuration [9].

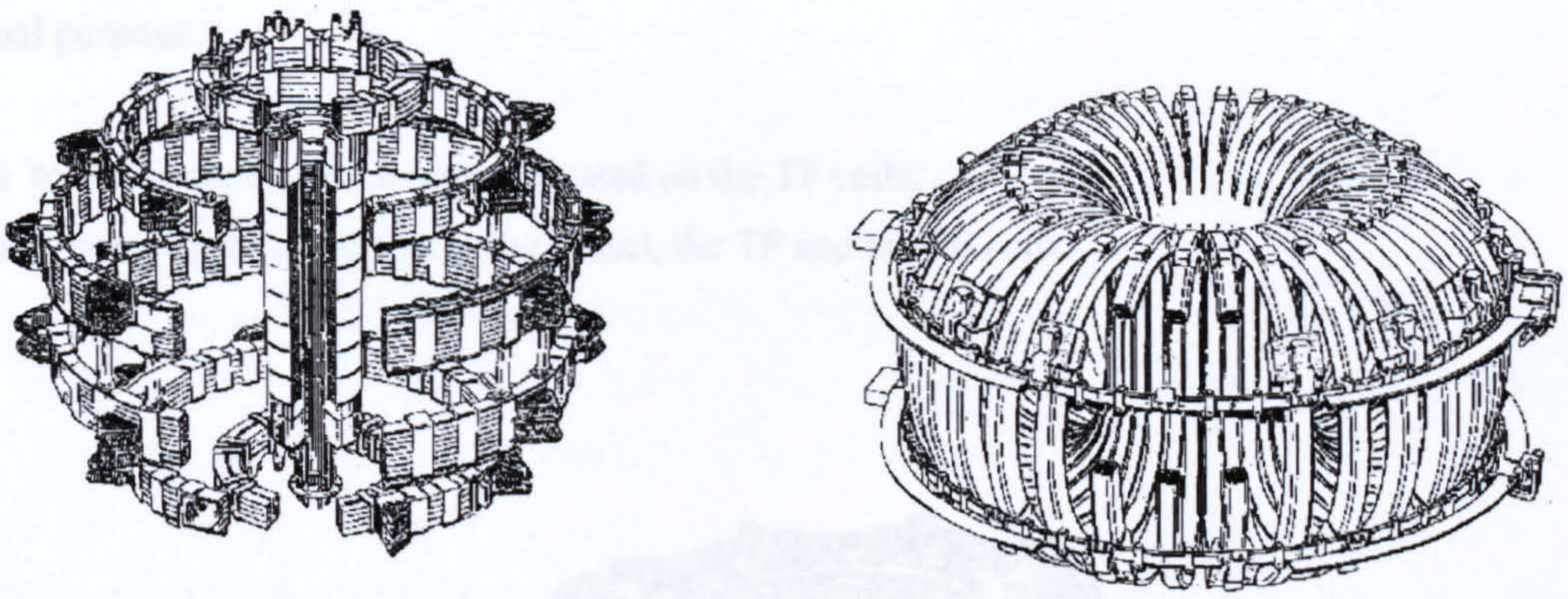


Fig. 1.3 - Poloidal and Toroidal Field coil systems

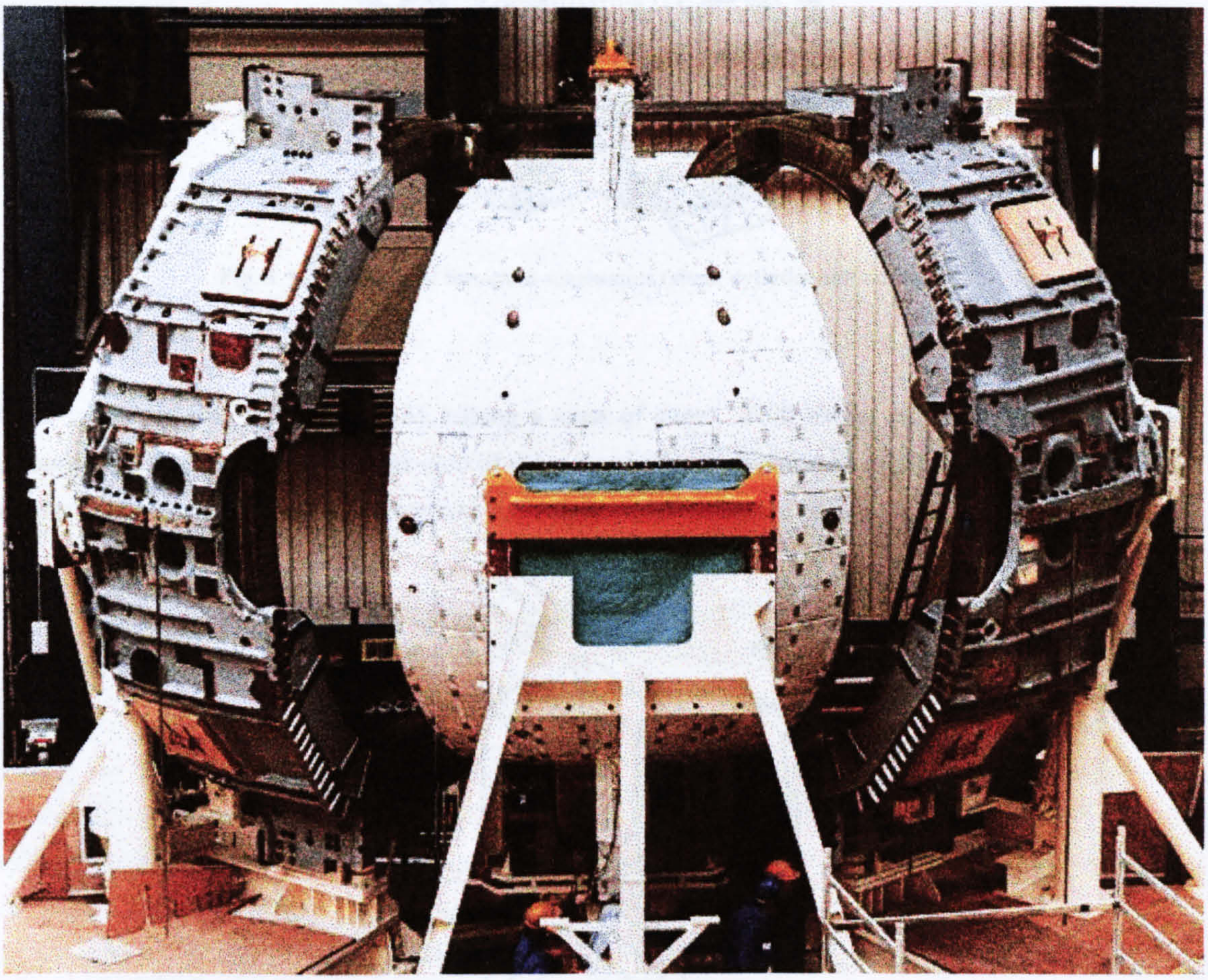


Fig. 1.4 - Assembly of a JET octant showing the vacuum vessel, four TF coils and part of the MS shell.

1.1.1.3 Mechanical Structure and Iron Core

The Mechanical Structure (MS) is a thick toroidal shell weighing about 450 tonnes, made of cast iron and Inconel, which represents a distinctive design choice in JET respect to other tokamaks (Fig. 1.5). This structure, characterised by a high torsional stiffness, encloses vacuum vessel and TF coils and serves a dual purpose:

1) to bear out-of-plane forces generated on the TF coils;
2) to provide static support to the vessel, the TF and the PF coils.

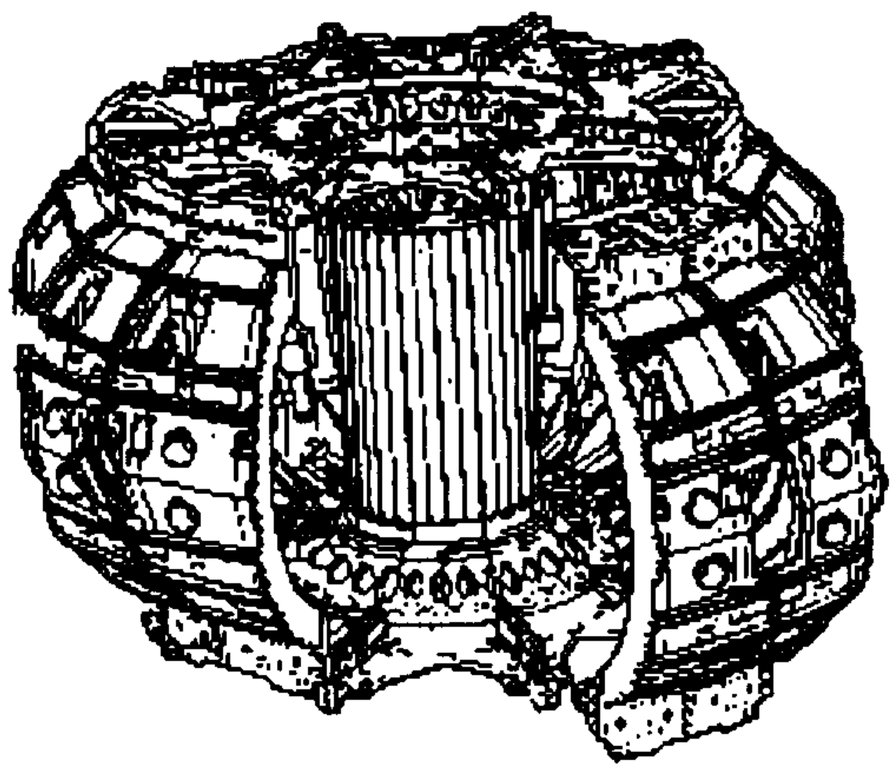


Fig. 1.5 - Mechanical Structure schematics (shell, cylinder and collar)

Eight laminated iron limbs (Fig. 1.6), having a mass of about 2700 tonne, represent the mechanical backbone of the machine and form the core of the magnetic circuit linking P1 and plasma. The Iron Core provides support to the Mechanical Structure with eight pedestals on the bottom horizontal limbs.

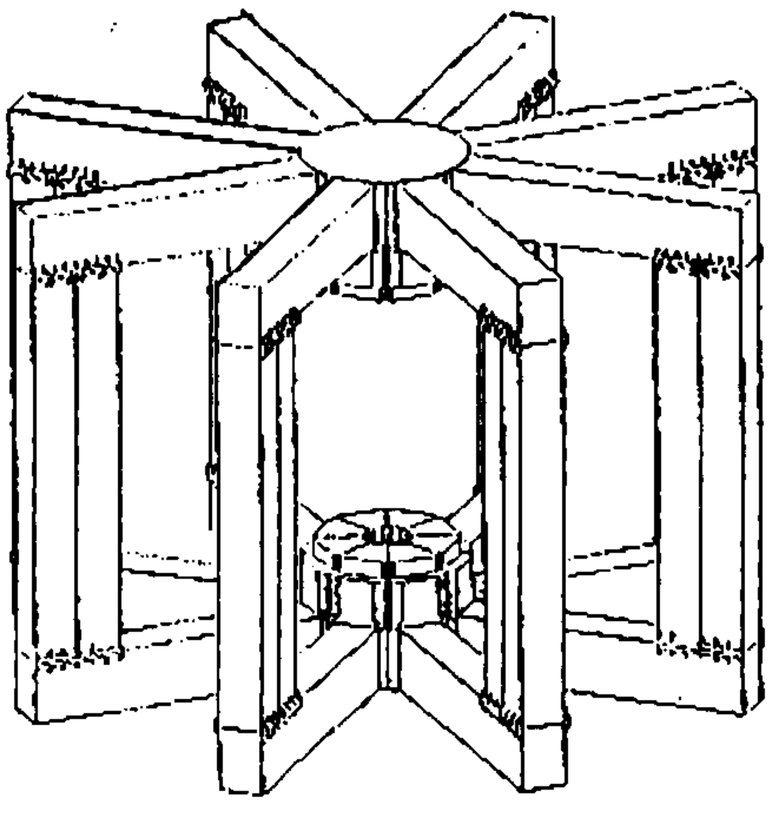


Fig. 1.6 - Iron Core limbs

1.1.1.4 Vacuum vessel

The vacuum vessel (VV) is a toroidal shell made of Inconel, depicted in Fig. 1.8 in its present configuration. The vessel has the following primary functions:

- to contain the plasma in ultra-vacuum (~10^{-7} Pa), ultra-clean conditions;
- to withstand static, impulsive and fatigue operational loads without permanent or excessive deformations;
- to have an optimal electrical resistance as a trade-off between two opposite requirements: high resistance to facilitate plasma breakdown, low resistance to maximise the passive stabilising effect on plasma movements (see section 1.2).

The vessel, originally designed to be a compliant, lightly loaded structure, is subject to disruption forces of several MN which are much higher than anything previously foreseen. These loads cause large displacements and stresses and make the vessel the most critical component of the machine from the safety standpoint. Because of this, the vessel is at the centre of this investigation and will be described here in some more detail.

Fig. 1.9 shows how each octant is made by five rigid sectors, alternated by bellows to increase the toroidal resistance. The bellows are bridged by spacers (Fig. 1.7) which prevent them from being crushed by the atmospheric pressure. The spacers practically cannot take any significant tension, introducing a non-linearity in the structure; moreover, they may have a role in determining the friction forces (see 3.2.1.5) The vessel is double-walled in order to maximise the bending stiffness, to provide a double vacuum barrier and to allow hot fluid in the interspace (necessary to get the vessel up to operating temperature, which may be as high as 320°C).

Each octant has a number of access conducts of which the largest are the Main Horizontal Port (MHP) on the equatorial plane and the two Main Vertical Ports (MVP) at the top and bottom. These were designed primarily for pumping, maintenance and diagnostics, although they have been used to attach some of the external restraints and supports progressively added over the years. This misuse, forced by the lack of access, is causing some problems because of the cantilevered geometry of supports.

The arrangement of restraints and external supports, showed schematically in Fig. 1.11, is important in order to understand the dynamic models described in chapter 3. The supports are listed and briefly described in Table 1.1, which also indicates the JET pulse ranges in which particular combinations of supports and restraints were present. During each one of these periods the mechanical properties of the machine may be assumed to be relatively stable. However, one should keep in mind that more than 80 shutdowns have occurred during JET's life and each time some intervention has been carried out on the machine, possibly affecting its mechanical response in way which is practically impossible to track.

Period	I	II	III	IV	V	VI	VII
Start Date	**11/84**	**5/87**	**3/89**	**6/90**	**1/94**	**3/96**	**7/96**
Start JET Pulse	3200	11217	19096	21324	28276	35804	37186
Octant Joint/MHP Spring Supports: elastic supports attached to the MS and carrying the dead weight of the VV	✓	✓	✓	✓	✓	✓	✓
MHP Support Legs: introduced to prevent vertical VV movements when VDEs were first noticed.	✓	✓	✓	✓	✓	✓	✓
MVP Dynamic Brakes: support legs connected to the horizontal limbs and preventing tangential and vertical MVP movements. Originally activated by a friction mechanism that would lock only during a fast transient while allowing slow thermal expansions. As the performance was erratic, now are locked manually (see also [17]).		✓	✓	✓	✓	✓	✓
Inner Rings: Inconel plates welded on the inner wall which make the vessel much stiffer respect to both radial and vertical forces (Fig. 1.8)			✓	✓	✓	✓	✓
MVP Dampers Mark I: hydraulic dampers working in the radial direction (2×port), retired because thought to be obsolete when the Dynamic Brakes were installed	✓						
MVP Dampers Mark II: single-piston hydraulic cylinders, connected to the MS, installed to prevent observed MVP movements.				✓	✓		
MVP Dampers Mark III: refurbished versions with better oil-leak prevention and pressure relief valve to limit maximum force.						✓	✓
MHP Tangential Straps: these are oil cylinders linking the MHP to the MS, designed to provide a hoop force around the VV preventing sideways movements. Trapped air makes them behave like a combination spring+damper.						✓	✓
NBI: 2*80 tonne Neutral Beam injectors at octants 2&6 (see Fig. 1.10)		✓	✓	✓	✓	✓	✓
Divertor coils + MkI target: ~100 tonne mass increment					✓	✓	
Divertor target MkII.							✓

Table 1.1 - Evolution of JET VV support & restraint system

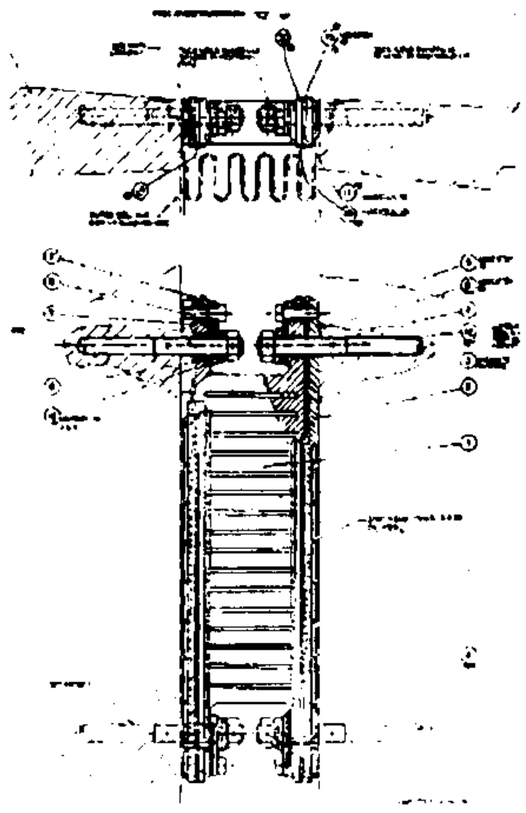


Fig. 1.7 - Spacers mounted across the bellows

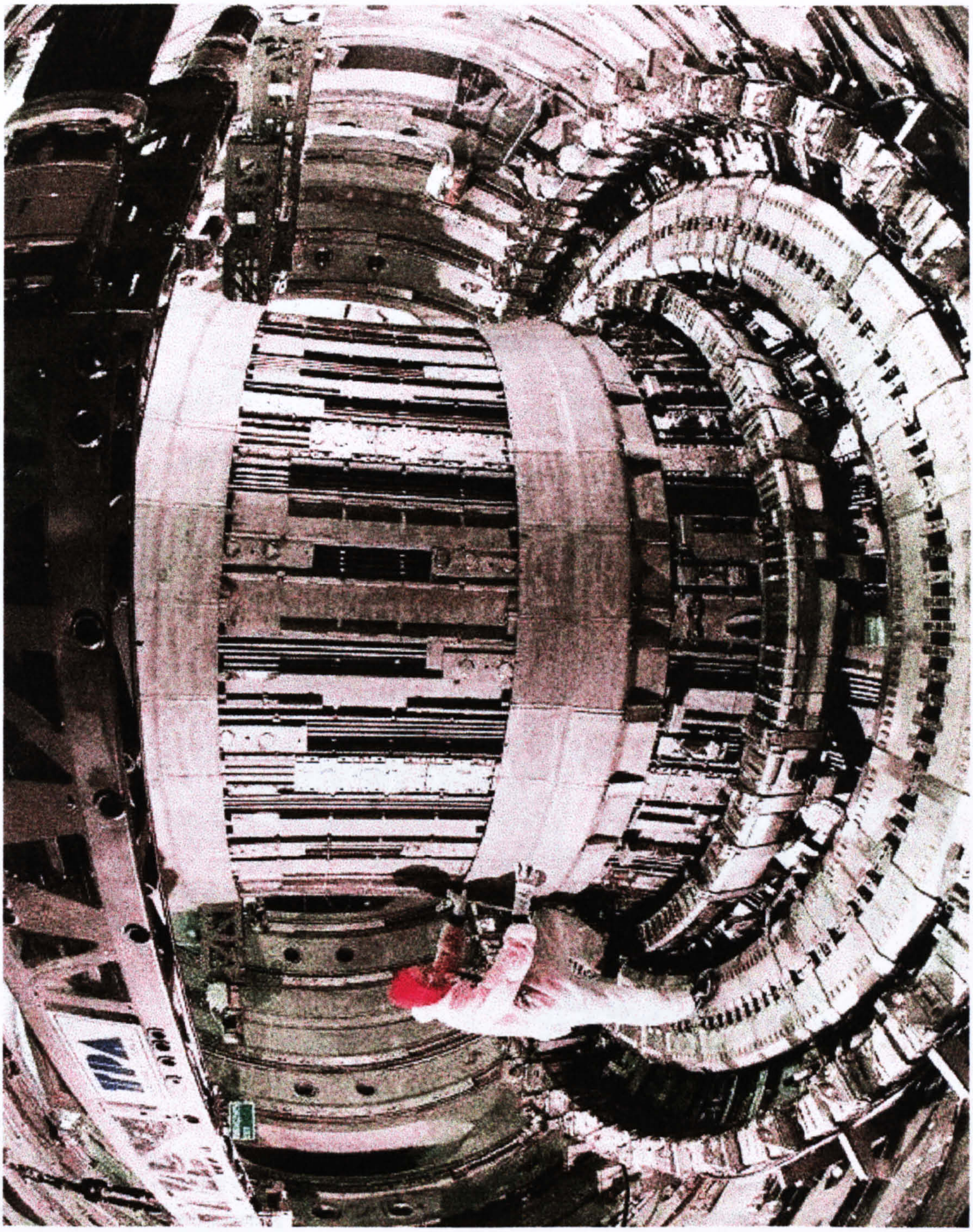


Fig. 1.8 - Internal view of the VV in the 1998 configuration

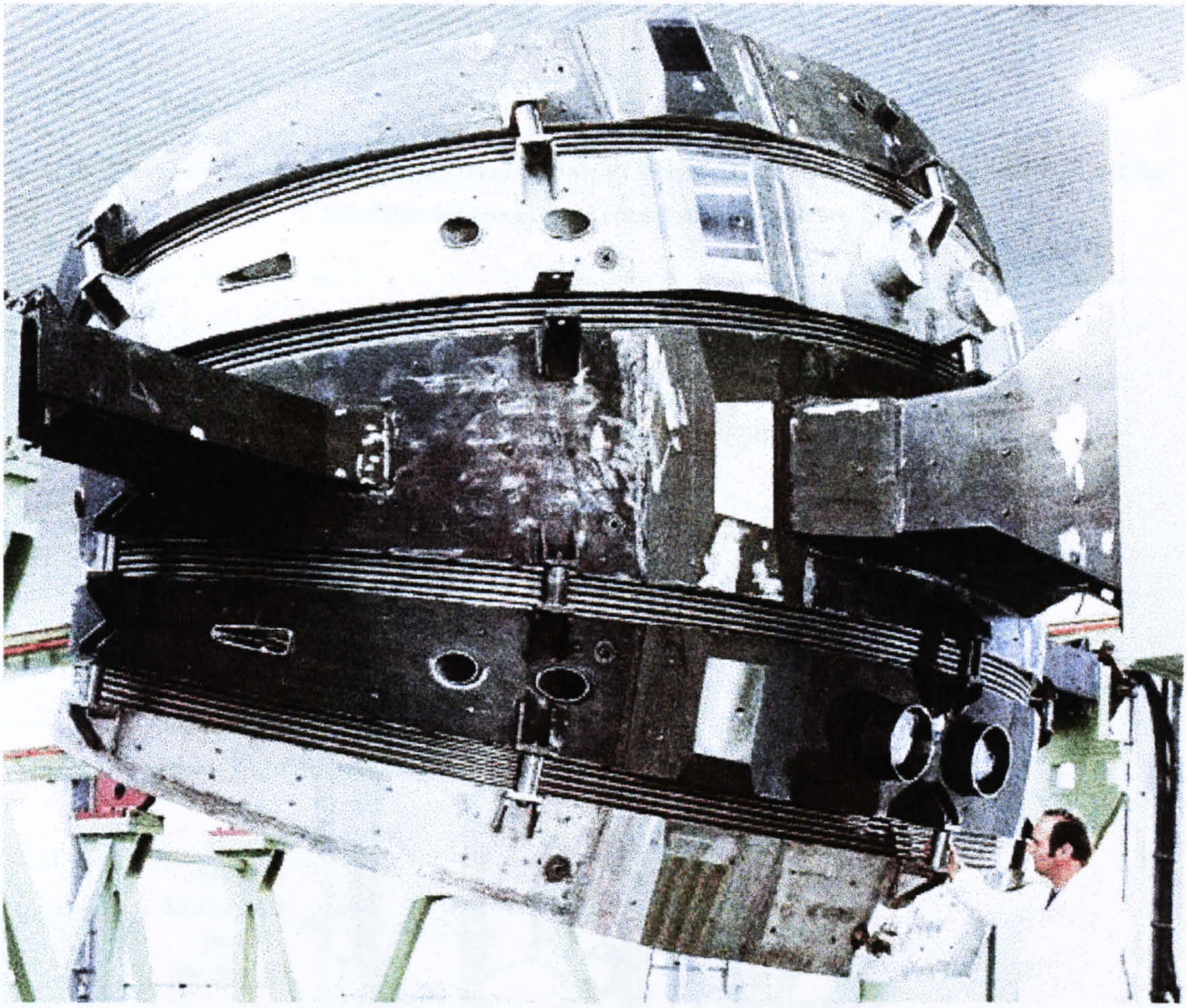


Fig. 1.9 - External view of a vessel octant before assembly. The 5 rigid sectors and the bellows can be seen clearly. The sectors are: 1 Central (carrying two Main Vertical Ports and one Main Horizontal Port), 2 Limiter and 2 Octant joint.

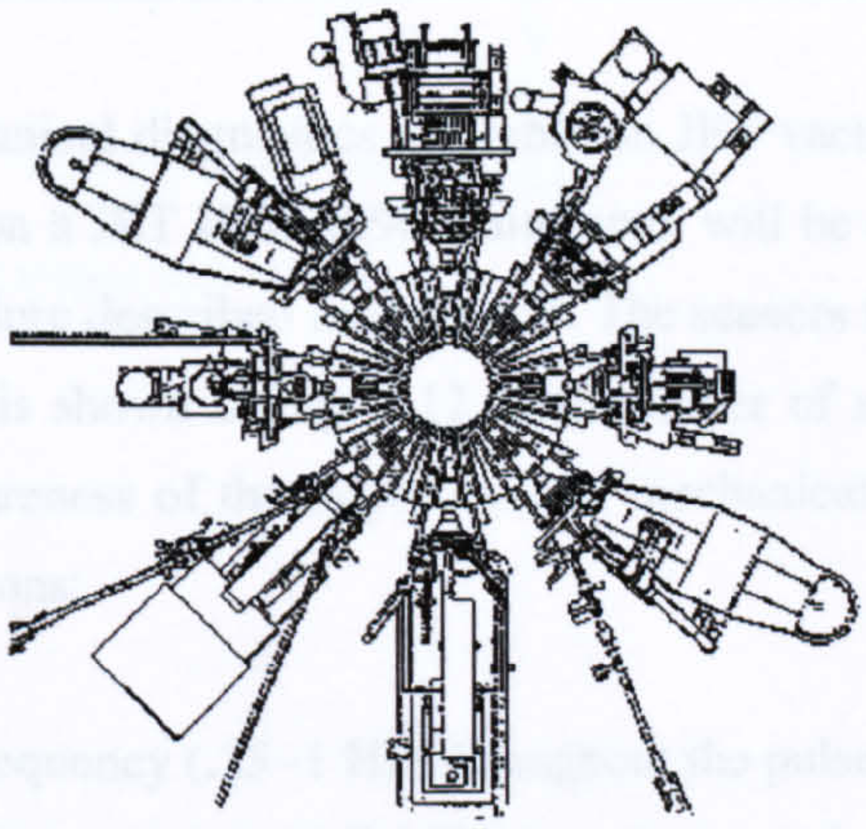


Fig. 1.10 - Vessel restraints at the equatorial plane (top view). The two large Neutral Beam Injector boxes and the two Pellet Injectors can be seen at opposite octants

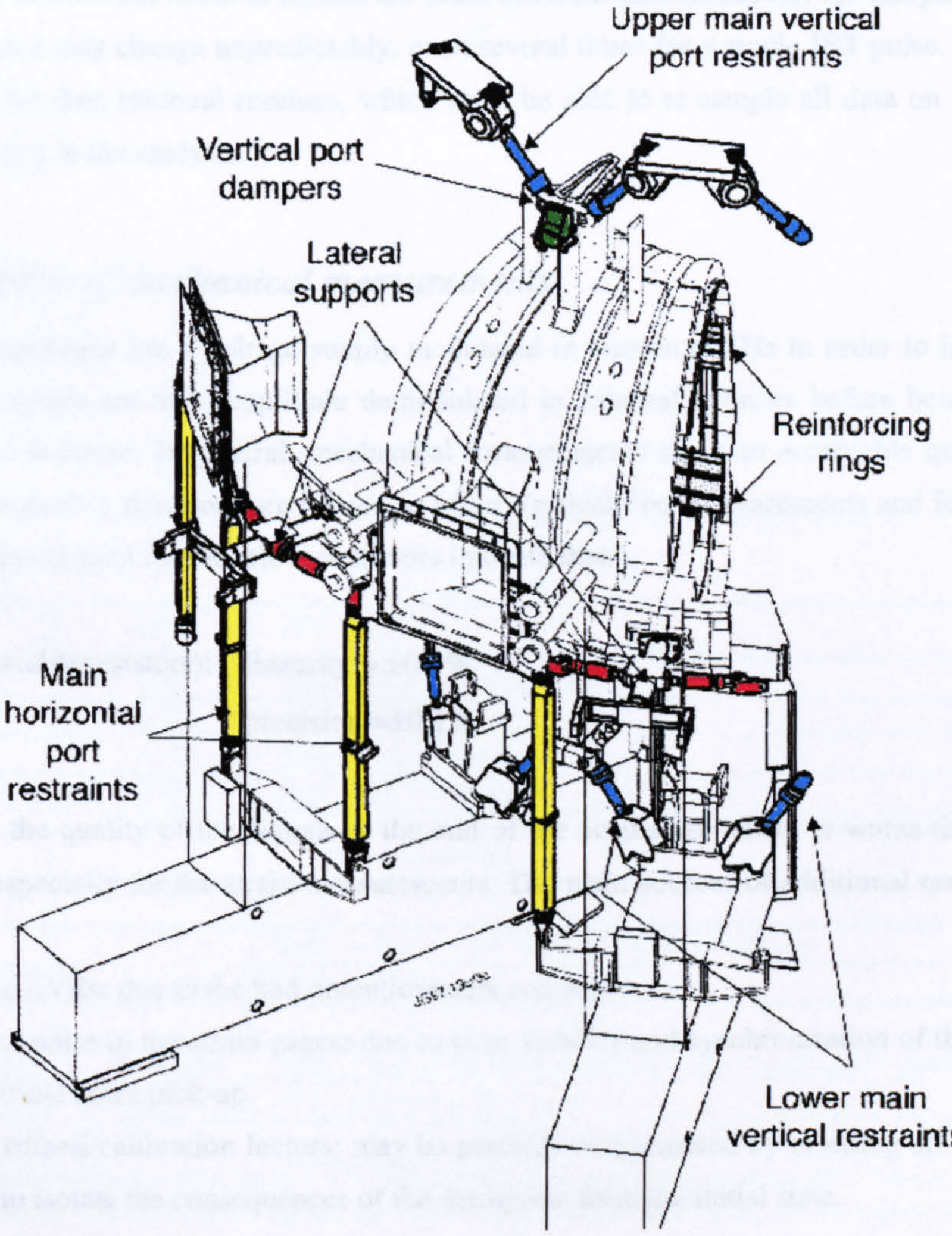


Fig. 1.11 - Vacuum vessel support system in the 1997 configuration

1.1.2 Mechanical vessel diagnostics

In this section the range of mechanical diagnostics available on JET vacuum vessel is described. These signals, stored in digital database on a JET IBM 3090 mainframe, will be used as the experimental basis for the parameter estimation procedure described in chapter 4. The sensors installed are listed in Table 1.2 and their position on the machine is shown in Fig. 1.12. The number of sensors has been growing with time, following the increasing awareness of the importance of mechanical effects. For disrupted pulses, each signal is recorded in two versions:

slow signal: sampled at low frequency (.25~1 Hz) throughout the pulse (duration ~50 s);

fast signal: sampled at high frequency (1 to 5 kHz) in a time window lasting ~2 s, centred on the disruption event by a post-trigger mechanism.

The time bases of different kinds of signals are often different and, moreover, the sampling frequency of any individual trace may change unpredictably, even several times for a single JET pulse. This adds some complication to the data retrieval routines, which must be able to re-sample all data on a common time base for consistency in the analysis.

1.1.2.1 Reliability of mechanical measurements

Mechanical diagnostics use a voltage supply modulated in tension at 5Hz in order to improve the S/N ratio [10]. The signals are then amplitude demodulated in external cubicles before being sampled and stored in the JPF database. In general, mechanical measurements show an acceptable quality. The most important signals used in this work are related to Main Vertical Port displacements and forces. For these, manufacturer-supplier data for the relevant sensors indicate that:

LVR (linear variable resistors): linearity = ±0.5%

Strain gages: precision =±0.1%;

Unfortunately, the quality of the signals at the end of the acquisition chain is worse than these values would suggest, especially for the strain measurements. The main sources of additional error can be listed as follows:

— spikes in the LVRs: due to the bad potentiometers contacts

— high level of noise in the strain gages: due to poor stability and synchronisation of the demodulators and/or electrical noise pick-up

— fluctuating offsets/calibration factors: may be partially compensated by resetting all initial offsets to zero, so as to isolate the consequences of the disruption from the initial state.

— signal swapping and polarity errors

Recently, the electronics has been moved to a new system and the reliability of the system has been dramatically improved.

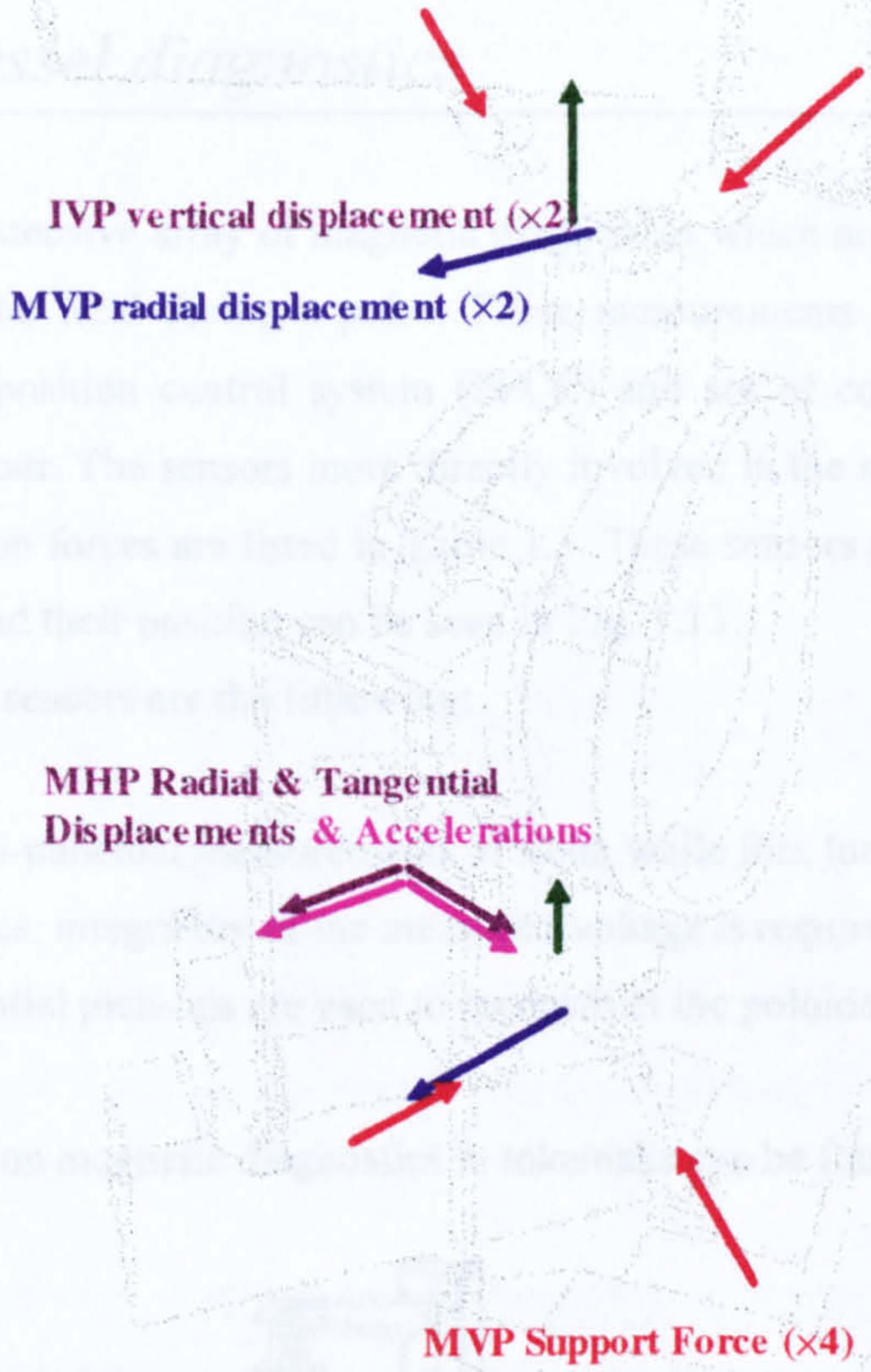


Fig. 1.12 - Main mechanical measurements on JET vacuum vessel

Displacement	Type	N°	Notes
MVP radial	LVR	8×2	odd octants only up to 1996
IVP vertical	LVR	8×2	odd octants only
MHP radial	LVR	8×1	from 1996 onwards
MHP tangential	LVR	8×1	from 1996 onwards
Inner wall vertical	optical	1×4	obtained with interferometric techniques from laser plasma density diagnostic. Not fully validated yet
Acceleration			
MHP radial		8×1	very noisy, low sensibility at low frequencies
MHP tangential		8×1	as above
Force			
MVP support legs	strain gage	8×4	2 sensors per leg are averaged to offset bending±15% precision [Tiziano]
MHP tang. strap	pressure	8×1	oil pressure on the piston

Table 1.2 - Mechanical diagnostics on JET VV (N° indicates the number of instrumented octants × the number of sensors per octant). Not all of these signals have been used, for the time being, for the parameter estimation procedure.

1.1.3 Magnetic vessel diagnostics

JET is equipped with an extensive array of magnetic diagnostics which are meant primarily to measure the evolution of the magnetic field during a pulse. These measurements are used in real-time by the plasma current, shape and position control system (PPCC) and are of course essential for any study related to the plasma behaviour. The sensors more directly involved in the assessment of induced or halo currents and related disruption forces are listed in Table 1.3. These sensors are placed all over inside and outside the vacuum vessel and their position can be seen in Fig. 1.13.

The main features of these sensors are the following:

- pick-up coils give quasi-punctual measurements of field, while flux loops give values averaged over large areas (in both cases, integration of the measured voltage is required);
- saddle loops and tangential pick-ups are used to reconstruct the poloidal field inside the vessel.

More detailed information on magnetic diagnostics in tokamaks can be found in [4].

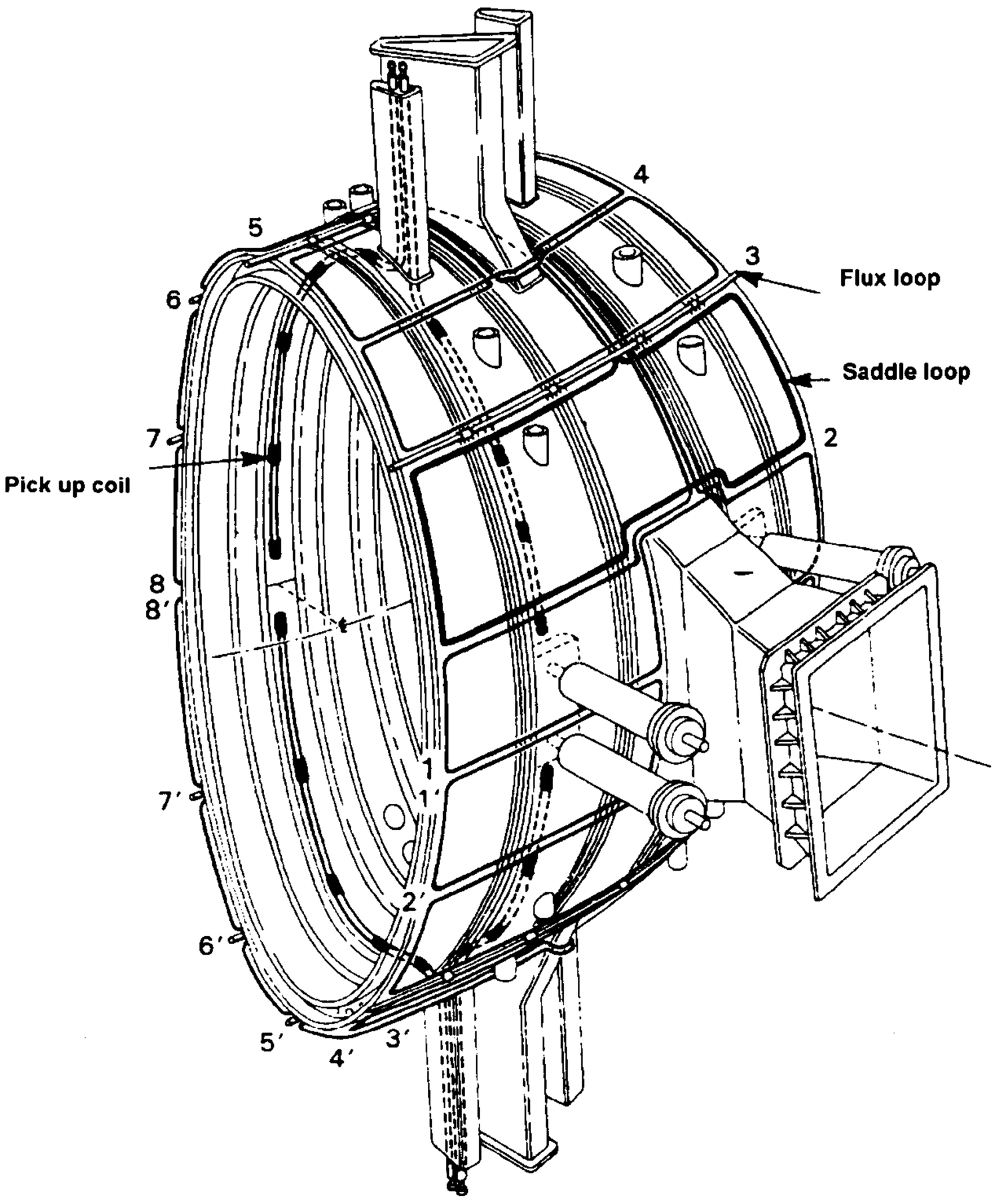


Fig. 1.13 - Magnetic field and current sensors (isometric view)

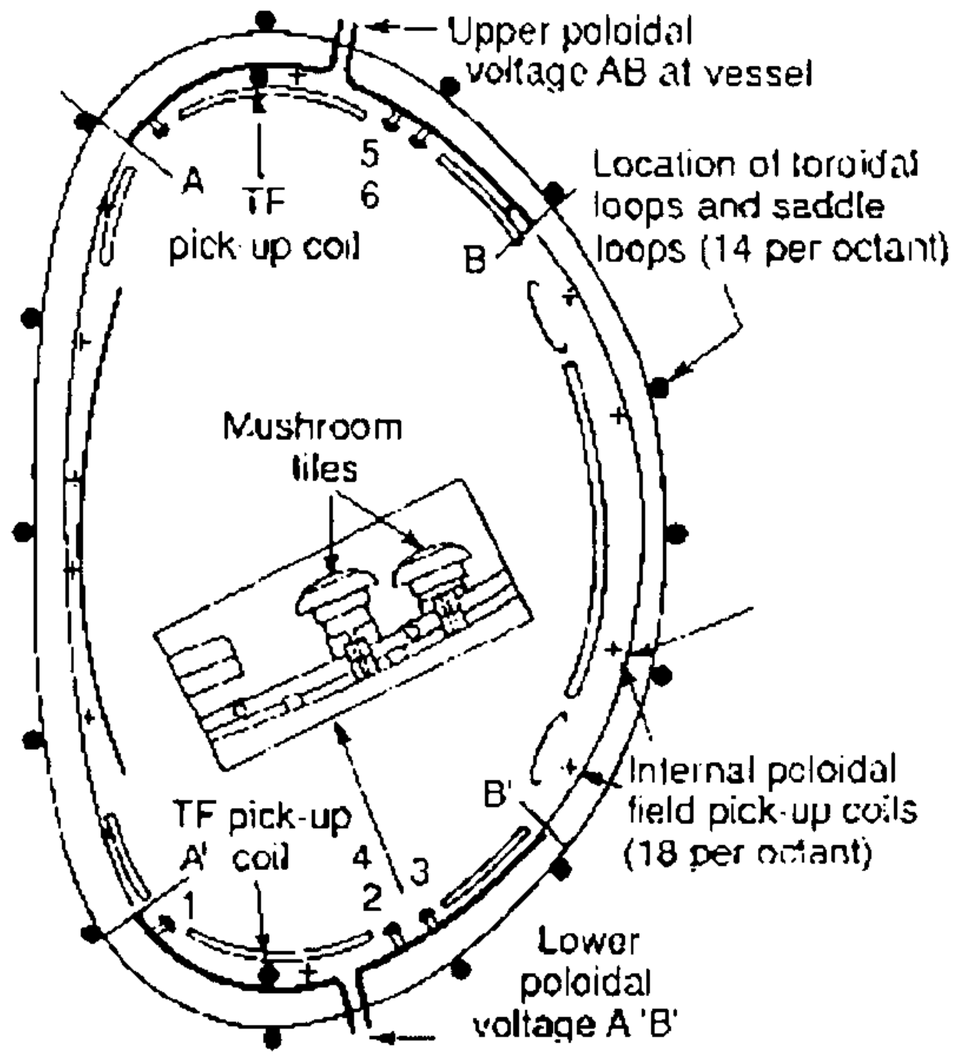


Fig. 1.14 - Magnetic field/current sensors in the VV cross-section

Field	Type	N°	Notes
Tangential PF	pick-up	4×18	internal field
TF	pick-up	8×2	top and bottom B_T (the difference gives total I_{HALO})
Flux			
VV saddle loops	flux loop	4×14	give the averaged normal PF at the outer VV wall
Current			
Mushroom Tiles	shunt	8×4	local detectors of poloidal Halo current density
Total toroidal I_{PLA}	rogowski coil	1×4	at VV outer wall
Inner toroidal I_{PLA}	rogowski coil	1×1	at VV inner wall
Voltage			
Poloidal VV	voltage loop	2×4	

Table 1.3 - Magnetic diagnostics on JET VV
(N° indicates the number of instrumented octants times the number of sensors per octant)

Note that the different locations of the Poloidal Field sensors (i.e. inside the vessel for the tangential component and outside for the normal component) makes the extrapolation of the field more difficult and prone to interference effects due toroidal eddy currents in the vessel.

1.2 Electromechanical modelling of plasma instabilities

This section complements the background information by outlining the sequence of events occurring in a Tokamak during an instability in terms of induced currents and forces, emphasising the peculiarities of JET respect to other devices. A logically "forward" approach is followed, starting from first principles (as opposed to the "backward" parameter estimation adopted in the rest of the work), in order to explain more clearly the relationship between the various coupled phenomena. The mathematical models involved are briefly described with their input and output parameters and the computational tools available to solve them. The limits of the direct approach are discussed and the potential benefits of the parameter estimation procedure are pointed out.

1.2.1 Axisymmetric VDEs

Macroscopic and microscopic plasma instabilities are one of the major problems affecting Tokamak devices and are amply referenced in the literature (see e.g. [2,3,11]). The present work is concerned with a much narrower class of events called Vertical Displacement Events (VDE), characteristic of large scale, high performance machines with elongated plasma cross-sections [12,13,16]. VDEs terminate about 5% of JET pulses and are recognised as the principal source of dangerous loads and mechanical failures. Throughout this work the terms 'VDE', 'plasma instability' and 'disruption' will be used interchangeably (if somewhat improperly).

1.2.1.1 Sequence of events during a VDE

Elongated plasmas are intrinsically unstable respect to vertical movements. Basically, the problem originates from the instability of the equilibrium of any current in the middle of two other currents of the same sign. More specifically, two such pairs of destabilising currents exist in JET [13]:

a) the currents in the shaping turns of the P2 coils;
b) the image currents[1] in the iron limbs, which are much smaller in magnitude but give a quadratic effect as they mirror the position of I_{PLA} across the air/iron interface.

The growth rate γ of the plasma movement without passive structure is around 100~400 s^{-1}. The vessel shell, however, has a dramatic stabilising effect since it decreases the growth rate by about one order of magnitude. Even so, elongated plasmas in JET can be sustained only with an active control system (the PPCC), which uses the radial field as the main actuator [23].

1 The so-called image currents, which arise inside high-permeability materials facing currents flowing in a low-permeability medium, have the same sign as the real currents and tend to mirror them across the interface (if the geometry allows it). Image currents represent a convenient way to calculate the total field, equivalent to impose the vanishing of the normal component of the field inside the ferromagnetic medium.

The attention will be given here in particular to upward VDEs, which are far more frequent and dangerous than downward events in the current, vertically asymmetric machine configuration [21,22]. The typical sequence of events during an upward axisymmetric VDE, as derived from both observations and simulations, may be summarised in these steps (see Fig. 1.15 or Fig. 5.6 as an example):

I) initially the plasma is in a steady-state equilibrium position when the vertical instability is triggered, for example, by MHD activity which saturates the control system, excessive current or field rates or deliberate exclusion of the control system during tests;
II) the plasma accelerates upward inducing toroidal eddy currents of the same sign at the bottom of the vessel and of opposite sign at the top.
III) the plasma impacts the vessel, remaining for typically 10~20 ms in a state of so-called attached equilibrium as the induced currents exert their stabilising effect and reverse the sign of the vertical motion, pushing it back downward [14]. If the plasma current at this stage is still large, a substantial amount of poloidal halo currents will flow in the vessel.
IV) a disruption finally occurs, causing the current to quench in a time of the order of 20~50 ms. and inducing toroidal eddy currents of the same sign of the plasma all over the vessel. During the quench, the plasma is pushed inwards by the vertical field as it moves downwards. When the disruption occurs before any vertical displacement the event is usually far less violent.

The force on the vessel is given by the magnetic interaction of the eddy and halo currents respectively with the poloidal and toroidal field. In the very first approximation, this scales with the square of the plasma current and with the vertical plasma displacement [19]:

$$\mathbf{F}_V \propto I^2_{PLA} Z_{PLA} \tag{1.1}$$

Simulations of VDEs are routinely performed at JET with the Finite Element code MAXFEA, which solves Grad-Shafranov equation on a 2D axisymmetric mesh [15]. Fully predictive calculations are usually rather inaccurate, while on the other hand fairly accurate simulations can be obtained by incorporating experimental measurements of the plasma current and position.

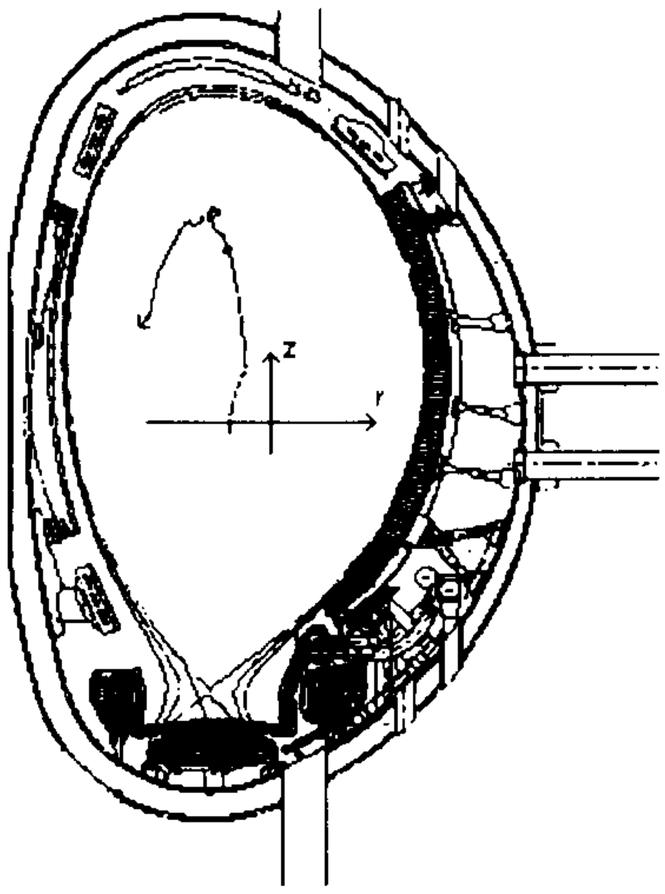


Fig. 1.15 - Trajectory of the plasma in the vessel during pulse 34078 (averaged toroidally)

1.2.1.2 Halo currents

Halo Currents are a kind of induced currents flowing in the hybrid circuit formed by the vessel and the plasma halo, i.e. the part of the plasma scrape-off-layer where confinement is lost, temperature and pressure drop substantially and the resistivity is of the same of magnitude as in the metal walls [20,(7.30)]. From the steady-state momentum conservation equation in the halo [2]:

$$\mathbf{J}\times\mathbf{B}=\nabla p\approx 0 \qquad (1.2)$$

one can see clearly that halo currents will follow the field lines in the plasma, while in the vessel they will tend to be mostly poloidal as the toroidal resistivity of the walls is one order of magnitude greater[2].

Halo currents are observed in most of the other large tokamaks; however, in JET they have a special importance due to:

- overall magnitude: poloidal halo current in the vessel can reach 20~30% of I_{PLA} and are usually the major source of load during disruptions
- uneven distribution; since halo currents arise essentially by contact, they can reach high local concentrations on internal components which protrude towards the plasma. This phenomenon is highly non-linear and clearly opens the possibility for non-axisymmetric effects.

To date, no fully consistent models able to predict the amount of halo currents in a particular VDE exists. So far, information on the halo current (I_H) has been inferred with various methods, including:

1. current measurements: the local current density in the halo is worked out from shunt measurements
2. field measurements: the total amount of poloidal current in the vessel can be estimated from top-bottom differences in the toroidal field
3. plasma force unbalance: as the total mass of plasma in the vessel is <0.1g, the plasma is always in a state of mechanical equilibrium and therefore the following force balance holds:

$$\mathbf{F}_{PLASMA}=\mathbf{F}_{HALO}+\mathbf{F}_{EDDY,VV}+\mathbf{F}_{PF\ COILS}+\mathbf{F}_{DIVERTOR}=0 \qquad (1.3)$$

This may be solved for $\mathbf{F}_{HALO}$ if the other terms are known (e.g. from a MAXFEA simulation). The total amount of halo current may then be estimated by making suitable assumptions on the halo width.

All these methods, as one can see, are limited by heavy approximations.

---

2 This question, as others related to the quantitative aspects of halo currents, is subject of debate.

1.2.2 Non-axisymmetric VDEs

The simple VDE model outlined above has been recently extended with the superposition of a n=1, m=1 external kink mode in order to explain the non-axisymmetric mechanical effects described in section 1.3.2.1 [23]. The corresponding deformation of the plasma, roughly in accord with observations, is approximately equivalent to the sum of a tilt $\Delta\alpha$ plus a shift $\Delta y = R\Delta\alpha$ along the tilt axis (see Fig. 1.16). While the destabilising factors at the origin of axisymmetric VDEs are easily understood, the situation for kink modes is rather more complicated. The following basic effects are expected:

vertical forces the differential vertical movement of the plasma, according to (1.1), gives rise to non-toroidally axisymmetric vertical forces.

horizontal forces the tilted/shifted plasma interacts mainly with the toroidal field, leading to forces and moments in the horizontal plane.

Experimental data analysis and calculations are much more complicated in this case than for a standard axisymmetric VDE. Additional problems which will not be addressed further in this work include:

- rotation of the mode with frequencies up to a few kHz; at low frequency the mechanical response might be enhanced by resonance effects, while at high frequency the response would be smeared out by the inertia of the structure;
- possibility of higher-order modes (e.g. with n=2, m=2 or 3) which could influence the poloidal distribution of the halo currents and generate non-axisymmetric force components [49].

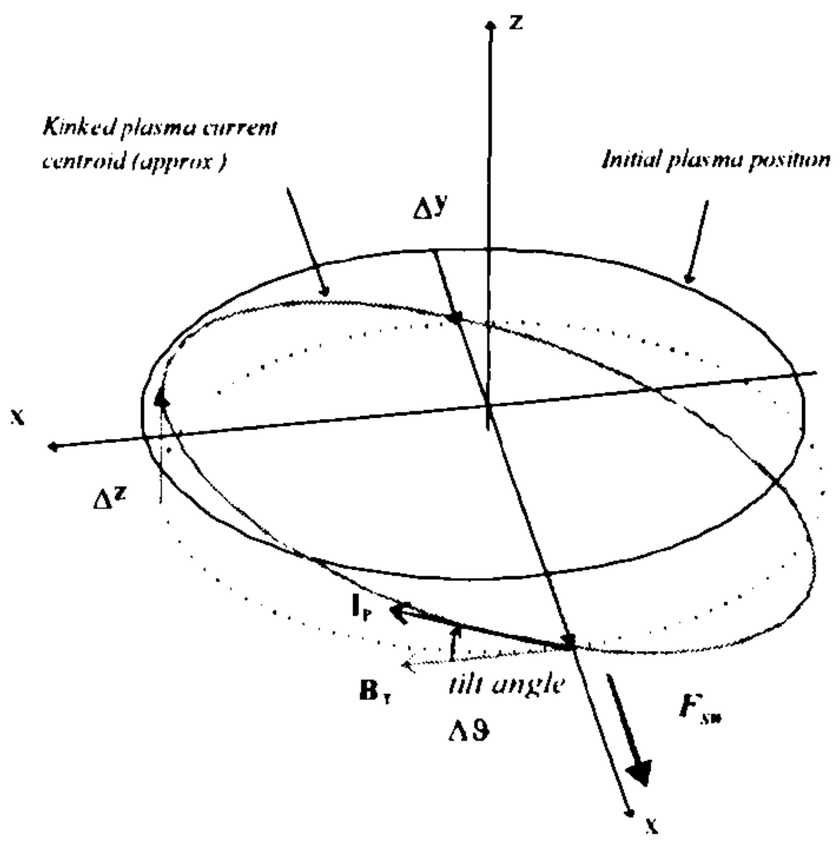


Fig. 1.16 - n=1, m=1 plasma kink mode

1.2.3 Global VDE model

On the basis of the phenomenology just reviewed it is possible to build a simplified model able, in principle, to simulate all main aspects of the electromechanical behaviour of a tokamak during a VDE (Fig. 1.17). This global model does not yet exist as a single entity but, rather, represents an ideal synthesis of all engineering work done in this area at JET during the last decade. The model links the initial parameters which control the experiment to the mechanical effects of the instability via a series of intermediate, tightly coupled steps. Any considerations of transport, energy balance or confinement have been neglected; temperature, resistivity, current profile and other properties of the plasma which change during the disruption are considered as input data. These assumptions makes it impossible to carry out fully self-consistent predictive simulations, as a certain amount of experimental data (or prior knowledge) will have to be included. However, experience shows that the level of accuracy that can be attained with this kind of simplification is adequate for engineering purposes, at least as an intermediate step towards a more detailed analysis.

The variables of this model are:

Initial parameters The open-loop waveforms of the TF and PF amplifiers control voltages, chosen and fixed in the control systems prior to each pulse;

TF/PF currents The currents in the magnetic coils, driven by the power supplies plus any additional e.m.f.s induced during the transient;

Induced currents The currents induced in all the conductors, including toroidal eddy currents and poloidal halo currents in the vessel;

Plasma parameters The plasma current magnitude and distribution, which may be defined approximately by the position of the centroid, the minor radius and the current profile;

Magnetic forces Computed from the interaction between plasma, coils and induced currents;

Displacements Resulting from the magnetic forces applied to the structural components;

Safety indicators Ultimate effects of the VDE in terms of peak stresses and displacements.

The following submodels are considered:

MHD submodel

This includes Grad-Shafranov's equation to describe the evolution of a toroidal, axisymmetric plasma [2] plus the low-frequency Maxwell's equations for the induction phenomena taking place in air or vacuum. The standard tool used at JET is the 2D MHD code MAXFEA, which includes a simplified model of the halo currents and a non-linear solver to model ferromagnetic materials [15]. The main limitations of this code lies in the absence of resistive effects and in the inability to model the real 3D geometry. It should be remarked that no code with fully self-consistent 3D MHD modelling capabilities could be found, during a recent search, either from commercial sources or referenced in the literature.

Control systems submodel

This submodel incorporates the algorithms implemented by the control systems regulating JET power supplies, including in particular the Plasma Position and Current Control System which stabilises the plasma vertically [23].

This control system can provide a feedback path between the deformations of the vessel and the currents in the coils. The control algorithm is in fact based on magnetic field measurements coming from the sensors attached to the surface of the vessel, which are erroneously assumed to be fixed with respect to the laboratory frame. Under certain conditions (e.g. in JET pulse 38692), coil and plasma currents and, therefore, the vessel force have been observed to oscillate at a frequency matching the structural resonance in the phase that precedes a disruption. A detailed representation of the control algorithms and of the way they are coupled to the rest of the machine is therefore essential in order to simulate correctly the evolution of a JET pulse.

Mechanical submodel

This submodel, ideally, would include detailed Finite Element meshes representing the major structural components, all their interconnections and the ground supports. So far, static and dynamic simulations of individual components have only been run, mainly because of lack of the huge resources needed for a global model.

An interesting feature of the problem is the full coupling between the mechanical response and the field and current distributions. Structural displacements affect the position and magnitude of induced currents in at least two obvious ways:

- the structure, while deforming dynamically, sees a change in flux linkage which induces eddy currents (see for instance the magnetic damping effect described in 3.2.1.6)
- internal vessel components may be deflected towards the plasma and thus may intercept halo currents, which would deflect them even more leading thus to an exponentially growing deflection and final breakage. This phenomenon may have been the cause of some observed failures, e.g. in the case of the glow discharge electrodes.

This outline shows clearly that, even with simplifying assumptions, a full predictive simulation of a VDE represents a formidable challenge, if only from the computational viewpoint. In summary:

- no single existing code includes the required multi-physics models;
- no general-purpose 3D MHD code is available;
- the computational cost of a comprehensive simulation would be orders of magnitude greater than any other calculation performed so far at JET

For the time being, therefore, the only feasible approach is to investigate partial models.

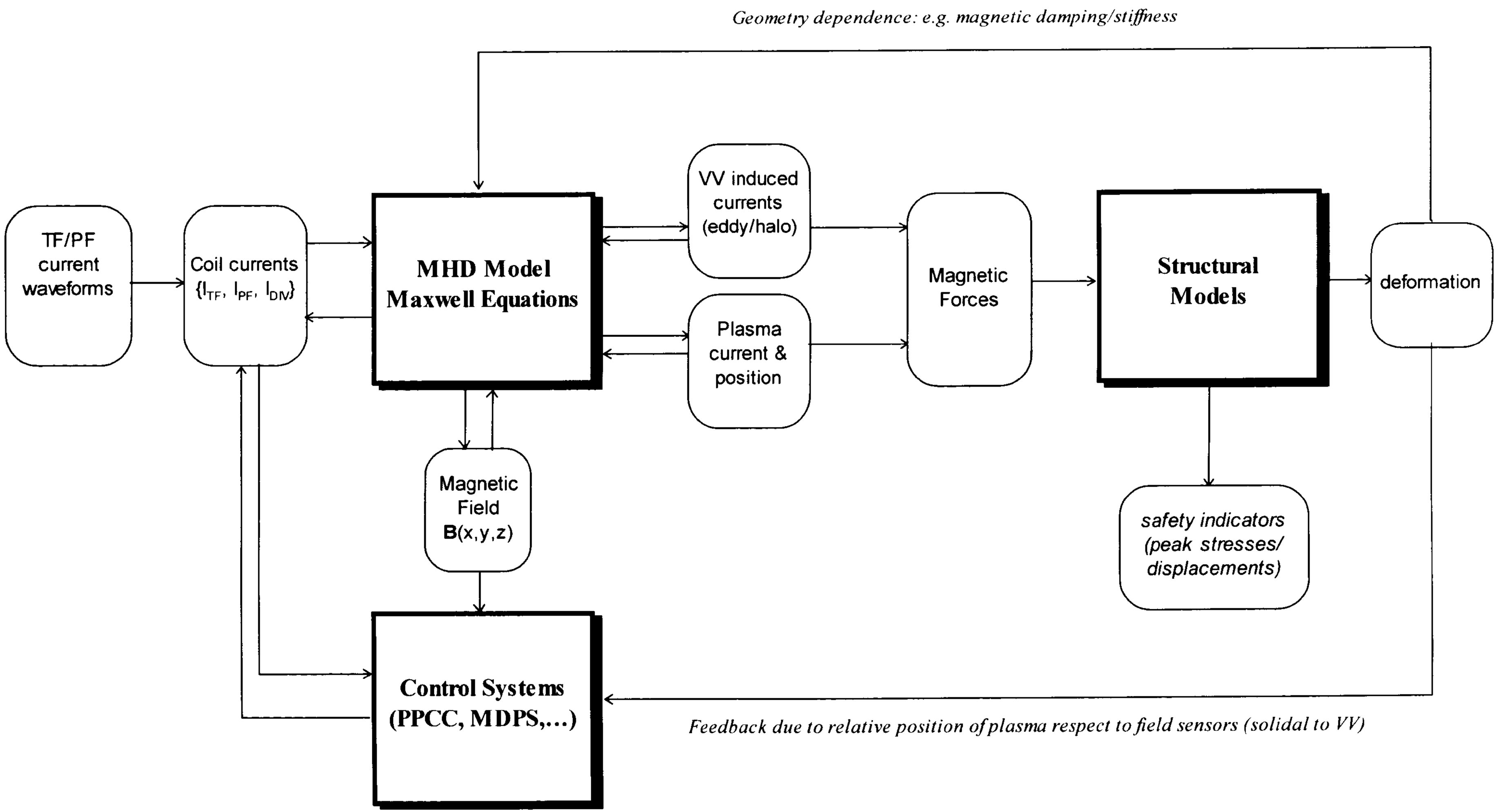


Fig. 1.17 - Global VDE model (square boxes represent equations, round boxes data)

1.3 Structural effects of plasma instabilities

This section is concerned with the main structural effects observed in JET, including the large scale vacuum vessel movements which are the main object of this work. In general, plasma instabilities have adverse effects on tokamak structures and components, particularly those of the first wall. These can be classified as follows:

Thermal effects: intense localised heat fluxes can cause thermal stresses and metallurgical damages;

Surface effects: sputtering, runaway electrons or arcing may seriously degrade material properties and surface quality;

Mechanical effects: large, impulsive J×B forces may induce excessive stresses or displacements of the main structure or any of the internal components, leading to permanent deformations, impact with nearby components or rupture.

In the history of JET many failures of minor components have occurred, including protection tiles, glow discharge electrodes and NBI unit connections [21]. In all cases, repair and prevention of future occurrences could be carried out easily, for example by strengthening the damaged part and eliminating cantilevered supports protruding into the vessel.

As for the main structural components, support forces of the order of 5 MN have been recorded in the past. Although no major failure has ever occurred, stress assessments indicate that the yield limits of the materials may have been approached; moreover, extrapolations to future operating conditions (in particular the upcoming 4T/5MA campaign) indicate that fatigue limits may be reached unless suitable constraints are applied on the magnetic configuration. A better understanding of the response of the machine to disruptions, which motivates the present work, is therefore necessary in order to achieve maximum performance (see also section 7.3.2).

1.3.1 Axisymmetric VDE effects

The observed axisymmetric[3] mechanical effects are represented in Fig. 1.18 and .1.19 These include:

1.3.1.1 Rolling motion

The basic component of the mechanical response of the vessel to disruption forces is the "rolling motion" (RM), defined by the averaged difference of the radial displacements measured at the top and the bottom MVPs [21] (Fig. 1.18):

$$x_{RM} = \frac{1}{2}\sum_{i=1}^{8}\frac{\delta r_{MVP}^{top} - \delta r_{MVP}^{bottom}}{8} \qquad (1.4)$$

Finite Element analysis shows that this effect is mainly due to the vertical component of the applied force which causes a rotation of the vessel around the major axis because the MVP are not free to move vertically. The mechanical models used to study this movement are explained in detail in 3.1.1. The average in (1.4), as in all other similar formulæ appearing below, may be restricted to fewer than two sensors per octant depending on the date of the event and on the quality of the signals.

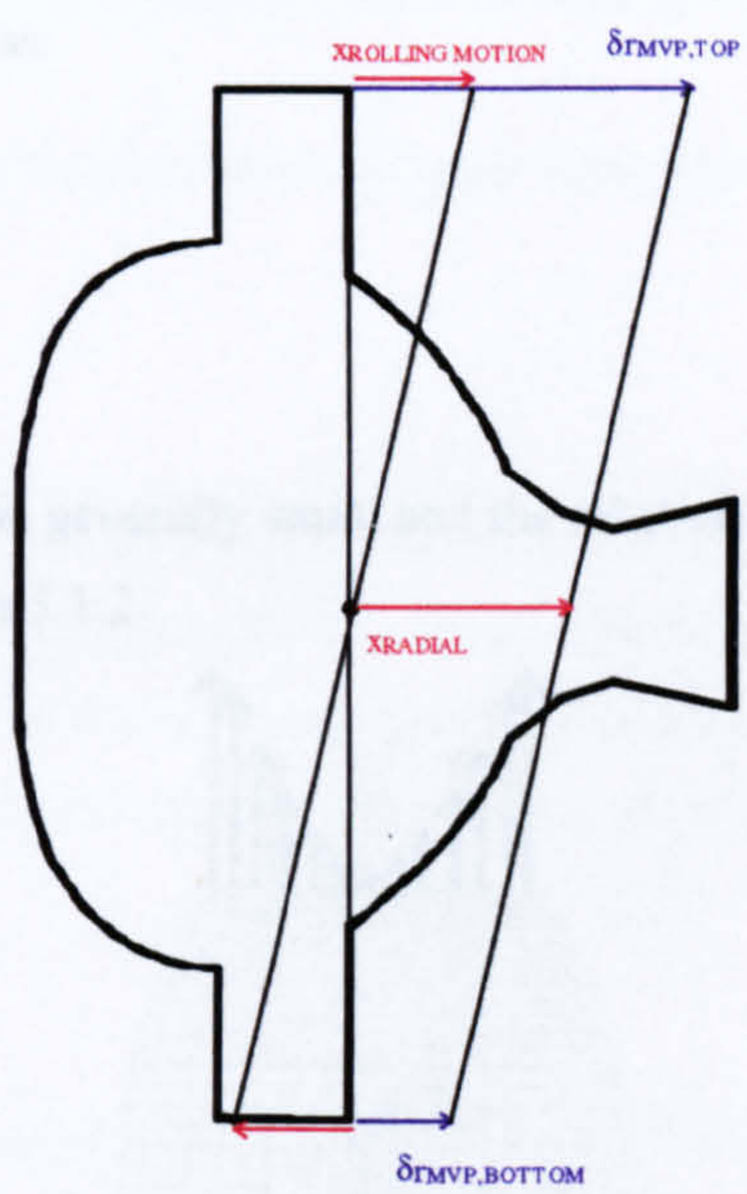


Fig. 1.18 - Axisymmetric movements of the vacuum vessel: rigid-body rolling and radial motion in the poloidal planes.

3 In the context of JET structures, made by eight equal octants with bilateral symmetry, the term 'axisymmetric' is used for brevity to mean 'cyclically symmetric with period π/8'.

1.3.1.2 Radial motion

Radial forces cause an uniform expansion and contraction of the vessel which is measured by the following average (see Fig. 1.18):

$$x_{RADIAL} = \frac{1}{2}\sum_{i=1}^{8}\frac{\delta r_{MVP}^{top} + \delta r_{MVP}^{bottom}}{8} \tag{1.5}$$

This movement is generally very small due to the high stiffness of the toroidal shell.

The superposition of rolling motion and radial motion is necessary and sufficient to describe the translation and rotation of the vessel cross-section, assumed rigid, in a poloidal plane.

1.3.1.3 Vertical motion

In the early vessel configuration (period I of Table 1.1) vertical forces caused the vessel to oscillate as a whole in the vertical direction. In the current configuration, due to the MVP supports, the vertical component of the vessel deformation is practically zero at the Central Rigid Sectors and rises to a maximum at the junctions between octants (see Fig. 1.19). The vertical movement is measured with the IVP transducers and can be defined as:

$$z_{IVP} = \frac{1}{2}\sum_{i=1}^{8}\frac{\delta z_{IVP}^{top} + \delta z_{IVP}^{bottom}}{8} \tag{1.6}$$

The magnitude of this movement is generally small and the relative oscillations are dynamically linked to the rolling motion, as explained in 3.1.2.

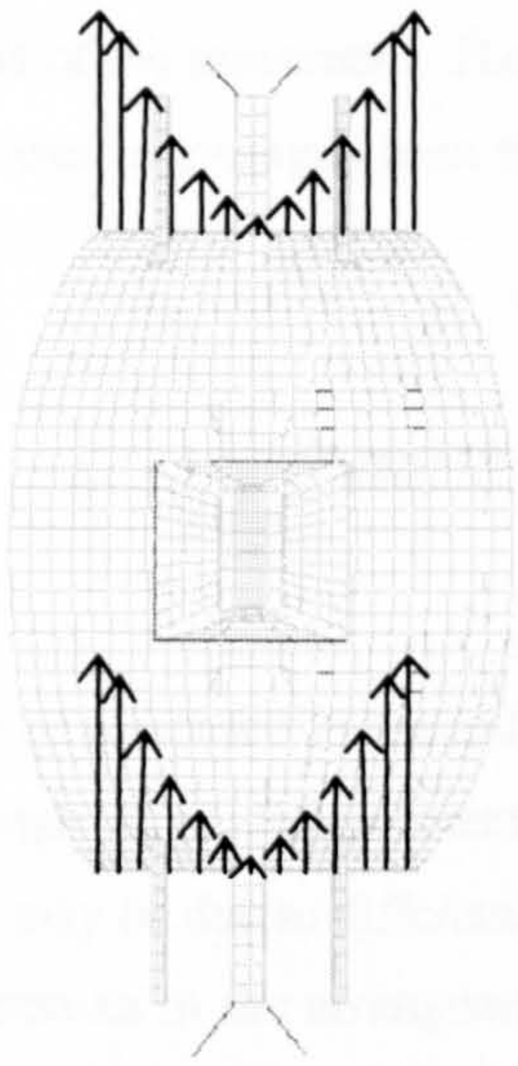


Fig. 1.19 - Vertical vessel deformation

1.3.2 Non-axisymmetric effects

Non-axisymmetric vessel movements (represented in Fig. 1.20) are the focus of much recent interest. Although events of extreme magnitude have been observed and recognised only recently, experimental evidence shows that non-axisymmetric effects have always been superimposed to the axisymmetric movements. Statistical analysis shows that these effects become relevant in about 20% of cases [29].

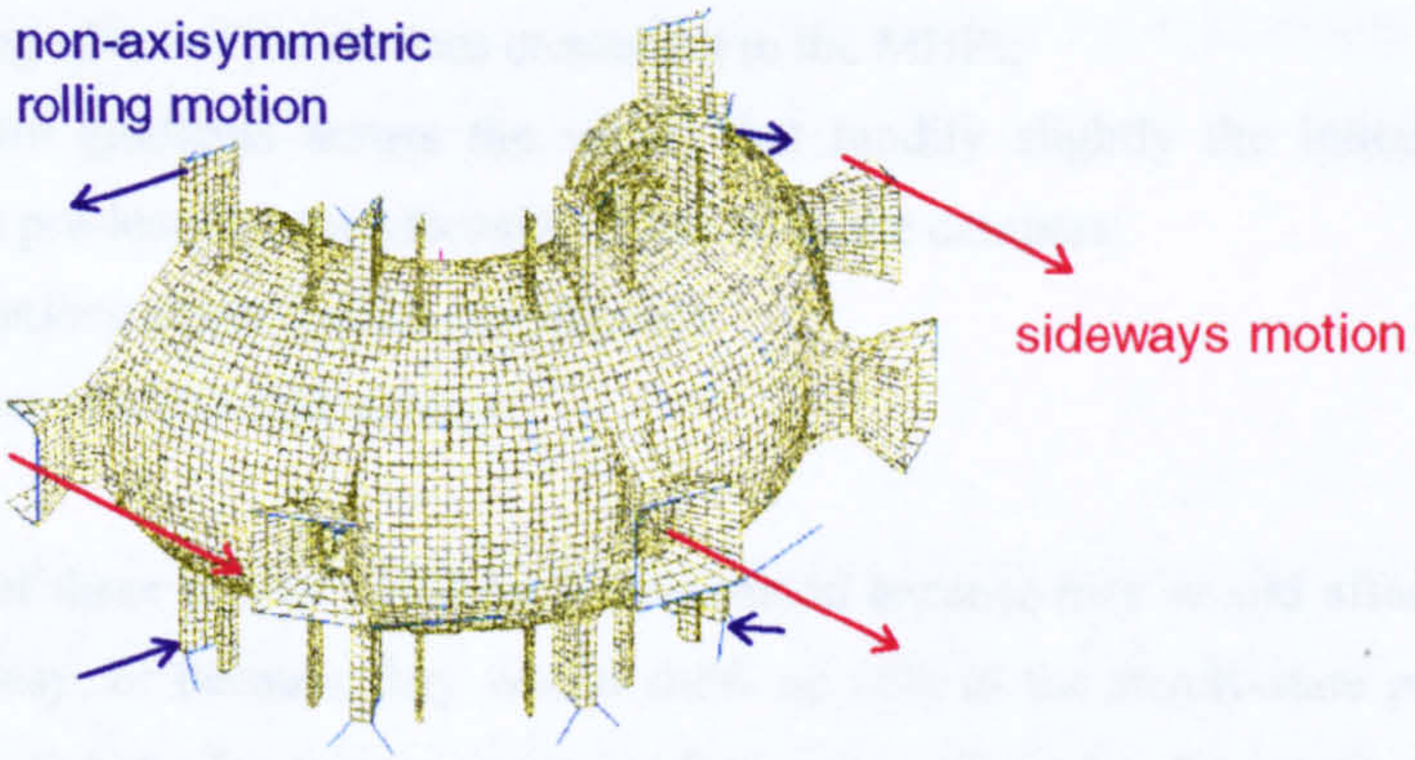


Fig. 1.20 - Non-axisymmetric movements of the vacuum vessel.

The non axisymmetric effects can be divided in two main categories:

1.3.2.1 Sideways motion

The sideways motion is the result of net horizontal disruption forces. Sideways motion events (SDE) can be easily identified because the radial motion (1.5) is much higher than usual and changes sign in the two octants aligned with the direction of the movement. The motion of the vessel as a whole along a given direction ϑ in the equatorial plane can be averaged from the port displacements, assuming that the ports do not bend appreciably:

$$\delta_{SW}(\vartheta) = \frac{1}{2}\sum_{i=1}^{8} \frac{\delta r_{MVP}^{top} + \delta r_{MVP}^{bottom}}{8 \cdot 2} \cos(\vartheta_i - \vartheta) + \frac{1}{2}\sum_{i=1}^{8} \frac{\delta r_{MHP} \cos(\vartheta_i - \vartheta) + \delta t_{MHP} \sin(\vartheta_i - \vartheta)}{8 \cdot 2} \qquad (1.7)$$

For older JET pulses this average may be restricted to the radial MVP displacements at 4 or 8 octants only. The direction ϑ is random, although large displacements have been observed mostly along the direction from octant 5 to octant 1. This may be due to different restraining effect of equipment attached to the Main Horizontal Ports, or to differences in the arrangement of internal vessel components which might favour halo currents in some octants.

1.3.2.2 Non-axisymmetric rolling motion

The rolling motion response often shows substantial differences between octants, up to 10-20% in cases where no sideways motion is observed, or even higher otherwise. This asymmetry is thought to be linked to the same mechanism that generates sideways forces, although the phenomenon is still not well understood [26]. Apart from non-uniform vertical forces, additional possible causes that may account for differences in the response of each octant to toroidally uniform forces include the following:

- different distribution of the mass of attached equipment and diagnostics
- different restraining effect of the devices connected to the MHPs;
- uneven temperature gradients across the vessel that modify slightly the initial deformation, the amount of support pre-loading, the viscosity of the oil in the dampers;
- unpredictable variations of the friction coefficients
- different calibration of individual sensors

In principle, some of these effects could be discriminated because they would affect always the same octants in the same way, or because they would show up also in the steady-state part of a JET pulse (where no physical reason for non-symmetric forces to arise can be envisaged). The current understanding is that these effects and non-uniforms forces contribute more or less equally to the observed asymmetries.

1.3.3 Vessel stress assessment

The ultimate goal of this analysis is assessment of the Vacuum Vessel stresses and comparison with their allowable limits. These stresses can be broadly divided in two categories, depending on the location where they occur:

- stresses at the MVP base: these are secondary[4] peak stresses due to the concentration effect of the 90° re-entrant corner geometry. Assuming that the port does not impact with nearby structures, these stresses depend mainly on the dynamic radial force applied at the top of the MVP, which in turn depends on the displacement x(t):

$$F_{MVP} = m_{MVP}\frac{\partial^2 x}{\partial t^2} + b_{damper}\frac{\partial x}{\partial t} \tag{1.8}$$

The peak strain, which is the reference to be used in fatigue life assessments, can be worked out from the ABAQUS model showed in Fig. 1.21. (this calculation cannot be done directly on the full NASTRAN Finite Element models because the mesh resolution is not sufficiently fine and the code lacks the necessary non-linear material model). Note that MVP base stresses are assumed not to depend on the vertical support force R_{MVP}; in fact, additional Finite Element calculations have shown that R_{MVP} generates peak stresses in the outboard corner which have relatively low magnitude and can safely be neglected.

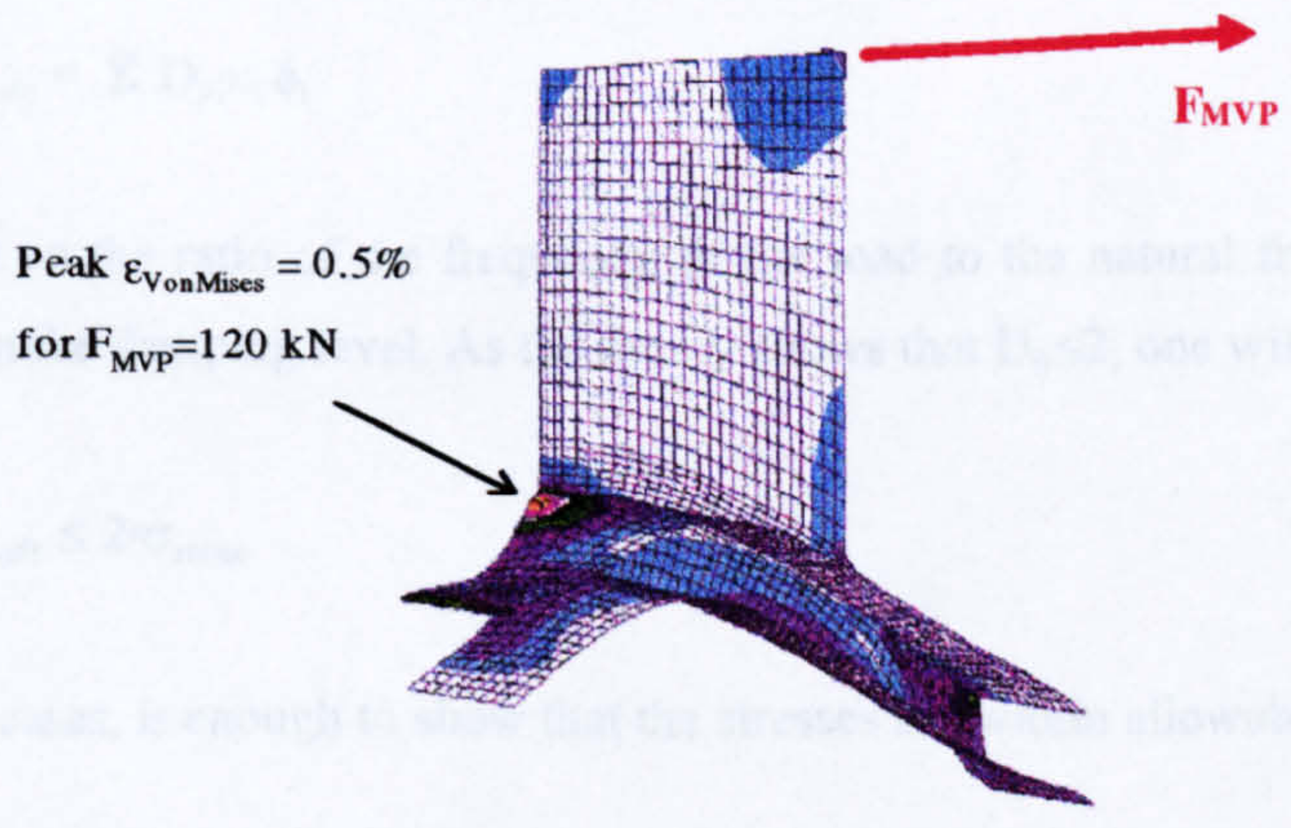


Fig. 1.21 - Stress concentration at the base of a Main Vertical Port (inboard) obtained with the non-linear FE ABAQUS local model

4 Following the ASME definition, a secondary stress is a self-limiting stress usually driven by the deformation of nearby material (such as stresses due to thermal or peak concentration effects). If a secondary stress exceeds its allowable limit the structure in general will not collapse, although fatigue cracks or permanent deformations may develop locally.

- stresses in the bellows rigid/sectors: these are primary stresses (i.e. stresses necessary to equilibrate the applied loads in the bulk of the structure). These may be calculated directly from the static NASTRAN Finite Element models and are generally found to be relatively low:

rolling motion (vertical force F_V=1 MN) $\Rightarrow \sigma_{max,\,RM} \approx 10$ MPa (rigid sector)
sideways motion (lateral force F_{SW}=1 MN) $\Rightarrow \sigma_{max,\,SW} \approx 200$ MPa (bellows, open)
$\sigma_{max,\,SW} \approx 3$ MPa (bellows, closed)

(The bellows open up when the tensile stress in the closed state reaches about 22 MPa). A quick assessment of these stresses in dynamic conditions may be obtained considering the decomposition of the structure in *n* eigenmodes of shape $\{\Phi_j\}$, which allows to express:

$$\sigma_{static} = \Sigma_i \kappa_i \phi_i \tag{1.9}$$

where the coefficients κ_i are derived from Finite Element calculations and:

$$\phi_i = \{\Phi_j\}^T\{F\} \tag{1.10}$$

is the generalised scalar load associated with the i-th eigenvector, obtained by projecting the vector {F} of applied forces onto the modal deformation shape. When the same loads are applied transiently, dynamic stresses can be obtained by scaling the static stresses with the *dynamic factors* D_{fi} [51]:

$$\sigma_{dynamic} = \Sigma_i D_{Fi}\kappa_i \phi_i \tag{1.11}$$

The D_{fi} depend on the ratio of the frequency of the load to the natural frequency of the mode considered and on the damping level. As the theory shows that $D_{fi} \leq 2$, one will have that:

$$\sigma_{dynamic} \leq \mathbf{2}\cdot\sigma_{static} \tag{1.12}$$

which, in most cases, is enough to show that the stresses are within allowable limits[5].

5 The material of the vessel walls is Inconel 600, which yields at 240 MPa at the operating temperature of 300 °C; the material of the bellows is Inconel 625 which yields at 440 MPa.

1.3.4 Mechanical effects in other Tokamaks

Since magnetic forces increase with the square of the plasma current and with the plasma elongation, their structural effects have some importance only in large, high-performance tokamaks. While thermo-mechanical failures of first wall components are relatively commonplace, vessel forces (which scale with I^2_{PLA}) are not usually regarded as a major problem in most existing machines. More specifically, for instance, in:

Asdex-U halo currents up to 55% of I_{PLA} are observed, with corresponding vertical forces up to 400kN [34].

Compass-D halo currents up to $1.2I_{PLA}/q_{95}$ have been observed, with no rotation and high toroidal peaking factors [37].

DIII-D the vessel experiences forces up to ~1.5 MN and vertical displacements up to ~2 mm, measured with a limited amount of sensors. The question of halo currents and their asymmetry is actively being investigated [33].

JT-60U halo currents up to $\sim^2/_3$ of I_{PLA} have been observed with an high degree of toroidal asymmetry; however, this machine is very strongly supported in four horizontal directions and therefore movements and forces have so far received little attention [1,32].

None of these devices has the range of mechanical sensors which can be found in JET. In these and other machines, therefore, mechanical effects of disruptions are studied more in view of future developments than because they represent a danger at present.

2

TOKAMAK LOAD PATHS DURING DISRUPTIONS

This chapter provides a global picture of the load paths throughout the whole Tokamak during a disruption, describing the interplay of magnetic forces and corresponding reactions in the various components of the JET machine.

The load distribution on the magnetic coils, which influences the pattern of reaction forces in other components, is obtained in fine detail by means of a numeric procedure based upon the semi-analytical integration of Biot-Savart's law. This procedure, described in section 2.1, has been implemented within a newly developed program called COMET (COil and Magnetic field Engineering Tool) which includes a geometric description of the coils in terms of Bézier curves. These enable a compact and efficient mathematical representation of a coil's centre line and facilitate the input of complex shapes.

In section 2.2, the force analysis is carried out in a simplified way on the basis of the magnetic interaction between the kinked plasma and the coils of the TF and PF systems. The attention is given, in particular, to the way in which non-axisymmetric loads arising during sideways motion events may be equilibrated between plasma and structural components.

2.1 Bèzier curve-based magnetic coil modelling

In this section the numerical method developed to compute the detailed distribution of magnetic field and forces on JET coils due to the plasma in an arbitrary kinked configuration is presented. The method is a semi-analytical application of the well-known Biot-Savart's law [42]:

$$\mathbf{B}(\mathbf{r}) = \frac{\mu_0}{4\pi} \iiint_{\mathcal{V}} \frac{\mathbf{J}(\mathbf{R}) \times (\mathbf{r} - \mathbf{R})}{\|\mathbf{r} - \mathbf{R}\|^3} d\mathcal{V} \qquad (2.1)$$

that gives the magnetic field **B** at the location **r** as the sum of elementary contributions all over the volume $\mathcal{V}$ where currents are distributed with density **J**(**R**). This integral has been adapted and optimised for the case where the geometry of the conductors is defined in terms of Bèzier curves, which allow easy input of complex 3D shapes. The numerical procedure has been implemented in a general-purpose interactive PC program, called COMET, described in more detail in Appendix 1.

2.1.1 Modelling of coil geometry via Bèzier curves

The procedure devised to model the geometry of magnetic coils is discussed in this section. The basic idea is to represent the centre line of a coil by a chain of segments defined by 3rd-order Bézier curves, a type of parametric splines making use of polynomial basis functions [38]. With reference to Fig. 2.1, a Bézier curve is defined by two end points (P_0 and P_3) plus two control points (P_1 and P_2) which determine the first and second derivatives at both ends. This kind of representation is very popular in computer applications[6] as it is well-suited for fast graphics processing and interactive shape editing [39]. More specifically, Bézier curves provide a compact analytical representation of arbitrarily complex shapes[7] with very good approximation: for example, a circle can be represented by just four 90° Bézier arcs with less than 0.03% peak error. In particular, Princeton-D shaped coils can be approximated by a sequence of circular arcs (see 1.1.1.2) and so can be input in a fully automatic way by simply specifying their width and thickness, with great simplification respect to the customary point-by-point representation.

The details of the geometrical representation will be now explained, introducing the nomenclature used in the computer code. The top-level building block of a COMET model is a *coil,* made up by one or more *segments* with rectangular cross section (see Fig. 2.3). Each segment is specified by a Bézier curve, which defines the centre line (℄), together with the values of width, height and orientation of the cross-section.

---

[6] Bézier curves are included in most CAD and drawing packages (e.g. IBM/Dassault's CATIA, CorelDraw), as well as in the standard PostScript graphics language. Bézier curves are also supported on many platforms at the operating system level: in Microsoft Windows they are provided as graphic primitives and are used, for example, to define TrueType font characters.

[7] For example, the ease of application of a 3D twist to a Bézier curve facilitates the modelling of Stellarator coils.

BIBL LONDON UNIV

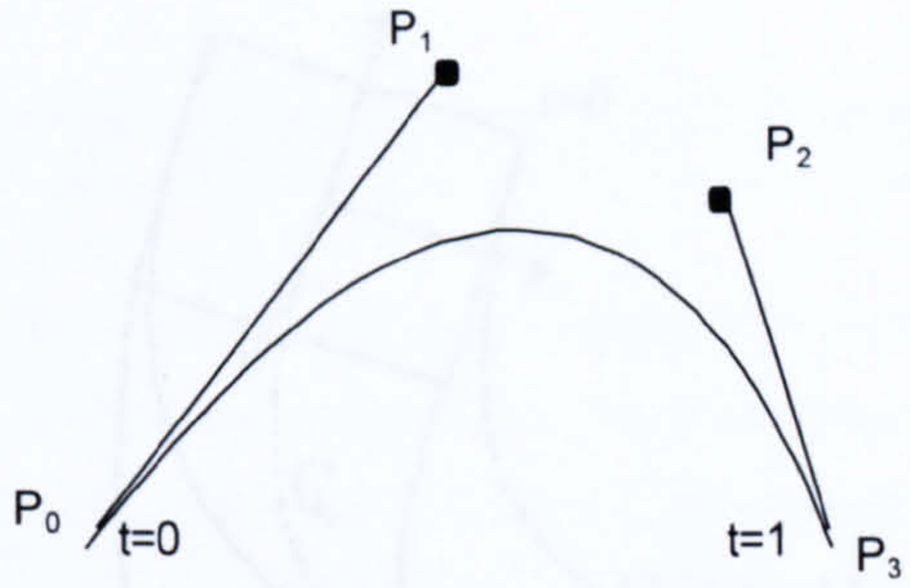


Fig. 2.1 - A Bézier curve

The geometry of the $\mathcal{C}$ is defined as follows:

$$\mathcal{C}:\ \underset{t=0\to 1}{P(t)} = \underbrace{\begin{cases} x(t) = \sum_{i=0}^{3} a_i \binom{i}{3} t^i (1-t)^{3-i} \\ y(t) = \sum_{i=0}^{3} b_i \binom{i}{3} t^i (1-t)^{3-i} \\ z(t) = \sum_{i=0}^{3} c_i \binom{i}{3} t^i (1-t)^{3-i} \end{cases}}_{\text{Bezier curve}} \quad \begin{matrix} \text{normal} \\ \text{tangent} \\ \text{binormal} \end{matrix} \begin{cases} \vec{n} = \vec{n}_0(1-t) + \vec{n}_1 t & \hat{e}_n = \frac{\vec{n}}{\|\vec{n}\|} \\ \vec{\tau} = \frac{dP}{dt} & \hat{e}_\tau = \frac{\vec{\tau}}{\|\vec{\tau}\|} \\ \vec{b} = \vec{\tau} \times \vec{n} & \hat{e}_b = \frac{\vec{b}}{\|\vec{b}\|} \end{cases} \underbrace{\qquad\qquad}_{\text{local reference system}} \tag{2.2}$$

where:

- $t=0\to 1$ is the non-dimensional parameter of the Bézier curve;
- $\{a_i\}$, $\{b_i\}$ and $\{c_i\}$ are the coefficients of the basis functions;
- $\mathbf{n}(t)$ is the vector normal to the $\mathcal{C}$, interpolated linearly between $\mathbf{n}_0$ and $\mathbf{n}_1$ (defined by the user at both ends of the segment);
- the versors (i.e. unit length vectors) $\hat{\mathbf{e}}_i$ define a local reference system along the segment. For the definition to be valid, the user must ensure that $\mathbf{n}$ is nonzero and not parallel to τ;
- the versors $\hat{\mathbf{e}}_n$ and $\hat{\mathbf{e}}_b$, respectively associated to the local coordinates (u,v), define the plane of the cross-section of the coil.

The volume $\mathcal{V}$ of the coil is therefore defined by the following bounds in the local reference system:

$$\begin{cases} -\frac{w(t)}{2} \le u \le \frac{w(t)}{2} & \text{coil width: } w(t) = w_0(1-t) + w_1 t \\ -\frac{h(t)}{2} \le v \le \frac{h(t)}{2} & \text{coil height: } h(t) = h_0(1-t) + h_1 t \end{cases} \tag{2.3}$$

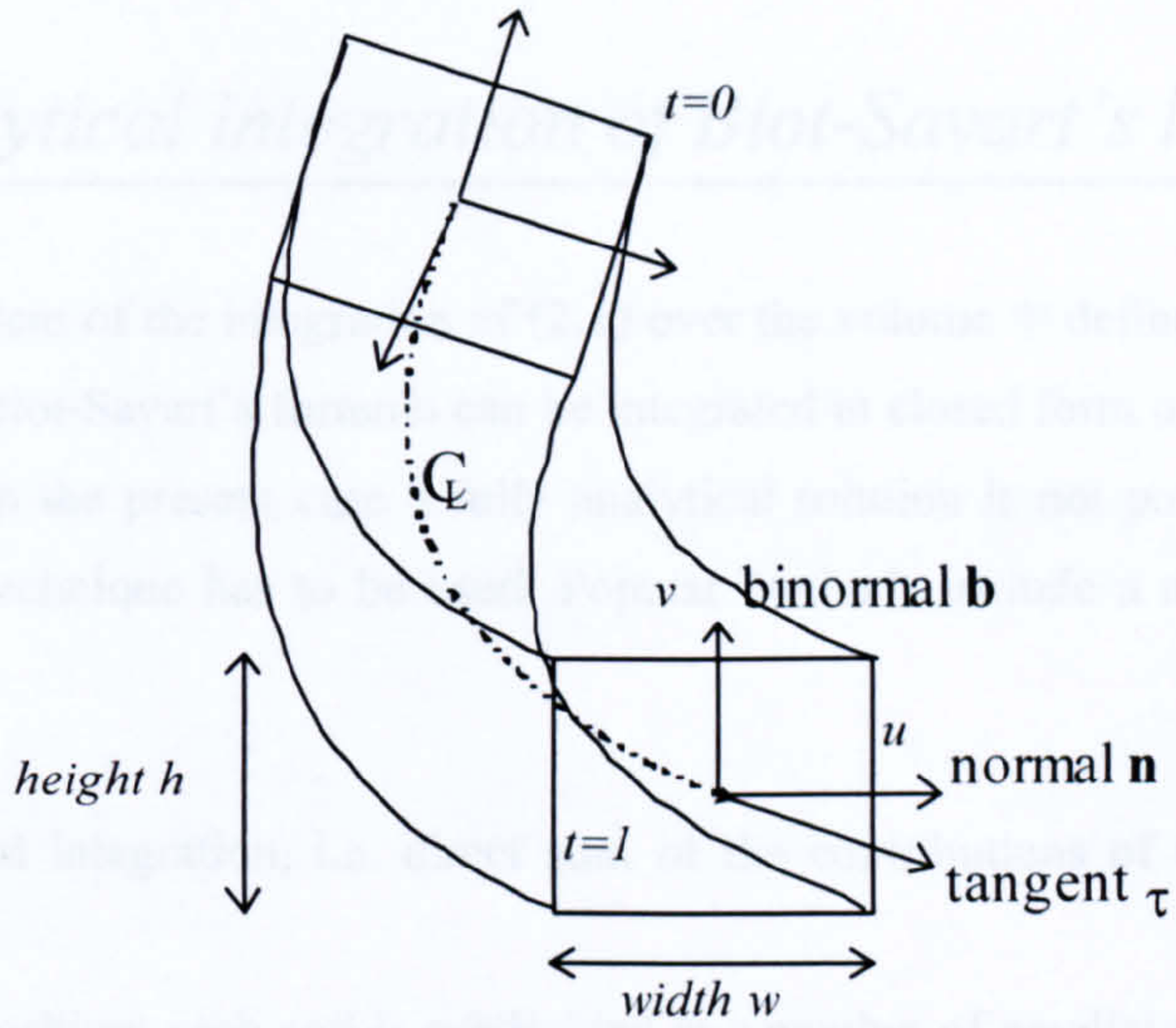


Fig. 2.2 - Geometry of a coil segment

where, also width and height are given at the ends of the segment and interpolated linearly in between. This definition allows the possibility to easily define coils which are tapered and twisted in 3D.

C^1 continuity of the coil's centre line requires alignment of the respective control points, while C^2 continuity can be achieved by controlling the distance from the control points to the common end point. The normal vectors at the junctions have to be defined with care in order to avoid voids or overlaps between adjacent coil segments. Of course, a trade-off has to be made between the number of segments used to model a coil and the associated workload.

References to this kind of usage of Bézier techniques could not be found in the literature on magnetics. The use of Bézier curves to model spirals (such as the Princeton-D shape) has also been described, from the purely geometrical viewpoint, in [40]. In some cases, Bézier surfaces have been used to model the field produced by solid bodies with the boundary element method [41].

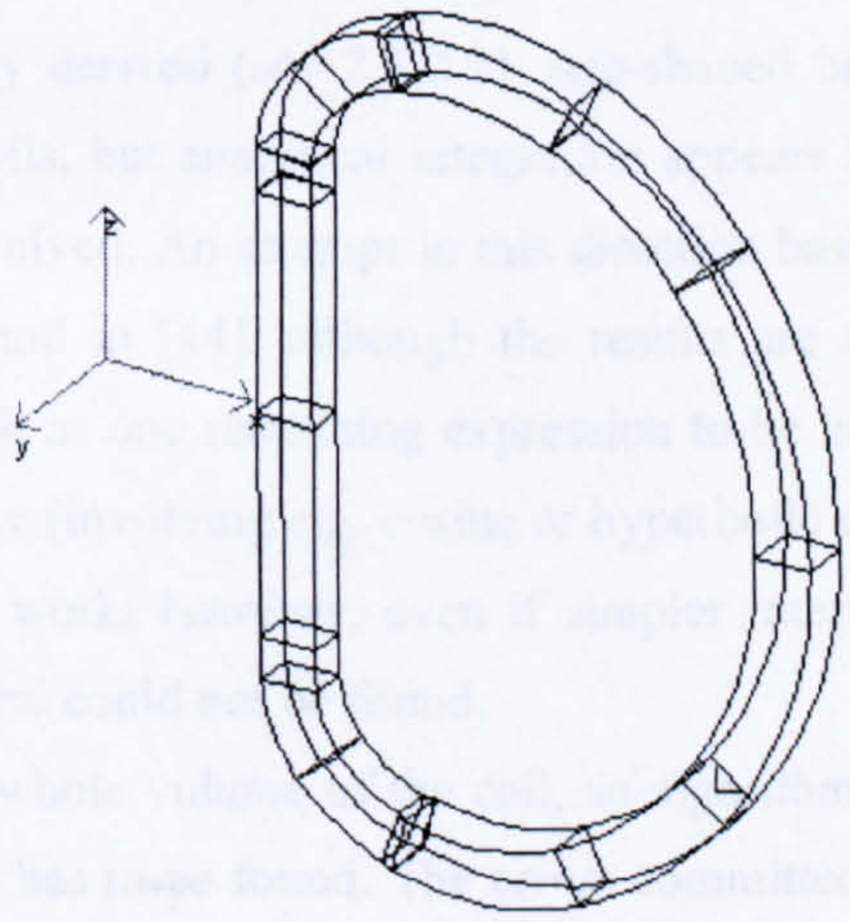


Fig. 2.3 - A TF coil represented by a chain of straight and curved Bézier segments

2.1.2 Semi-analytical integration of Biot-Savart's law

In this section the problem of the integration of (2.1) over the volume $\mathcal{V}$ defined by the (2.2) and (2.3) is discussed. Generally, Biot-Savart's formula can be integrated in closed form only when the integration domain is very simple: in the present case a fully analytical solution is not possible and some kind of approximate numerical technique has to be used. Popular methods include a mixture of symbolic and numeric techniques [43]:

- full 3D numerical integration, i.e. direct sum of the contributions of the infinitesimal current elements $\mathbf{J}d\mathcal{V}$;
- filament decomposition: each coil is subdivided in a number of parallel current filaments and the total field is recovered by summing all the contributions. If the filament shape is simple enough, 1D analytical integration may be possible.
- decomposition of the coil in a number of thin slices. 2D analytical integration may be possible if the cross-section has a simple shape, otherwise the integration will be numerical. The total field is integrated numerically anyway (see [45] for an application of this method to circular coils with rectangular cross-section).

In all these cases numerical difficulties arise when one tries to calculate the field inside the conductor region, due to the presence of the singularity in the Biot-Savart formula and in its indefinite integrals. To overcome this drawback it is necessary to go one step further and use analytical integration over whole 3D volume subdomains, where the singularities are automatically removed. In this way, a single mathematical expression can be conveniently used to evaluate the field both inside and outside the conductor.

The best suitable volume element for analytical integration is the rectangular brick, for which fully closed-form formulæ can be easily derived (see 2.1.2.1). Arc-shaped bricks would be of course more efficient in representing curved coils, but analytical integration appears in this case to be possible only over two of the three variables involved. An attempt in this direction based on a formulation in terms of the magnetic potential can be found in [44], although the results are rather complicated and include incomplete elliptic integrals as well as one remaining expression to be integrated numerically. Different formulations for the shape of the arc (involving e.g. cosine or hyperbolic cosine functions) have also been investigated in the course of this work; however, even if simpler intermediate expressions have been obtained, a fully closed form integral could not be found.

In order to cover efficiently the whole volume of the coil, an algorithm to subdivide $\mathcal{V}$ in the smallest possible number of brick elements has to be found. The errors committed when using rectangular bricks over curved domains will be discussed first in 2.1.2.2 and 2.1.2.3, while an adaptive discretisation procedure with the aim of optimising the size and position of the bricks for a given target accuracy when integrating over a whole coil set will be discussed in 2.1.2.4.

2.1.2.1 Field integration over rectangular bricks

Considering the rectangular brick in Fig. 2.4 referred to the local axes {u,v,t} (where t is dimensioned and is considered to very between -l/2 and +l/2) and assuming that the current density **J** is parallel to the *t* axis[8], the Biot-Savart integral giving the field in $\bar{\mathbf{r}}=\{\bar{u},\bar{v},\bar{t}\}$ can be rewritten as:

$$\mathbf{B}(\mathbf{r})=\frac{\mu_0\mathbf{J}}{4\pi}\times\int_{-l/2}^{+l/2}dt\int_{-h/2}^{+h/2}dv\int_{-w/2}^{+w/2}\frac{(\mathbf{r}-\mathbf{R})}{\|\mathbf{r}-\mathbf{R}\|^3}du=\frac{\mu_0 J}{4\pi}\int_{-l/2}^{+l/2}dt\int_{-h/2}^{+h/2}dv\int_{-w/2}^{+w/2}\frac{-(\bar{v}-v)\mathbf{i}+(\bar{u}-u)\mathbf{j}}{\left[(\bar{u}-u)^2+(\bar{v}-v)^2+(\bar{t}-t)^2\right]^{\frac{3}{2}}}du \tag{2.4}$$

where **R**={u,v,t} is the integration variable.

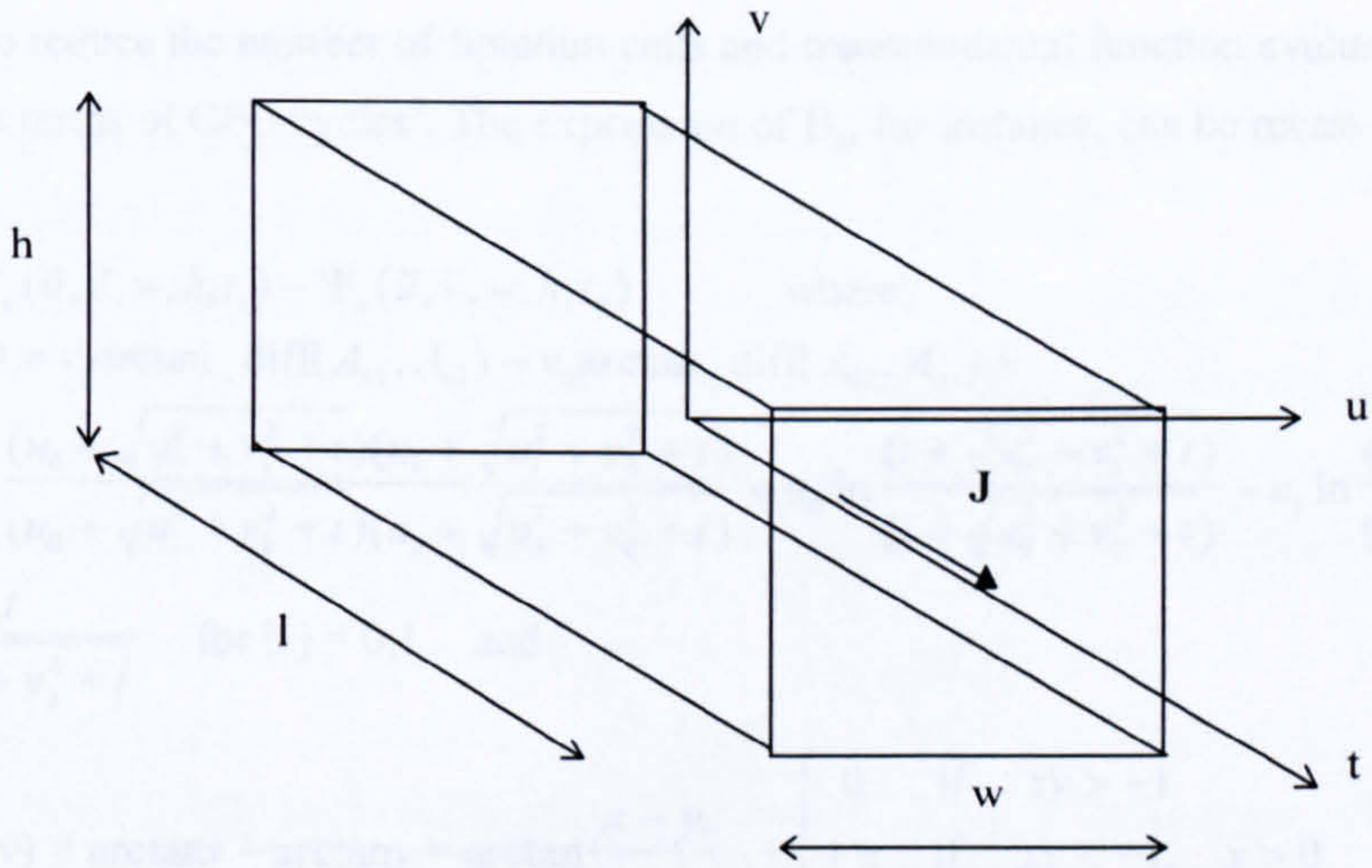


Fig. 2.4 - Rectangular brick geometry

The field components can be obtained in the following fully symbolic form (slightly different but equivalent to the formulation in [46]):

$$\begin{cases} B_u(\bar{u},\bar{v},\bar{t})=-\Phi(u_1,v_1,t_1)+\Phi(u_0,v_1,t_1)+\Phi(u_1,v_0,t_1)-\Phi(u_0,v_0,t_1)+ \\ \qquad +\Phi(u_1,v_1,t_0)-\Phi(u_0,v_1,t_0)-\Phi(u_1,v_0,t_0)+\Phi(u_0,v_0,t_0) \\ B_v(\bar{u},\bar{v},\bar{t})=-\Phi(v_1,u_1,t_1)+\Phi(v_0,u_1,t_1)+\Phi(v_1,u_0,t_1)-\Phi(v_0,u_0,t_1)+ \\ \qquad +\Phi(v_1,u_1,t_0)-\Phi(v_0,u_1,t_0)-\Phi(v_1,u_0,t_0)+\Phi(v_0,u_0,t_0) \\ B_t(\bar{u},\bar{v},\bar{t})=0 \end{cases} \tag{2.5}$$

8 The integral has a closed form solution also in the general case when **J** has an arbitrary orientation, but this option is not particularly useful for the discussion.

where:

$$u_1 = +\frac{w}{2} - \bar{u}, \quad v_1 = +\frac{h}{2} - \bar{v}, \quad t_1 = +\frac{l}{2} - \bar{t},$$
$$u_0 = -\frac{w}{2} - \bar{u}, \quad v_0 = -\frac{h}{2} - \bar{v}, \quad t_0 = -\frac{l}{2} - \bar{t}, \tag{2.6}$$

$$\Phi(u,v,t) = -t + v\left[\arctan\frac{t}{v} - \arctan\frac{ut}{v\rho}\right] + t\ln(u+\rho) + u\ln(t+\rho) = \int -\frac{v}{\rho}\,dudvdt, \tag{2.7}$$

and

$$\rho = \sqrt{u^2 + v^2 + t^2} \tag{2.8}$$

As could be expected, the field component parallel to the current is null, while the other components are given by expressions which are symmetric in the variables (u,v). Note also that (2.7) has no singularities in $\Re^3$.

Although the (2.5) are in a form which is very convenient for coding, they could be compacted and optimised so as to reduce the number of function calls and transcendental function evaluations, which are very expensive in terms of CPU cycles[9]. The expression of B_u, for instance, can be recast as follows:

$B_u(\bar{u},\bar{v},\bar{t}) = \Psi_u(\bar{u},\bar{v},w,h,t_1) - \Psi_u(\bar{u},\bar{v},w,h,t_0)$ where:

$$\Psi_u(\bar{u},\bar{v},w,h,t) = v_1\text{arctan_diff}(A_{11},A_{01}) - v_0\text{arctan_diff}(A_{00},A_{10}) +$$
$$t\ln\frac{(u_0+\sqrt{u_0^2+v_1^2+t})(u_1+\sqrt{u_1^2+v_0^2+t})}{(u_0+\sqrt{u_1^2+v_1^2+t})(u_1+\sqrt{u_0^2+v_0^2+t})} + u_0\ln\frac{(t+\sqrt{u_0^2+v_1^2+t})}{(t+\sqrt{u_0^2+v_0^2+t})} - u_1\ln\frac{(t+\sqrt{u_1^2+v_1^2+t})}{(t+\sqrt{u_1^2+v_0^2+t})},$$

$$A_{ij} = \frac{u_i t}{v_j\sqrt{u_i^2+v_j^2+t}} \quad \text{for i, j} = 0,1 \quad \text{and}$$

$$\text{arctan_diff}(x,y) = \arctan x - \arctan y = \arctan\frac{x-y}{1+xy} + \begin{cases} 0 & \text{if} \quad xy > -1 \\ +\pi & \text{if} \quad xy < -1, \quad x > 0 \\ -\pi & \text{if} \quad xy < -1, \quad x < 0 \end{cases} \tag{2.9}$$

A similar expression can be derived for B_v.

It is necessary to give some consideration to the computation of the arctangent function, which has theoretically an infinite number of determinations differing by integer multiples of π. For instance, a naïve calculation of the arctangents in (2.7) using the standard computer-supplied routine for arctan(y,x)=arctan(y/x), which returns values in the range $-\pi$ to π taking into account the signs of x and

---

[9] A function call takes typically ~50 clock cycles on an Intel Pentium processor [47]. Function calls can sometimes be avoided automatically in the C++ language by means of the inline keyword, which requests the compiler to insert the whole code of the function wherever a call to that function is made. However, this facility is not available in other languages (e.g. in FORTRAN) and even in C++ most compilers do not guarantee all inline requests to be satisfied. Arithmetic operations, on the other hand, are decoded into a single "μ-op", i.e. the basic instruction unit which, on a Pentium II, may take as little as $^1/_6$ of a cycle to execute (this figure depends upon the number of ALUs in parallel, the depth of the pipelines and the optimality of the instruction flow). Transcendental functions, by comparison, take on average from 15 to 50 times as long as arithmetic instructions to run, depending mostly on the rapidity of the local convergence of the series by which they are approximated (as can be seen running simple benchmarks).

y, may give wrong results depending on the path of the integrated variable. In particular, the value will jump by π every time that the integration variable becomes infinite (interestingly, a numerical integration would be better in this respect because it would automatically keep track of the correct value). In the relatively simple cases in (2.7) this eventuality does not arise since:

$$v\arctan\frac{t}{v}=\int\frac{1}{1+\frac{t^2}{v^2}}dt, \qquad v\arctan\frac{ut}{v\rho}=\int\frac{uv^2}{\rho(v^2+t^2)}dt \tag{2.10}$$

with t=0→1, so the fundamental determination (i.e. the one in the range –π to π) is correct. In the case of (2.9), two arctangents are merged together and the arctan_diff function (defined in [48]) is necessary to guarantee correct results, as each one of the terms $v_j\arctan A_{ij}$ is formally identical to the second of the (2.10).

2.1.2.2 Errors in single-brick modelling of arc-shaped coil segments

In the general case, a coil which is curved or made by straight segments not intersecting at 90° cannot be decomposed exactly in a finite number of rectangular bricks. In this and the next section, the quality of the approximation obtained from an imperfect subdivision is discussed.

For the sake of simplicity, let us consider first a planar, circular arc-shaped coil segment of angular extension $\Delta\vartheta$ and cross-section w×h approximated by a single brick spanning the chord between the middle point of the end cross-sections, as shown in Fig. 2.5. More complicated cases that can be modelled by COMET, like tapered or twisted coils, will not be considered in the present analysis.

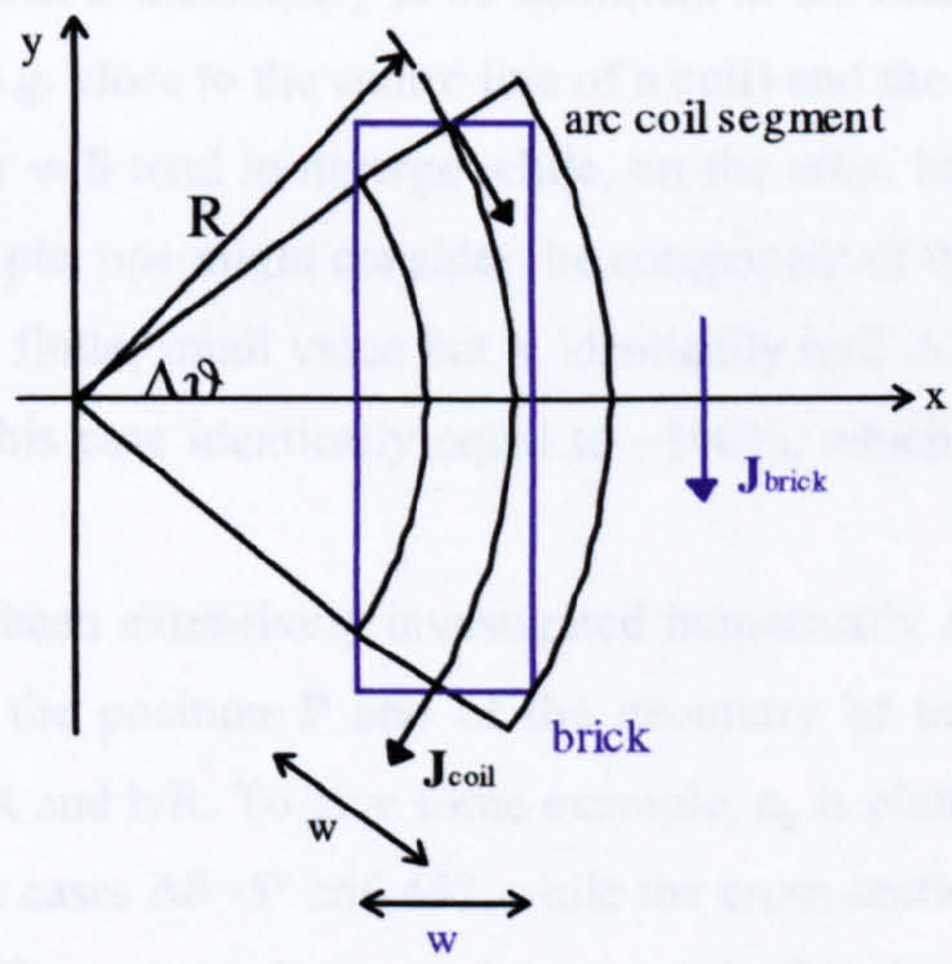


Fig. 2.5 - Geometry for the error study on the single-brick approximation of an arc-shaped coil segment

Errors will arise from the mismatch between the shapes of the brick and the coil and from the deviation of the current density vector **J**. The error vector ε(**P**) at point ***P*** shall be defined by the difference between the exact magnetic field $\mathbf{B}_{exact}(\mathbf{P})$ and the one obtained from the brick formulæ,

in general upon the geometry of the arc and will tend obviously to vanish as $\Delta\vartheta \to 0$. This error may be characterised defining two scalars, i.e. the relative error:

$$\varepsilon_{B,rel} = sign\left(\varepsilon_{B,rel,j}\right)\max_i\left\{\left|\varepsilon_{B,rel,i}\right|\right\}, \quad \text{with} \quad \varepsilon_{B,rel,i} = \frac{B_{i,brick} - B_{i,exact}}{B_{i,exact}}, \quad i = \{x, y, z\} \tag{2.11}$$

and the normalised error:

$$\varepsilon_{B,norm} = \text{sign}\left(\varepsilon_{B,norm,i}\right)\max_i\left\{\left|\varepsilon_{B,norm,i}\right|\right\}, \quad \text{with} \quad \varepsilon_{B,norm,i} = \frac{B_{i,brick} - B_{i,exact}}{B_{max}}, \quad i = \{x, y, z\} \tag{2.12}$$

where:

— $B_{i,exact}$ is the "true" value of the i^{th} magnetic field component, obtained by dividing the arc in a very high number of thin bricks (200 are usually more than enough to converge);

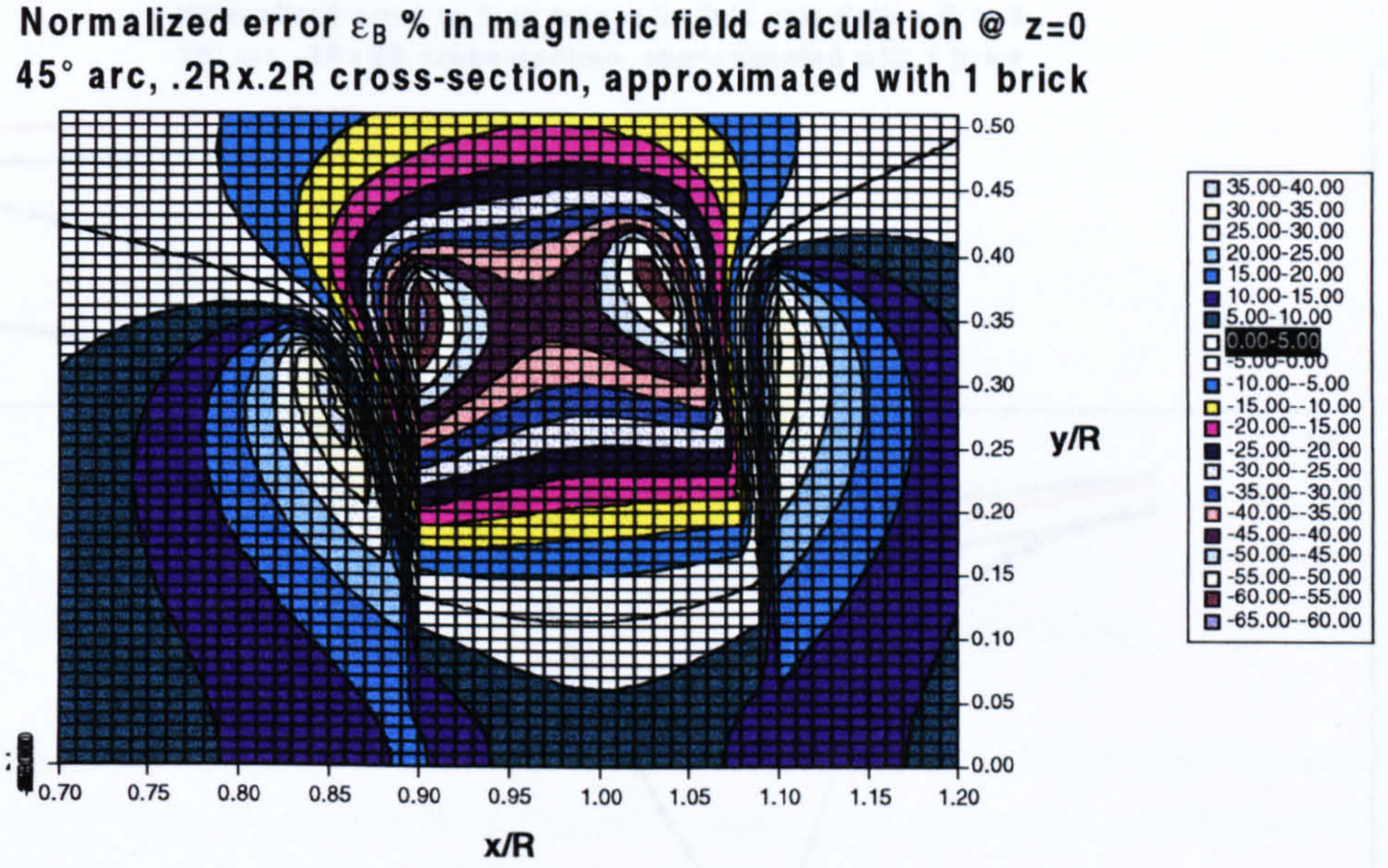
— $B_{max} = \dfrac{\mu_0 J}{\pi \min(w,h)}$ is a reference value corresponding approximately to the maximum magnetic field generated by the brick.

The normalised error $\varepsilon_{B,norm}$ given by (2.12) is the most meaningful quality indicator for the purposes of the present work and will be the only one considered in the following analysis (dropping the subscript *norm* for brevity). There are, as a matter of fact, some calculations for which the relative error $\varepsilon_{B,rel}$ would be more appropriate: one such example is field line integration, in which the difference between true and calculated field must be always minimised, whatever the magnitude of the field, for the line to be accurate. As far as the integration of the magnetic force over the volume of a coil is concerned, however, the normalised error is more meaningful as it gives a comparison between the local error and the maximum value of the field, which is most likely to be dominant in the final result. In fact, in those areas where the field is almost zero (e.g. close to the centre line of a coil) and the contribution to the total force is insignificant the relative error will tend to diverge while, on the other hand, the normalised error will remain small. As a further example, one might consider the component of the field along the brick's axis, B_y, which is has in reality some finite, small value but is identically null in the brick approximation. The relative error $\varepsilon_{B,rel,y}$ will be in this case identically equal to –100%, which clearly does not convey any useful information.

The distribution of $\varepsilon_B(\mathbf{P})$ has been extensively investigated numerically and it has been found to be a fairly complicated function of the position $\mathbf{P}$ and of the geometry of the arc expressed by the non-dimensional parameters $\Delta\vartheta$, w/R and h/R. To give some example, ε_B is plotted with colour-coding in Fig. 2.6 at z=0, w/R=h/R=0.2 for the cases $\Delta\vartheta$=5° and 45°, while the cross-sections of the surface for the case $\Delta\vartheta$=20°are charted in Fig. 2.7. The main findings can be summarised in the following points:

- the error, as expected, tends to peak close to the surface of the coil segment where the overlap between coil and brick is not perfect;
- Other things being equal, at any given position (ρ/R, $\vartheta/\Delta\vartheta$) relative to the brick the error tends to vanish approximately with quadratic rate as $\Delta\vartheta \to 0$.

- The error depends mainly on the relative thickness in the z direction (h/R) and is maximum on the z=0 symmetry plane.
- On z=0, the largest *positive* error ε^{+}_{Peak} occurs along the inner side, in points are outside of the coil arc but inside the brick (Fig. 2.6). The function $\varepsilon^{+}_{Peak}(\Delta\vartheta, {}^{h}/_{R})$ is plotted on the basis of numerical test data in Fig. 2.8. The maximum error appears to be relatively small for $0.2< {}^{h}/_{R} <1$, but grows very quickly for ${}^{h}/_{R} <0.12$ as the gap between coil and brick widens.
- The largest *negative* error ε^{-}_{Peak} occurs instead at the vertical edges of the end cross-sections, which tend to be outside the brick. Either of ε^{+}_{Peak} or ε^{-}_{Peak} can be in principle largest in magnitude.
- The error is theoretically zero on two symmetric curved surfaces which separate the positive error region from the negative one. The intersection of this surfaces with the centre line of the coil can be found typically at the angular position $\vartheta^{*}\approx\pm3°$, for $\Delta\vartheta<20°$ and ${}^{h}/_{R} >0.2$.
- the error is found to decay exponentially in all directions away from the coil arc with a characteristic length of the order of the dimension of the arc.



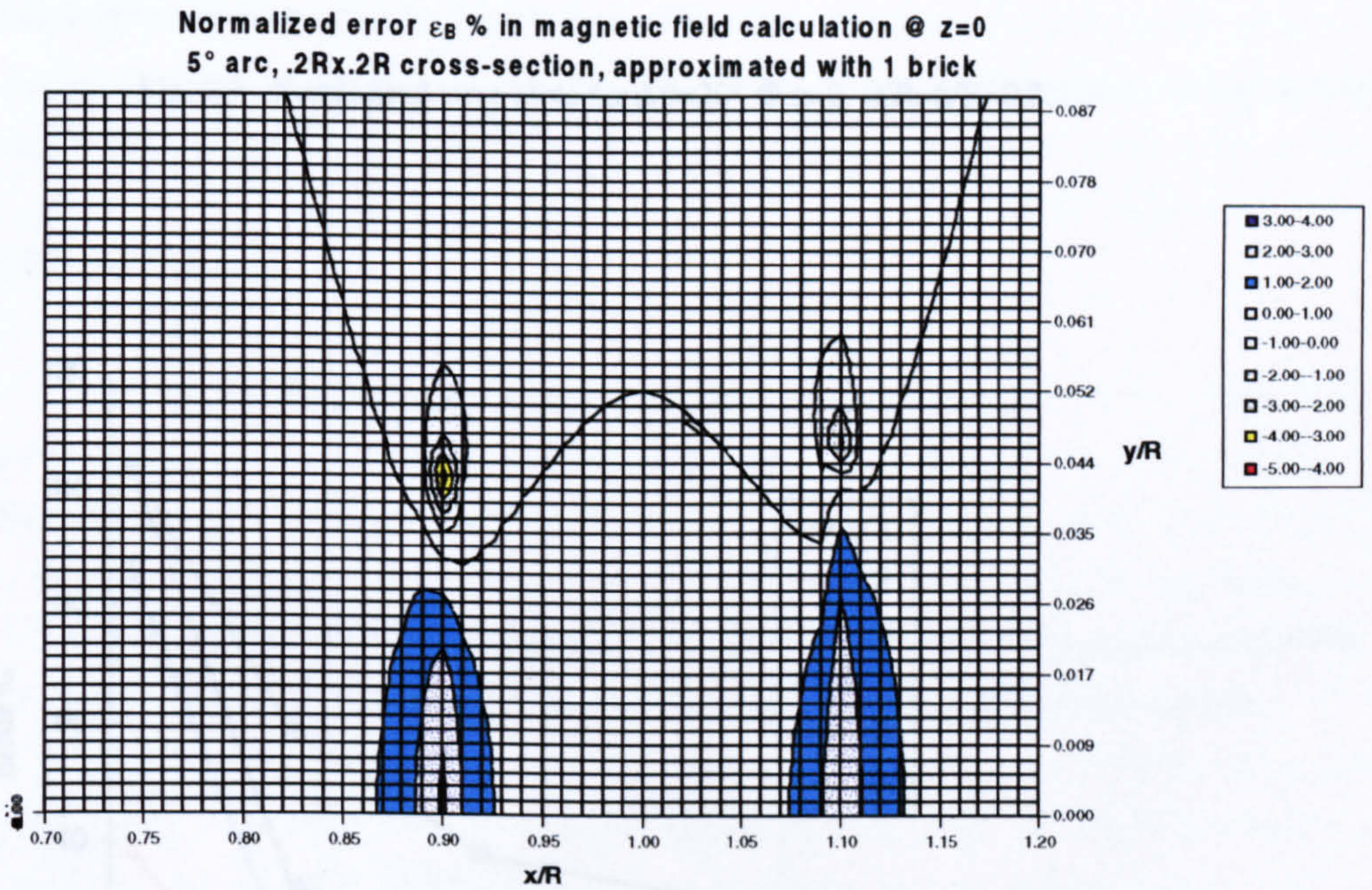


Fig. 2.6 - 2D normalised error plots for $\Delta\vartheta$=5° and 45° @ z=0, w/R=h/R=0.2 (color map).

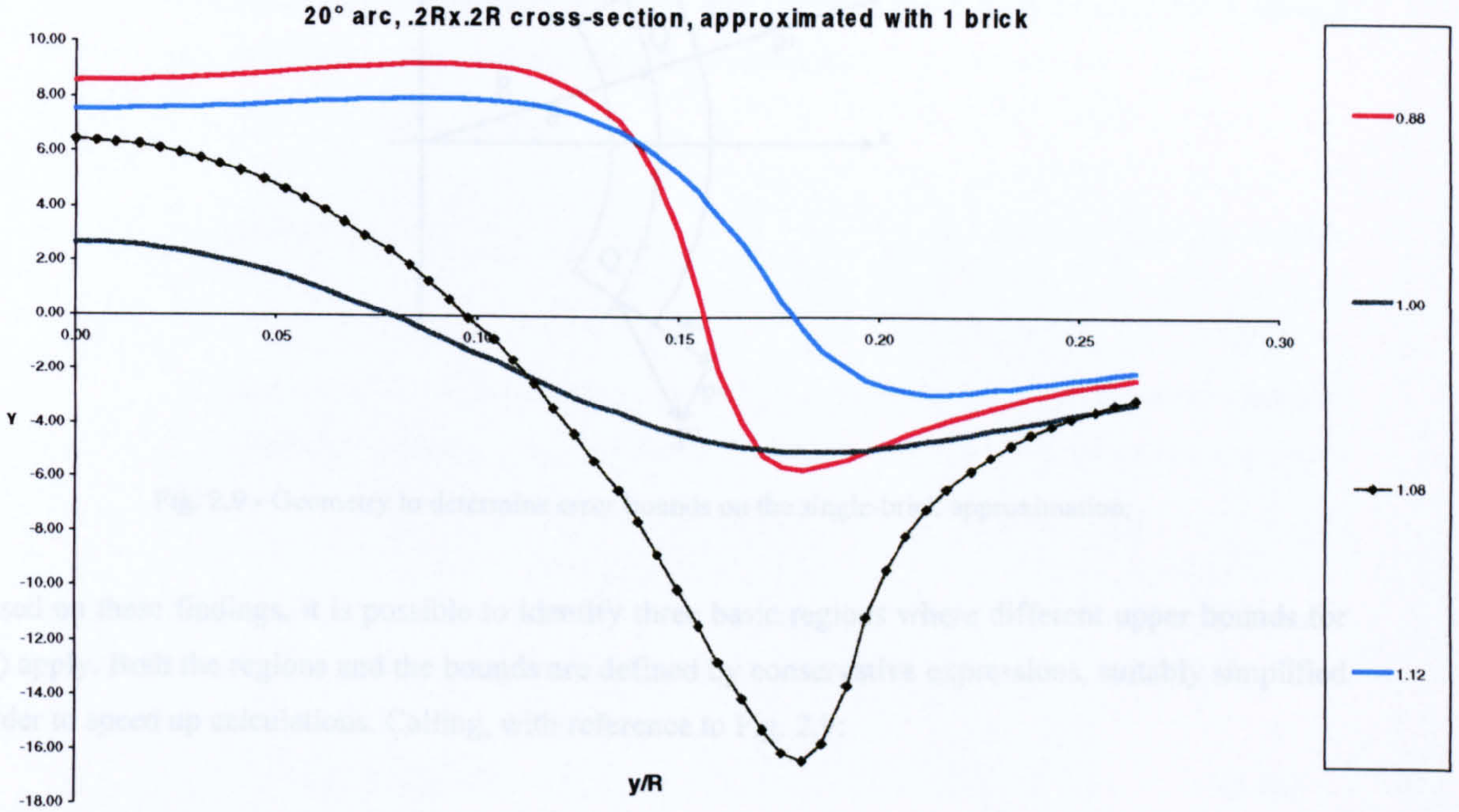


Fig. 2.7 - Normalised error plots for $\Delta\vartheta$=20° @ z=0, w/R=h/R=0.2.

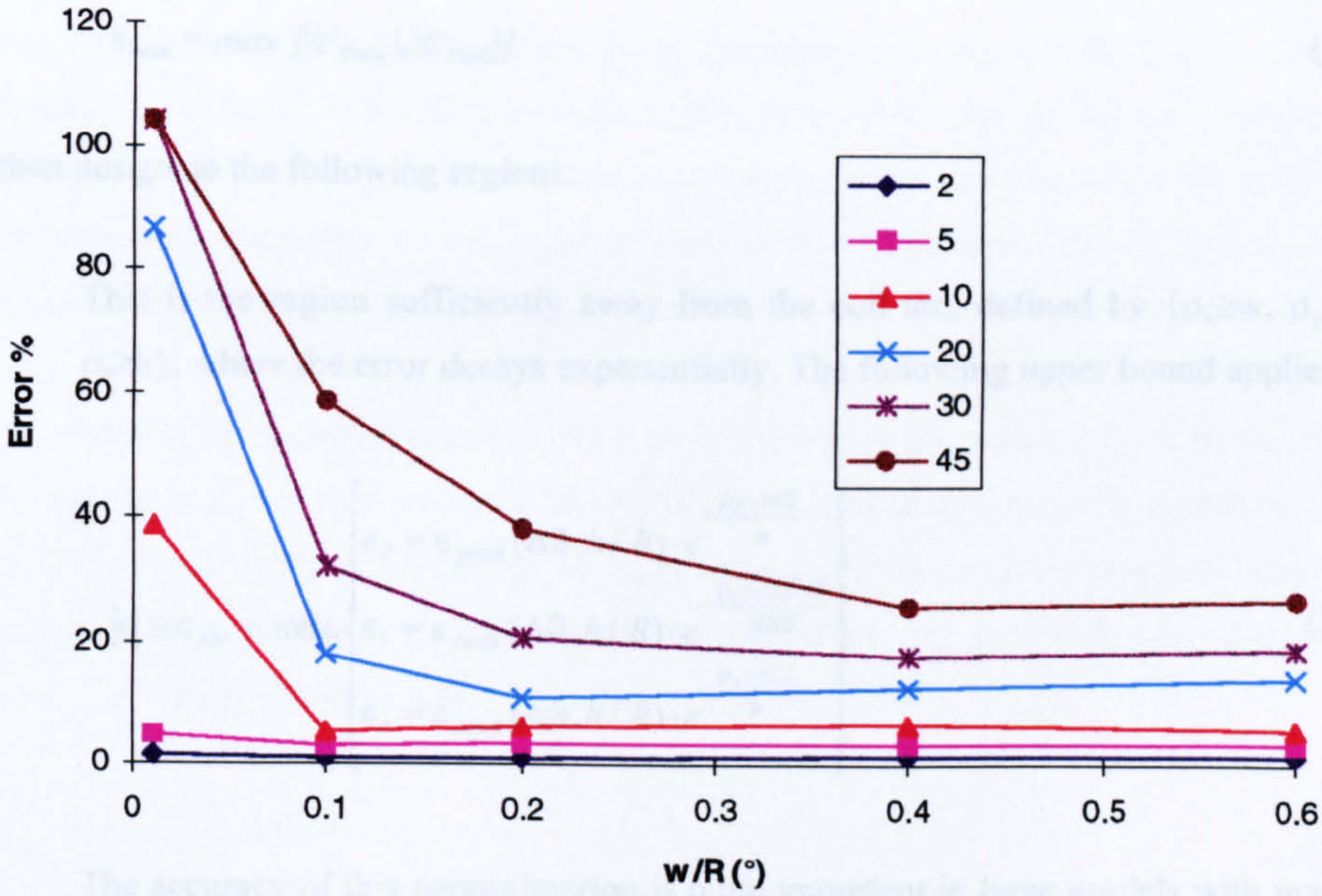


Fig. 2.8 - Peak error as a function of coil arc geometry.

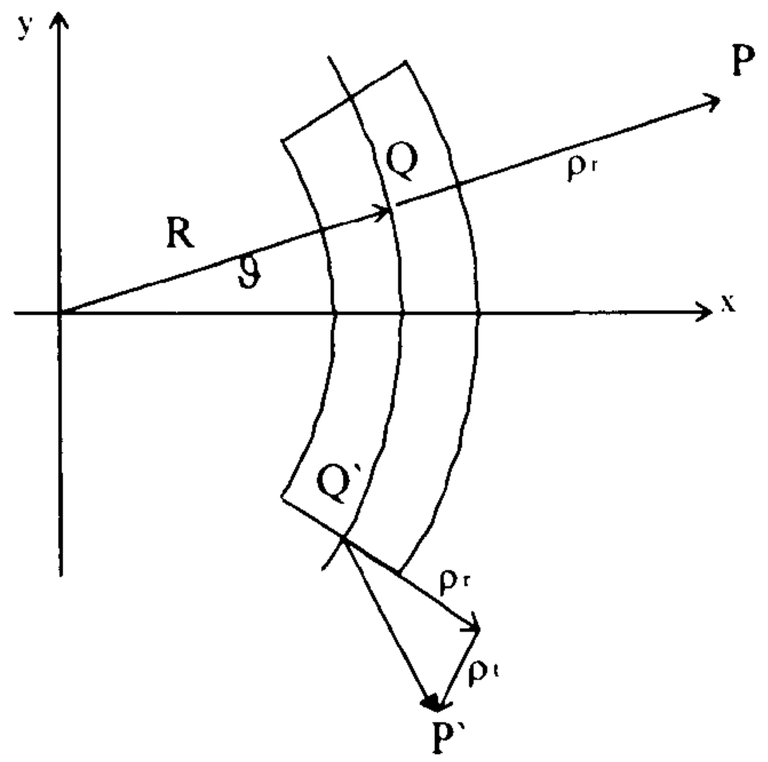


Fig. 2.9 - Geometry to determine error bounds on the single-brick approximation.

Based on these findings, it is possible to identify three basic regions where different upper bounds for $\varepsilon_B(\mathbf{P})$ apply. Both the regions and the bounds are defined by conservative expressions, suitably simplified in order to speed up calculations. Calling, with reference to Fig. 2.9:

— $\boldsymbol{Q}$ the point on the arc centre-line which is closest to $\boldsymbol{P}$;

— $\rho = \{\rho_r, \rho_t, \rho_z\}$ the vector (**P**–**Q**) expressed in the cylindrical reference system (r,t,z), taking $\rho_t = 0$ if **Q** is internal to the arc segment;

and defining the peak error as:

$$\varepsilon_{Peak} = max\ \{|\varepsilon^{+}_{Peak}|, |\varepsilon^{-}_{Peak}|\} \tag{2.13}$$

one could then designate the following regions:

Far region: This is the region sufficiently away from the coil arc, defined by $\{\rho_x \geq w,\ \rho_y \geq \frac{1}{2} R\Delta\vartheta,\ \rho_z \geq h\}$, where the error decays exponentially. The following upper bound applies:

$$|\varepsilon| \leq \varepsilon_{far} = \max. \left\{ \begin{aligned} \varepsilon_r &= \varepsilon_{peak}(\Delta\vartheta, h/R) \cdot e^{-\frac{\rho_r - w/2}{w}} \\ \varepsilon_t &= \varepsilon_{peak}(\Delta\vartheta, h/R) \cdot e^{-\frac{\rho_t - R\Delta\vartheta/2}{R\Delta\vartheta}} \\ \varepsilon_z &= \varepsilon_{peak}(\Delta\vartheta, h/R) \cdot e^{-\frac{\rho_z - h/2}{h}} \end{aligned} \right\} \tag{2.14}$$

The accuracy of this approximation is quite important in large models with many coils, where, on average, one can expect any given coil to be far from the point where the field is being computed.

Inner region: This is the internal volume of the coil, defined by $\{\rho_r \le \frac{1}{2}w,\ \rho_t = 0,\ \rho_z \le \frac{1}{2}h\}$. An upper bound for $|\varepsilon_B|$, independent from ρ_z, can be represented schematically by a surface $\varepsilon_{inner}(r,\vartheta)$ defined by parabolic radial cross-sections:

$$|\varepsilon_B| \le \varepsilon_{inner} = A(\vartheta) + B(\vartheta) r^2$$

$$A(\vartheta) = \alpha\varepsilon_{peak}\left\{1 + \frac{\alpha(1-\eta^2)+\eta^2}{\alpha\eta(\eta-1)}\frac{\vartheta}{\Delta\vartheta/2} - \frac{\alpha(1-\eta)+\eta}{\alpha\eta(\eta-1)}\frac{\vartheta^2}{\Delta\vartheta^2/4}\right\}, \quad B(\vartheta) = \frac{4}{w^2}(\varepsilon_{peak} - A(\vartheta)) \tag{2.15}$$

where $\eta = 2\vartheta^*/\Delta\vartheta$ is the fraction of the angular extension at which the error vanishes. This function gives $\varepsilon_{inner} = \varepsilon_{peak}$ all along the border ($r = \pm\frac{1}{2}w$), except on the symmetry plane where $\varepsilon_{inner} = \alpha\varepsilon_{peak}$ with, typically, $\alpha \approx 0.5$.

Surface region: This is the intermediate zone between the far and the inner regions where the error is observed to peak. The upper bound for the magnitude of the error can be taken to be simply:

$$|\varepsilon| \le \varepsilon_{Peak} \tag{2.16}$$

This assumption is very conservative, since there are always locations on the surface of the coil where the error is theoretically zero. However, this circumstance has not been found worthwhile to exploit as it occurs only in a very narrow area which is very difficult to identify numerically because of the large local gradient of the error.

2.1.2.3 Errors in multi-brick coil modelling

In real calculations a coil will be discretized by a sequence of many bricks and, in general, the simplified bounds (2.14) to (2.16) will no longer apply. The errors due to adjacent bricks tend to interfere: in particular, the error ε^-_{Peak} at the end cross-sections tends to increase, while the errors ε^+_{Peak} at the inner sides cancel out partially. As the negative error peak is usually the largest in magnitude, the upper bound indicated in the previous section appear to be too optimistic and further investigation has been carried out.

The effect of refining the discretisation of a coil (i.e. of increasing the number n_B of bricks employed for the subdivision) on ε_{Peak} has been studied with another run of numerical tests, the results of which are plotted in Fig. 2.11. For the sake of simplicity the cases considered include only bricks of equal lengths, even if the adoption of larger bricks far away from the point where the field is being calculated could prove beneficial. The results obtained define a function (in tabular form):

$$\varepsilon_{Peak} = \varepsilon_{Peak}(n_B, \Delta\vartheta, {}^h/_R) \tag{2.17}$$

which can be calculated, for instance, by means of a triple linear interpolation. In the first approximation, the error tends to decrease with the reciprocal of the number of bricks used:

$$\varepsilon_{Peak} \propto 1/n_B \propto \Delta\vartheta_{BRICK} \tag{2.18}$$

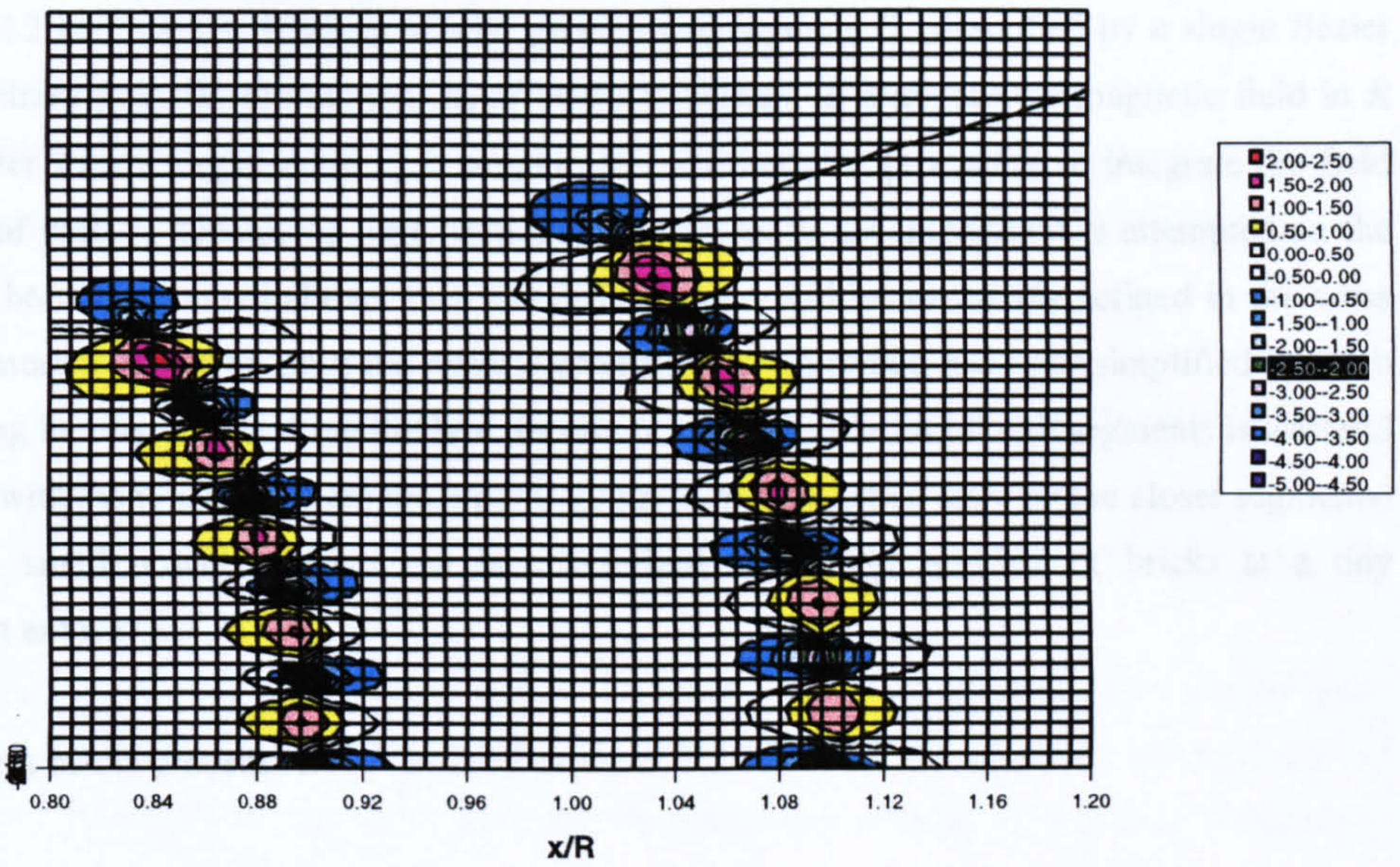


Fig. 2.10 - 2D normalised error plot in case of 10-bricks discretisation for $\Delta\vartheta$=45° @ z=0, w/R=h/R=0.2

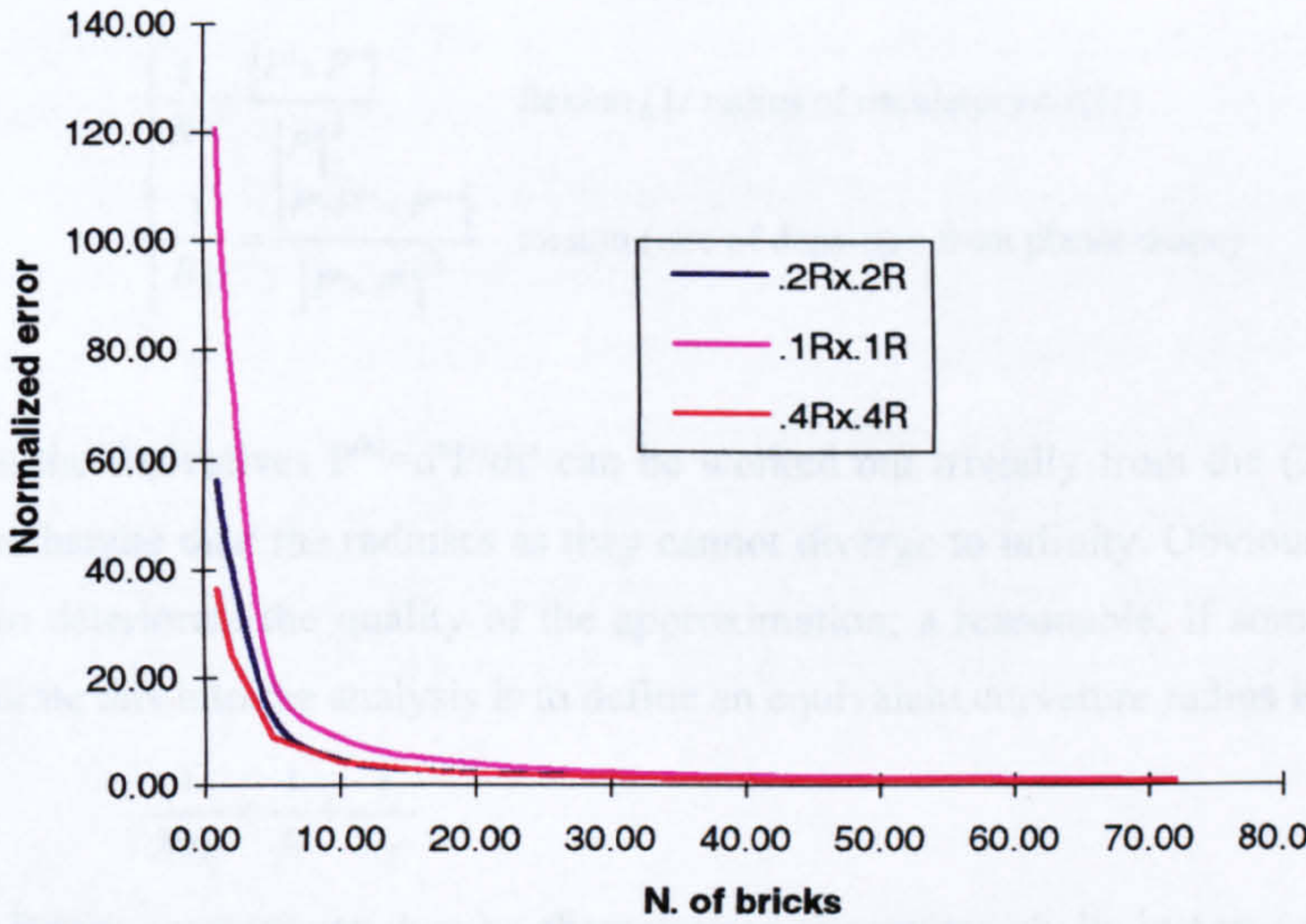


Fig. 2.11 - Maximum error as a function of the number of bricks used

2.1.2.4 Adaptive coil discretization

The problem of the optimal decomposition of coils into bricks will be considered now on the basis of the results of 2.1.2.2 and 2.1.2.3. More precisely, given a coil segment $\mathcal{C}$ (described by a single Bézier curve) and an arbitrary point $\boldsymbol{R}$, the number n_B of bricks necessary to integrate the magnetic field in $\boldsymbol{R}$ with accuracy better than a target value ε_T is sought after. An iterative procedure to integrate the field over a whole set of coils is considered here. Initially, a preliminary decomposition is attempted on the basis of the error bounds obtained above; then the discretisation will be iteratively refined in the areas which contribute more to the error, until the result converges. The algorithm has been simplified as much as possible, keeping in mind that seeking the best decomposition possible for all coil segments is wasteful in case of models with many coils (where the error is going to be dominated only by the closer segments) and is useless in small models (which can be discretized with large number of bricks at a tiny computational cost anyway).

These are the steps of the procedure:

1) *Analysis of coil segment geometry*

The level of refinement needed depends, in the first place, on the radius of curvature of the coil centre line (R) and on the angular extension of the length over which this can be considered to be approximately constant. From basic calculus, a parametric line P(t) in 3D space is characterised by two measures of curvature:

$$\begin{cases} \dfrac{1}{R} = \dfrac{\left|P' \times P''\right|}{\left|P'\right|^3} & \text{flexion (1/ radius of osculatory circle)} \\ \dfrac{1}{R_T} = \dfrac{\left|P' \cdot P'' \times P'''\right|}{\left|P' \times P''\right|^2} & \text{torsion (rate of departure from planar shape)} \end{cases} \tag{2.19}$$

where the derivatives $P^{(n)}=d^nP/dt^n$ can be worked out trivially from the (2.2). The curvatures are easier to handle than the radiuses as they cannot diverge to infinity. Obviously, a nonzero torsion is going to deteriorate the quality of the approximation; a reasonable, if somewhat arbitrary, way to incorporate this into the analysis is to define an equivalent curvature radius R_{eq} such as:

$$\frac{1}{Req} = \frac{1}{R} + \frac{1}{R_T} \tag{2.20}$$

Each Bézier segment can then be characterised conservatively by just two equivalent values:

$$\begin{aligned} R_{eq,\min} &= \min_{t=0..1} \{R_{eq}(t)\} \\ \Delta\vartheta_{eq} &= \frac{length(\mathcal{C})}{R_{eq,\min}} \end{aligned} \tag{2.21}$$

These values need to be computed just once for each segment.

2) *Estimate of number of bricks needed*

The minimum number of bricks n_B necessary to get $\varepsilon_B \leq \varepsilon_T$ is estimated on the basis of the upper bounds previously found, expressed as a function of the value of ε_{Peak} calculated from (2.17). More precisely, the calculation proceeds differently depending on the region in which **R** lies respect to the coil:

Far region: The required number of bricks may be found by substituting first the (2.17) and (2.21) into the (2.14) and then inverting numerically.

Surface region: Similarly, n_B may be found by substituting first the (2.17) and (2.21) into the (2.16) and then inverting.

Inner region: In this case, direct application of the (2.15) becomes difficult since the parabolic pattern is repeated many times along the coil segment and the relative position of **R** cannot be known in advance. The worst-case estimate is therefore obtained by assuming, as in the surface region, that $|\varepsilon_B| < \varepsilon_{peak}$.

The n_B so obtained will be of course rounded up to the next integer.

3) *Initial coil subdivision*

The initial brick decomposition can be generated by dividing the Bézier parameter range [0,1] in n_B equal intervals $\Delta t = 1/n_B$. If the curvature of the segment is high the resulting subdivision will not be perfectly uniform, however this has been found to have little practical effect.

In the case where **R** belongs to the inner or boundary regions, an improvement could be obtained by positioning exactly the brick including **R** so as to make it coincide with the position of zero error (namely, the ϑ^* defined in 2.1.2.2). Unfortunately, when multiple bricks are used the zero error surface keeps zigzagging in and out the boundary region, as one can see in Fig. 2.10; in other words, for a given distance ρ_r from the coil centre line an angular position which guarantees zero error does not necessarily exist. For this reason, taking also into account that prediction of the position of minimum error is very complicated, the optimal positioning of the brick relative to **R** has not been pursued.

4) *Iterative refinement*

While the subdivision carried out in 3) represents a reasonably conservative choice, the approximate nature of the procedure makes it difficult to prove it. It is therefore necessary to proceed with a cycle of iterative refinements, which will consent to establish an objective convergence criterion.

Considering a typical situation in which the field in **R** results from the contributions of N_C coil segments (summed over the index k):

$$\mathbf{B}(\mathbf{R}) = \sum_k \mathbf{B}_k(\mathbf{R}) \tag{2.22}$$

At the i^{th} iteration (with i>1), the error relative to each segment may be estimated from the vector difference:

$$\varepsilon_{k,j} = \frac{\boldsymbol{B}_{k,j} - \boldsymbol{B}_{k,j-1}}{\max_k \left| \boldsymbol{B}_{k,j} \right|} \tag{2.23}$$

The normalising term at the denominator guarantees that the inaccuracies of different contributions are weighted in comparison with the largest; it also represents a safeguard against the case where the total field is zero because all contributions cancel out. The decision whether to refine the discretisation will be taken individually for each coil segment on the basis of (2.23):

$$if \begin{cases} \varepsilon_{k,i} \le \dfrac{\varepsilon_T}{N_C} & \text{stop calculating } \boldsymbol{B}_k \\ \varepsilon_{k,i} > \dfrac{\varepsilon_T}{N_C} & \text{iterate } \boldsymbol{B}_k \text{ with } n_{Bk,i+1} = \dfrac{\varepsilon_{k,i}}{\varepsilon_T} N_C n_{Bk,i} \end{cases} \tag{2.24}$$

When $\varepsilon_{k,j} \le \varepsilon_T \; \forall k$ also the global convergence condition:

$$\varepsilon_i = \frac{\left| \sum_k \left(\boldsymbol{B}_{k,i} - \boldsymbol{B}_{k,j-1} \right) \right|}{\max_k \left| \boldsymbol{B}_{k,i} \right|} \le \varepsilon_T \tag{2.25}$$

will be satisfied.

To conclude, note that different strategies can be adopted in different situations:

— in large models with many coils, of which just a few are going to give significant contributions to the field at any given point, it is convenient to evaluate the first subdivision with a very coarse accuracy (say, ε_T=20%); in the following iterative phase ε_T can be decreased and only the coils closest to **R** are likely to need further refinement.
— smaller models, instead, may be integrated more efficiently if ε_T is kept very low from the beginning, which should give a fine initial discretisation and thus minimise the number of subsequent iterations needed.

This particular algorithm, unlike all other methods discussed in this chapter, has not been fully implemented and tested yet within the COMET code.

2.1.3 Numerical integration of magnetic forces

The procedure used to integrate magnetic forces is discussed in this section. The basis for this calculation is the subdivision of the integration domain in a series of rectangular bricks, following the same idea as in 2.1.2. On each of these bricks, the resultant of the elementary forces and moments (taken respect to an arbitrary centre O) can be written down as:

$$\boldsymbol{F}_{brick} = \frac{\mu_0}{4\pi} \iiint_{brick} \boldsymbol{J}_{brick} \times \left[\iiint_{\mathcal{V}} \frac{\boldsymbol{J}(\boldsymbol{R}) \times (\boldsymbol{r} - \boldsymbol{R})}{\|\boldsymbol{r} - \boldsymbol{R}\|^3} d\mathcal{V} \right] d\mathcal{V}_{brick}$$
$$\boldsymbol{M}_{brick} = \frac{\mu_0}{4\pi} \iiint_{brick} \boldsymbol{J}_{brick} \times \left[\iiint_{\mathcal{V}} \frac{\boldsymbol{J}(\boldsymbol{R}) \times (\boldsymbol{r} - \boldsymbol{R})}{\|\boldsymbol{r} - \boldsymbol{R}\|^3} d\mathcal{V} \right] \times (\boldsymbol{r} - \boldsymbol{O}) d\mathcal{V}_{brick} \quad (2.26)$$

Where **r** is the integration variable. These expressions are too complex to calculate symbolically, which makes numerical integration the only choice. The approach adopted to ensure the desired level of precision ε_T is the following:

1. The initial decomposition of each coil segment in $n`_B$ bricks is performed according to point 2) of 2.1.2.4. The brick mesh for the calculation of the field, in principle, is totally independent for the mesh used for the calculation of the force (i.e. $n_B \neq n`_B$).
2. Each brick is further decomposed in $m_W m_H$ smaller bricks across its thickness (see Fig. 2.12). This additional level of decomposition may be necessary to capture the gradient of the field inside coil.
3. The field **B** is evaluated at the centre C of each brick only, applying the adaptive procedure described in section 2.1.2.4.
4. The mechanical actions on each brick are evaluated from:

$$\boldsymbol{F}_{brick} = \frac{\mu_0}{4\pi} \boldsymbol{J}(C) \times \boldsymbol{B}(C) \mathcal{V}_{brick}$$
$$\boldsymbol{M}_{brick} = \frac{\mu_0}{4\pi} \left[\boldsymbol{J}(C) \times \boldsymbol{B}(C) \right] \times (\boldsymbol{r} - \boldsymbol{O}) \mathcal{V}_{brick} \quad (2.27)$$

   and then added up to obtain the resultant on any particular coil.
5. The total number of bricks $n_B m_W m_H$ is progressively incremented, applying criteria equivalent to (2.23) and (2.24), until the required precision has been reached.

The subdivision across the thickness is usually unimportant in the case of forces between coils far away from each other, but becomes essential in the calculation of the coil's self-force (since the self-field on the coil centre line tends to be zero).

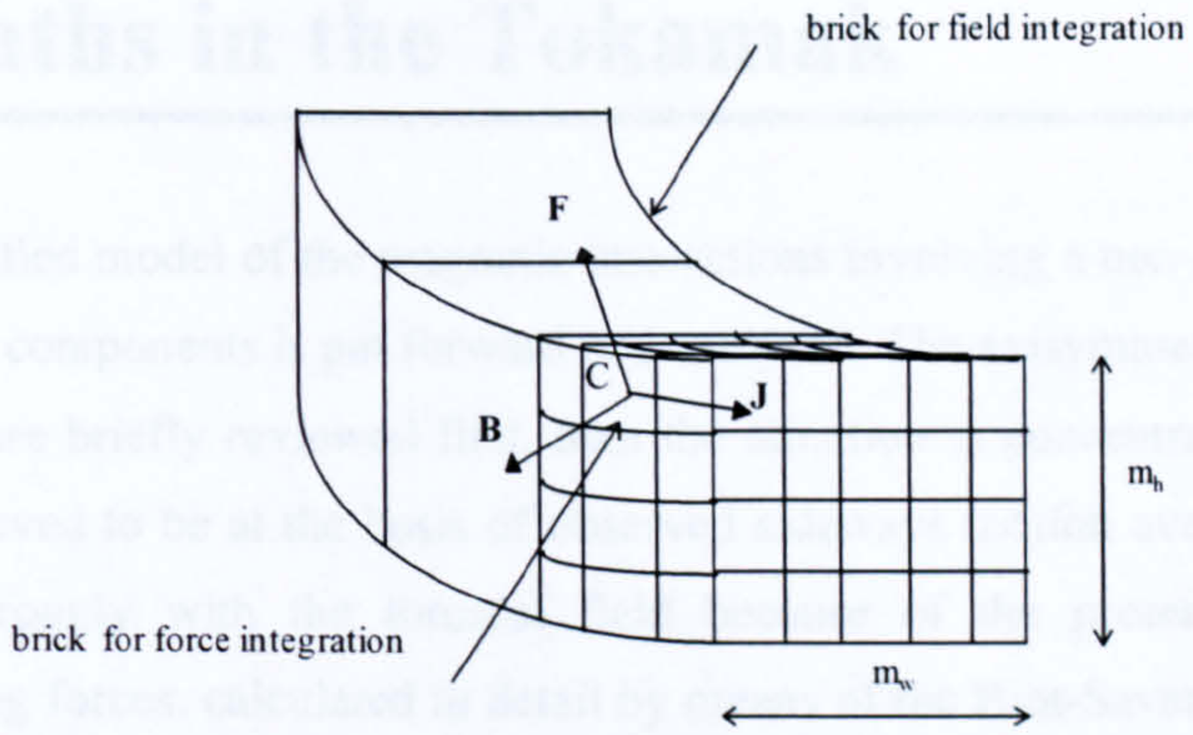


Fig. 2.12 - Coil decomposition for magnetic force integration (the picture represents a particular case where the boundaries of the bricks for the force coincide with the bricks for the field).

This method for force calculation presents some characteristic pitfalls. Typically, if the brick mesh used to integrate forces is much finer than the mesh used to integrate the field, some of the centres *C* will be close to the brick boundaries and will be affected by higher errors; paradoxically, the errors in the computed forces may become larger when the number $n`_B$ of cross-section subdivisions is increased. Possible ways around this problem are:

— the number of subdivisions is forced to be greater for the calculation of the field than for the calculation of forces: e.g. $n_B = 4 \sim 6\ n`_B$

— the accuracy ε_T required for the calculation of $\mathbf{B}(C)$ is adjusted, for example, as a function of the position of *C* inside the coil segment. This method is the only consistent with a fully automatic and adaptive approach.

2.2 Load paths in the Tokamak

In this section a simplified model of the magnetic interactions involving a non-axisymmetric disrupting plasma and the tokamak components is put forward and analysed. The axisymmetric conditions occurring during standard VDEs are briefly reviewed first, then the attention is concentrated upon the m=1, n=1 plasma kink model believed to be at the basis of observed sideways motion events. A kinked plasma is expected to interact strongly with the toroidal field because of the presence of poloidal current components; the resulting forces, calculated in detail by means of the Biot-Savart procedure described in the previous section, are assumed to be the essential input for the subsequent analysis of the load paths throughout the machine.

The scope of such an analysis is vast, ranging from general MHD instability theory to detailed mechanical assessment of JET connections between components. For this reason, no attempt is made here to discuss exhaustively all aspects; rather, this section is meant to be a "proof-of-concept" aimed at a few specific issues only:

- assessment in detail the upper bounds of TF/PF coil load distributions;
- to analyse qualitatively the interplay of forces and reactions arising throughout the machine in sideways events (which will also help in defining the mechanical models for the vacuum vessel in the next chapter);
- to seek out areas and connections which may become critical under these loads;
- to provide a first-order assessment of the magnitude of the forces involved in particular events, which will provide a basis for a comparison with some of the forces estimated in chapter 6.

2.2.1 Axisymmetric force balance

The distribution of forces due to purely axisymmetric instabilities is briefly reviewed here with the main purpose of providing a comparison term for the non-axisymmetric case examined in next section.

The succession of events taking place during a VDE has been broadly outlined in section 1.2.1 and the qualitative magnetic force balance on the vessel is represented in Fig. 2.13. The following considerations can be made:

— the plasma and the toroidal eddy currents in the vessel interact essentially with the divertor and the PF coils. These forces, which are routinely computed with codes such as MAXFEA or PROTEUS are usually found to be within allowable limits. The effects of additional currents, such as image currents in the iron or eddy currents in the Mechanical Structure have been estimated to be much smaller and are usually neglected [15].

— poloidal halo currents, on the other hand, interact essentially with the TF coils. Since halo currents form a small closed loop inside the vessel, the net force that they exert on the TF coils will be zero

in the first approximation. The main structural effect of the halo currents is therefore just a repulsive (stabilising) force between plasma and vessel.

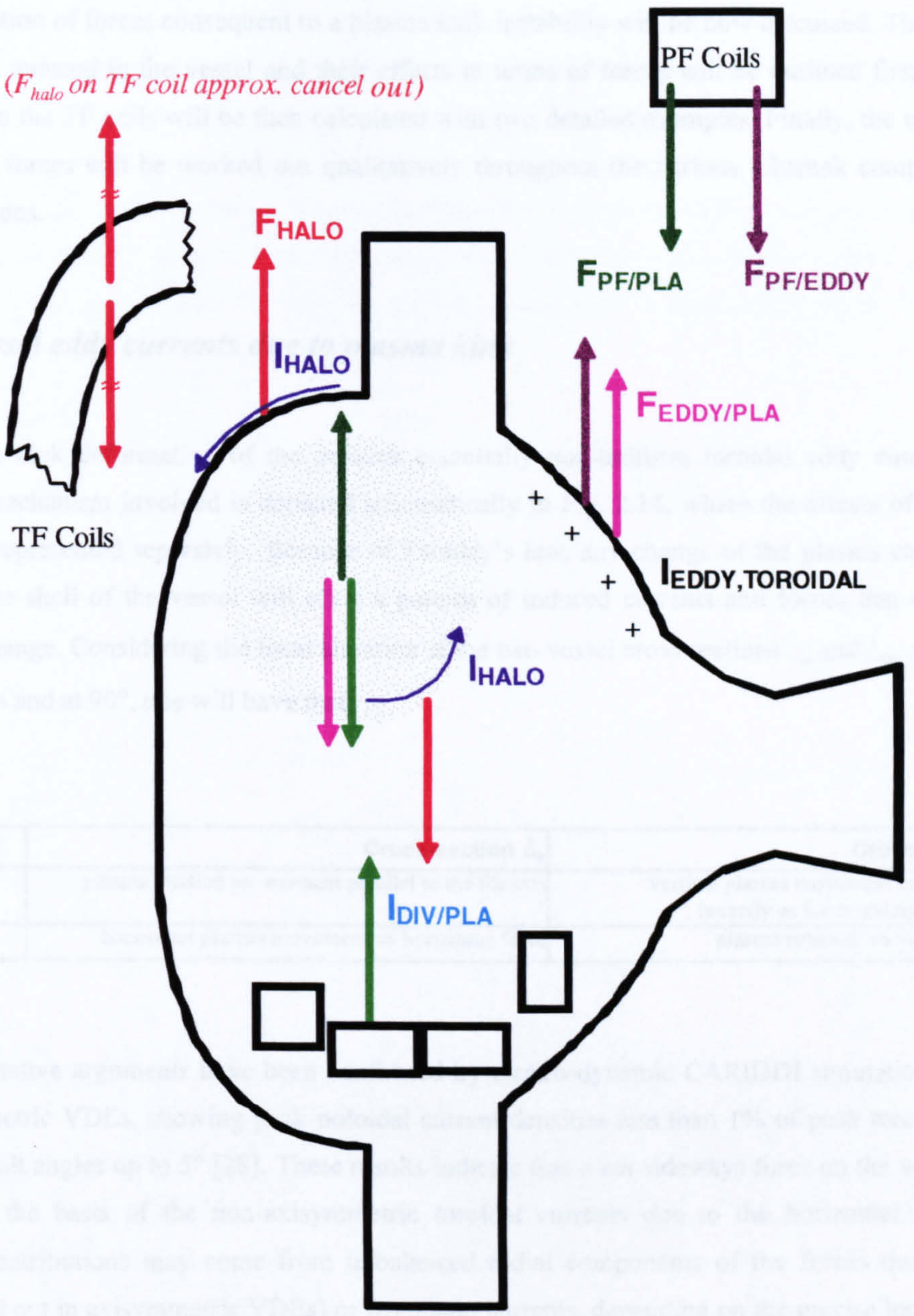


Fig. 2.13 - Qualitative vertical force balance during an axisymmetric VDE (only magnetic forces are considered)

2.2.2 Non-axisymmetric force balance

The distribution of forces consequent to a plasma kink instability will be now discussed. The pattern of eddy currents induced in the vessel and their effects in terms of forces will be outlined first. The force distribution on the TF coils will be then calculated with two detailed examples. Finally, the transmission path of these forces will be worked out qualitatively throughout the various tokamak components and their connections.

2.2.2.1 Vessel eddy currents due to plasma kink

The plasma kink deformation of the induces essentially non-uniform toroidal eddy currents in the vessel. The mechanism involved is depicted schematically in Fig. 2.14, where the effects of the tilt and the shift are represented separately. Because of Faraday's law, any change of the plasma current inside the conductive shell of the vessel will elicit a pattern of induced currents and forces that will tend to oppose the change. Considering the local situation at the two vessel cross sections $_0$ and $_{90}$, respectively on the tilt axis and at 90°, one will have that:

Deformation	Cross-section λ_0	Cross-section λ_{90}
Tilt	plasma rotation ⇒ moment parallel to the tilt axis	vertical plasma movement ⇒ vertical force (exactly as for an axisymmetric VDE)
Shift	horizontal plasma movement ⇒ horizontal force	plasma rotation ⇒ vertical moment

These qualitative arguments have been confirmed by electro-dynamic CARIDDI simulations of ITER non-axisymmetric VDEs, showing peak poloidal current densities less than 1% of peak toroidal current densities for tilt angles up to 5° [28]. These results indicate that a net sideways force on the vessel can be expected on the basis of the non-axisymmetric toroidal currents due to the horizontal shift alone. Additional contributions may come from unbalanced radial components of the forces due to the tilt (which cancel out in axisymmetric VDEs) or from halo currents, depending on the precise location of the impact point of the plasma on the vessel.

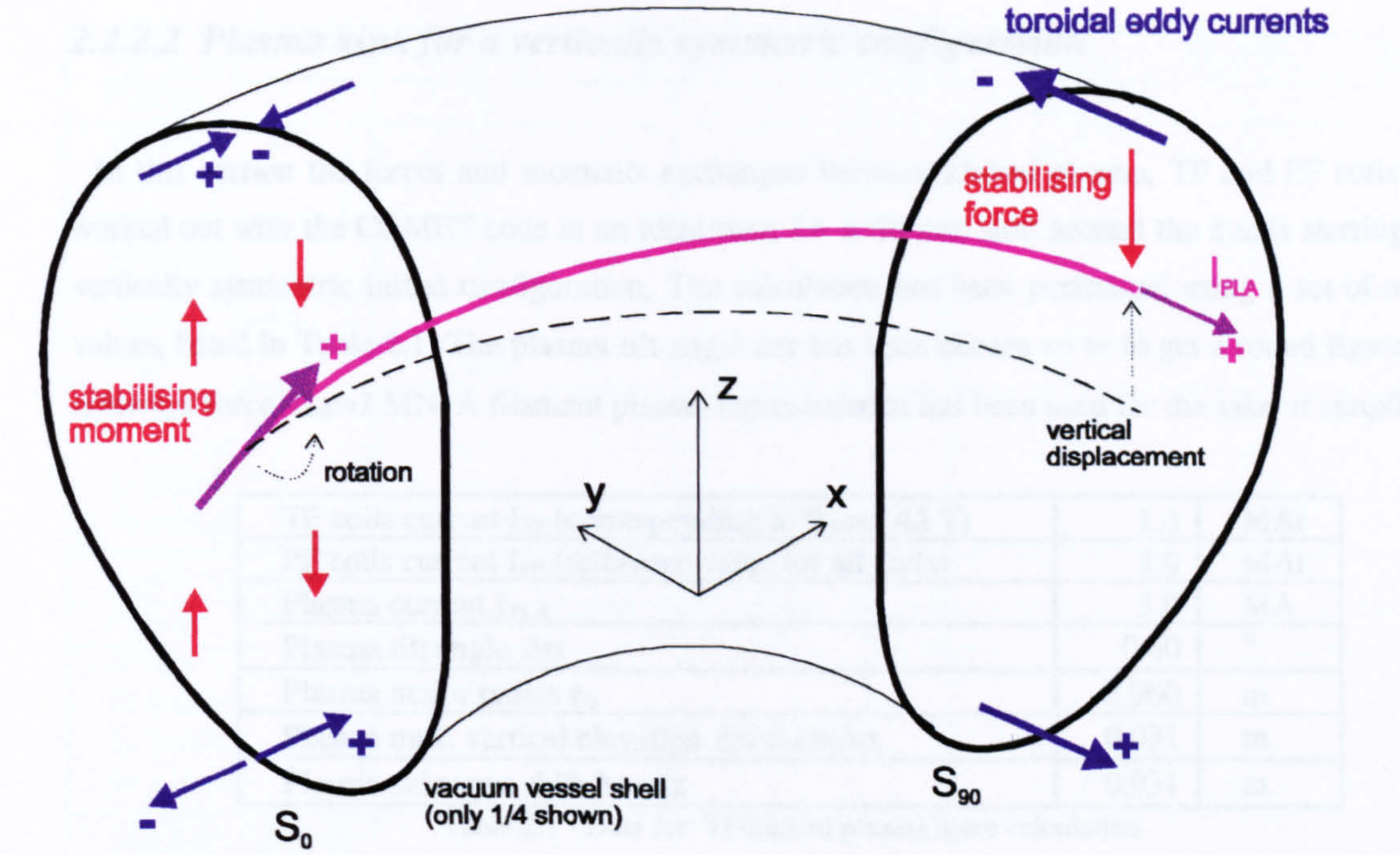
Understanding the nature of the eddy currents in the vessel is important to establish the relevance of the Biot-Savart integration carried out in the next section, where the plasma is assumed to be frozen at the maximum extent of its deformation. In a static calculation, in fact, the shielding effect of eddy and halo currents is not taken into account.

In general, calculations and measurements show that the PF currents vary little during a disruption, indicating thus that the vessel acts as an effective screen. TF currents, on the other hand, could be screened by changes taking place inside the vessel only by virtue of poloidal currents in the vessel.

However, one has that:

- poloidal eddy currents, as seen above, are not expected;
- poloidal halo currents in the vessel are matched by equal and opposite currents in the halo at a close distance (as discussed in the previous section); therefore, their effects on the TF coils tends to cancel out.

Therefore, one can conclude that no major screening effect is expected and the static calculation of the forces applied on the TF coils is a slightly pessimistic, but substantially accurate upper bound. The statically calculated forces on the PF coils, on the other hand, will be substantially higher than the real ones.



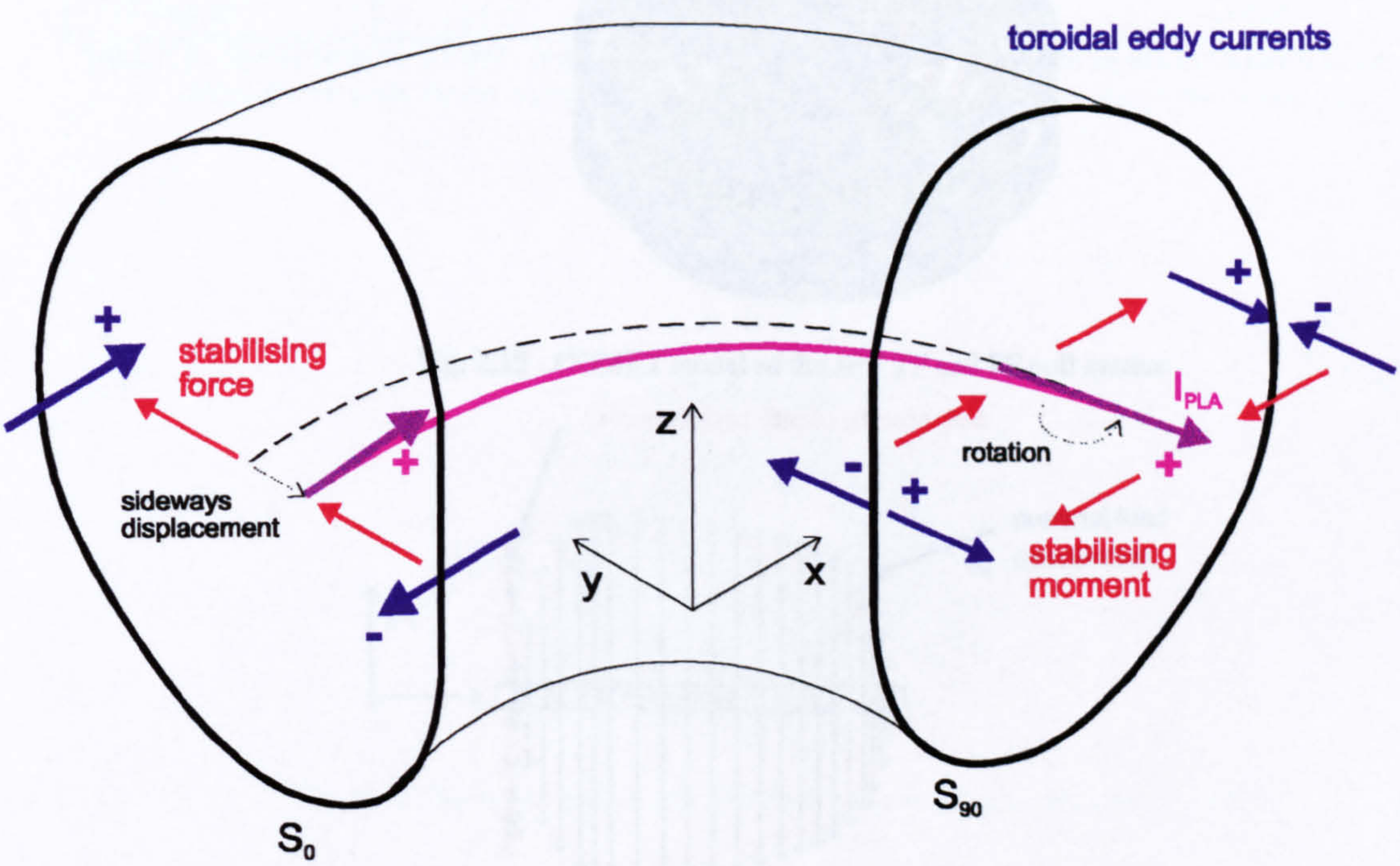


Fig. 2.14 - Qualitative pattern of non-axisymmetric toroidal eddy currents in the vessel due to a plasma tilt + shift. The stabilising forces arising on the vessel are also indicated.

2.2.2.2 Plasma kink for a vertically symmetric configuration

In this section the forces and moments exchanged between kinked plasma, TF and PF coils will be worked out with the COMET code in an ideal case, i.e. a tilt and shift around the x axis starting from a vertically symmetric initial configuration. The calculation has been performed using a set of reference values, listed in Table 2.1. The plasma tilt angle $\Delta\alpha$ has been chosen so as to get a round figure for the sideways force, F_{SW}=1 MN. A filament plasma representation has been used for the sake of simplicity.

TF coils current I_{TF} (corresponding to B_{T0}=3.45 T)	1.6	MAt
PF coils current I_{PF} (reference value for all coils)	1.0	MAt
Plasma current I_{PLA}	3.0	MA
Plasma tilt angle $\Delta\alpha$	0.60	°
Plasma major radius r_0	2.960	m
Plasma max. vertical elevation $\Delta z=r_0 tan\Delta\alpha$	0.031	m
Plasma sideways shift $\Delta x=\Delta z$	0.031	m

Table 2.1 - Data for TF/kinked plasma force calculation

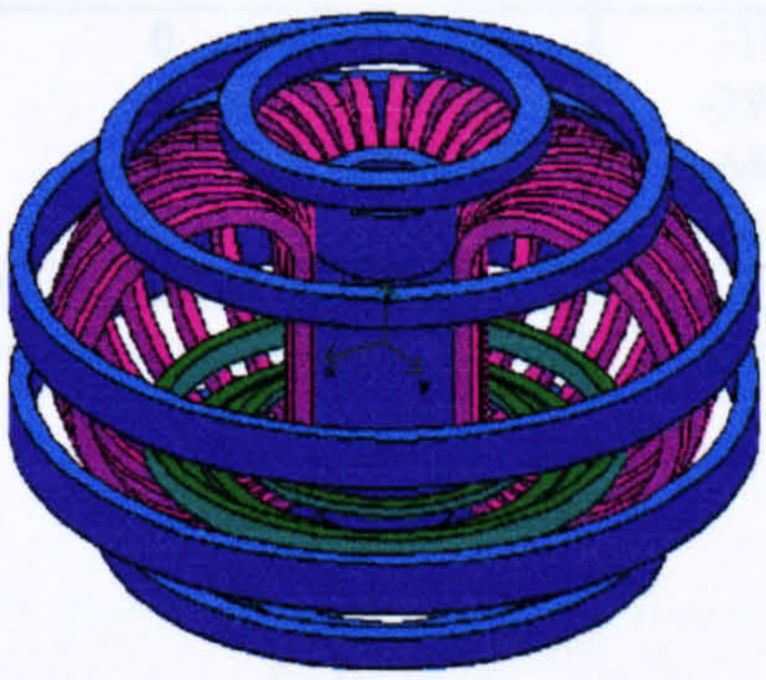


Fig. 2.15 - COMET model of the JET TF and PF coil system

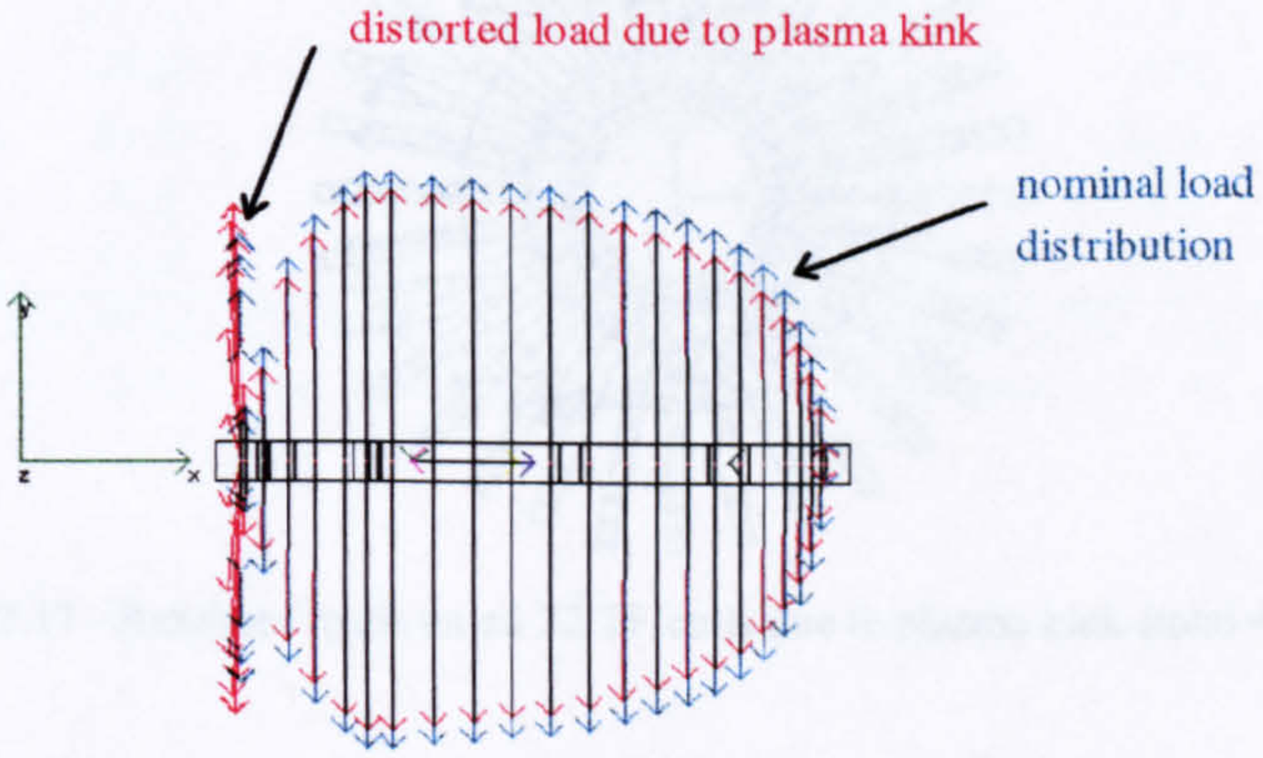


Fig. 2.16 - Distributed load on TF coil 1 due to plasma kink.

The results of the TF and PF runs are respectively in Tables 2.2 and 2.3 (for brevity, results have been reported only for the two TF coils aligned and the two perpendicular to the tilt axis).

$\Delta\alpha=0, \Delta x=0$	F_x (kN)	F_y (kN)	F_z (kN)	M_x(kNm)	M_y(kNm)	M_z(kNm)
Plasma	0	0	0	0	0	0
TF Coil 1	0	0	0	3068	0	0
TF Coil 17	0	0	0	-3068	0	0
TF Coil 9	0	0	0	0	3068	0
TF Coil 25	0	0	0	0	-3068	0
$\Delta\alpha=0.6° \Delta x=0$						
Plasma	1000	0	0	0	0	0
TF Coil 1	-41.1	0	0	3068	0	0
TF Coil 17	-41.1	0	0	-3068	0	0
TF Coil 9	-21.8	0	0	0	3068	0
TF Coil 25	-21.8	0	0	0	-3068	0
$\Delta\alpha=0, \Delta x=0.03$						
Plasma	0	0	0	-2974	0	0
TF Coil 1	0	0	0	3190	0	0
TF Coil 17	0	0	0	-2947	0	0
TF Coil 9	0	0	-17.1	64.6	3068	0
TF Coil 25	0	0	17.1	64.6	-3068	0
$\Delta\alpha=0.6°, \Delta x=0.03$						
Plasma	1000	0	0	-2974	0	0
TF Coil 1	-41.1	0	0	3190	0	0
TF Coil 17	-41.0	0	0	-2947	0	0
TF Coil 9	-21.8	0	-17.1	64.6	3067	32.1
TF Coil 25	-21.8	0	17.1	64.6	-3067	-32.1

Table 2.2 - Forces between TF coils and tilted/shifted plasma. The force indicated on plasma is the resultant due to all of the TF coils; the forces on individual coils 1, 9, 17 and 25 are those due to the plasma only.

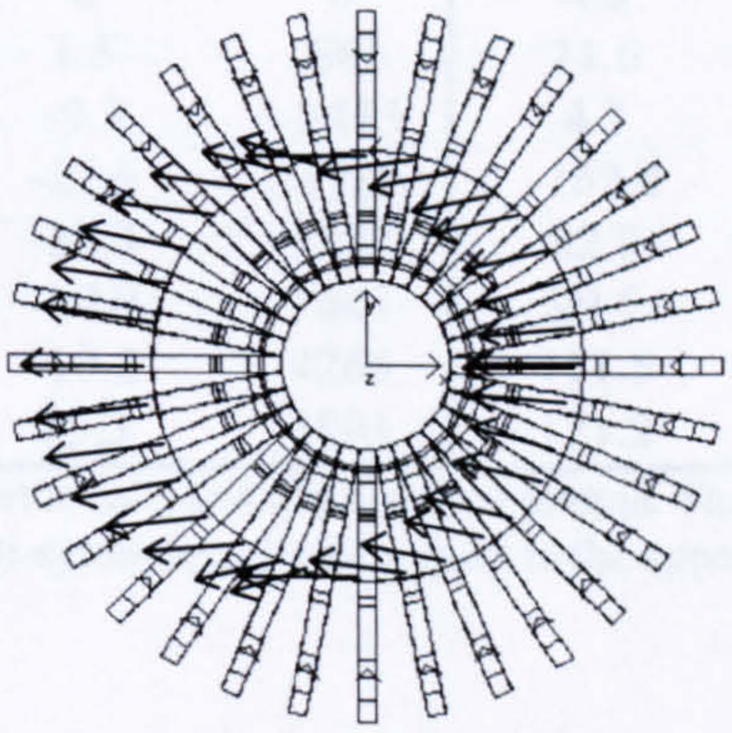


Fig. 2.17 - Resultant loads on all 32 TF coils due to plasma kink (total = 1 MN)

$\Delta\alpha=0, \Delta x=0$	F_x (kN)	F_y (kN)	F_z (kN)	M_x(kNm)	M_y(kNm)	M_z(kNm)
Plasma	0	0	0	0	0	0
TF Coil 1	0	0	0	3068	0	0
TF Coil 17	0	0	0	-3068	0	0
TF Coil 9	0	0	0	0	3068	0
TF Coil 25	0	0	0	0	-3068	0
$\Delta\alpha=0.6° \Delta x=0$						
Plasma	1000	0	0	0	0	0
TF Coil 1	-41.1	0	0	3068	0	0
TF Coil 17	-41.1	0	0	-3068	0	0
TF Coil 9	-21.8	0	0	0	3068	0
TF Coil 25	-21.8	0	0	0	-3068	0
$\Delta\alpha=0, \Delta x=0.03$						
Plasma	0	0	0	-2974	0	0
TF Coil 1	0	0	0	3190	0	0
TF Coil 17	0	0	0	-2947	0	0
TF Coil 9	0	0	-17.1	64.6	3068	0
TF Coil 25	0	0	17.1	64.6	-3068	0
$\Delta\alpha=0.6°, \Delta x=0.03$						
Plasma	1000	0	0	-2974	0	0
TF Coil 1	-41.1	0	0	3190	0	0
TF Coil 17	-41.0	0	0	-2947	0	0
TF Coil 9	-21.8	0	-17.1	64.6	3067	32.1
TF Coil 25	-21.8	0	17.1	64.6	-3067	-32.1

Table 2.2 - Forces between TF coils and tilted/shifted plasma. The force indicated on plasma is the resultant due to all of the TF coils; the forces on individual coils 1, 9, 17 and 25 are those due to the plasma only.

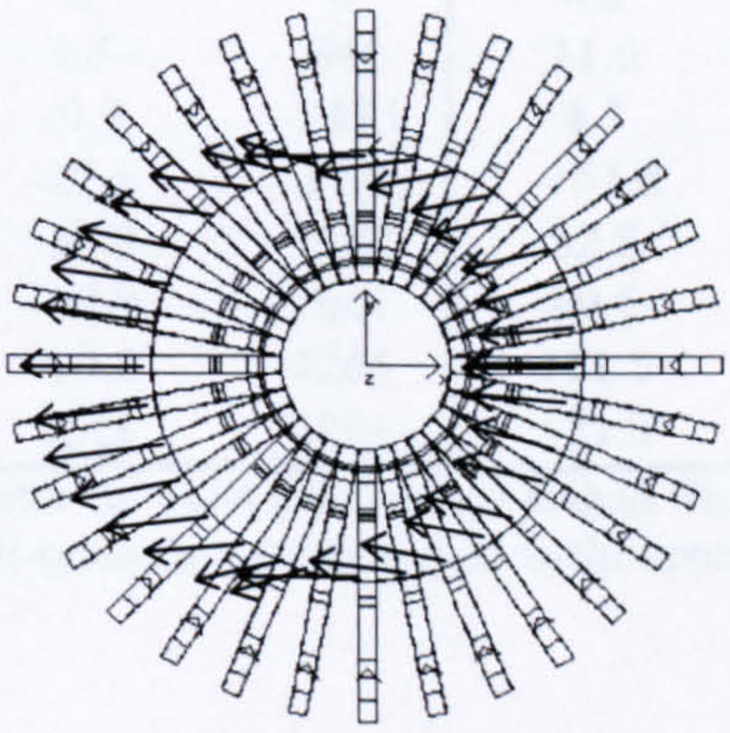


Fig. 2.17 - Resultant loads on all 32 TF coils due to plasma kink (total = 1 MN)

$\Delta\alpha=0, \Delta x=0$	F_x (kN)	F_y (kN)	F_z (kN)	M_x (kNm)	M_y (kNm)	M_z (kNm)
PF1	0	0	0	0	0	0
PF2U	0	0	-860	0	0	0
PF3U	0	0	-2455	0	0	0
PF4U	0	0	-1788	0	0	0
D1	0	0	3188	0	0	0
D2	0	0	3642	0	0	0
D3	0	0	4265	0	0	0
D4	0	0	5892	0	0	0
$\Delta\alpha=0.6°, \Delta x=0$						
PF1	0	0	0	4.8	0	0
PF2U	0	1.5	-860	11.6	0	0
PF3U	0	-9.3	-2456	4.3	0	0
PF4U	0	-21.5	-1788	-162.0	0	0
D1	0	-36.3	3188	82.8	0	0
D2	0	-20.9	3642	99.5	0	0
D3	0	-10.2	4265	111.5	0	0
D4	0	25.3	5892	121.2	0	0
$\Delta\alpha=0, \Delta x=0.031$						
PF1	0.2	0	0	0	0	0
PF2U	7.6	0	-860	0	-22.2	0
PF3U	18.4	0	-2455	0	-103.6	0
PF4U	-15.2	0	-1789	0	-119.1	0
D1	29.8	0	3188	0	-8.5	0
D2	41.2	0	3641	0	50.9	0
D3	50.3	0	4265	0	102.0	0
D4	67.6	0	5891	0	257.4	0
$\Delta\alpha=0.6°$, $\Delta x=0.031$						
PF1	0.2	0	0	4.8	0	0
PF2U	7.6	1.5	-860	11.6	-22.2	0
PF3U	18.4	-9.3	-2455	4.3	-103.6	0
PF4U	-15.2	-21.5	-1789	-162.0	-119.1	0
D1	29.8	-36.3	3188	82.8	-8.5	0
D2	41.2	-20.9	3641	99.5	50.9	0
D3	50.3	-10.2	4265	111.5	102.0	0
D4	67.6	25.3	5891	121.2	257.4	0

Table 2.3 - Forces between PF and divertor coils and tilted/shifted plasma. The forces and moments on the lower PF coils are anti-symmetrical with respect to the upper PF coils.

The results obtained confirm prior expectations:

— mechanical actions scale linearly with the currents, but depend non-linearly on their positions.
— the plasma tilt generates a sideways force on the TF coils and a moment on the PF coils. The sideways force is in good accord with the following theoretical value [27]:

$$F_{SW}=\pi I_{PLA}B_{T0}r_0\Delta\alpha\approx 1.01 \text{ MN} \tag{2.28}$$

The distributed load on the plasma can be seen in Fig. 2.18 to follow closely the cosine distribution expected in an ideal toroidal field.

— the plasma shift, conversely, generates a resultant moment on the TF coils but sideways forces on the PF coils. The moment is in accord with [27]:

$$M_{SW}=\pi I_{PLA}B_{T0}r_0\Delta x\approx 2.98 \text{ MNm} \tag{2.29}$$

The load distribution on a TF coil can be seen in Fig. 2.16, where the distribution due to the plasma in its initial undeformed state is also plotted for reference. The load contributing to the sideways force appears to be concentrated essentially on the straight vertical part, in a similar way for all the coils. The difference due to the kink represents a very small percentage of the initial loads, which does not raise any significant concern over the safety of the coils for all except the most severe cases (e.g. the I_{PLA}=5MA reference disruption at B_T=4T with F_{SW} extrapolated at 8MN [29]). The distribution of the resultant sideways force on each of the 32 coils is plotted in Fig. 2.17, which shows that the load is shared in a fairly uniform way .

Also the forces on the PF and divertor coils appear to be affected very little by the plasma kink (less than 3%). The net force on the plasma has not been reported in Table 2.3 because it depends on the amount of current in each of the coils, which in principle varies from pulse to pulse (a specific case, however, can be calculated simply by taking an opportune linear combination of the forces). At any rate, taking also into account the signs of the PF currents, it is safe to state that the PF coils contribute to the sideways force by less than 10%.

2.2.2.3 Plasma kink case II: JET pulse 34078

In this section, the case of JET pulse 34078 is examined. The mechanical actions between plasma and TF coils have been estimated following the same scheme of the previous section, using the following assumptions:

Plasma current	I_{PLA}	–2.7	MA
Toroidal field	B_{TOR}	–2.38	T
Plasma major radius	r_{PLA}	2.65	m
Plasma vertical position	z_{PLA}	1.19	m
Plasma shift	Δx	0.10	m
Plasma tilt	$\Delta\alpha$	2.16	°

Table 2.4 - Plasma parameters for JET pulse 34078 at the time of maximum difference in vertical current moments.

The distribution of the sideways force on the plasma is plotted in Fig. 2.18, while the components of the resultant force and moment are listed in Table 2.5.

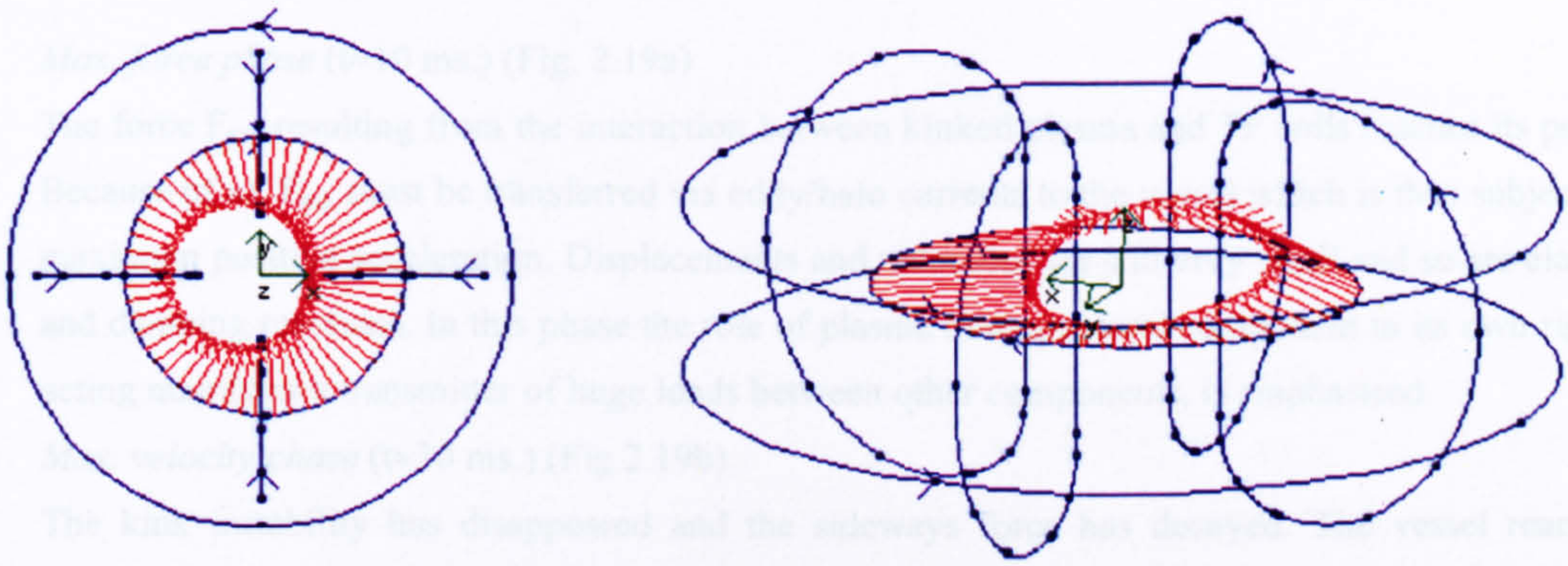


Fig. 2.18 - Sideways force on the plasma (top and isometric views)

	F_x (kN)	F_y (kN)	F_z (kN)	M_x (kNm)	M_y (kNm)	M_z (kNm)
I_{PLA} ↑↑ B_{TOR}	–2674	0	3250	6500	330	0
I_{PLA} ↑↓ B_{TOR}	*2773*	*0*	*3250*	*-7950*	*330*	*0*

Table 2.5 - Forces on kinked plasma in JET pulse 34078. The second row, as an example, represents the results that would have been obtained by reversing the plasma current sign.

The computed value $F_{SW}\approx 2.7$ MN is very close to the value estimated for the same pulse in section 6.1.1.

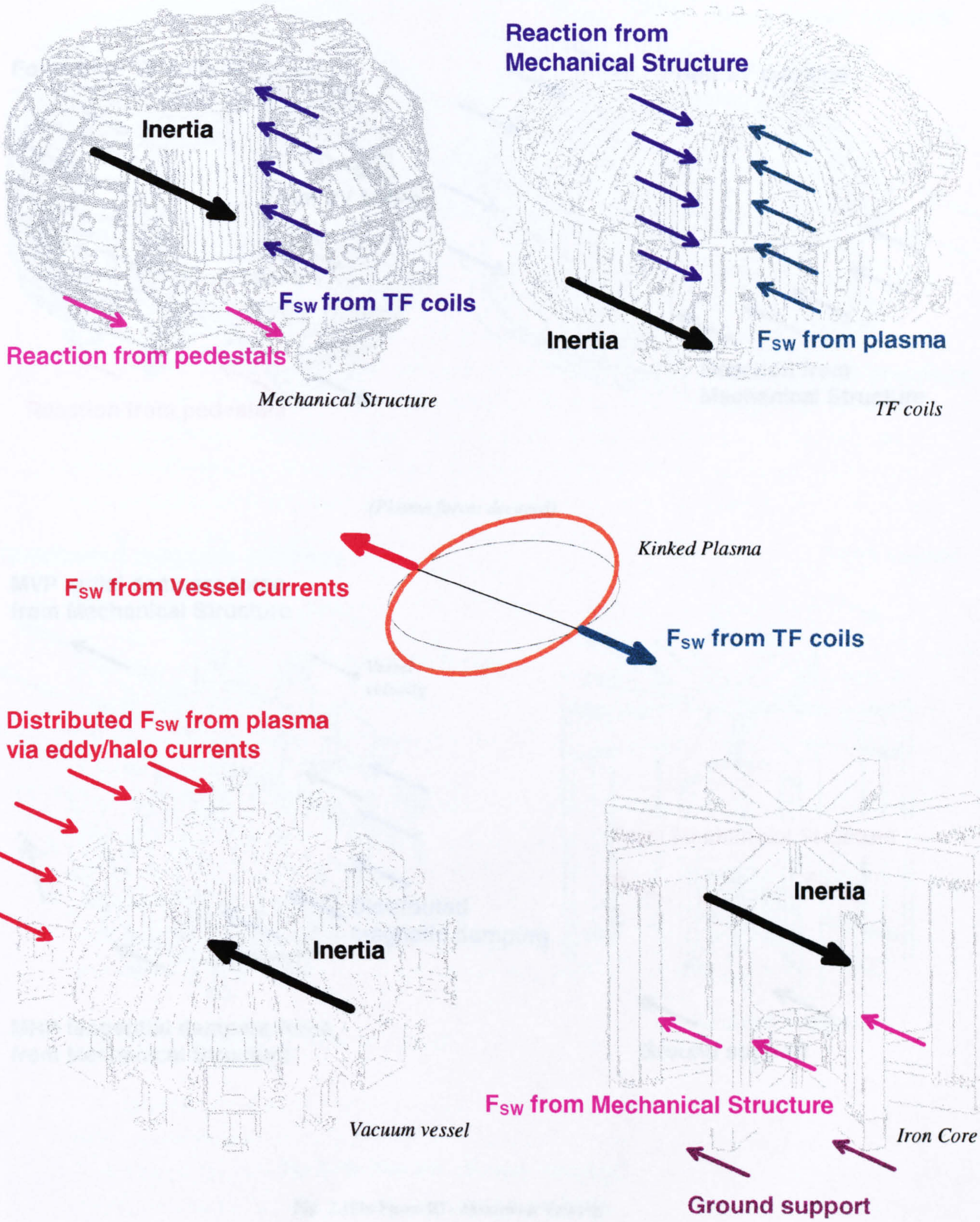
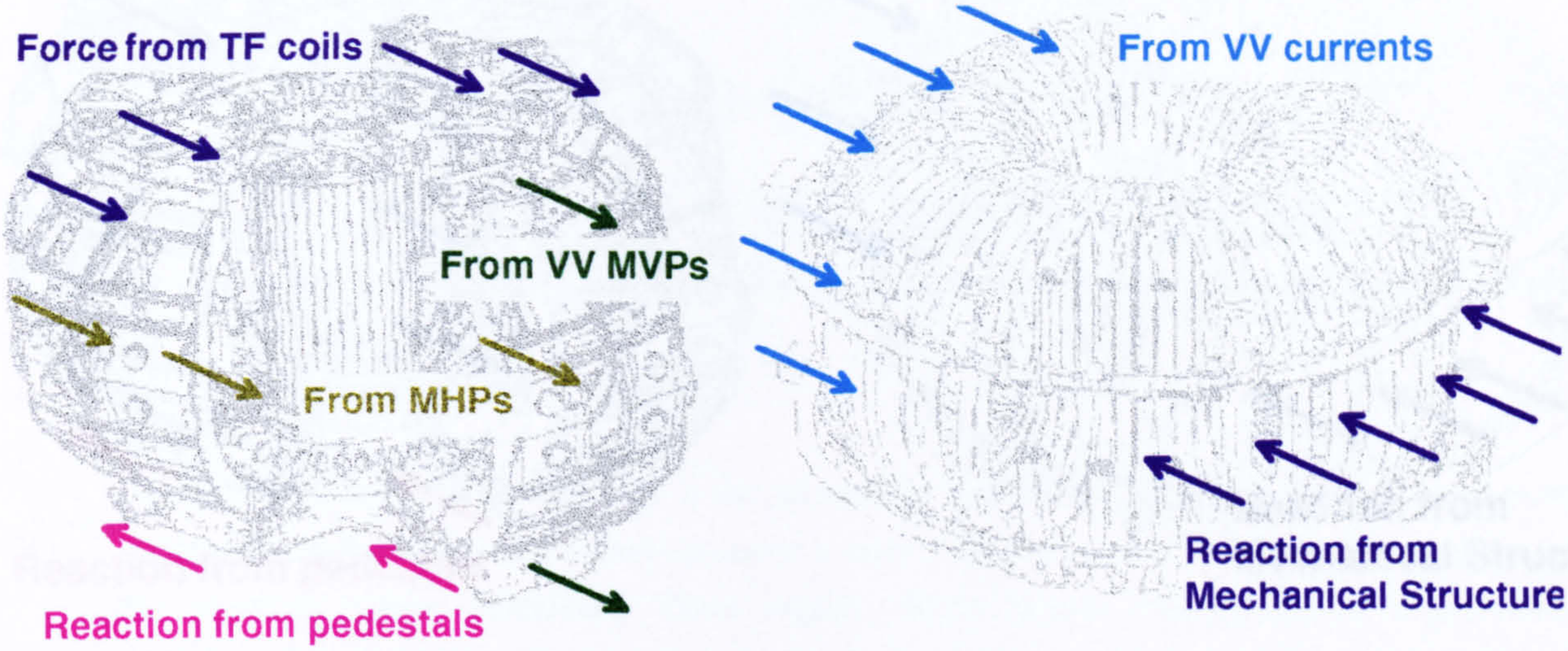


Fig. 2.19a - Force balance throughout Tokamak components during a sideways event
(Phase I - Maximum Acceleration).
The various force components can be identified by colour and appear in equal and opposite pairs.



(Plasma force: decayed)

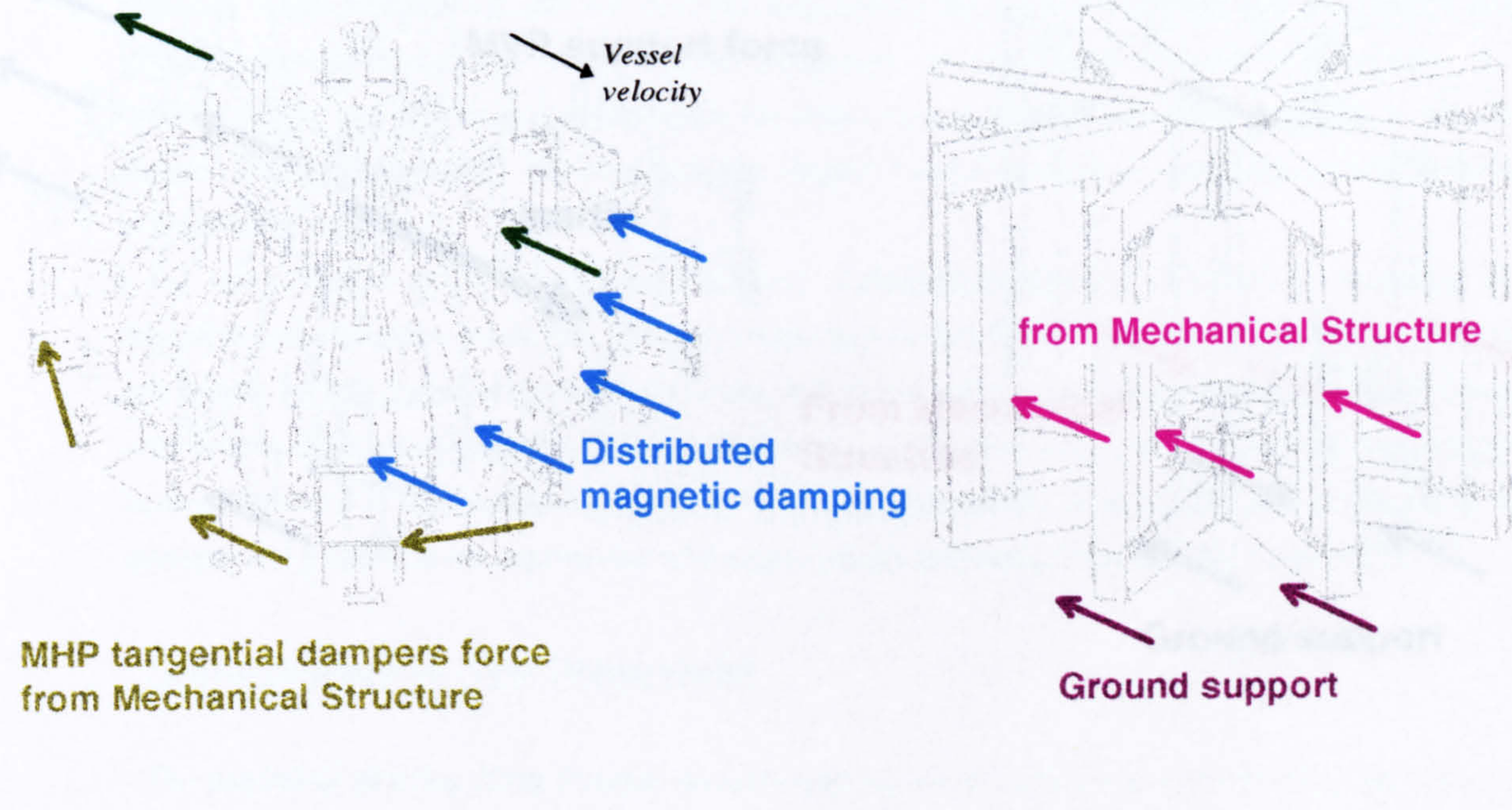


Fig. 2.19b: Phase II) - Maximum Velocity

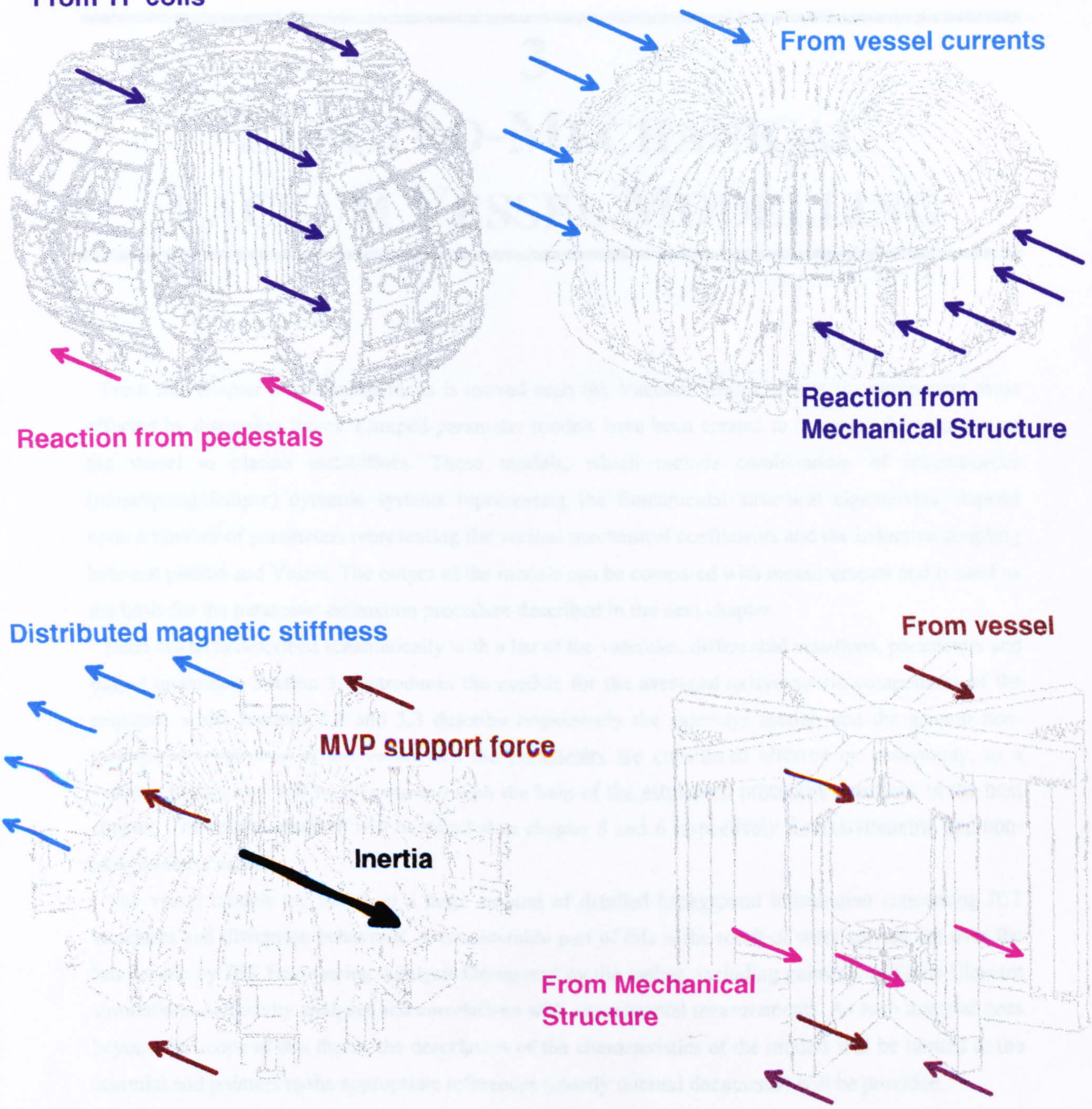


Fig. 2.19c: Phase III) - Maximum Elongation

3

ELECTRO-MECHANICAL VACUUM VESSEL MODELLING

From this chapter onwards the focus is moved onto the Vacuum Vessel, that is the component most affected by disruption forces. Lumped-parameter models have been created to represent the response of the vessel to plasma instabilities. These models, which include combinations of second-order (mass/spring/damper) dynamic systems representing the fundamental structural eigenmodes, depend upon a number of parameters representing the various mechanical coefficients and the inductive coupling between plasma and Vessel. The output of the models can be compared with measurements and is used as the basis for the parameter estimation procedure described in the next chapter.

Each model is described schematically with a list of the variables, differential equations, parameters and output quantities. Section 3.1 introduces the models for the averaged axisymmetric components of the response, while sections 3.2 and 3.3 describe respectively the sideways motion and the general non-axisymmetric motions of the vessel. All the parameters are considered affected by uncertainty, to a variable extent, and will be investigated with the help of the estimation procedure described in the next chapter. The results obtained will be detailed in chapter 5 and 6 respectively for axisymmetric and non-axisymmetric cases.

The vessel models are based on a large amount of detailed background information concerning JET structures and disruption behaviour. A considerable part of this is the result of work carried out over the last decade by JET Engineering Analysis Group and by the author, including painstaking Finite Element simulations, sensitivity analyses and correlations with experimental measurements. As such material goes beyond the scope of this thesis, the description of the characteristics of the models will be limited to the essential and pointers to the appropriate references (mostly internal documents) will be provided.

Lumped-Parameter vs. Finite Element models

The possibility of using Finite Element models (with distributed rather than concentrated parameters) to make systematic comparisons was considered at a preliminary stage and rejected. Actually, detailed Finite Element discretizations of the vacuum vessel are already available and represent indeed essential analysis tools, as will be shown in the next sections. However, the use of these models in the parameter estimation procedure would be extremely impractical, as can be seen from the following comparison table:

Finite Elements	Lumped Parameter
✓ Arbitrarily good spatial resolution	✗ Quantities averaged over the geometry
✗ Difficult to modify and update	✓ Flexible (few lines of code define a model)
✗ Slow: 1 transient run for the half-vessel model = 1~100 min. of networked computing server CPU (equivalent to 10~1000 min. in real time)[10]	✓ Fast: 1 transient run ≤1 sec. of PC CPU (no time sharing)
✗ Difficult integration: structural and magnetic codes currently available at JET require complicated interface routines to communicate between themselves and with other software modules	✓ Multiphysics models, data retrieval routines and parameter estimation algorithms are easily integrated in the same package
✗ Complex; results may be difficult to interpret	✓ Simple; give immediate physical insight into the problem

Therefore, within the constraints imposed by the currently available hardware and software, the flexibility offered by lumped-parameter models far outweighs the better precision that could be achieved with the Finite Element.

10 A typical run of the parameter estimation procedure may require dozen of steps and therefore, considering the numerical differentiation, hundreds of integrations of the model equations (see A2.4.1).

3. Models for axisymmetric motions

This section describes the models created to represent the combination of axisymmetric movements observed during disruptions. These components, which are usually dominant respect to the non-axisymmetric fluctuations, can be isolated by averaging the measurements taken around the torus as shown in section 1.3. The basic input parameters in these models describe the magnetic force in magnitude, position and timing.

3. 1 Rolling motion model

The rolling motion model (see Fig. 1.6) will be treated here in particular detail because is excited in practically all events and usually dominates the response, being the main source of vessel stresses. The rationale for the various simplifications will be explained first, and the mathematical formulation will then be written down.

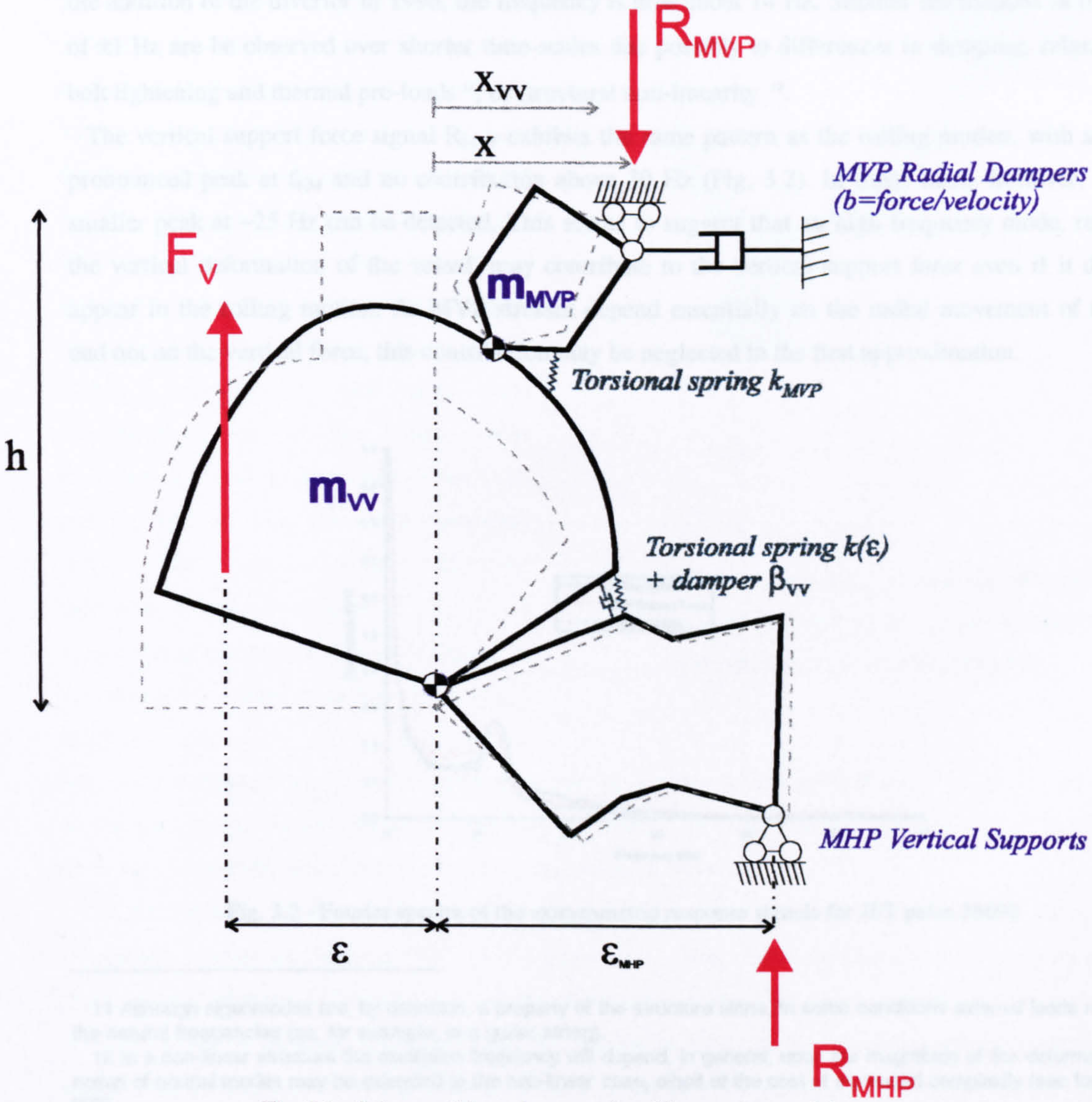


Fig. 3.1 - Scheme of the axisymmetric rolling motion model

3.1.1.1 Experimental evidence

The post-disruption rolling motion signal usually looks like a damped sine wave typical of a single d.o.f. oscillator (see for example the time traces plotted in chapter 5). This is confirmed by the Fourier spectrum, plotted in Fig. 3.2, which shows a marked peak at the frequency $f_{RM} \approx 14$ Hz of the sine wave. The smearing of the peak is due to the variation of amplitude with time and is consistent with theoretical results for the case of exponential decay. The additional initial peak at frequency $f_0=1/T$, where T is the duration of the signal, is inherent in the discrete formulation of the transform and has no physical meaning [90]. In all cases, the spectral energy content (which is proportional to the square of the Fourier component amplitudes) can be seen to vanish rapidly for f>30 Hz.

The frequency f_{RM} has changed over the years in the range 9-18 Hz, following the changes of support stiffness and mass distribution inside and outside the vessel. The maximum values were reached around JPN 21600, after the replacement of one TF Coil and the cutting and re-welding of a whole octant; the lowest are related to the very early operating phase when no port restraints were yet installed [17]. After the addition of the divertor in 1996, the frequency is now about 14 Hz. Smaller fluctuations of the order of ±1 Hz are be observed over shorter time-scales due possibly to differences in damping, relaxation of bolt tightening and thermal pre-loads [11], or structural non-linearity [12].

The vertical support force signal R_{MVP} exhibits the same pattern as the rolling motion, with a clearly pronounced peak at f_{RM} and no contribution above 30 Hz (Fig. 3.2). In some cases, however, a much smaller peak at ~25 Hz can be detected. This seems to suggest that an high frequency mode, related to the vertical deformation of the vessel, may contribute to the vertical support force even if it does not appear in the rolling motion. As MVP stresses depend essentially on the radial movement of the port and not on the vertical force, this contribution may be neglected in the first approximation.

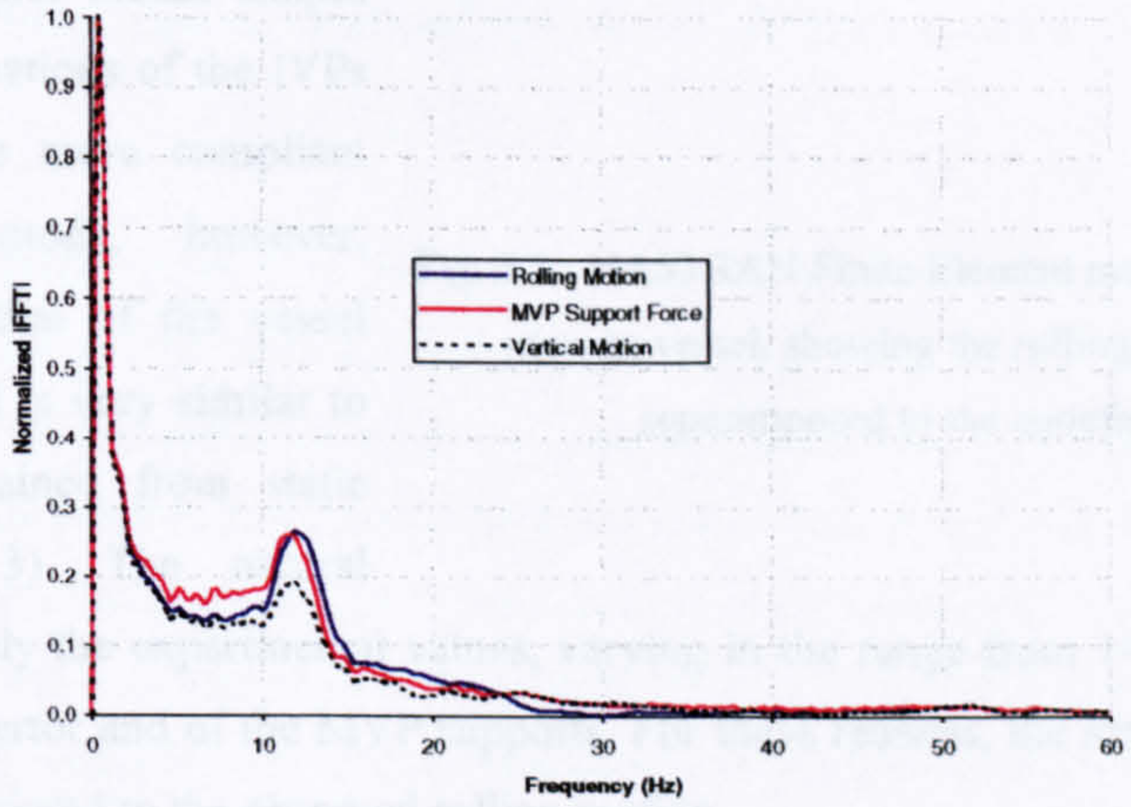


Fig. 3.2 - Fourier spectra of the axisymmetric response signals for JET pulse 38690

---

11 Although eigenmodes are, by definition, a property of the structure alone, in some conditions external loads may affect the natural frequencies (as, for example, in a guitar string).

12 In a non-linear structure the oscillation frequency will depend, in general, upon the magnitude of the deformation. The notion of normal modes may be extended to the non-linear case, albeit at the cost of increased complexity (see for example [55]).

3.1.1.2 Finite Element analysis

A detailed linear NASTRAN Finite Element model of half of a vessel octant is available (see Fig. 3.3). This model, which includes approx. 3500 shell and beam elements, is able (with the appropriate symmetry boundary conditions) to represent axisymmetric deformations of the vessel and has been extensively used in the last decade to investigate the effects of static and dynamic loading conditions.

Results indicate that vertical forces are the main cause for the rolling motion and that the actual position of the force matters little on the global deformation pattern. In particular, local stresses where loads are applied tend to be small compared with the concentration peak at the base of the MVP. The NASTRAN eigendecomposition capability has been used to calculate the vessel's natural frequencies, which may be worked out in ascending order starting from the fundamental. As is customarily admitted in the study of free, lightly damped vibrations, linearity of the structure is assumed and dissipative effects are neglected (in particular, the non-linear nature of the hydraulic dampers is not taken into consideration). Most of first modal shapes are related to local deformations of the IVPs and the bellows (i.e. the more compliant parts). The second mode, however, represents exactly a rotation of the vessel around the major axis and is very similar to the deformed shape obtained from static loading cases (Fig. 3.3). The natural frequency matches precisely the experimental values, varying in the range from 14 to 17 Hz depending on the presence of the divertor and of the MVP supports. For these reasons, the single d.o.f. represented by Mode II is usually associated to the observed rolling motion.

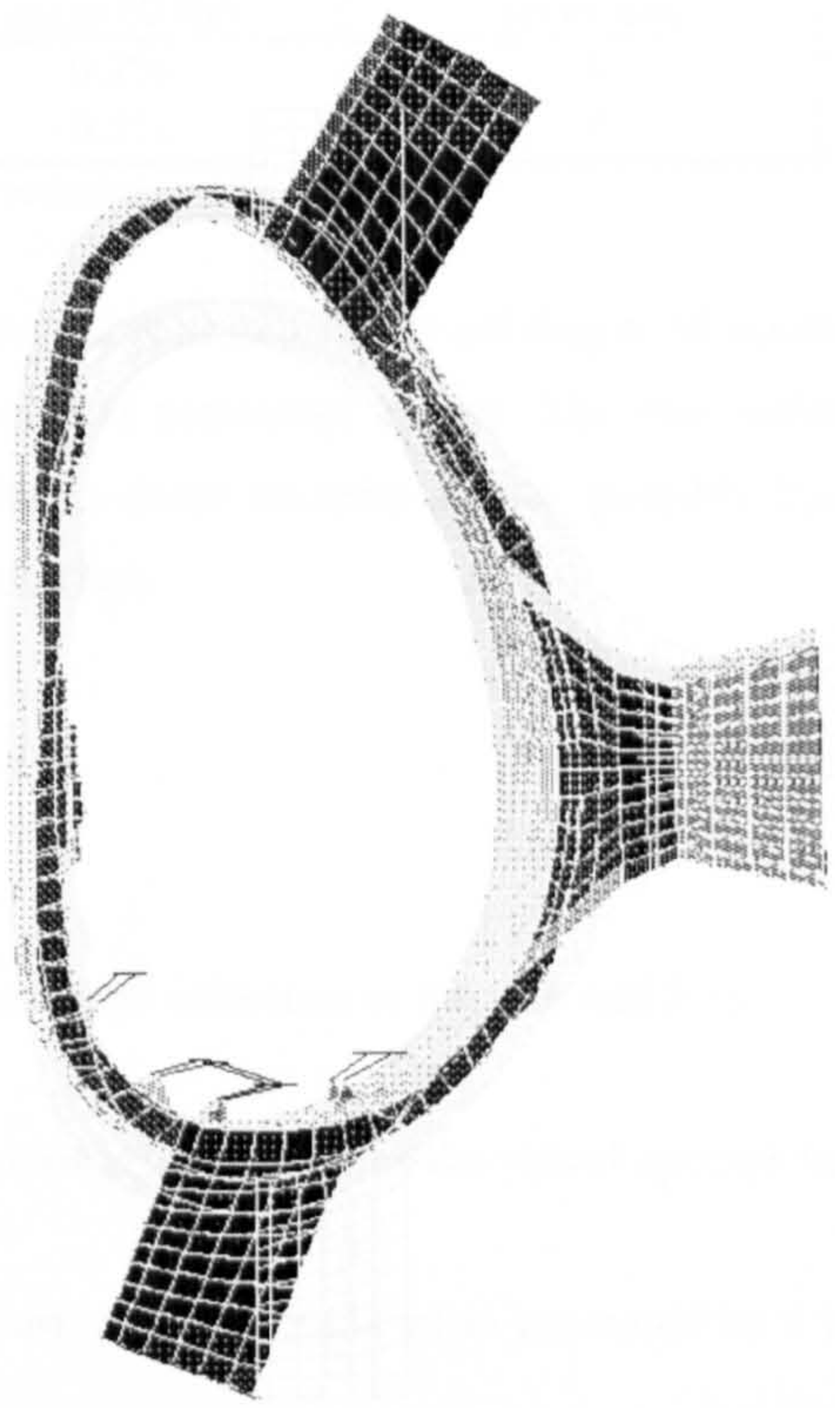


Fig. 3.3 - NASTRAN Finite Element model of half-octant of the vacuum vessel, showing the rolling motion eigenmode superimposed to the undeformed shape

The participation of this mode in the response of the vessel has been quantified by means of a comparative series of dynamic NASTRAN runs. These have been carried out with reference loads representative of typical disruption conditions, characterised by a frequency content not exceeding 100 Hz. Both available methods of dynamic analysis have been used, i.e. the modal superposition method (in which a specified number of eigenmodes is used to set up a reduced-order set of uncoupled dynamic

equations) and the more expensive direct transient method (which integrates the full matrix system and is therefore equivalent to use all existing modes at once). Assuming that the direct integration gives the "true" response, i.e. the one that uses all the available information in the model, the superposition of a small number of modes will result in a relative error on both peak-to-peak displacement and support forces, as reported in the Table below:

Relative error in:	**1 mode** (rolling motion mode)	**20 modes** (up to 80 Hz)	**Direct integration** (all modes)
Peak-to-peak x_{RM}	0.5%	0.1%	0
Peak-to-peak R_{MVP}	30.0%	0.5%	0

Table 3.1 - Peak-to-peak error with reduced number of modes

These results confirm that the rolling motion can be approximated to a very good degree of accuracy by a single d.o.f. system like the one proposed in the lumped parameter model. The less satisfactory approximation of the vertical support force indicates that a more accurate model, possibly including additional d.o.f.s, would be necessary to get the complete picture.

3.1.1.3 Model formulation

Static and dynamic Finite Element calculations show that (with reference to Fig. 1.6 and 3.3):

- since all the main ports are prevented from moving vertically, the bulk of the vessel appears to rotate around the pivot point O.
- the rotation is due to a moment around O which, in turn, can be thought of as generated by a vertical force F_V at a distance ε from the pivot.
- the vertical load is reacted mainly by the MVP and MHP supports. The spring supports at the Octant Joint and at the MHP, being relatively soft and close to the pivot, take only a small part (<3%) of this force.

On the basis of these considerations, it is possible to lump the structural mass into three rigid bodies able to translate and rotate in the poloidal plane. The arrangement shown is the simplest to be kinematically consistent with the deformed shape, as obtained from the Finite Element model, and the external restraints. Note that relative movements between vessel bulk and MHPs are constrained by the rotational spring k_{VV}, which effectively makes the pair behave as a single d.o.f.. As the movement of the MHP section is much smaller, the dynamics of the system can be conveniently approximated by just two masses. The rolling motion model is therefore defined by the following equations (referred to the whole of the vessel):

$$\begin{cases} F_V\left(\varepsilon+\varepsilon_{MHP}\right) = R_{MVP}\varepsilon_{MHP} + m_{VV}\dfrac{\rho(\rho+\varepsilon_{MHP})}{h}\ddot{x}_{VV} + 16F_{MVP}h & \text{(global equilibrium around P)} \\ F_V\varepsilon = m_{VV}\dfrac{\rho^2}{h}\ddot{x}_{VV} + 16F_{MVP}h + \beta\dot{x}_{VV} + k(\varepsilon)x_{VV} & \text{(VV bulk equilibrium around O)} \end{cases} \tag{3.1}$$

where the meaning of the variables is explained in Table 3.2. The fact that x, $x_{VV} << \varepsilon$ has been used to approximate the equations. F_{MVP} represents the dynamic radial force on an individual Main Vertical Port (i.e. the most important quantity for stress calculation) and is related to the other variables by the equations:

$$m_{MVP}\ddot{x} + b(\dot{x})\dot{x} = -k_{MVP}(x - x_{VV}) = F_{MVP} \tag{3.2}$$

expressing the rotational equilibrium of the MVP around the pivot Q.

In theory, the addition of the second d.o.f. m_{MVP} may seem to contradict the statement that the rolling motion is dynamically equivalent to a single d.o.f.. In practice, however, as the radial port stiffness is very high the deflection $x\text{-}x_{VV}$ will be less than 5% of the total port displacement and the corresponding eigenfrequency ($f_{MVP}\approx 90$ Hz) is practically undetectable in the experimental data.

The equations (3.1) can be recast in normal form for the purposes of the computer integration routine:

$$\left\{\begin{aligned} x_0 &= x \\ x_1 &= \dot{x} \\ x_2 &= x_{VV} \\ x_3 &= \dot{x}_{VV} \end{aligned}\right\} \qquad \left\{\begin{aligned} \dot{x}_0 &= x_1 \\ \dot{x}_1 &= \frac{F_{MVP} - b(x_1)x_1}{m_{MVP}} \\ \dot{x}_2 &= x_3 \\ \dot{x}_3 &= \frac{-16F_{MVP}h + F_V\varepsilon - \beta x_3 - k(\varepsilon)x_2}{\mu} \end{aligned}\right. \tag{3.3}$$

where $F_{MVP}=k_{MVP}(x_2-x_0)$ and $\mu=m_{VV}\rho^2/h$.

All spring rates have been computed using the Finite Element model. According to the results of sensitivity analyses, these calculations have been found to be rather accurate and a nominal uncertainty of ±5% has been assigned to the values obtained. In the following subsections, some of the terms in these equations will be discussed in more detail.

	Variables	Value	Unit
x, x_{RM}	radial displacement of the mass at the top of the MVP, corresponding to the measured rolling motion defined in 1.3.1 (the suffix RM is dropped for brevity).		m
x_{VV}	static radial displacement of the MVP, corresponding to the rotation of the bulk VV mass ($x_{VV} \equiv x_{RM}$ when velocity and acceleration are negligible).		m
	Forces		
F_V	Vertical vessel force	/	MN
R_{MVP}	Vertical component of the MVP support reaction force, obtained projecting the individual measured axial forces on the z axis	/	MN
R_{MVP}	Vertical component of the MVP support reaction force, obtained projecting the individual measured axial forces on the z axis	/	MN
F_{MVP}	Radial dynamic force at the MVP top (inertia + damping force)	/	MN
	Geometry parameters		
ε_{MHP}	Horizontal distance between MVP and MHP supports	2.0	m
h	Vertical distance between MVP top and pivot point O. The error bar is due to different positions of the attached masses.	3.2÷4.2	m
ρ	Inertia radius of vessel mass about pivot point O	2.5	m
	Mechanical parameters		
m_{VV}	Bulk of the vessel mass considered as lumped at a distance ρ from the pivot O. This is not the actual vessel mass, since it is equivalent in terms of inertia moment $m_{VV}\rho^2$. This value is consistent with the observed frequency of oscillation of ~15 Hz.	11000	kg
m_{MVP}	Lumped mass $m_{MVP} = 1/3 m_{PORT} + m_{FLANGE} + m_{DIAGNOSTIC}$ at the end of the MVP, also equivalent in terms of inertia moment	250÷500	kg
$k(\varepsilon)$	Spring ratio relating the torque on the vessel bulk to the displacement x (from FE model). The stiffness increases when the application point of the force gets further away from the pivot because of the greater hoop stresses resisting the local vessel deformation under F_V.	118+436·ε	MNm/m
k_{MVP}	is the spring ratio between the F_{MVP} and the dynamic component of the displacement, x-x_0 (from FE model).	50	MNm
β	damping coefficient representing all sources of dissipation such as internal material friction, joint friction etc.., excluding the hydraulic dampers. This value is in accord with the non-dimensional damping ratio $\xi \approx 7\%$ observed in pulses prior to the introduction of the hydraulic dampers.	400÷500	kNs
	Hydraulic dampers (nominal)		
b_0	Low-speed MVP damping coefficient	300	kNs/m
b`	High-speed MVP damping coefficient	0	kNs^2/m^2
$F_{D,MAX}$	Saturation damping force	120	kN

Table 3.2 - Parameters for the rolling motion model. The figures represent nominal values only

3.1.1.4 Non-linear hydraulic damping

The modelling of the non-linear characteristic of the MVP hydraulic dampers (Fig. 3.4), which is essential for the correct assessment of stresses at the base of the MVP, is described here in more detail. On the basis of elementary fluid dynamics and of experimental data [54] the damping force can be expressed by the following function of the velocity $\dot{x}$:

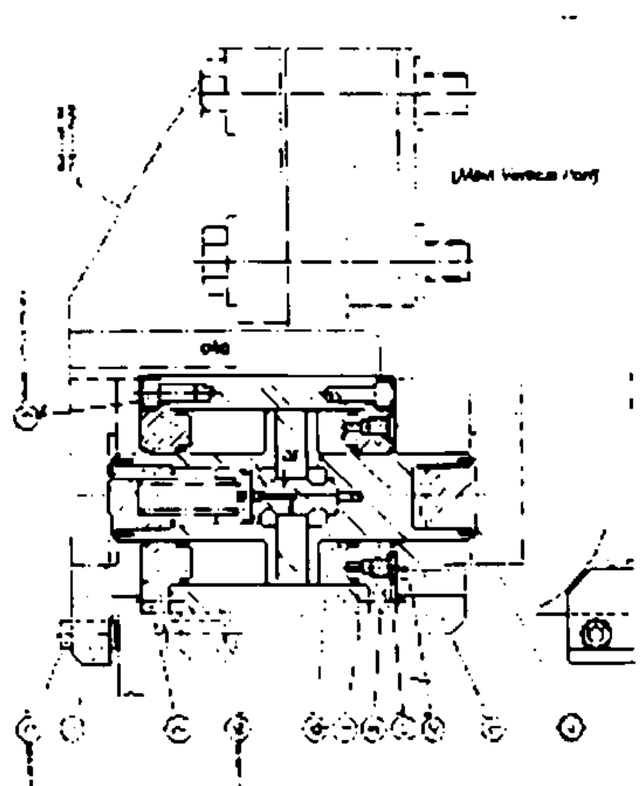


Fig. 3.4 - Hydraulic Damper at the Main Vertical Ports

$$F_{damping} = F_{damping,MAX} \tanh \frac{\left(b_0 + b'|\dot{x}|\right)\dot{x}}{F_{damping,MAX}} \qquad \Rightarrow \qquad b(\dot{x}) = \frac{F_{damping}}{\dot{x}} \tag{3.4}$$

where:

— b_0 is the low-velocity damping coefficient, valid when the flow of the oil inside the gap is laminar and the force is proportional to $\dot{x}$.

— b` is a correction term valid at intermediate velocities, when the flow becomes turbulent and the force is proportional to $\dot{x}^2$.

— $F_{damping,MAX}$ is the saturation force, approximately constant with the velocity[13], corresponding to the opening of the pressure relief valves.

The hyperbolic tangent function is the simplest way to represent a smooth transition between the low- and medium-velocity (valves closed, $F_{damping}$ parabolic) and the high-velocity (valves open, $F_{damping}$ constant) regimes. By setting an high value for $F_{damping,MAX}$ it is possible to remove the saturation effect from the curve and therefore represent the status of the dampers before the refurbishment done in the 1996 shutdown.

The test measurements indicate a damping force which is much higher than that derived from the comparison with the rolling motion data. A discussion of the possible reasons for this discrepancy is given in section 7.2.2.2. It should be emphasised that getting the correct damping force in the model is absolutely essential, since this is the single most important factor in the calculation of F_{MVP} and of stresses MVP base stresses.

13 At very high velocities, of no concern for the present analysis, the damping force will increase anyway with the velocity even if the pressure relief valves are open.

3.1.1.5 Transient plasma force model

The rolling motion model is concerned essentially with the vertical component of the magnetic force F_V. The dynamic radial component F_R can be neglected, in the first approximation, because detailed MHD and mechanical simulations of typical cases have shown it to have a much smaller magnitude and much less effect on the rolling motion. The history $F_V(t)$ assumed in the model, qualitatively in agreement with MAXFEA VDE simulations, is characterised by the following schematic pattern depending on the scalar parameters $\{F_0, F_{max}, F_{min}, t_0, \tau_1, \tau_2, \tau_3, \tau_4, \varepsilon_0, \varepsilon_1\}$ values (see Fig. 3.5):

— a slow rise to a constant positive plateau (F_0) corresponding to the flat-top phase of the pulse, during which the force is transmitted to the Vessel by the divertor coils, which are strongly attracted upward to the plasma. The force, in this phase, is assumed to be applied at the distance ε_0 from the pivot.

— an increase to F_{max} (from t_0 to $t_0+\tau_1$) due mainly to the toroidal eddy currents induced in the vessel by the plasma movement

— a sustained phase of duration τ_2 corresponding to the force from the Halo Currents developed by the plasma/wall interaction

— a drop to $F_{min} < 0$ in τ_3, due the current quench leading to eddy currents in the top part of the vessel with the same sign as the plasma current. The position of the force is assumed to change linearly from the initial value to ε_0 at the end of this phase.

— a slow exponential decay, dominated by the residual attraction between divertor currents and image currents in the iron limbs. The characteristic time τ_4, which can be estimated from divertor current measurements and is of the order of 1 s, depends upon the R/L constant of the individual coils and on the particular combination of currents.

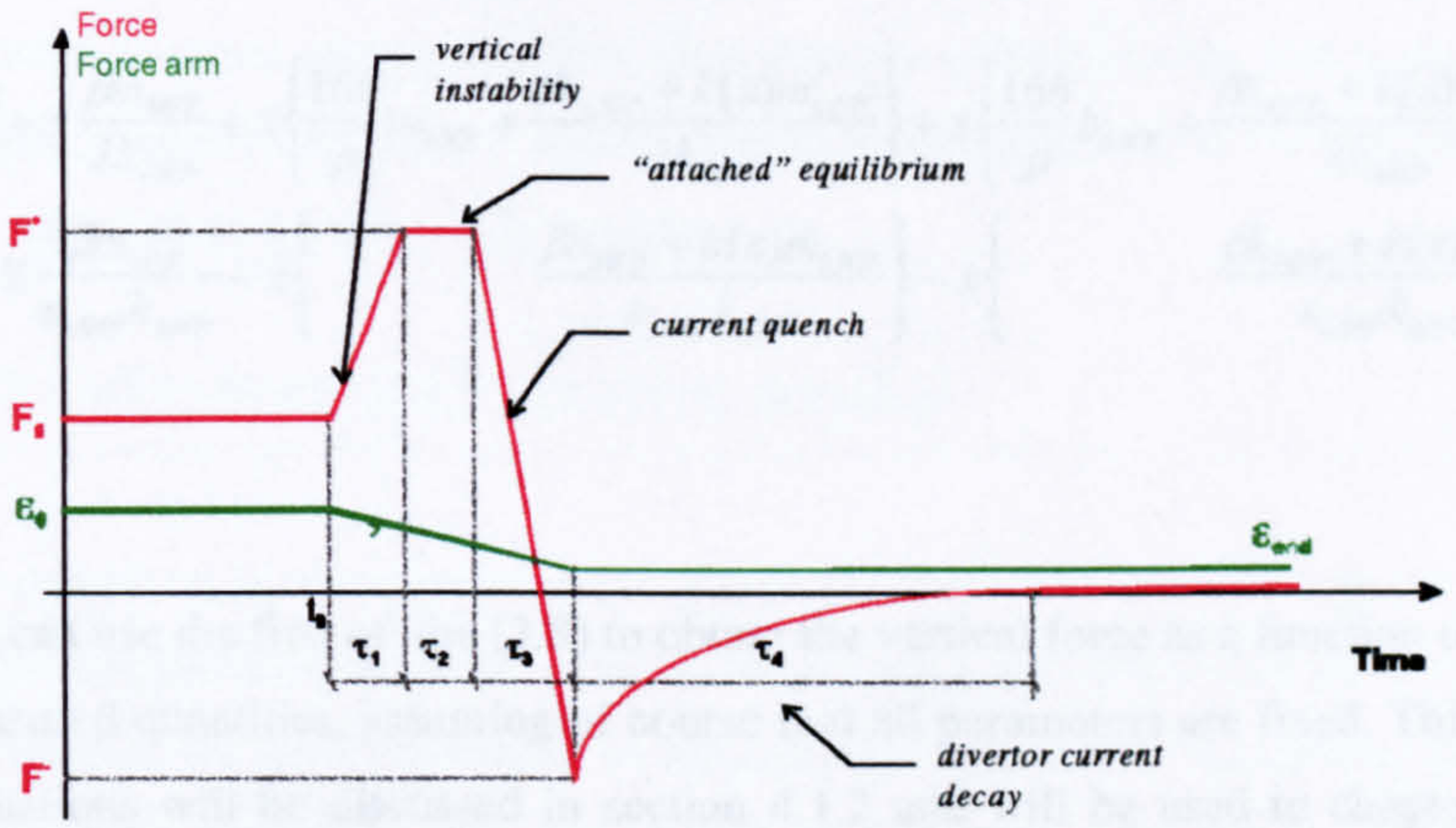


Fig. 3.5 - Qualitative history of the vessel vertical force during a VDE

The principal feature of this load history is the downward swing $\Delta F=F_{max}-F_{min}$. Force and displacement swings (defined, in general, as the maximum difference between two successive peaks) are important because they enter directly into fatigue life calculations.

Note that it is also possible to use this schematic representation to describe the qualitative time history of the vertical loads in pre-divertor pulses; the force, in those cases, will be given simply by a load pulse with $F_0=F_{MIN}=0$.

3.1.1.6 Support forces

The balance of vertical forces on the model can be expressed as:

$$R_{MVP} + R_{MHP} + \ddot{x}_0 m_{VV} \frac{\rho}{h} = F_V \tag{3.5}$$

from here, it is possible to solve for the support forces:

$$\begin{cases} R_{MVP} = F_V\left(1+\dfrac{\varepsilon}{\varepsilon_{MHP}}\right) - \left[\dfrac{16h}{\varepsilon_{MHP}}F_{MVP} + \ddot{x}_0 m_{VV}\dfrac{\rho}{h}\left(1+\dfrac{\rho}{\varepsilon_{MHP}}\right)\right] = F_V\left(1-\dfrac{\varepsilon}{\rho}\right) + \dfrac{16h}{\rho}F_{MVP} + \dfrac{\beta\dot{x}_0 + k(\varepsilon)x_0}{\lambda} \\ R_{MHP} = \underbrace{-F_V\dfrac{\varepsilon}{\varepsilon_{MHP}}}_{\text{static part}} + \underbrace{\left[\dfrac{16h}{\varepsilon_{MHP}}F_{MVP} + \ddot{x}_0 m_{VV}\dfrac{\rho^2}{h\varepsilon_{MHP}}\right]}_{\text{dynamic part}} = -\dfrac{\beta\dot{x}_0 + k(\varepsilon)x_0}{\varepsilon_{MHP}} \end{cases} \tag{3.6}$$

with: $\dfrac{1}{\lambda} = \dfrac{1}{\varepsilon_{MHP}} + \dfrac{1}{\rho}$ (3.7)

where the static terms represent the elementary balance when inertia and velocity forces are negligible. It is possible, eliminating x_0 via the (3.2), to express both support forces as a function of F_V and x(t):

$$\begin{cases} R_{MVP} = F_V\left(1-\dfrac{\varepsilon}{\rho}\right) + \ddot{x}\dfrac{\beta m_{MVP}}{\lambda k_{MVP}} + \ddot{x}\left\{\dfrac{16h}{\rho}m_{MVP} + \dfrac{\beta b_{MVP} + k(\varepsilon)m_{MVP}}{\lambda k_{MVP}}\right\} + \dot{x}\left\{\dfrac{16h}{\rho}b_{MVP} + \dfrac{\beta k_{MVP} + k(\varepsilon)b_{MVP}}{\lambda k_{MVP}}\right\} + x\dfrac{k(\varepsilon)}{\lambda} \\ R_{MHP} = -\ddot{x}\dfrac{\beta m_{MVP}}{\varepsilon_{MHP}k_{MVP}} - \ddot{x}\left\{\dfrac{\beta b_{MVP} + k(\varepsilon)m_{MVP}}{\varepsilon_{MHP}k_{MVP}}\right\} - \dot{x}\left\{\dfrac{\beta k_{MVP} + k(\varepsilon)b_{MVP}}{\varepsilon_{MHP}k_{MVP}}\right\} - x\dfrac{k(\varepsilon)}{\varepsilon_{MHP}} \end{cases} \tag{3.8}$$

Interestingly, one can use the first of the (3.8) to obtain the vertical force as a function of R_{MHP} and x(t), which are both measured quantities, assuming of course that all parameters are fixed. This alternate view of the dynamic equations will be discussed in section 4.1.2 and will be used in chapter 5 to get an *a posteriori* confirmation of the quality of the assumption on the shape of the waveform of F_V.

3.1.2 Vertical motion model

In this section the model relating the vertical vessel movement in response to the vertical force F_V is discussed. Because of the arrangement of vessel supports, which block the central rigid sector of each octant (see 1.1.1.4), only the Octant Joint and Limiter sectors are free to move vertically. The response to a vertical force, as shown in Fig. 1.19, includes thus a toroidally cyclic (n=8) bending deformation which is measured by the vertical displacement transducers at the IVPs (z_{IVP}). This deformation is included in the rolling motion eigenmode described in the previous section and, indeed, the Fourier spectrum of z_{IVP} invariably shows a single dominant peak at the corresponding frequency (see Fig. 3.2).

Thus, z_{IVP} can be taken to be proportional to x_{RM} via a scaling factor (ρ^*z) which is always the same during the free phase of the response but which will depend, in general, upon the position of the force in the steady-state phase:

$$z_{IVP} = \rho_z x_{RM}, \quad \rho_z = \begin{cases} \rho_z(\varepsilon) = \dfrac{k_{IVz}(\varepsilon)}{k_{z0} + k'_z\varepsilon} & t \le t_0 \\ \text{linearly interpolated} & t_0 \le t \le t_0 + \tau_3 \\ \rho^*_z = 0.28 & t \ge t_0 + \tau_3 \end{cases} \tag{3.9}$$

Preliminary results from the half-octant Finite Element model indicate that $k_{z0} \approx 3.2$ GN/m and $k'_z \approx -1.3$ GN/m^2.

3.1.3 Radial motion model

An additional model relating the axisymmetric expansion/contraction of the vessel x_{RAD} (defined in section 1.3.1) in response to the radial component of the force F_R has also been considered. Such model is given simply by the following second-order system:

$$\{m''_{VV}\ddot{x}_{RAD} + b''_{VV}\dot{x}_{RAD} + k''_{VV}x_{RAD} = F_R(t) \tag{3.10}$$

Because of the high stiffness of the toroidal shell (k''_{VV}=2.0 GN/m from the Finite Element model), this movement is in practice an order of magnitude smaller than the rolling motion and is usually masked by noise. For this reason, interpretation of the measurements has been found to be very difficult and this model has not been included in the rest of the analysis.

3.1.4 Global axisymmetric motion model

The three models described in the previous sections can be combined in a single global "super-model" which includes all the axisymmetric motions of the vacuum vessel and couples all the relevant parameters at the same time. Although the code developed to implement the parameter estimation procedure is able to merge multiple models automatically, the procedure becomes increasingly complex and time-consuming. For this reason, just an example of the combination of the rolling motion and vertical motion models will be given in section 5.2.

3.1.5 Inductive coupling model

In this section a simple model of the inductive coupling between plasma and vacuum vessel is presented. This model, which links the vessel force with plasma current and position via induced (eddy and halo) currents, is very time-consuming to set up and run because of the high number of measurements involved and has not been used in the present work.

The model is based on a filament representation of the toroidal currents in the system including (see Fig. 3.6):

- n_E=18 unknown toroidal vessel eddy currents[14] $\{I_{eddy,i}\}$
- n_{PF}=8 measured PF coil currents $\{I_{PF,j}\}$
- n_{DIV}=4 measured divertor coil currents $\{I_{DIV,k}\}$
- the measured plasma current I_{PLA}.

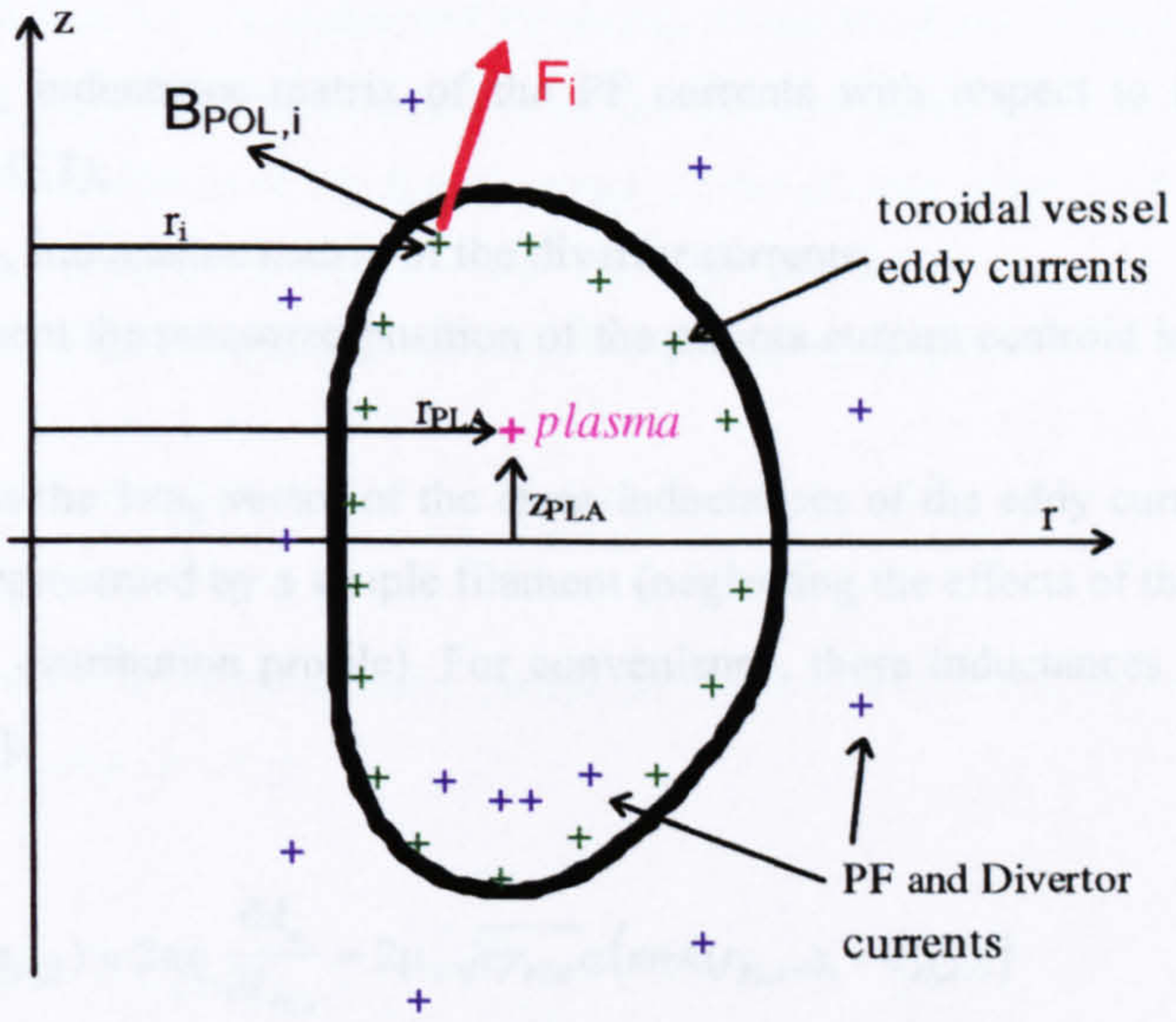


Fig. 3.6 - Simplified model of the electrodynamic interaction between plasma, PF/divertor currents and eth toroidal eddy currents in the vessel

14 The position of these lumped currents corresponds to the 18 internal tangential field pick-up coils. As explained in 1.1.3, these measurements cannot be used directly to estimate the poloidal field inside the vessel and therefore have not been used in the present work, although more refined future versions of the model might incorporate them.

3.1.5.1 Toroidal vessel eddy currents

The evolution of the eddy currents in the vessel is expressed in matrix form by the following equation (derived from [23]):

$$[L_{eddy}]\left\{\frac{dI_{eddy,i}}{dt}\right\}+\left\{\frac{I_{eddy,i}}{R_i}\right\}=-[L_{PF}]\left\{\frac{dI_{PF,j}}{dt}\right\}-[L_{DIV}]\left\{\frac{dI_{DIV,k}}{dt}\right\}$$
$$-\left\{L_{PLA,i}(r_{PLA},z_{PLA})\right\}\frac{dI_{PLA}}{dt}-I_{PLA}\left\{\frac{\partial L_{PLA,i}}{\partial r_{PLA}}\dot{r}_{PLA}+\frac{\partial L_{PLA,i}}{\partial z_{PLA}}\dot{z}_{PLA}\right\} \tag{3.11}$$

where:

— $[L_{eddy}]$ is the $n_E \times n_E$ inductance matrix of the eddy currents calculated with COMET (which takes correctly into account the geometry of the poloidal sectors);

— $R_i=2\pi r_i \rho_{avg}/A_i$ is the electrical resistance of the i-th poloidal sector of the vessel, with A_i= cross-sectional area and $\rho_{avg}\approx 8\rho_{inconel}$ =averaged toroidal resistance of the vessel (the factor 8 is due to the bellows).

— $[L_{PF}]$ is the $n_{PF} \times n_E$ inductance matrix of the PF currents with respect to the eddy currents (also obtained with COMET);

— $[L_{DIV}]$ is the $n_{DIV} \times n_E$ inductance matrix of the divertor currents;

— z_{PLA} and r_{PLA} represent the measured position of the plasma current centroid in the poloidal plane (see 1.1.3);

— $\{L_{PLA,i}(z_{PLA},r_{PLA})\}$ is the $1 \times n_E$ vector of the cross-inductances of the eddy currents with respect to the plasma, which is represented by a simple filament (neglecting the effects of the elliptical cross-section and of the current distribution profile). For convenience, these inductances have been expressed in symbolic form [50]:

$$L_{PLA,i}(r_{PLA},z_{PLA})=2\pi r_i\frac{\partial A_\varphi}{\partial I_{PLA}}=2\mu_0\sqrt{r_i r_{PLA}}\,\alpha\Big(m(k(r_{PLA},z_i-z_{PLA}))\Big) \tag{3.12}$$

where:

$$A_\varphi=\frac{\mu_0 I_{PLA}}{\pi}\sqrt{\frac{r_i}{r_{PLA}}}\alpha(m) \tag{3.13}$$

is the toroidal component of the vector potential of the plasma current and:

$$\alpha(m)=\frac{K(m)-E(m)}{\sqrt{m}},\quad m(k)=\frac{1-\sqrt{1-k^2}}{1+\sqrt{1-k^2}},\quad k(r,z)=\frac{4r_{PLA}r}{(r_{PLA}+r)^2+z^2} \tag{3.14}$$

K(m) and *E(m)* are complete elliptic integrals of the first and second kind which, for example, may be computed by means of a power series expansion in *m* as shown in [48].

3.1.5.2 Vessel force balance

The balance of the transient forces acting on the vessel, which includes all major15 sources of applied loads can be written as:

$$\boldsymbol{F}_V = \sum_{i=1}^{n_E} 2\pi r_i I_{eddy,i} \boldsymbol{B}_{POL}(r_i, z_i) + \sum_{k=1}^{n_{DIV}} 2\pi r_k I_{DIV,k} \boldsymbol{B}_{POL}(r_k, z_k) + \boldsymbol{F}_{HALO} \tag{3.15}$$

where the poloidal field B_{POL} can be decomposed in two contributions:

- the field due to PF, divertor and vessel eddy currents, which can be calculated accurately with COMET;
- the field due to the plasma, which may be approximated analytically from the magnetic potential (3.13) [50].

The (3.15) may be solved for the force due to the poloidal halo currents ($\mathbf{F}_{HALO}$) as a function of the total vessel force $\mathbf{F}_V$, which will be estimated by means of the mechanical models seen in the previous sections. This method represents an alternative to the method generally followed in the past, which derived $\mathbf{F}_{HALO}$ from the unbalance of the forces acting on the plasma rather than on the vessel [13]. The new approach is made possible by the fact that a direct estimate of the total vessel force $\mathbf{F}_V$ is now available, instead than just the measure of the MVP support force ($\mathbf{R}_{MVP}$).

3.1.5.3 Halo current estimate

Focusing the attention on the vertical force components only (which are, as previously seen, the most important), it is then possible to write:

$$F_{V,HALO} \approx I_{\mathrm{HALO}} w_{\mathrm{HALO}} B_T = I_{\mathrm{HALO}} w_{\mathrm{HALO}} \frac{B_{T0} r_0}{r_{MVP} - r_{PLA}} \tag{3.16}$$

where the horizontal halo width w_{HALO} can be assumed, for simplicity, to be equal to the plasma minor radius [27](see Fig. 3.7).

The estimate of I_{HALO} obtained from (3.16) is admittedly quite rough and should be considered only as an order-of-magnitude indication. This, besides, has to be compared with results obtained with other (analytical and Finite Element) methods which may be more accurate but share the same fundamental drawbacks: the lack of 3D effects and of an underlying, fully self-consistent halo current model. The procedure described here, which should be seen as an interim step towards a more refined model, has the

15 Additional contributions to the vessel force, such as those due to the poloidal eddy currents caused by the plasma diamagnetic effect and to the image currents in the iron have been neglected for the sake of simplicity.

advantages of being very quick to run and of fitting well with the other lumped-parameter models used to estimate disruption quantities.

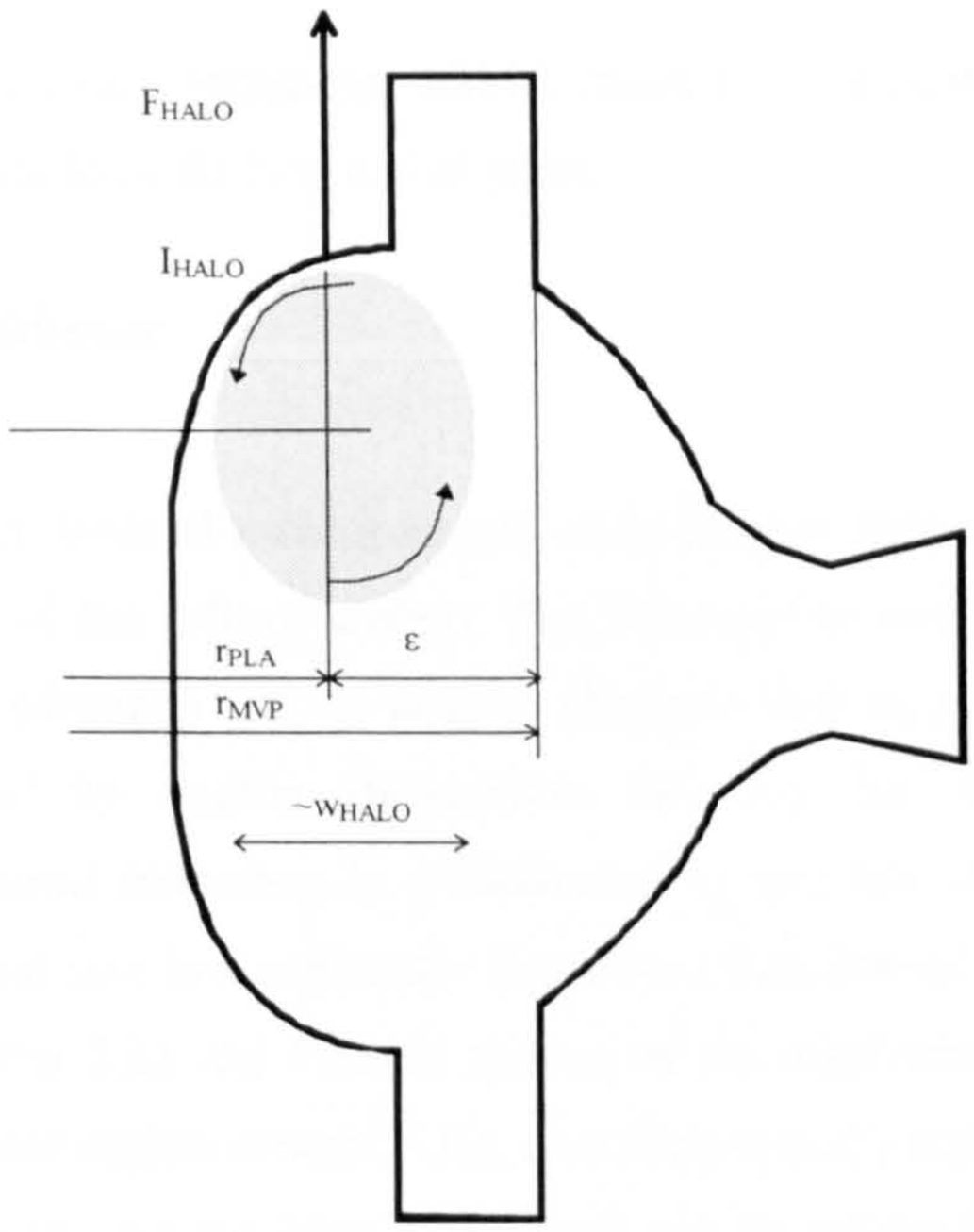


Fig. 3.7 - Halo current force model

3.2 Model for sideways motion

This section describes the lumped-parameter model created to simulate, in a simplified form, the movement of the vessel as a whole in the horizontal plane.

3.2.1.1 Experimental evidence

In case of sideways events, individual measurements taken at each port show clearly the superposition of a slower oscillation on top of the rolling motion. The sideways motion signal x_{SW} (defined in 1.3.1), where the rolling motion is averaged out, is usually characterised by a single, heavily damped low-frequency half-cycle followed by smaller fluctuations (see e.g. the figures in section 6.1). The identification of the fundamental frequency is complicated by the fact that, theoretically, the Fourier spectrum of a critically damped sine is a uniformly decreasing function of the frequency with no clearly defined peak. In real cases (Fig 2.3), the Fourier spectra of the displacement and of the support force signals show a small peak in the region around 5 Hz, revealing that the underlying frequency component has a damping slightly below the critical level. This peak can be artificially enhanced by removing the *trend* from the signal, i.e. by subtracting the line going from the start to the end point. This technique removes, in fact, the substantial offset generated by the friction in the tail of the signals and therefore alleviates the large initial peak at $f_0=1/T$, which would otherwise mask numerically the other features in the spectrum.

Additional, poorly defined peaks can also be seen in the spectra. This corresponds to the oscillations in the last part of the signal which may be interpreted as due to the dynamics of NBI units or to higher-order structural eigenmodes. As in the case of rolling motion, the spectral content of the sideways motion signals becomes negligible above 30 Hz.

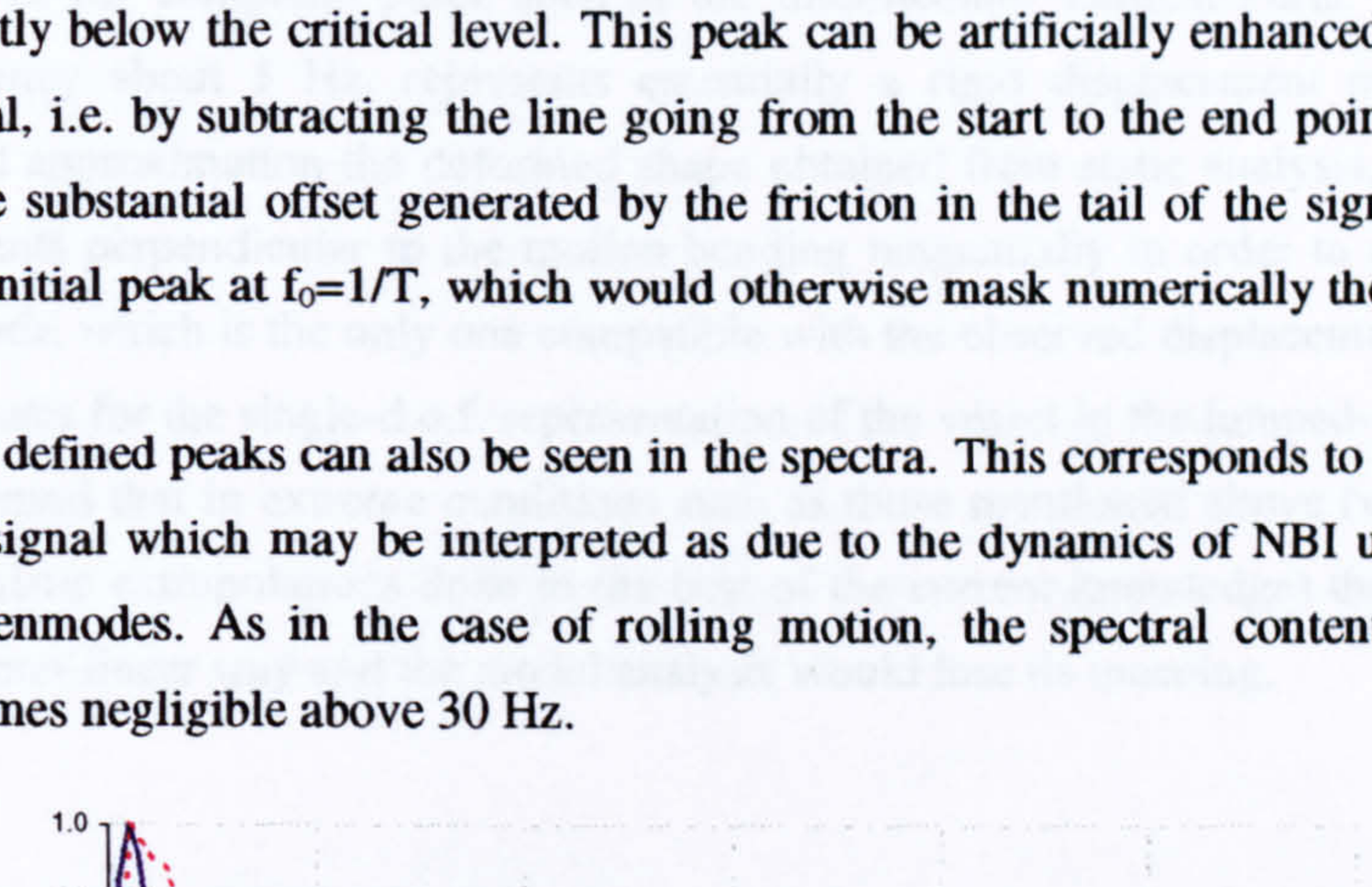


Fig. 3.8 - Fourier spectrum of the measurements sideways response of JET pulse 34078

3.2.1.2 Finite Element model of ½ vessel

A large NASTRAN model has been created in order to represent four octants of the vacuum vessel. This model, totalling about 120,000 d.o.f. (the limit for the current computer system), can be used to simulate the effects of arbitrary loads with the addition of the proper symmetric or anti-symmetric boundary conditions[16].

An extensive range of static and modal analyses has been carried out with this model, while dynamic runs, being at the limits of the capabilities of the available computer system, will be considered at a later time. A number of static loading cases has been investigated, including theoretical sideways force distributions predicted from magnetic models based on different assumptions and characterised by peaking factors[17] up to 8. These results have shown that the global deformation pattern is relatively insensitive to the shape of the load distribution and that stresses are in general low. Stresses in the bellows become important only in extreme conditions (e.g. F_{SW}>10 MN with p_f=8), where the load exceeds locally the atmospheric pressure and the bellows spacers may open up.

Eigenmodes have been extracted for frequencies up ~30 Hz. Most of the modes in this range are related to local deformation of the compliant parts, such as the Intermediate Vertical Ports. The fundamental mode, with a frequency about 5 Hz, represents essentially a rigid displacement of the vessel and reproduces with good approximation the deformed shape obtained from static analysis, characterised by the MVPs in the octants perpendicular to the motion bending tangentially in order to accommodate the deformation. This mode, which is the only one compatible with the observed displacements of the vessel, is considered as the basis for the single-d.o.f. representation of the vessel in the lumped-parameter model. It should be kept in mind that in extreme conditions such as those mentioned above (which are beyond even the most pessimistic extrapolations done to the best of the current knowledge) the structure would behave in a strongly non-linear way and the modal analysis would lose its meaning.

---

16 Any model representing $1/n^{th}$ of the vessel circumference could be used, in theory, to simulate the effect of an arbitrary load. This can be accomplished breaking down of the load into a sum of n components obeying a set of n cyclic symmetry conditions. However, this way of proceeding becomes rapidly impractical for large values of n since an equal number of runs of the model are necessary.

17 The peaking factor of non-toroidally symmetric loads is usually defined as the ratio between the maximum to the average load density.

3.2.1.3 Model formulation

The mechanical effects of sideways forces will be approximated by a 1 d.o.f. system representing the mass of the vessel lumped at its centre and moving along a fixed horizontal line. The direction ϑ which gives the best fit to the data will be determined beforehand and the initial guesses of values of the parameters depending upon ϑ will be fixed accordingly.

An additional d.o.f. is necessary to represent the lumped mass of both the Neutral Beam Injector boxes, which affect significantly the movement of the vessel. This gives the possibility to estimate the elastic force at the connection which is believed to be responsible for some recent mechanical failures. Three further auxiliary massless d.o.f. are required to represent the series connections of spring and damper modelling the effect of MHP and MVP restraints and the dynamic interaction with the magnetic field.

The set of first and second-order ODEs defining the sideways motion model is the following:

$$\begin{cases} M_{VV}\ddot{x} + k_{MVP}^{TANG}x + k_{NBI}(x - x_{NBI}) + k^{*}_{MHP}(x - x_{MHP}) + k_{MVP}^{RAD}(x - x_{MVP}) + b_M(\dot{x} - \dot{x}_M) = F_{SW} + F_F & \text{[Vacuum Vessel]} \\ M_{NBI}\ddot{x}_{NBI} + k_{NBI}(x_{NBI} - x) + b_{NBI}\dot{x}_{NBI} = 0 & \text{[NBI units]} \\ b_{MVP}\dot{x}_{MVP} = k_{MVP}^{RADIAL}(x - x_{MVP}) & \text{[MVP hydraulic dampers]} \\ b_{HH}\dot{x}_{MHP} = k^{*}_{MHP}(x - x_{MHP}) & \text{[MHP hydraulic dampers]} \\ k_m x_m = b_m(\dot{x} - \dot{x}_{magn}) & \text{[magnetic damping]} \end{cases} \tag{3.17}$$

The variables used are listed in Table 3.3. The following subsections expand on some of the principal features of this model.

3.2.1.4 Transient plasma force model

The time evolution of the sideways force, in contrast to the axisymmetric case, cannot be predicted with the currently available magnetic codes but has to be inferred from the plasma current evolution. The simple qualitative model used here is the following:

$$F_{SW}(t) = \begin{cases} F_{SW,max}\sin^2\left(\frac{\pi t}{\tau}\right) & 0 \le t \le \tau \\ 0 & \tau < t < 0 \end{cases} \tag{3.18}$$

The squared sine ensures smoothness of the waveform, although it should be remarked that in the case of impulsive loads the response depends mainly on the integral of the force, rather than on its shape.

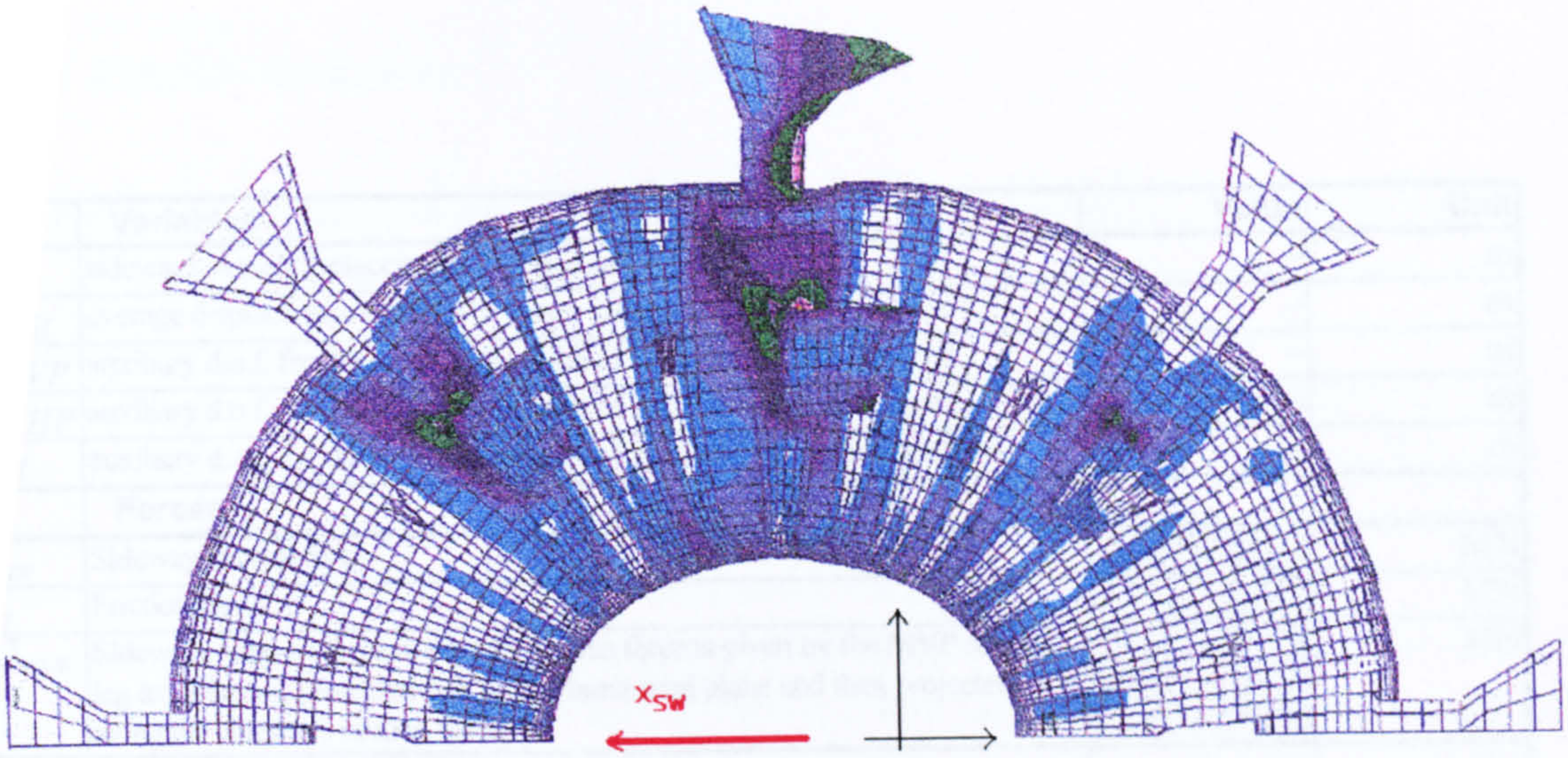


Fig. 3.9 - Deformed shape of the vessel due to sideways load.
This practically coincides with the lowest eigenmode at ~5 Hz.

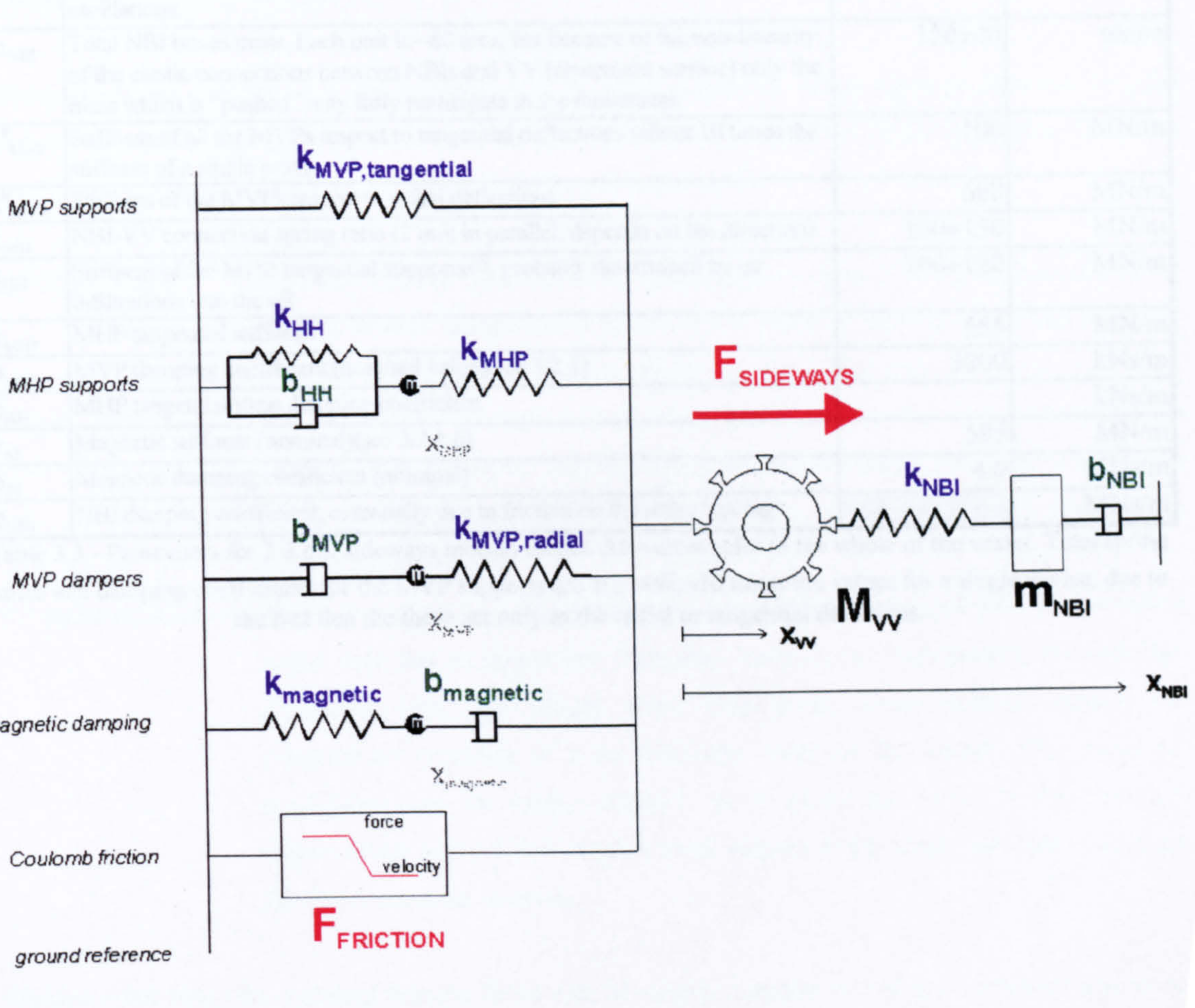


Fig. 3.10 - Lumped-parameter model for the sideways motion of JET vacuum vessel

	Variables	Value	Unit
x	sideways vessel displacement (dropped suffix SW)	–	m
x_{NBI}	average displacement of the NBI boxes along the sideways direction	–	m
x_{MVP}	auxiliary d.o.f. for the series connection of MVP spring and dampers	–	m
x_{MHP}	auxiliary d.o.f. for the series connection of MHP spring and dampers	–	m
x_M	auxiliary d.o.f. for the series connection of magnetic spring and dampers	–	m
	Forces		
F_{SW}	Sideways vessel force		MN
F_F	Friction force		MN
R^T_{MVP}	Sideways support force at the MVP. This force is given by the MVP support leg axial forces, projected first on the horizontal plane and then projected along the sideways motion direction		MN
	Mechanical parameters		
M_{VV}	Vacuum Vessel bulk mass. Total mass actual estimates (based on support spring measurements and original weighting of the single components). From the oscillation frequency of 5Hz, a much lower estimate $4\pi^2 f^2 / k^T_{MVP} \approx 100$ tonne can be obtained, due to the fact that not all the mass participates to the oscillations.	200÷240	tonne
m_{NBI}	Total NBI boxes mass. Each unit is ~80 tons, but because of the non-linearity of the elastic connections between NBIs and VV (abatement surface) only the mass which is "pushed" may fully participate in the movement.	120±40	tonne
k^T_{MVP}	Stiffness of all the MVPs respect to tangential deflections (about 10 times the stiffness of a single port)	100	MN/m
k^R_{MVP}	Stiffness of the MVPs respect to radial deflections	600	MN/m
k_{NBI}	NBI-VV connection spring ratio (2 unit in parallel, depends on the direction)	100÷150	MN/m
k_{HH}	Stiffness of the MHP tangential supports[18], probably determined by air infiltrations into the oil	100÷120	MN/m
k_{MHP}	MHP tangential stiffness	555	MN/m
b_{MVP}	MVP damping coefficient (nominal value)(see 3.2.1)	3000	kNs/m
b_{HH}	MHP tangential strap damping coefficient		kNs/m
k_M	Magnetic stiffness (nominal)(see 3.2.1.6)	595	MN/m
b_M	Magnetic damping coefficient (nominal)	4.9	MNs/m
b_{NBI}	NBI damping coefficient, essentially due to friction on the roller bearings		MNs/m

Table 3.3 - Parameters for 2 d.o.f. sideways motion model. All values refer to the whole of the vessel. Total spring ratios and damping coefficients for the MVP supports are $2(2+4\sqrt{2}) \approx 10$ times the values for a single device, due to the fact that the these act only in the radial or tangential directions.

18 As a mnemonic aid, the subscript HH stands for Hans Hemmerich (the designer of the device).

3.2.1.5 Friction mechanism

When external forces vanish, a system tied to the ground by elastic springs and linear dampers (which cannot provide any force at zero velocity) will always tend to come back to the initial position. In the majority of cases, however, sideways motion measurements show a significant offset between the pre- and post-disruption steady state conditions. This offset tends to persist between subsequent JET pulses, as clearly shown in the slow time traces in Fig 3.11. The offset can be observed to accumulate from disruption to disruption, although sometimes particularly violent events seem to shake the structure loose and reset the original position. In this way, the long-term average is about zero.

The addition of friction effects into the model is necessary in order to reproduce these observations. Since the microscopic mechanism at the basis of friction is very complex, the representation of friction effects in large, real-world structures relies generally upon simplified phenomenological models. Two friction models have been considered:

Micro-sliding in the restraints

When the vessel vibrates it is conceivable that, in some locations, micro-slippage between coupled surfaces may occur, leading to the same surfaces getting locked in a different position by static Coulomb force. This could happen, for instance, in the following components:

Outer Ring Spacers — the spacers of the Outer Restraining Ring (see section 1.1.1.4), which are subject to considerable compression forces, could slide or deform under the effect of sideways forces shearing and stretching locally the bellows.

Attached equipment — a multitude of mechanical items like pipes, diagnostics and connectors are attached to the vessel, both internally and externally. Although a complete survey would be very difficult, some of these components could conceivable provide friction forces.

MVP Dynamic Brakes — the MVP support legs are locked in position by a friction-operated device which might slide due to tangential disruption loads. As a consequence, the two legs supporting each port would retain respectively some residual tension and compression resulting in a net sideways force on the vessel. This particular mechanism can be easily verified, as it alters the ratio of the sideways displacement to the MVP support force respect to the ideal value obtained from the Finite Element analysis.

Whatever the case, the resulting friction force can be simply lumped in a single constant term to be added to the external vessel force after the onset of the disruption:

$$F_{SW,total} = F_{SW} + F_{friction} \tag{3.19}$$

with, for example:

$$F_{friction}(t) = \begin{cases} 0 & t < t_0 \\ F_{friction,slip} & t \geq t_0 \end{cases} \tag{3.20}$$

Coulomb friction

Coulomb theory represent the classical approach to friction modelling. The following approximate representation in terms of a non-hysteretic Coulomb force-velocity relationship has been considered [52]:

$$F_{friction} = \begin{cases} F_{F,max} \dfrac{\Delta v}{\Delta \bar{v}} & |\Delta v| \leq \Delta \bar{v} \\ F_{F,max}\, \mathrm{sgn}(\Delta v) & |\Delta v| > \Delta \bar{v} \end{cases} \qquad F_{F,max} = \mu F_N \tag{3.21}$$

where μ is a friction coefficient, F_N is the force normal to the sliding surfaces, Δv is their relative velocity and $\Delta \bar{v}$ defines the sticking conditions. This model appears to neglect static attrition as it gives zero force for zero velocity; in fact, if $\Delta \bar{v}$ is small, any attempt to slide off an initial rest position will be immediately counteracted, resulting in the correct dynamic behaviour. The following smoothed formulation has been implemented:

$$F_{friction} = F_{F,max} \tanh \frac{\Delta v}{\Delta \bar{v}} \tag{3.22}$$

which has been found to help preventing instability in the numerical integration. From the numerical viewpoint, anyway, the presence of a near-discontinuity is detrimental for the adaptive Runge-Kutta integration algorithm and the time step necessary to achieve the prescribed accuracy becomes very small as $\Delta \bar{v}$ decreases.

Two independent sources of Coulomb friction have been included in the sideways motion model, acting on both the vacuum vessel and NBI mass.

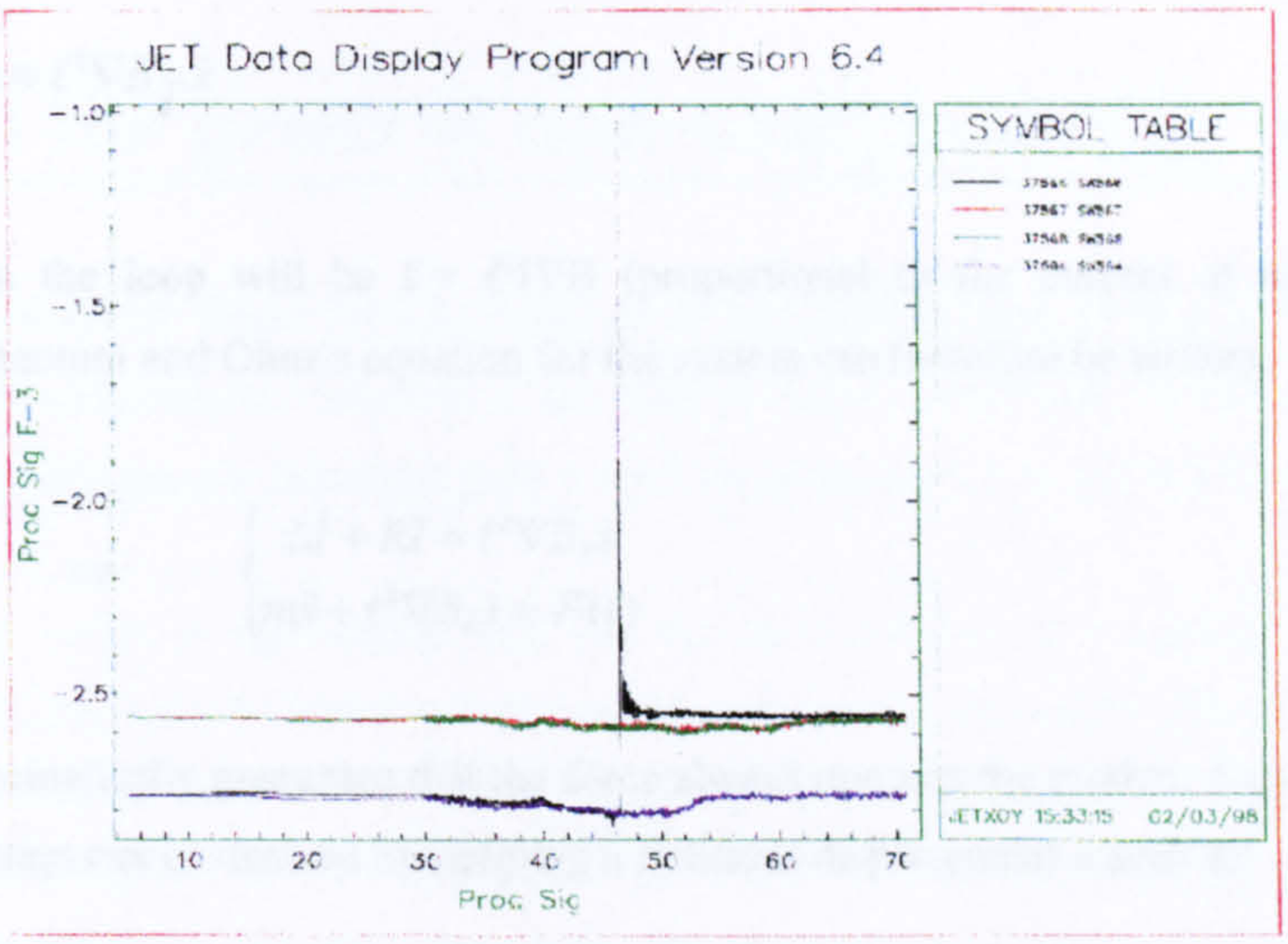


Fig. 3.11 - Persistence of the offset in the sideways displacement signal between subsequent JET pulses

3.2.1.6 Magnetic damping

The magnetic damping effect, which was overlooked for a long time at JET, has actually been proved to be the major restraining mechanism for the sideways movements of the vessel [24, 30]. This phenomenon is essentially due to poloidal eddy currents arising when the vessel crosses the toroidal field. A qualitative understanding can be achieved by considering the simplified model in Fig. 3.12 , where a conductive loop with characteristic size ℓ, mass m, resistance R and inductance L is shown.

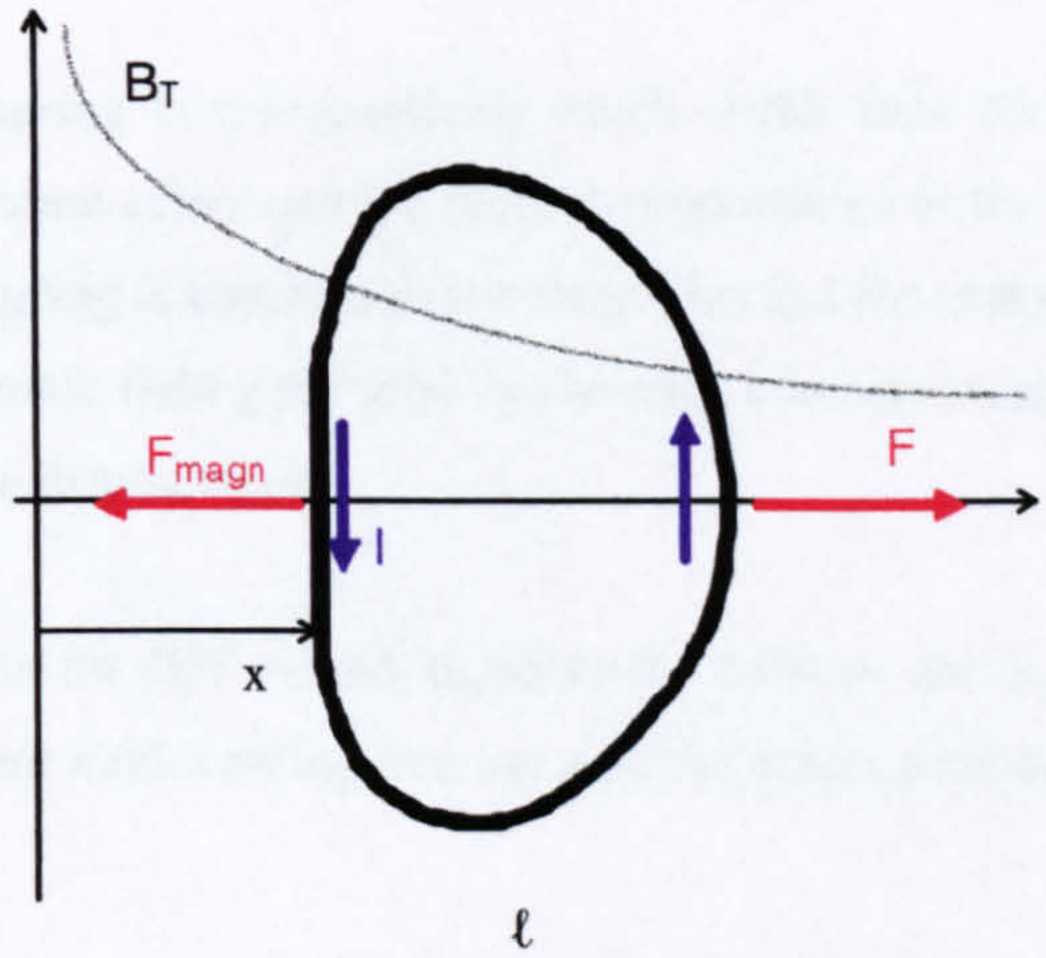


Fig. 3.12 - Qualitative scheme for the magnetic damping effect

The loop crosses a field $B_T(x)$, parallel to the y direction, having a scalar gradient ∇B_T in the x direction. Assuming that ℓ is small compared to $B/\nabla B_T$, the e.m.f. arising in the loop due to a small movement along x will be:

$$\varepsilon = -\frac{\partial \Phi}{\partial t} = -\frac{\partial \Phi}{\partial x}\dot{x} \approx \ell^2 \nabla B_T \dot{x} \tag{3.23}$$

while the force on the loop will be F= $\ell^2 I \nabla B$ (proportional to the current at any given time). Conservation of momentum and Ohm's equation for the system can therefore be written:

$$\begin{cases} L\dot{I} + RI = \varepsilon \\ m\ddot{x} + F_{magn} = F(t) \end{cases} \Rightarrow \begin{cases} L\dot{I} + RI = \ell^2 \nabla B_T \dot{x} \\ m\ddot{x} + \ell^2 \nabla B_T I = F(t) \end{cases} \tag{3.24}$$

where the signs automatically guarantee that the force always opposes the motion. A purely mechanical equivalent of this system can be derived by defining a fictitious displacement u such as:

$$u = \frac{L}{\ell^2 \nabla B} I \quad \Rightarrow \quad \begin{cases} \dot{u} + \frac{R}{L} u = \dot{x} \\ m\ddot{x} + k_m u = F \end{cases}, \quad \text{where } k_m = \frac{\ell^4 \nabla B_T^{\,2}}{L} \tag{3.25}$$

This allows the first dynamic equation to be rewritten so as to be dimensionally homogeneous to a force:

$$\begin{cases} k_m u = b_m (\dot{x} - \dot{u}) \\ m\ddot{x} + k_m u = F \end{cases}, \quad \text{where } b_m = \frac{\ell^4 \nabla B_T^{\,2}}{R} \tag{3.26}$$

This system is equivalent to the connection in series of the mass m to a damper b_m and an elastic spring k_m, with the spring connected to the ground (see (A.3). Two limit cases arise:

resistive limit (R/L→∞) the spring is comparatively much stiffer than the damper; dissipation is the dominant effect and the force is proportional to the velocity.

inductive limit (R/L→0) the spring is comparatively compliant and the energy is stored reversibly in the magnetic field generated by the eddy currents, resulting in a force proportional to the displacement.

The values of the coefficients for JET vessel, $b_m = 0.41 \cdot B_T^2$ MNs/m and $k_m = 50 \cdot B_T^2$ MN/m, have been determined with a Finite Element model taking into account the actual geometry [49].

3.3 Model for general non-axisymmetric motions

A global lumped-parameter model with 8×4 degrees of freedom has been created to represent general axisymmetric and non-axisymmetric motions of the vacuum vessel. This model is very complex and still at an early stage of development, therefore only a brief description will be given and no results will be discussed here.

In this model each octant is represented with two masses oscillating in a poloidal plane, as in the rolling motion model, but with the additional freedom to move in the horizontal plane. Longitudinal and torsional elastic connections between octants, with spring ratios obtained from the large Finite Element model, are provided to simulate the total stiffness of the structure. The main loading condition currently being investigated is related to the n=1, m=1 kink plasma mode described in 1.2.2 and includes the superposition of a non-axisymmetric vertical force to a sideways force. As an example of the approach followed, Fig. 3.13 shows a reference static Finite Element assessment of the effects of a toroidally non-uniform vertical load. The result indicates clearly that the shell has a very high torsional stiffness which contributes to smear out the asymmetry between the octants; a peaking factor p_f=2 in the load corresponds, in fact, just to p_f=1.1 in the rolling motion. This implies that using the non-uniformity of the response to infer the non-uniformity of the load is inherently an ill-posed problem; when the model will be completed, all mechanical measurements available on the machine will probably have to be fitted at the same time in order to get satisfactory results.

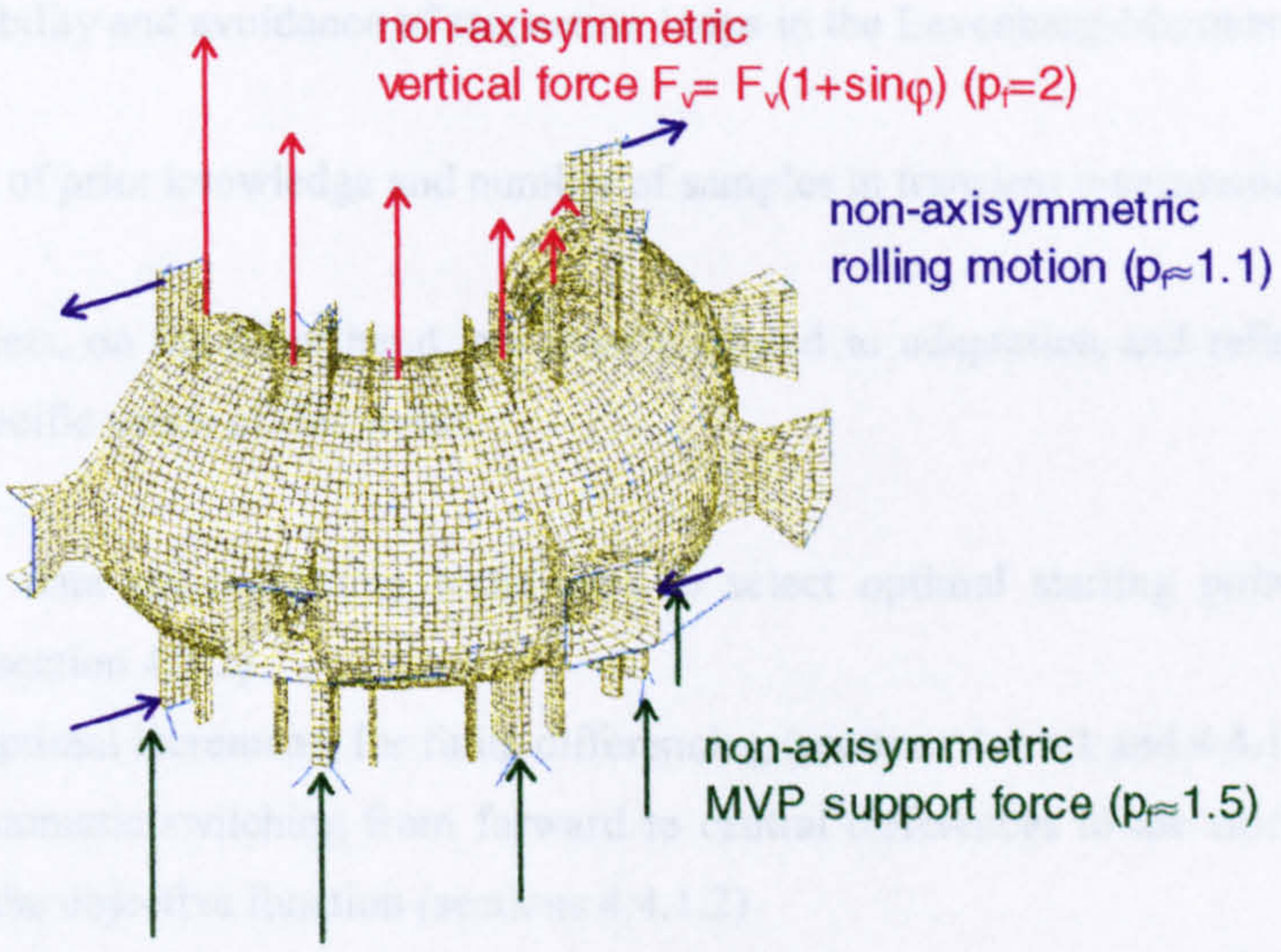


Fig. 3.13 - Finite Element model for the non-axisymmetric rolling motion

4

MODEL-BASED PARAMETER ESTIMATION

In this chapter the technique devised to fit the predictions of the electromechanical models to the experimental data is explained in detail. The rationale for this new kind of approach is discussed first in section 4.1 and a short review of the previous attempts in this direction, both in the general field of fusion technology and, more specifically, at JET is presented. The necessary mathematical background is briefly outlined in section 4.2, where the roots of the estimation problem in the areas of statistics and optimisation theory are underlined. Next, section 4.3 covers the various kinds of signal processing and pre-conditioning that can be applied to JET measurements before they are fed to the estimation procedure. The rest of the chapter (sections 4.4 and 4.5) is devoted to discuss the various adaptations and improvements made to the existing algorithms, giving particular emphasis to the incorporation of all the available forms of prior knowledge.

From the viewpoint of numerical analysis, a number of issues are believed to be significant (if small) contributions to the theory and practice of optimisation techniques. These topics include two theoretical considerations which have received so far only scarce attention in the application-oriented literature:

- occurrence, stability and avoidance of stagnation loops in the Levenberg-Marquardt method (section 4.4.2.1)
- relative weight of prior knowledge and number of samples in transient measurements (section 4.5.1)

The following points, on the other hand, are mostly related to adaptation and refinement of existing algorithms to the specific needs of this work:

- use of *ad-hoc* data pre-processing techniques to select optimal starting point for the iterative minimisation (section 4.3.2)
- choice of the optimal increments for finite differencing (sections 4.4.1.1 and 4.4.1.4)
- strategy for automatic switching from forward to central differences in the calculation of the first derivatives of the objective function (sections 4.4.1.2)
- selection of the damping factor in the Levenberg-Marquardt algorithm as a function of the local topology (i.e. eigendecomposition obtained from quadratic approximation) of the objective function (section 4.4.3.2)
- smoothed elimination strategy for the null singular values of the damped hessian via prior scaling of the linearized equations (section 4.4.4.3)
- multiple prioritised termination criteria (section 4.4.5)

- enforcement of global parameter bounds (section 4.5.2)

Some of these topics refer to generic-type problems where the function to be minimised may be given also in analytical form; others concern the field of differential model-based parameter estimation (MBPE); the remainder refer specifically to second-order mechanical models generating damped sinusoidal transients, as is mostly the case with JET measurements. The material in sections 4.3 through 4.5 has been grouped by reference to different functional aspects of the estimation algorithm.

The parameter estimation procedure has been implemented into a general-purpose computer code called TEMPEST (Tool for Enhanced Model-based Parameter ESTimation), which includes all the algorithms discussed in this chapter and has been used throughout the work to obtain the results reported. The development of a standalone program has been motivated by reasons of flexibility and efficiency which are fully detailed in Appendix 2, where the architecture and the implementation details of the program are also discussed.

4.1 Using mechanical models as diagnostics

This section introduces the philosophy behind the method at the core of the present work, that is the use of lumped-parameter models in order to infer information on the forces and on the plasma behaviour. The motivations for this approach, the references to similar applications found in the literature and a brief history of the activities in this area at JET are first outlined in section 4.1.1.1. The flexibility inherent in the lumped-parameter approach is particularly emphasized in section 4.1.1.2, where the potential of the models for extracting knowledge in various ways from the measurements is also pointed out.

4.1.1 Inferring information via parameter estimation

The current state-of-the-art models representing electromagnetic and mechanical properties of a tokamak during a disruption suffer from many uncertainties which prevent fully predictive simulation from being carried out satisfactorily. Narrowing the scope to the response of JET vacuum vessel, the uncertainties may be confined to a relatively small number of parameters describing some of the properties of the lumped-parameter models including masses, damping coefficients and forces (in terms of magnitude, timing and position). Intuitively, it is evident that the uncertain parameters can be somehow estimated by adjusting the models until their output resembles the actual measurements. This indirect way of proceeding makes use of the models in a "backward" fashion, as opposed to the direct "forward" approach which follows the logical progression from causes (MHD instabilities) to effects (forces and mechanical response).

In order to clarify the problem, let us consider the following minimal mechanical model:

$$m\ddot{x} + b\dot{x} + kx = F(t; p_j) \qquad (4.1)$$

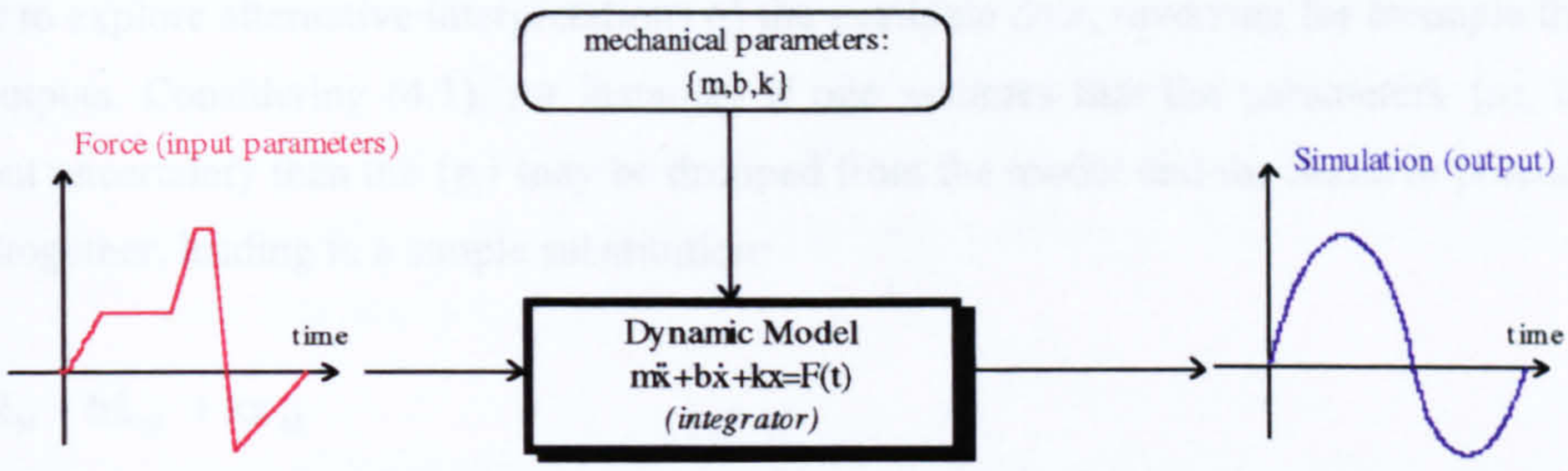
where x(t) represents a measured displacement, F is the external force and m, b, k and the $\{p_j\}$ are the uncertain parameters. A fundamental difference exists between the parameters {m, b, k}, and the $\{p_j\}$: the former describe the internal properties of the system, whereas the latter define a family of functions to which F(t) is assumed to belong. The parameter estimation procedure consists in integrating repeatedly (4.1) and updating the parameters until the simulation x(t) will coincide with the measurement $x_M(t)$ in some approximate, usually least-squares sense. This problem can formalised mathematically in the context of the statistical model-based parameter estimation (MBPE) theory, which is firmly established as a standard tool in practically every discipline of physics and engineering. MBPE belongs to the broader context of inverse problems, which have received much theoretical attention recently and where general results are available for recognising and dealing with ill-conditioning [59].

The strongest merits of the MBPE approach can be summarised as follows:

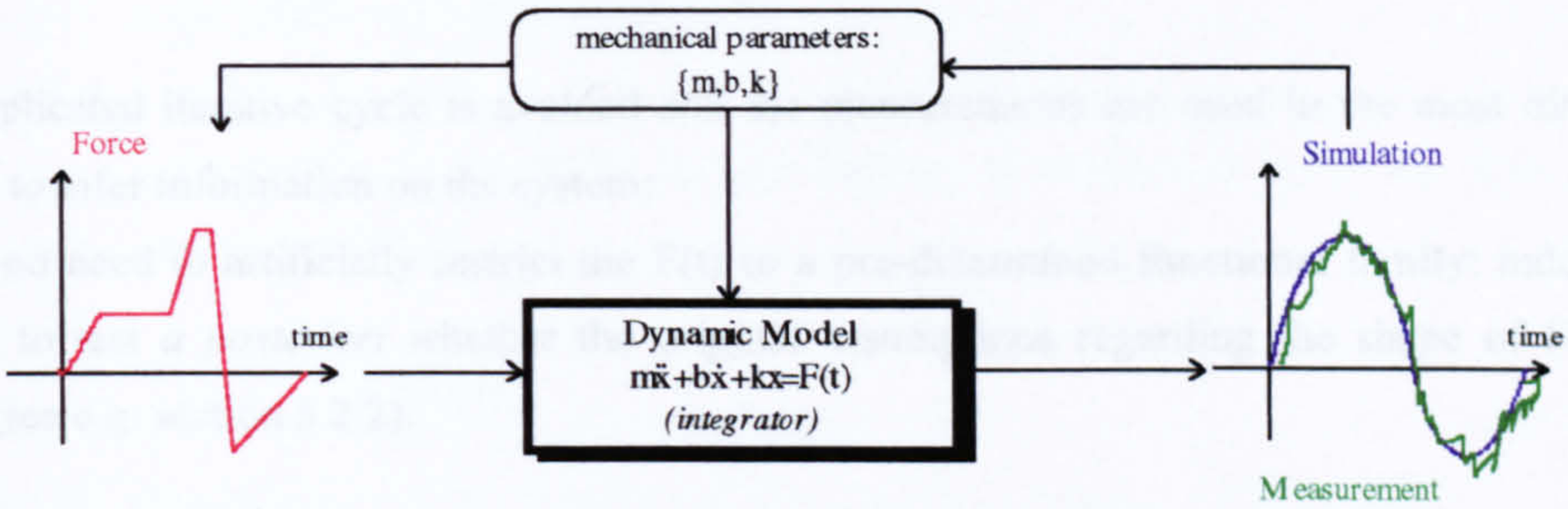
- ✓ The estimation is based mainly on mechanical measurements which are very reliable, especially if compared to magnetic ones;
- ✓ The results obtained can be easily understood on the basis of first principles: for instance, if a body having mass m accelerates more or less uniformly to velocity v in the time Δt, then the acting force cannot be much different from $mv/\Delta t$;
- ✓ The confidence in the results can be vastly increased if fitting multiple sub-models to multiple independent measurements gives closely similar results.
- ✓ The method can be viewed as a new kind of diagnostic system: although indirect and off-line, MBPE is both efficient and cost-effective since it maximises the usefulness of instrumentation which is already there.

In this work the following general issues have not been considered in detail:

- Identification of the mathematical model. The order and structure of the set of differential equations describing the systems under investigation is based on well-established physics and engineering arguments and is assumed to be correct. All the preliminary identification work has very briefly reviewed in chapter 3.
- Optimal experiment design. In theory, the input into the model's equations could be designed so as to minimise the uncertainty in the estimated parameters. Unfortunately, the force F(t) cannot be controlled directly with the current technology, which of course is precisely the reason why disruptions are dangerous. The present investigation, therefore, is simply focused on the extraction of information from the existing database.



I) "Open loop" (forward) integration



II) "Feedback loop" (backward) parameter estimation

III) "Input reversal" parameter estimation

Fig. 4.1 - Direct and indirect approaches in model-based parameter estimation to infer information from models and measurements

4.1.2 Alternative inference method: input reversal

The simplicity of the physical representation that can be obtained with the lumped parameter models makes it easy to explore alternative interpretations of the available data, reversing for example the role of inputs and outputs. Considering (4.1), for instance, if one assumes that the parameters {m, b, k} are known without uncertainty then the $\{p_j\}$ may be dropped from the model and the iterative procedure may be skipped altogether, leading to a simple substitution:

$$F^*=F(t)=m\ddot{x}_M + b\dot{x}_M + kx_M \tag{4.2}$$

(the star superscript will be used in the following to distinguish the variables estimated with this method). In this case, the causal relationship between x and F is clearly reversed. This way of proceeding yields two important benefits:

- the complicated iterative cycle is avoided and the measurements are used in the most direct way possible to infer information on the system;
- there is no need to artificially restrict the F(t) to a pre-determined functional family: indeed, it is possible to test *a posteriori* whether the original assumptions regarding the shape of F(t) were correct (see e.g. section 5.2.2).

The models defined in chapter 3 are substantially more difficult to treat than (4.1), also because parameters related to the external force (like ε) appear on the l.h.s. of the equations. Hybrid situations may be envisaged in which only some of the parameters are estimated iteratively while, at the same time, a subset of the available measurements is diverted and used as an input. In general, complex cases require more assumptions but also leave more freedom in deciding which variables can be solved for, with the only obvious constraint to retain as many unknowns as equations.

Unfortunately, the direct evaluation of the r.h.s. from measurements is typically an ill-conditioned problem, prone to all sorts of numerical pitfalls. The following main error sources can be briefly described:

Measurement noise Considering, for instance, an ideal signal with frequency content *f* affected by noise at frequency f_N:

$$x(t)=A\cdot\sin(2\pi ft)+\varepsilon\cdot\sin(2\pi f_N t) \tag{4.3}$$

the S/N ratio of the n-th derivative of x(t) will be clearly:

$$S/N = \frac{A}{\varepsilon}\left(\frac{f}{f_N}\right)^n \tag{4.4}$$

The differentiation of a measurement containing even a small amount of high-frequency noise[19] will be therefore affected by errors diverging very rapidly, which enter linearly equation (4.1) and affect the calculated force.

Frequency response If the frequency response of a system has any zeroes in the range included in the excitation, all the information contained in the input at those frequencies is obviously destroyed making the calculated F(t) worthless. Errors may also arise in correspondence of resonance frequencies, although these affect harmonic loads more than transient ones.

Modelling errors Let us consider the effects of errors of modelling in (4.1) where, for the sake of simplicity, the damping will be neglected. The errors will be expressed by the variations *dm* and *dk* in the mass and stiffness coefficients:

$$(m+dm)\ddot{x} + (k+dk)x = F(t) \tag{4.5}$$

Assuming, for example, a step loading of magnitude F_0 at the time t=0, the response will be:

$$x(t)=F_0[1-\cos\omega t]/k \tag{4.6}$$

where $\omega^2=k/m$. By substitution in the variated model, the computed force will be:

$$F(t) = F_0\left\{1+\left(\frac{dm}{m}-\frac{dk}{k}\right)\cos\omega t\right\} \tag{4.7}$$

which shows that, as a general circumstance, an error component will arise with the same frequency as the free vibrations of the system and of the same order of magnitude, in relative terms, as the errors committed on the parameters.

In light of these considerations, the parameter estimation approach in which F(t) is arbitrarily assigned to a specific family of functions may be seen as a way to enforce well-posedness into the problem (this might be called a regularization technique in inverse problem theory); the accuracy of the answer may be limited *a priori* (e.g. if the family does not include the real waveform), but at least the result will have a clearly defined meaning. Examples of applications of these concepts to JET models will be discussed in chapters 5 and 6.

---

19 For typical JET signals the maximum frequency of interest is typically around 50~100 Hz; some noise is however always present up to the Nyquist frequency (~1 kHz).

4.1.2.1 Input reversal on Finite Element models

Similar arguments represent a serious limit in the application of input reversal calculations not only to lumped parameter but also to Finite Element models. Given a discretized structural system described by the dynamic matrix equation (omitting for clarity damping effects) [57]:

$$[M]\{\ddot{x}\}+[K]\{x\}=\{F\} \tag{4.8}$$

the r.h.s. can be worked out, in theory, if the vector of the nodal displacements $\{x\}$ is measured as a function of time. In those frequent cases where the mesh includes a large number N of nodal points but displacements are measured only at $n<<N$ locations x_j, the movement of all other nodes will have to be interpolated somehow. Note that standard methods available in Finite Element codes for enforcing motion at a node[20] usually assume that an external force is acting on that node, which in our case is false. A reasonable way to proceed is to make use of the modal superposition method, in which the vector $\{x(t)\}$ is expressed as the linear combination of a subset of the N available modal shapes $\{\Phi_i\}$:

$$\{x(t)\}=\Sigma_i \varphi_i(t)\{\Phi_i\} \qquad i=1..n \tag{4.9}$$

The number of modes included has of course to be the same as the number of measurements as a necessary (but not sufficient) condition to find the scaling factors $\varphi_j(t)$ from the linear system:

$$x_{j,measured}(t)=\Sigma_i \varphi_i(t)\Phi_{ij} \qquad j=1..n \tag{4.10}$$

The modes included should be those whose frequency matches more closely the spectrum of the excitation, assuming some prior knowledge on that is available. In general, however, the error committed in the estimate of x(t) at all the (N-n) interpolated nodes will contain contributions at the frequencies of the discarded modes and these, added to the noise in the measurements, may have the detrimental square-frequency effect seen above. This problem may be bypassed by measuring accelerations directly, although in this case errors on the low frequency components become dominant due to the double integration necessary (in addition, the substantial energy content usually found in accelerometer signals due to vibrations at acoustic frequencies may interfere with the calculation).

To conclude, also the application of input reversal techniques to Finite Element models is severely constrained by numerical problems, which add to the inherent complexity and slowness of the approach.

---

[20] These include typically the introduction of constraints into the dynamic equations through Lagrange multipliers. As an alternative, one could also enforce a prescribed acceleration *a* at a node by adding locally a very large point-like mass *M* and applying the external load *Ma* [57].

4.1.3 Literature survey

The general subject of force estimation in mechanical systems is vast, although the overwhelming majority of the literature is concerned with vibration problems, where the loads are random oscillations (see [61] for a comprehensive overview). These problems are usually treated with spectral techniques which essentially consist in deconvolving the system's output with its transfer function, adopting regularization techniques to circumvent the intrinsic ill-conditioning that arises close to the zeroes of the transfer function [60]. A few references may be found to the more specific case of estimation of impulsive loads, although these are mostly focused on laboratory test case rather than real-world problems [62]. In some cases the estimation of moving loads where also the point of application is unknown is considered [63], while in [64] an application including the estimation of mass and geometry parameter in rigid-body system is discussed. Applications to electromechanical systems, in particular, are extremely scarce.

In the field of fusion research MBPE finds many applications especially in the area of plasma physics and transport models, which most heavily rely on experimental data[21]. Considering more specifically the mechanical effects of disruptions, however, very little literature can be found about this subject in general on machines other than JET and no references at all, to the best of the author's knowledge, exist on the subject of parameter estimation of tokamak mechanical systems. This is perhaps unsurprising since JET is the only large machine where the combination of high plasma current, vertically unstable plasma and relatively flexible structure makes disruption events frequent and structurally dangerous. For this very reason, JET is also historically the only machine where comprehensive mechanical diagnostics have been installed and therefore is in a unique position to investigate this kind of problems.

A recent JET study is related to the prediction of force measurements on the basis of the magnetic configuration of a pulse, although this follows an approach based on neural networks completely different from MBPE [65]. As for lumped parameter models, these have been used ever since early observations of the dramatic effects of disruptions [53]. Earlier models concerned the rolling motion only and included one or two d.o.f. with relative masses and spring constants. Adjustment of the parameters of these models was essentially manual, varying for instance the oscillating frequency until a visually satisfactory match between simulation and experiment was obtained. These models, even if approximated, were used successfully to assess stress conditions and to design the first generation of vessel supports which, up to now, has managed well to keep the machine together. In the last few years these models have been updated with the addition of more degrees of freedom and extended to the new phenomenon of sideways motion [58]; the models presented here are inspired by and based on all the previous work, complementing it with the mathematical soundness of the MBPE approach.

---

21 See e.g. [86] and [87] for applications of Bayesian inference method (described in section 4.2.2.1) to respectively a gyro-Bohm model and confinement scaling laws, and [88] for an application to an optimisation study of the Levenberg-Marquardt method, the minimisation algorithm selected for the procedure and described in section 4.2.3.4.

To conclude, it is possible to state with reasonable confidence that the systematic application of parameter estimation techniques to electromechanical models represents a novel idea in the field of fusion research. Moreover, the method devised in the present work may be regarded as innovative even in the broader context of mechanical system analysis as far as the impulsive nature of the forces, the complexity of the models and the level of detail considered are concerned.

4.2 Review of parameter estimation theory

In this section the basic concepts of model-based parameter estimation are briefly reviewed in order to introduce the problem and the notation used, as well as to show more clearly the role and the extent of the adaptations made. In accord to the various possible interpretations, throughout the work the estimation problem will be interchangeably referred to as the fitting, minimisation or optimisation problem.

4.2.1 Maximum-likelihood parameter estimation

4.2.1.1 Parametric dynamic models

Let us consider first the general mathematical representation of a physical system in terms of a set of first-order ODEs of order N, the *standard dynamic model* [74]:

$$\begin{cases} \dot{u}_k = f_k(t, u_h, p_j) \\ u_k(t_0) = u_{k0} \end{cases} \qquad (4.11)$$

where:

— $u_{k,h=1\ldots N}$ are N scalar variables describing the state of the system, having initial values u_{k0}. If, for instance, the system represents a mechanical model with point-like masses, ruled by second-order motion equations, each physical d.o.f. corresponds to two variables in the canonical system (position and velocity).

— $p_{j=1\ldots M}$ are M scalar parameters.

This system is associated to a number n_M of measurements, x_k, i.e. physically observable variables defined by the equations:

$$\{x_k = g_k(t, u_h, p_j) \qquad (4.12)$$

In the simplest case, the observed quantity is just a variable of the model and it will be $x_k \equiv u_h$ for a certain h (e.g. the displacement x_{MVP} in the Rolling Motion model, see 1.3.1.1). In general, however, each measured quantity will depend upon the state of the system, the values of the parameters and, possibly, the time (e.g. the vertical support force R_{MVP} in the Rolling Motion model). The subscript M will distinguish the actual measurements $x_{Mk}(t)$ from the calculated values $x_k(t)$. Both will be treated as discrete functions of time sampled at a rate τ_s^{-1}; in other words, each will be given as an array of n scalar values $\{x_{ki}\}=\{x_k(t_i)\}=\{x_k(t_0+i\tau_s)\}$ and, similarly, $\{x_{Mki}\}$ defined over the interval $n\tau_s$[22] (see Fig. 4.2).

22 The extension to the case where each observed time trace has a different sampling rate and number of samples is trivial.

For a given realisation of the experiment, comparing measurements and calculation will generally show that $x_{ki} \neq x_{Mki}$ for any combination of these reasons:

1) the model is wrong (i.e. it does not represent the physical system)
2) the values of the parameters p_j are incorrect
3) the measurements are affected by noise

This problem is usually approached by selecting somehow the parameters so as to best fit the observations, taking measurement errors into account. In the process, it is necessary to derive additional information that will allow one to judge whether the model is adequate to reproduce the observations and, if this is the case, what is the level of confidence in the obtained values of the parameters.

4.2.1.2 Statistical assumptions

The standard dynamic model represents a stochastic process, i.e. a system in which the variables are affected by random fluctuations that have to be described in statistical terms. This problem, which is mathematically very complicated, is usually simplified by a standard set of assumptions of which ones that apply to the present case are listed hereafter [77]:

1. *Additive errors*

   The errors in the measurements do not depend explicitly on the various error sources in the model, but can be lumped in a single term which affects just the final value. In other words, $x_k = g_k(t, u_h, p_j + \varepsilon_j) + \varepsilon_k$ can be replaced by $x_k = g_k(t, u_h, p_j) + \varepsilon_{k,\,TOTAL}$

2. *Zero mean error*

   Any systematic bias has been removed from the measurements.

3. *Normal error distribution*

   The distribution of the errors follows a Gaussian curve. This assumption can often be wrong for data with many outliers, like e.g. electrical noise spikes which are often found in JET's measurements. The possible corrective actions in this case will be discussed later on.

4. *Constant/uncorrelated variances*

   The measurement errors have the same variance throughout any given JET pulse; moreover, the variances do not depend on the errors at any other time (i.e. the cross-variances are identically zero).

5. *Error-free independent variable*

   The errors in the values of time throughout the integration of the model (given by the digital sampling circuitry) are negligible.

4.2.1.3 Likelihood maximisation

Any realisation of the experiment (the underlying physical model being fixed) will yield a different array of measured data $\{x_{Mki}\}$ because of the noise. The goal of the fitting procedure may be simply stated as follows: to determine the set of parameters $\{p_j^*\}$ that has the maximum likelihood of generating the measured values. To do so, one must assume that this is equivalent to the probability that those measurements might have been produced by a model with $\{p_j=p_j^*\}$. This subtle reversal of viewpoint allows one to replace the intuitive concept of *likelihood* of the set of parameters with the mathematically well-defined notion of *probability* of occurrence of a certain sequence of events, which is computable in a rigorous way. The joint probability $\wp$ of realisation of the $n \cdot n_M$ observed values within an error bar of width Δx_k, different for each observed variable, can in principle be expressed by the product of $n^2 n_M$ normally distributed probabilities (adapted from [71]):

$$\wp = \prod_{k=1}^{n_M} \frac{e^{-\frac{1}{2}\left\{x_{ki}-x_{Mki}\right\}^T\left[\sigma^2_{Mkij}\right]^{-1}\left\{x_{kj}-x_{Mki}\right\}}}{\sqrt{2\pi}\prod_{i,j=1}^{n}\sigma_{Mkij}} \Delta x_k^n \tag{4.13}$$

where the covariance matrix for the k^{th} observed variable $[\sigma^2_{Mkij}]$ represents the statistical dependence of the distribution of errors at the time t_i upon the distribution at the time t_j. On the basis of assumption 4 in the previous section, the covariance matrix is diagonal and its elements do not depend upon the time: therefore, $\wp$ can be rewritten as:

$$\wp = \prod_{k,i} \frac{1}{\sqrt{2\pi}\sigma_{Mk}} e^{-\frac{1}{2}\frac{\left(x_{ki}-x_{Mki}\right)^2}{\sigma^2_{Mi}}} \Delta x_k \tag{4.14}$$

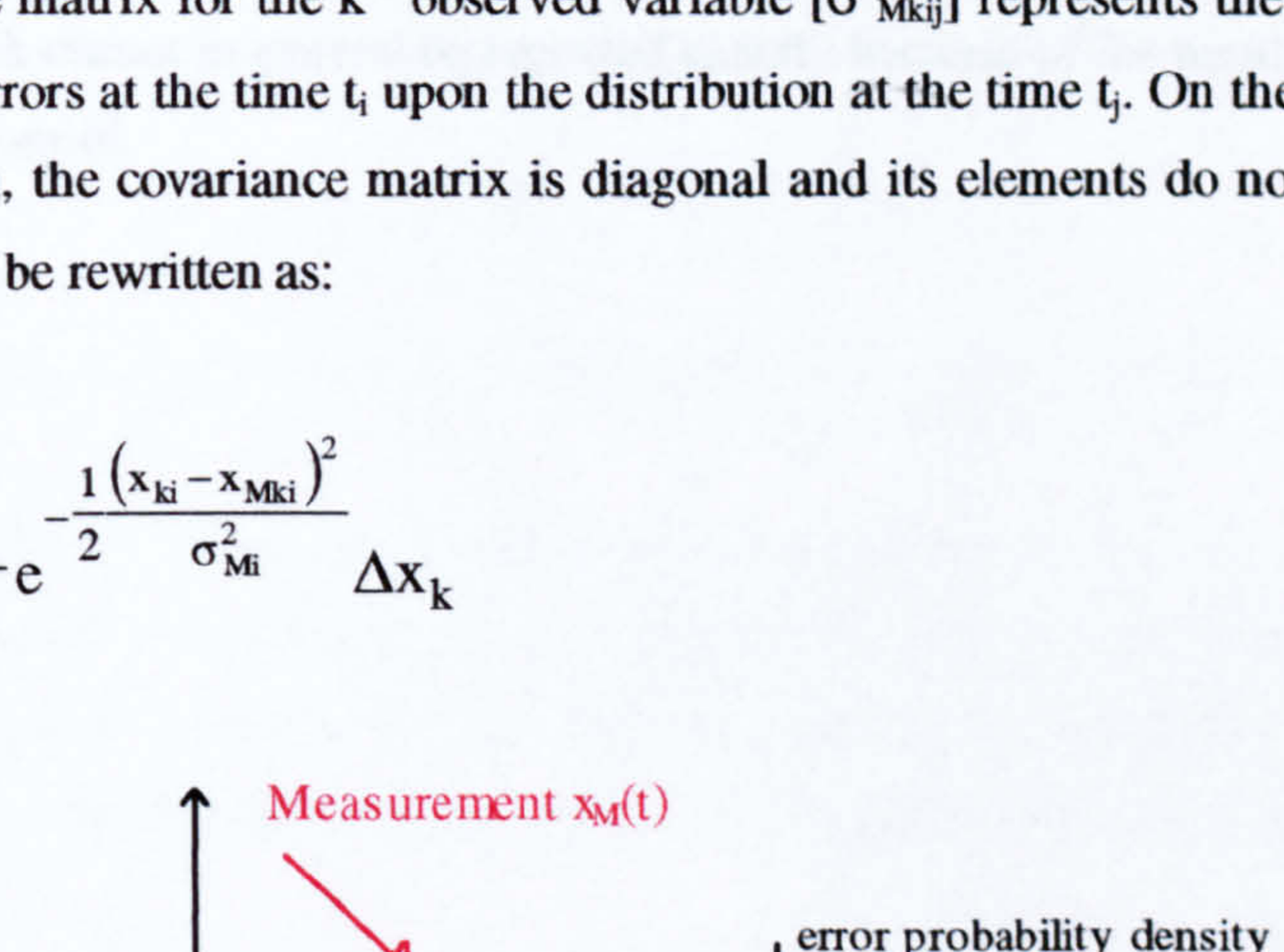


Fig. 4.2 - Distribution of measurement errors. The measured values are spread around their "true" value, ideally given by the simulation, following a gaussian distribution

Here, the term under the product sign is (approximately) the area under the normal distribution curve between the bounds $x_{Mki} \pm \Delta x_k/2$, representing the probability of getting a value within these bounds (see Fig. 4.2).

The probability $\wp$ can be maximised by minimising the sum of the exponents:

$$\chi^2 = \sum_k \frac{1}{\sigma_{Mk}^2} \sum_i \left(x_i - x_{Mki}\right)^2 \tag{4.15}$$

This expression is called *chi-square* because it follows a χ^2 distribution of order $n \cdot n_M$, which is by definition the sum of the squares of $n \cdot n_M$ normally distributed random variables with null average and unit variance (in optimisation theory parlance, this represents the *objective function* to be minimised). An iterative minimisation procedure will allow one to find the set of parameters $\{p_j^*\}$ corresponding to the minimum value $\chi^2=\chi^{2*}$. It can be shown that, at the minimum, χ^{2*} follows the chi-square distribution with $n-n_M$ degrees of freedom.

In the literature this method is often applied to the situation in which each scalar observation is the output of an experiment which gets repeated many times; in the case considered, conversely, the observations are made on a few variables at many different times during the same experiment (a JET plasma discharge), which cannot in general be repeated exactly because of the number of variables and of circumstances beyond control.

4.2.2 Inclusion of prior knowledge

In this section the statistical relevance of prior information about the parameters is discussed and the way in which it is possible to incorporate it into the likelihood maximisation procedure is described.

4.2.2.1 Bayesian inference

Bayes' theorem, published in 1763, gives an intuitive way of inferring statistical information in those cases where some knowledge is available on a random variable (the parameter p) before an experiment is done. The theorem can be stated as follows (see [66] for a concise introduction and [68] for a detailed mathematical analysis):

$$\wp(p|x) \propto \wp(x|p)\ \wp(p) \tag{4.16}$$

where x represents a generic observation depending upon the parameter p, and:

- $\wp(p|x)$ is the *posterior probability*, i.e. the probability of the value p to have occurred on the basis of the measurement x;
- $\wp(p)$ is the *prior probability*, i.e. the probability of p to occur according to pre-existing knowledge. For the sake of simplicity, this will be assumed to be normal:

$$f(p) = \frac{1}{\sqrt{2\pi}\sigma_P} e^{-\frac{(p-p_0)^2}{2\sigma_P^2}} \tag{4.17}$$

- $\wp(x|p)$ is the *likelihood distribution*, i.e. the probability of x to occur, given p;

Bayes' theorem is a general and powerful tool to keep track of the current level of knowledge during the progress of any scientific investigation (seen as a cycle of modelling, experiment and criticism) and it is very popular because of its mathematical simplicity. However, the profound meaning of prior probability has been the subject of much controversy since it is open to two major interpretations [66]:

1. The prior distribution is actually a probability density obtained from the analysis of pre-existing data or from previous instances of the same experiment. The application of the theorem is, in this case, commonly accepted.
2. The prior distribution is an educated guess expressing the subjective degree of belief of the investigator in certain values of the parameter. In this case the computed posterior distribution assumes the character of an inductive probability and, as such, is rejected by many as non-empirically verifiable.

In the following analysis both versions of the prior will be used: an initial, subjective guess of the parameters will be progressively refined, incorporating experimental evidence as the number of cases analysed grows.

4.2.2.2 Maximum a-posteriori (MAP) estimation

The incorporation of a prior distribution into the maximum-likelihood estimation method leads to the maximum a-posteriori (MAP) estimation problem. Assuming the distribution to be normal, the probability of the simultaneous occurrence of the measurements $\{x_{ki}\}$ within $\pm \Delta x_k/2$ and of the parameters $\{p_j\}$ within $\pm \Delta p_j/2$ is given by the following expression (adapted from [74]):

$$\wp = \prod_{k=1}^{n_M} \frac{e^{-\frac{1}{2}\{x_{ki}-x_{Mki}\}^T\left[\sigma^2_{Mkij}\right]^{-1}\{x_{kj}-x_{Mki}\}}}{\sqrt{2\pi}\prod_{i,j=1}^{n}\sigma_{Mkij}} \Delta x_k^n \prod_{j=1}^{M} \frac{e^{-\frac{1}{2}\{p_r-p_{r0}\}^T\left[\sigma^2_{Prs}\right]^{-1}\{p_s-p_{s0}\}}}{\sqrt{2\pi}\prod_{r,s=1}^{M}\sigma_{Prs}} \Delta p_j \qquad (4.18)$$

Assuming that the errors on the parameters, too, are uncorrelated, the maximisation of the probability is equivalent to the minimisation of the chi-square defined as:

$$\chi^2 = \sum_k \frac{1}{\sigma^2_{Mk}} \sum_i \left(x_{ki} - x_{Mki}\right)^2 + \sum_j \frac{\left(p_j - p_{j0}\right)^2}{\sigma^2_{Pj}} \qquad (4.19)$$

Intuitively, it is clear that when the parameters are known to a great degree of precision, the variances matrix σ_{Pj} will be very small and χ^2 will be dominated by the second term: the minimisation will then lead to a set of parameters very close to the $\{p_{j0}\}$. The meaning of this term is therefore to "attract" the solution so as to better accommodate the initial knowledge. Conversely, if the initial uncertainty about the values of the parameters is large, the second term is small and the minimisation procedure is equivalent to a standard least-squares fit.

4.2.3 Levenberg-Marquardt minimisation method

4.2.3.1 Formulation of the problem

The χ^2 will be, in general, a highly non linear function of the parameters via the x_k. This minimisation problem cannot therefore be solved in a single step and requires an iterative procedure in which the increment $\{\delta p_j\}$ to be applied to the current guess are recalculated at each step. The numerical algorithm chosen to solve the problem is the Levenberg-Marquardt method, an iterative procedure of widespread use in the field of non-linear minimisation problems, in a form which has been adapted mainly from [71]. In essence, the method uses a mixture of two of the most basic algorithms to minimise a multi-dimensional function: the steepest descent method and the inverse hessian (Gauss-Newton) method. Since these methods rely on the information contained in the first- and second-order derivatives of χ^2, it is convenient to write these down in full:

$$\begin{cases} \{J\}^T = \nabla\chi^2 = \left\{\dfrac{\partial\chi^2}{\partial p_j}\right\} = 2\left\{\sum_k \dfrac{1}{\sigma^2_{Mk}}\sum_i \left(x_{ki} - x_{Mki}\right)\dfrac{\partial x_{ki}}{\partial p_j} + \dfrac{p_j - p_{j0}}{\sigma^2_{Pj}}\right\} \\ [H] = \nabla^2\chi^2 = \left[\dfrac{\partial^2\chi^2}{\partial p_j \partial p_h}\right] = 2\left[\sum_k \dfrac{1}{\sigma^2_{Mk}}\sum_i \left[\dfrac{\partial x_{ki}}{\partial p_j}\dfrac{\partial x_{ki}}{\partial p_h} + \left(x_{ki} - x_{Mki}\right)\dfrac{\partial^2 x_{ki}}{\partial p_j \partial p_h}\right] + \dfrac{\delta_{jh}}{\sigma^2_{Phj}}\right] \end{cases} \tag{4.20}$$

Where the 1×M matrix J (i.e. the transpose of the gradient) is called the Jacobian, and the M×M matrix H is called the Hessian of the scalar function χ^2 (i.e. twice the curvature tensor of the hypersurface).

4.2.3.2 Steepest descent method

The crudest and most general method to minimise a function $\chi^2(p_j)$ consists simply in moving along the direction of steepest descent, given by the opposite of the gradient, until a local minimum is found (usually by means of some kind of line minimisation algorithm based on information from the first derivatives only). Although simple and general, this method is usually a poor performer and can be very inefficient when the problem is badly conditioned, that is, when the topology of the local minimum is highly non-isotropic. In most cases an accurate minimisation along the descent direction is not worthwhile and a reasonable step length can be obtained simply by dividing each component of the gradient by a damping parameter $\lambda>1$, which helps to prevent from overshooting past the minimum (at the cost, of course, of incrementing the number of iterations required):

$$\left\{\delta p_j\right\} = -\frac{1}{\lambda}\left\{\frac{\partial\chi^2}{\partial p_j}\right\} \tag{4.21}$$

4.2.3.3 Inverse Hessian method

Another approach makes a more targeted use of the information contained in the derivatives. Considering the Taylor expansion of $\chi^2(p_j)$ around an initial set of values $\{p_{j0}\}$, truncated to the second-order term:

$$\chi^2 \approx \text{const.} + \{\delta p_j\}^T \left\{\frac{\partial \chi^2}{\partial p_j}\right\} + \frac{1}{2}\{\delta p_j\}^T \left[\frac{\partial^2 \chi^2}{\partial p_j \partial p_k}\right]\{\delta p_i\} \qquad (4.22)$$

where the $\{\delta p_j\}$ represent the (small) differences respect to the current values, let us impose that all the first-order partial derivatives are null as a necessary condition for χ^2 to be minimum. By derivation, one gets then the linear system:

$$\left[\frac{\partial^2 \chi^2}{\partial p_j \partial p_k}\right]\{\delta p_j\} = \left\{-\frac{\partial \chi^2}{\partial p_k}\right\} \qquad (4.23)$$

In the vicinity of a local minimum (or, unfortunately, a maximum) the series expansion will reproduce accurately the behaviour of χ^2 and, by repeatedly replacing $\{p_{j0}\}$ with the incremented set $\{p_{j0}+\delta p_j\}$, the method will converge quadratically to the local extreme. This method is a straightforward multi-dimensional generalisation of the Newton algorithm applied to the set of first derivatives of χ^2. By comparison with the conjugate directions family of methods, which are the standard choice when information on the first derivatives only is easily available, one can see that:

— the computational efficiency is about the same;
— the inverse hessian method is much simpler to implement, plus (as shown in the next section) it matches well with the steepest descent for the purposes of the Levenberg-Marquardt method.
— the method is insensitive to the scaling of the variables, since it can easily be proven to be invariant under an arbitrary linear transformation of the $\{p_j\}$.

4.2.3.4 Levenberg-Marquardt (LM) method

It is possible to combine the two above methods in one single formula, which may simply be written:

$$\left[\frac{\partial^2 \chi^2}{\partial p_j \partial p_k} + \lambda \delta_{jk}\right]\{\delta p_k\} = \left\{-\frac{\partial \chi^2}{\partial p_j}\right\} \qquad (4.24)$$

This contains both the steepest descent method (in the limit $\lambda >> 1$) and the inverse hessian method (if $\lambda = 0$); the parameter λ is said to damp the solution obtained by means of the inverse hessian method

alone. This formulation, which in its original form is due to Levenberg [69] and Marquardt [70], is called additive and is relatively efficient for well-conditioned problems.

An alternative strategy consists in scaling the components of the steepest descent vector with the reciprocal of the absolute value of the diagonal elements in the Hessian. In this way the components are intuitively guaranteed to have a reasonable order of magnitude, independently from the scale of the variables, although the resulting direction may deviate sensibly from the steepest descent[23]. This approach is called multiplicative and leads to the following matrix equation [76]:

$$\underbrace{\left[\frac{\partial^2\chi^2}{\partial p_j \partial p_k} + \lambda\delta_{jk}\left|\frac{\partial^2\chi^2}{\partial p_j \partial p_k}\right|\right]}_{[H_D]}\left\{\delta p_j\right\} = \left\{-\frac{\partial\chi^2}{\partial p_j}\right\} \tag{4.25}$$

where δ_{jk} is the Kronecker delta and $[H_D]$ will be called the damped Hessian. As it will be explained more in detail in section 4.4.3, the purpose of the absolute value is to invert the step direction away from a maximum which may occur when a diagonal element is negative. Some authors, concentrating the attention on problems where local maxima do not exist, give a simpler definition where the absolute value is not included [73].

The damping parameter λ gives a way to switch smoothly between two kinds of behaviour:

$\lambda >> 1$	steepest descent	most suitable when far from a minimum ("global" search), when it is necessary to proceed cautiously through the non-linearity
$0 < \lambda << 1$	inverse hessian	faster convergence (~ quadratic) when close to a minimum

The idea is to start the iterations with a small value of λ (i.e. testing the hypothesis that the current guess is close to a local minimum) and to proceed:

— increasing λ by a constant boost (damping) factor β^+ when χ^2 increases (i.e. when the estimate is moving away from a minimum and the steepest descent works better)
— decreasing λ by a constant drop (or undamping) factor β^- when χ^2 decreases (i.e. when the estimate is moving towards a minimum and the inverse hessian is faster)

The Levenberg-Marquardt method with multiplicative damping is the most widely adopted and will be used for the parameter estimation procedure in the following chapters. The strategy for an optimal choice of the factors β^+ and β^- has been researched in the course of this work and is the subject of section 4.4.2.

23 If the Hessian is diagonal the damped direction is exactly the same as in the Newton method and the contribution from the steepest descent direction is neglected.

4.2.3.5 Alternative minimisation methods

Other methods, such as for example the variable metric family of algorithms, have considered as possible alternatives to the Levenberg-Marquardt algorithm. The methods reviewed are very sophisticated but they are usually much more difficult to program and still have the major drawback common to all descent methods: the inability to seek out the absolute minimum of a functions with a complex topology.

The main merits and drawbacks of the Levenberg-Marquardt method, as they emerge from the comparative analysis, can be summarised as follows:

- ✓ Works well in practice
- ✓ Easy to implement
- ✓ Gets closer to steepest descent when other methods fail
- ✓ Insensitive to the scaling of the hessian
- ✘ Slow local convergence when H is rank-deficient

Because of these advantages the Levenberg-Marquardt method is extremely popular and is employed in many routine libraries, commercial and individually developed programs. Hundreds of examples can be found in the recent literature, documenting its use in fields as disparate as image and speech recognition, neural network training and of course model and curve fitting. Note also that, in contrast with more sophisticated methods, a Levenberg-Marquardt step is considered acceptable even if it does not lead to a decrease in χ^2; this means that more steps may be needed to get to a minimum, but the greater freedom in choosing a route may lead to better solutions.

4.2.4 Statistical measure of the goodness-of-fit

The goodness of the fit obtained can be estimated by taking into account from the theory that the minimum value of χ^* is actually a random variable following the chi-square distribution for a total of :

$$n_M n + M(\text{variables}) - M(\text{degrees of restraint}) = n_M n$$

degrees of freedom. Consequently, the probability that χ^2 will exceed by chance the value χ^2_{min} is given by the incomplete Gamma function Q [71]:

$$Q\left(\frac{n_M n}{2}, \frac{\chi^2_{min}}{2}\right) = \frac{\Gamma\left(\frac{n_M n}{2}, \frac{\chi^2_{min}}{2}\right)}{\Gamma\left(\frac{n_M n}{2}\right)} \qquad (4.26)$$

The value of Q may be so interpreted:

— if Q is high enough (say, Q>0.1) then any other realisation of the measurements is likely to give an higher χ^2 when compared to the model found and, therefore, it is believable that the values found for our parameters are really optimal;

— if Q is low enough (say, Q<0.001) then any other randomly chosen set of measurements would have given as "good" a fit as we actually got, and this means that the fit is not good at all and, probably, the underlying model and/or the procedure are wrong.

— if Q assumes intermediate values it might mean that the measurement errors are either non-normally distributed or underestimated; further investigation is then recommended.

The condition Q≈1 should not to be mistaken for a small residual. A fit which is good in the statistical sense may also occur when the model does not match the data at all: in this case Q≈1 simply means that the solution $\{p_j^*\}$ has a high likelihood to be the one for which the fit is anyway the best possible.

Another important indicator of the quality of the fitness achieved is the relative error, which can be defined by either an average or a maximum value (assuming the measurement is not identically null):

$$\varepsilon_{avg} = \frac{\sum_i \left| x_i - x_{Mi} \right|}{x_{M,\max} - x_{M,\min}} \qquad \varepsilon_{\max} = \frac{\max_i \left| x_i - x_{Mi} \right|}{x_{M,\max} - x_{M,\min}} \tag{4.27}$$

These quantities, which are perhaps more intuitive than either Q or the χ^2, give a clear percentage indication of the correspondence between simulation and measurement.

It is anyway important to keep in mind that, however good is the fit, in general data can only disprove, never prove conclusively that a model is true [74].

4.2.5 Variance of the estimated parameters

The covariance matrix of the estimated parameters at the minimum of χ^2 expresses the level of uncertainty in their values and, if this is lower than the initial one, it serves then to quantify the improvement in our knowledge.

4.2.5.1 Variance matrix

Considering for simplicity the case with one measurement only (n_M=1), the variance matrix can be written down by virtue of the propagation of the errors through the functions $p_j(x_i)$ in the following form, adapted from [74]:

$$\left[\sigma^2_{Pj,k}\right] = \sigma^2_M \left[\sum_i \frac{\partial p_j}{\partial x_i}\frac{\partial p_k}{\partial x_i}\right] = \sigma^2_M \sum_i \left\{\frac{\partial p_i}{\partial x_i}\right\}\left\{\frac{\partial p_k}{\partial x_i}\right\}^T \tag{4.28}$$

By differentiating (4.23) (which holds exactly at the minimum) one gets:

$$\left[\frac{\partial^2 \chi^2}{\partial p_j \partial p_k}\right]\left\{\frac{\partial p_j}{\partial x_i}\right\} = \frac{1}{\sigma_M^2}\left\{\frac{\partial x_i}{\partial p_j}\right\} \tag{4.29}$$

and, by substitution into (4.28) (taking into account the symmetry of the hessian):

$$\left[\sigma_{Pj,k}^2\right] = \sigma_M^2 \sum_i \frac{\left[\frac{\partial^2 \chi^2}{\partial p_j \partial p_k}\right]^{-1}}{\sigma_M^2}\left\{\frac{\partial x_i}{\partial p_j}\right\}\left\{\frac{\partial x_i}{\partial p_j}\right\}^T \frac{\left[\frac{\partial^2 \chi^2}{\partial p_j \partial p_k}\right]^{-1}}{\sigma_M^2} \tag{4.30}$$

From this, substituting one more time and neglecting the second derivatives, one has that:

$$\left[\sigma_P^2\right] = \frac{1}{4}\left[\frac{1}{2}\frac{\partial^2 \chi^2}{\partial p_j \partial p_k}\right]^{-1}\left\{[I_M] - \left[\sigma_{P0}^2\right]^{-1}\left[\frac{1}{2}\frac{\partial^2 \chi^2}{\partial p_j \partial p_k}\right]^{-1}\right\} \tag{4.31}$$

In case of no prior knowledge of the values of the parameters, the inverse of the matrix $[\sigma^2_P]$ vanishes and the final variance matrix is simply given by the inverse of the hessian.

4.2.5.2 Confidence intervals for the estimated parameters

Intervals of confidence for each single parameter, which express the level of uncertainty in a more intuitive form, can be derived directly from the variance matrix. While a rigorous approach would require to build the M-dimensional ellipsoid describing the boundary of the wanted confidence region when all the parameters at once are allowed to change ($\{dP\}^T[H_{min}]\ \{dP\} \leq 2\varepsilon$ [74]) , working out the confidence intervals for each parameter on its own is much simpler but equally useful. This means to find the interval $\pm\Delta p_k$ that includes all the values of p_k that could occur by chance with a given probability c (that is, the confidence). The width of this interval depends only upon the corresponding principal components in the covariance matrix can be simply written down as [76, 77]:

$$\pm \Delta p_k = \pm \eta \sqrt{\sigma_{Pkk}^2} \qquad \left(\text{with } c = \mathrm{Erf}\left(\frac{\eta}{\sqrt{2}}\right) = \frac{2}{\pi}\int_0^{\frac{\eta}{\sqrt{2}}} e^{-t^2} dt\right) \tag{4.32}$$

Typically, the interval with confidence c=95.4% will correspond to a width η=2 times the standard deviation, which in this case is simply given by the square root of the terms on the diagonal of $[\sigma^2_P]$.

It is necessary to stress the importance of this value in order to quantify the actual improvement in our knowledge gained with the estimation procedure. A large Δp_k means actually that any other choice of the parameter within a wide interval would have produced as good a fit and, therefore, the final value of the parameter has not much meaning. The sensitivity of χ^2 to variations in any parameter, at the minimum, is

intuitively connected to the M-dimensional "curvature" of the function, that is the inverse of the hessian, consistently with the formula for $[\sigma^2_{Pjk}]$ when the prior knowledge is negligible.

4.3 Preliminary analysis

This section explains the techniques adopted to prepare the data to be submitted to the parameter estimation algorithm. Sections 4.3.1 and 4.3.2 are concerned with the general issue of choosing the best possible initial guess for the parameters $\{p_{j0}\}$, while in section 4.3.3 a possible approach to analyse the noise component and to estimate measurements variances is discussed. From the viewpoint of the parameter estimation procedure all these techniques represent alternative expressions of the underlying theme of this work, i.e. the best possible use of prior knowledge, which is also discussed in section 4.5.

4.3.1 Global minimum search

This section lists briefly the most general methods which may be used to find an optimal choice for the $\{p_{j0}\}$ and which have been incorporated in the present work. The selection of a good starting point, in general, is found to have only a marginal effect on the performance of the algorithm in finding a particular minimum, although it has often an enormous impact in determining which minimum is reached (or if a minimum is reached at all). In cases such as the present, where many local minima are likely to exist, it is therefore very important to start from an initial guess which is as close as possible to the global minimum.

Trial and error - This is the crudest method of all, consisting simply in starting from the average of the prior distributions and changing manually the values of the parameters with the aid of the plot of the estimated model output against the experimental data, possibly augmented by information on the gradient and Hessian. Even if unsophisticated, this way of proceeding is surprisingly effective and gives the analyst a "feel" for the sensitivity of the model which cannot be obtained otherwise.

Grid scan - This is another rudimentary method which can be also used as a foolproof backup in case should more refined procedures fail. Bounds are fixed for each one of the M parameters and all intervals are divided in an equal number of n_{GS} steps (uniformly or logarithmically spaced), which are then scanned in sequence. The lowest χ^2 obtained represents of course the desired result, which can be used as the starting point for a subsequent LM search. The main drawback of this brute force approach is that the number of steps required is n_{GS}^{M}, which becomes rapidly intractable in typical cases with M>5~6.

Random search - In case of sampling problems with high dimensionality (like, typically, multiple integrations) the systematic scan can be conveniently replaced by a Monte Carlo-type search, in which successive random points are tried until a satisfactory low value of χ^2 is found. In the present implementation, a pseudo-random number generator supplies

initially a uniformly distributed variable θ with $0 \le \theta \le 1$. The random values have to be mapped to the $\{p_k\}$, which in accord with the Bayesian viewpoint are normally distributed with variances σ_{pk} around some initial guesses p_{k0} (see 2.). The formula for the mapping $\theta(p_k)$ can be derived considering that the slope of the curve $d\theta/dp_k$ must be equal to the density $f(p_k)$, since this corresponds to the original uniform distribution being "stretched" to cover most densely the regions where p_k is more likely. Therefore one will have:

$$\theta(p_k) = \int_{-\infty}^{p_k} f(p_k)\,dp_k = \frac{\operatorname{erf}\left(\frac{p_k - p_{k0}}{2\sigma_{pk}}\right) + 1}{2} \tag{4.33}$$

which, being monotonic, may be easily inverted numerically to give $p_k(\theta)$.

4.3.2 Measurement analysis

This section explains the signal processing techniques that have been applied to estimate the initial values of some of the parameters in the models. By contrast to the methods discussed in section 4.3.1, which are perfectly general, the techniques listed here are based on physical insight into the nature of the system and are specifically targeted to waveforms characterised by an initial quiescent phase interrupted by a rapid transient and followed by a vanishing oscillation with one predominant frequency component[24].

It should be noted that whenever more than one measurements are being fitted simultaneously with the same model, these preliminary estimates should be extracted from each of them and then averaged. In this case, their agreement (or lack of) can be used to validate (or disprove) the underlying model and to get more accurate final estimates. The following kinds of information have been considered:

4.3.2.1 Frequency

The analysis of the frequency of the oscillatory signals is an essential first step in the identification of the underlying physical model and in the estimation of the stiffness/mass ratio of the involved eigenmodes. Some crude manual techniques used in the past to provide this estimate, such as simply measuring the interval between consecutive peaks, may be deceptive especially when two frequencies are superimposed (as may be in the case of the sideways motion). Therefore, two well-established methods of frequency analysis have been implemented, based on the following integral transforms:

Fourier spectrum The power spectrum of a signal x(t), defined as $S(f)=|\Im[x(t)]|^2$, contains the information on the amplitudes of the sinusoidal components of x(t) as a function of the frequency, (neglecting the information on their phase) [92]. Typically, if x(t) represents the free response of a system to an impulsive excitation, the peaks in S(f) will reveal the number and the frequencies of the excited eigenmodes. All local

maxima in S(f) can be trivially found and then, assuming that the overall shape of the frequency distribution is approximately known, the irrelevant peaks in the high-frequency range (due to noise) can be discarded while the peaks in the region of interest (~2 to 20 Hz) will be retained.

The Fourier transform here is calculated by means of the FFT algorithm, utilising a base-2 computer routine taken from [71] which assumes that the samples are right-padded with zeroes up to next integer power of 2. The discrete version of the Fourier transform has a few pitfalls which have been circumvented here by simply preconditioning x(t) [90].

- the trend of x(t) (i.e. the straight line passing by the first and last sample) has been subtracted in order to minimise the spurious peak corresponding to $f_0=1/T$, where $T=n\tau_s$ is the total sampling time;
- the mean of x(t) has also been subtracted in order to remove the spurious peak at f=0, corresponding to the steady-state component of x(t);
- x(t) has been Hanning-windowed in order to reduce the so-called leakage effect.

Hilbert transform The Hilbert transform, defined by the convolution (t)=x(t)*1/πt, is a powerful tool used especially in the context of modulated signals analysis [92][25]. Considering the complex signal defined as ζ(t)=x(t)+ i (t), it is possible to show that the Hilbert transformation simply rotates the phase of each sinusoidal component of x by 90°. It is therefore possible to define instantaneous values for the amplitude, phase and frequency of ζ(t) as [93]:

$$\begin{cases} A_I(t) = \sqrt{x^2(t) + \cdot^2(t)} \\ \varphi_I(t) = \tan^{-1}\dfrac{\cdot(t)}{x(t)} \end{cases} \quad \Rightarrow \quad f_I(t) = \frac{\partial \varphi_I}{\partial t} \tag{4.34}$$

The value of $f_I(t)$ computed in this way will practically coincide with the actual oscillation frequency in case of a mono-component signal, while in the general case the interpretation is less clear-cut. The potential advantage of this technique lies in the capability to reveal the variation of frequency with time linked to the non-linear character of the system.

On the practical side, since the inverse tangent in (4.34) is defined between ±π, $f_I(t)$ will be discontinuous each time that a cycle of oscillation is completed and this will show up as a large spike masking the underlying trend in the computed data. The rigorous treatment of this problem would require to unwrap the phase of $\varphi_I(t)$, which

---

24 This kind of shape is the natural output of a stable second-order system excited by an impulsive input and, therefore, the "specialisation" of these techniques retains a scope which is indeed vast.

25 Incidentally, the Hilbert transform of a Gaussian is also known in plasma physics as the dispersion function Z(ζ). Z(ζ) appears, for instance, in the expression of the dispersion tensor relating wavenumber and oscillating frequency in the context of linearized theory of kinetic waves [84].

would add considerable complexity to the algorithm. As an alternative, simple smoothing of $f_l(t)$ with the method outlined in 4.3.3.2 has been implemented.

Once an estimate for the frequency f of a signal has been obtained, since the spring ratios k in the models may be considered known in advance, the relative masses may be readily estimated from:.

$$m=4\pi^2 f^2 k \tag{4.35}$$

4.3.2.2 Damping ratio

The non-dimensional critical damping ratio ξ, which is defined in the single d.o.f. case by the formula:

$$\xi = \frac{b}{4\pi fm} \tag{4.36}$$

affects mainly the long-term system response to transient loads. Since the damping coefficient in the vessel models may be a function of the velocity, different estimated values will refer to different parts of the response. In particular:

Transient peak: The damping coefficient at the first peak in the transient response, i.e. during the high-velocity phase, may be determined by means of a simple method involving four characteristic points in the x(t) curve [94]. The value thus obtained may be used to assign the high-speed coefficient b` in the parabolic damper characteristic (see 3.1.1.4).

Decay phase: The damping coefficient during the final and more uniform decay phase can be calculated from the logarithmic ratio $\xi=1/2\pi\ln(x_{peak+1}/x_{peak})$, averaged over the last 3 or 4 oscillations. This value may be used to fix the low-speed coefficient b_0 of the characteristic.

The damping coefficient can be calculated as a function of the damping ratio and of the stiffness, which usually is the best known parameter, by eliminating the mass in (4.36):

$$b = \frac{k\xi}{\pi f} \tag{4.37}$$

4.3.2.3 Force pulse start time

The start time t_0 for the force pulse is a critical parameter since an incorrect initial value may cause the simulated response to fit the measurement with a phase error given by an integer number of full cycles, corresponding to a local minimum of χ^2. The heuristic method which has been implemented in order to estimate t_0 may be summarised in the following steps:

1) define x_{SS} as the steady-state value of x(t) in the initial, quiescent phase
2) detect the first peak in x(t) larger than a significant fraction of the whole spanned range (say, 30%)
3) track x(t) backwards from there until the value x_{SS} is crossed.

There are many instances, however, where the initial transient is heavily corrupted by noise or confused by small oscillations which cannot be easily interpreted as the result of a single impulse of excitation (see for example JET pulse 37628 in chapter 5). In these cases it has been found useful to supplement the method with information from measurements more intimately connected with the physical force generation mechanism, such as:

Disruption time: The time of the energy quench measured and stored in the JPF database.

Plasma current: Since plasma current decay is one of the main causes for vessel force, the time t_{IP0} at which this starts may give a good indication of t_0. As the decay usually proceeds smoothly from an initial stationary phase, t_{IP0} can be estimated fairly precisely by the time of peak of the second derivative of $I_{PLA}(t)$.

Plasma position: Similarly, the time of departure of the vertical plasma position from its original equilibrium configuration can be estimated from the time of peak of the second derivative of z_{PLA}.

4.3.2.4 Analysis by sub-modelling

There are many practical cases where the analysis techniques listed above do not provide easily clear-cut results; e.g. the frequency analysis of sideways motion signals does not show a clearly defined peak from which the oscillating frequency can be estimated (see section 3.2.1.1).

Simplified models able to simulate just a few features of the signal to be analysed have proved, in these cases, to be a very satisfactory alternative way of proceeding. For instance, consider the following minimal model:

$$\begin{cases} \ddot{x} + 2\xi\Omega\dot{x} + \Omega^2 x = 0 \\ \dot{x}(0) = \dot{x}_0, \quad x(0) = 0 \end{cases} \tag{4.38}$$

corresponding to the well-known solution:

$$x(t) = \frac{\dot{x}_0}{\sqrt{1-\xi^2}\Omega} e^{-\xi\Omega t} \sin\sqrt{1-\xi^2}\Omega t \tag{4.39}$$

representing in non-dimensional form the response of a second-order system to an impulsive input. By fitting the output of this model to the measurement, using the techniques described in this chapter, estimates of the critical damping ratio and of the oscillating frequency $\Omega/2\pi$ can be readily obtained, even

if the fit will be in general bad (otherwise, the problem would be already solved !). This technique, which may be seen as a complement to the more traditional signal analysis tools, is a particular case of the progressive modelling concept described in section 4.5.4.3.

4.3.3 Noise analysis and removal

In this section the analysis carried out on the measured signals in order to estimate the noise level and the associated measurement variances (i.e. the matrix $[\sigma_M]$) is explained.

4.3.3.1 Noise modelling

Working under the assumption of additive noise discussed at 4.2.1.2, three major noise sources can be singled out as the ones most affecting JET signals:

- *Finite accuracy of the sensor:* this is supplied by the manufacturer and is usually a very small fraction of the full range.
- *Quantization noise*: this is equal to a fraction 2^{-b+1}=.016% of the analog-digital converter (ADC) range, where b=16 is the number of bits used. This may be very clearly noticeable for low amplitude signals.
- *Electrical noise:* this is due to the combination of the e.m. field fluctuations during the disruption (which generates induced currents and sparks all over the machine) plus the noise in the modulation/demodulation process (see section 1.1.2). This is the dominant component, which is usually a few percent of displacement signals but can be as high as 20~30% in strain gage signals.

A technique based on the concept of optimal (Wiener) filtering has been adapted in order to estimate the total amount of noise in a specific signal. Optimal filtering is based on the hypothesis that it is possible to isolate approximately the contribution of noise in the Fourier spectrum of a signal, $\Im(f)=\Im[x(t)]$. Assuming, for instance, that the contribution of the signal is negligible above a certain cutoff frequency f_C, it is possible to define a simple affine noise model in the frequency domain as:

$$N(f)=N_0+N_{/f}f \tag{4.40}$$

where the constants N_0 and $N_{/f}$ are determined by a least-squares fit to the spectrum $\Im(f)$ for $f\geq f_C$ (and N_0 therefore represents an extrapolation of the noise model in the low frequency range). The optimal filter may be defined by the real-valued function [71]:

$$\Phi(f)=\frac{|\Im(f)|^2}{|\Im(f)|^2+|N(f)|^2} \tag{4.41}$$

and the corresponding optimal estimate of the signal will be given by $\Im^{-1}[\Im(f)/\Phi(f)]$, which is very close to the original signal where the noise level is low. From (4.41) one can see that first-order differences in the noise model produce second-order effects in the filtered result; therefore, the precise

choice of model is not critical. The estimated noise signal in the time domain may now be derived by subtraction:

$$\eta(t) = x(t) - \Im^{-1}\left[\frac{\Im[f]}{\Phi(f)}\right] = \tag{4.42}$$

In order to extract the required information from $\eta(t)$ it is necessary to move on to the amplitude domain by calculating the amplitude density α_D [95]:

$$\alpha_D(\eta) = \frac{1}{n}\frac{dn}{d\eta} \approx \frac{1}{n}\frac{\Delta n|_{\eta}^{\eta+\Delta\eta}}{\Delta\eta} \tag{4.43}$$

where n is the total number of samples, dn is the number of samples falling between n and $n+dn$, and the rightmost side represents the discrete approximation to the distribution (depending on the choice of the bin width $\Delta\eta$). The analysis of the similarity of $\alpha_D(\eta)$ to a normal distribution with zero average may be seen as a test on the randomness on the estimated noise; indeed, should α_D be much different, that would indicate that the noise model is wrong. On the contrary, the variance of α_D represents the wanted estimate of error magnitude and one can assume $\sigma_M=\sigma_{\alpha_D}$.

4.3.3.2 Data smoothing

In some cases the data can be so noisy as to need to be smoothed prior to be submitted to the parameter estimation procedure. Typically, in JET, this is true for strain gage signals Data smoothing should always be applied very cautiously since it makes it is easy either to erase important features or to introduce spurious effects in the signals. The following are the options considered:

Filtering - It is possible to clean up the signal by simply removing the high frequency components from the Fourier spectrum before transforming back to the time domain. In a slightly more sophisticated way, it is also possible to replace the signal with the optimally filtered version calculated in 4.3.3.1. In either case, the calculated measurement variances are not longer valid and smaller values (which are also more difficult to find rigorously) should be used. Some sort of windowing of the signal (e.g. with the Hanning function [92]) should be used in order to minimise leakage effects which may generate spurious ringing in the tails. These, in turn, may affect adversely the parameter estimation procedure unless they are removed from the signal.

Moving average - The easiest and, perhaps, most intuitive way to smooth a stream of sampled data consists in replacing each data point with the average of its neighbours. More generally, the following moving weighted average can be implemented:

$$x_{\text{filtered},i} = \sum_{j=-N}^{N} \omega_j x_{i+j} \qquad (4.44)$$

This formula, equivalent to the discrete convolution of x(t) with a window function $\omega(t)$, represents a non-recursive digital filter where the Fourier transform of $\omega(t)$ is the transfer function of the filter [91]. In the case of rectangular window, which corresponds to the arithmetic average when the weights are normalised to $\omega_j=(2N+1)^{-1}$, the transfer function becomes $H(f)=\tau\sin(\pi f\tau)/\pi f\tau$ (where $\tau=2N\tau_s$) and the nominal cutoff frequency is $f_c\approx 1/2\tau$. This kind of filter has two major drawbacks:

1) the transfer function is of very poor quality since it is characterised by a narrow central peak and large oscillating side lobes;
2) since $H(f)\in\Re$, the phase information in the signal is destroyed and the shape of filtered signal might be severely distorted

Although better results can be obtained by means of more sophisticated window shapes, in order to overcome 2) it would be necessary to use more complicated recursive filters, which make use of previously computed values of the filtered variable. Therefore, since the performance of the FFT based filter is anyway far superior, just the basic rectangular- and triangular-window moving average has been implemented for those cases where a quick-and-dirty result is sufficient (and also for consistency with other software available at JET).

De-spiking - Disruption measurements in JET are often characterised by spikes, i.e. sharp noise bursts which typically last for less than 1~2 ms and therefore interest at most a few consecutive samples. Spikes may be explained considering the huge amount of e.m. energy emitted during disruptions, which shows up as wide-band RF noise and may lead to induced voltages and arching all over the machine (see also section 1.1.2.1). By the naked eye, they can be recognised easily as events extraneous to the underlying signal. In contrast to what has been said about continuous noise, spikes should by all means be removed from the measurements since they violate grossly the assumption of normally distributed errors and, consequently, can alter sensibly the results of the parameter estimation procedure. For example, a large spike occurring on the first maximum of the oscillatory rolling motion response will fool the procedure into overestimating the magnitude of the force and will lead to a result inconsistent with the rest of the transient. De-spiking has been obtained by reformulating the moving average algorithm as follows. Initially, the average of the signal over a rectangular-weighed window is computed:

$$x_{\text{avg},i} = \frac{1}{2N+1} \sum_{j=-N}^{N} x_{i+j} \qquad (4.45)$$

where ε_{SPIKE} simply represents a user-selected tolerance over the whole signal range ($x_{MAX} - x_{MIN}$). An updated average $x^*_{avg,i}$, representing the guessed smoothed local value of the signal, can be therefore worked out these points. A further level of refinement can be obtained by defining another average $x^{**}_{avg,i}$, where the excluded points are those whose distance from the first guess exceeds the tolerance:

$$x^{**}_{avg,i} = \frac{1}{N`} \sum_{j=-N}^{N} x_{i+j}, \quad j: \left| x_{i+j} - x^{*}_{avg,i} \right| \leq \varepsilon_{SPIKE} \left(x_{MAX} - x_{MIN} \right) \tag{4.47}$$

where N` is the number of regular data points satisfying the last condition. Although this method is very crude and is justified only heuristically, reasonable choices of N and ε_{SPIKE} give usually an acceptable performance (an example of application has been given in 5.1.1).

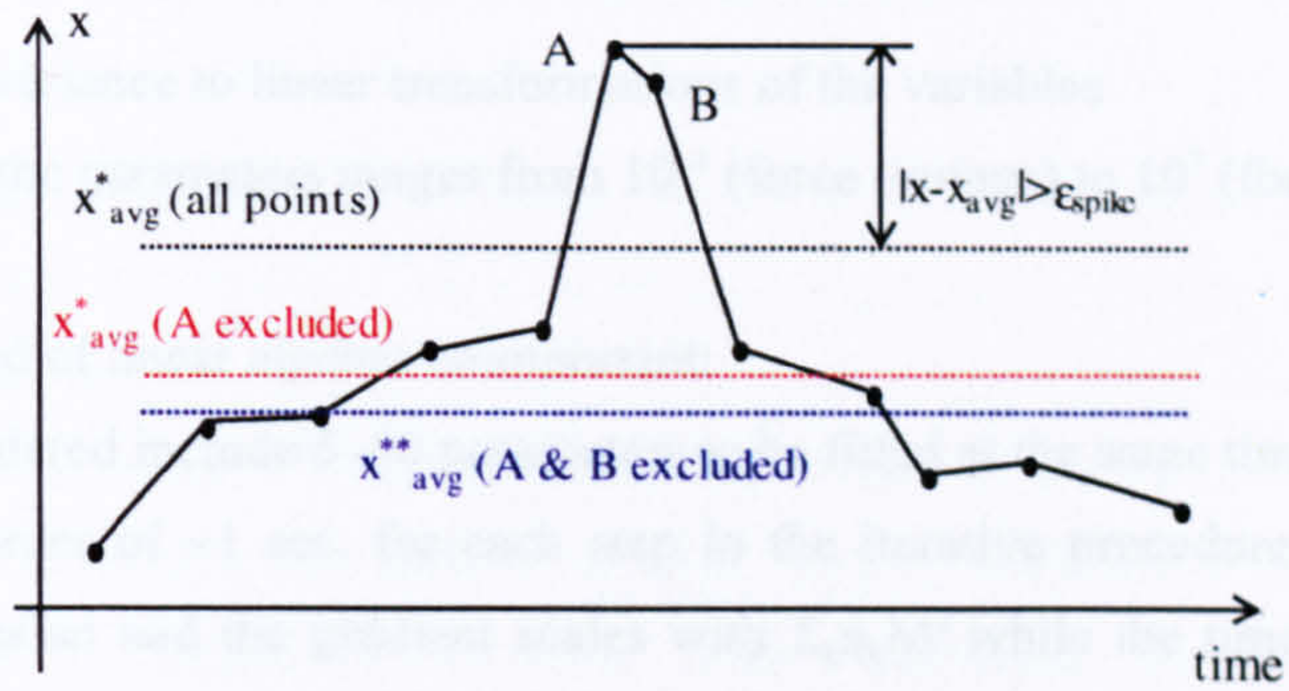


Figure 4.3 - De-spiking algorithm

4.4 Implementation of the iterative Levenberg-Marquardt minimisation algorithm

This section explains in detail the modifications and extensions made to the Levenberg-Marquardt algorithm in order to get a numerical implementation better suited for the current problem. In order to guide the strategic and algorithmic decisions taken below, it is useful to list the principal characteristic of the problem under investigation along with the requirements they impose to the algorithm:

- *Complex topology of the objective function* $\chi^2 \Rightarrow$ flexibility

  The χ^2 may be strongly non-linear with many local maxima, minima and discontinuities. The very sinusoidal shape of the waveform to be fitted, for instance, determines local minima when the model's output and the measurement have a phase shift $2k\pi$ (k integer), or maxima if the shift is $(2k+1)\pi$. Possible discontinuity of the first derivatives, in addition, represents a formidable challenge for the minimisation algorithm (see section 4.4.2).

- *Bad parameter scaling* $\Rightarrow$ invariance to linear transformations of the variables

  The order of magnitude of the parameters ranges from 10^{-3} (force timings) to 10^{7} (force)

- *Small dimensionality* $\Rightarrow$ speed of linear algebra unimportant;

  Typically the models considered include 5~50 parameters to be fitted at the same time, resulting in total running times of the order of ~1 sec. for each step in the iterative procedure. As the time required to evaluate the Hessian and the gradient scales with $\Sigma_k n_k M^2$ while the time for complex linear algebra operations (like SVD decomposition or eigenvalues extraction) scales typically with M^3, small values of M make it feasible to use relatively advanced techniques which may otherwise be considered too expensive.

- *Fast evaluation of objective function* $\Rightarrow$ no global speed constraints ;

  Each evaluation of the objective function $\chi^2(p_j)$ requires integration of the dynamic system and summation of the residuals, which altogether take typically <<1 second on a standard PC. This means that numerical evaluation of the derivatives is feasible.

- *Moderate amount of data* $\Rightarrow$ memory requirements unimportant;

  Not more than 30~40 measured signals need to be stored at the same for the parameter estimation of a JET pulse, requiring just a few MB of RAM.

4.4.1 Numerical calculation of the derivatives

In this section the problem of the finite-difference calculation of the first and second-order derivatives in the gradient and in the Hessian is considered and some improvements to the suggestions found in the literature are proposed.

The correct choice of the parameter increments Δp_k is surprisingly important. In the context of the algorithms described below, this is equivalent to an optimal setting of the various non-dimensional tolerances. Extensive tests on JET and test models have shown that, more than all other parameters in the algorithm (with the possible exception of the damping factors, see), for difficult problems the right Δp_ks may make the difference between rapid success or utter failure. Unfortunately, the selection strategy appears to very problem-dependent; smooth objective functions derived from analytic formulæ seem to require increments at the limit of the cancellation error to perform well, while real-world cases including measurement noise often fail unless the increments are relatively large. Therefore, understanding of the underlying theory is essential on the analyst's part.

4.4.1.1 Parameter increments for first-order forward differences

The most accurate way of calculating the derivatives $\partial x_i/\partial p_k$ appearing in the expression of the gradient and the Hessian would be simply to evaluate their analytical expressions, which in theory are straightforward to obtain. However, this would require the user to work out and input NM functions for the gradient and NM^2 for the Hessian, which is quite impractical for models of the size considered in this study. Following the advice of practically all authors on this subject, derivatives can usually be approximated with good results by means of one-sided finite differences, which are obtained incrementing one parameter at a time and which, in the first-order case, can be written as:

$$\frac{\partial \chi^2}{\partial p_k} = \frac{\chi^2(p_j + \delta_{jk}\Delta p_k) - \chi^2(p_j)}{\Delta p_k} \tag{4.48}$$

The choice of the increment size Δp_k to apply to each parameter is crucial in order to obtain a meaningful result. By writing the Taylor expansion of $x(p_k)$ it can be shown that the error in the calculation is bounded by [74]:

$$\varepsilon_{max} = \frac{2\varepsilon_{\chi^2}|\chi^2|}{\Delta p_k} + \frac{1}{2}\left|\frac{\partial^2 \chi^2}{\partial p_k^2}\right|\Delta p_k \tag{4.49}$$

where $\varepsilon_{\chi 2}$ is the relative error expected in the evaluation of the function χ^2, the first term in the sum represents the increasing roundoff as the increment gets smaller and the second term is the truncation error. Minimisation of this expression leads to:

$$\Delta p_k = 2\sqrt{\varepsilon_{\chi^2}\left|\chi^2\right|\left|\frac{\partial^2\chi^2}{\partial p_k^2}\right|^{-1}} \tag{4.50}$$

Some modifications have been made to this basic formula, on the basis of some general suggestions made in [75].

- The relative error $\varepsilon_{\chi 2}$ can be expected to be the same as the machine precision $\varepsilon_M=2^{-b}\approx 2.2\cdot 10^{-16}$ (where b=52 is the number of binary digits in the mantissa of an IEEE double-precision floating-point variable, which is the standard in current computers) only when χ^2 is obtained from a straightforward mathematical expression. Actually, $\varepsilon_{\chi 2}$ will be much greater than that when the function to be differentiated is obtained from a complex or iterative procedure. In the present case, the main source of error is the sequence of the Runge-Kutta steps in the dynamic system integration and, therefore, it may be assumed that the error at the i-th step accumulates from previous steps and $\varepsilon_{\chi 2i}=ik_\varepsilon\varepsilon_M$, where k_ε is a proportionality coefficient depending on the precision used in the adaptive Runge-Kutta integration which has to be determined empirically (values of the order 10^5~10^6 provide good results with large models, while values of order 1 work satisfactorily when the objective function is given in symbolic form). Since the integration is repeated only once for each incremented parameter, an average value $\varepsilon_{\chi 2}=\frac{1}{2}nk_\varepsilon\varepsilon_M$ will be used where n is the total number of integration steps.
- Errors in the estimated Hessian, which is inherently more inaccurate than the gradient, can easily generate unreasonable values for the increments Δp_k. It is therefore essential to put safety bounds on the computed values, which may be expressed as fractions of a "typical" value defined as:

$$p_{k,TYPICAL}=max\{p_k\,,\ \eta(p_{k,MAX}-p_{k,MIN})\} \tag{4.51}$$

with, for example:

$$10^{-8}\,p_{k,TYPICAL} \le \Delta p_k \le 10^{-2}\,p_{k,TYPICAL} \tag{4.52}$$

Where, for example, $\eta=0.05$. The definition of $p_{k,TYPICAL}$ takes into account the eventuality that $p_k\approx 0$, while the actual fractions used are just reasonable numbers which have been tested to work. Additionally, another constraint has to be enforced:

$$p_{k,MIN} \le p_k + \Delta p_k \le p_{k,MAX} \tag{4.53}$$

to ensure that the incremented parameter will not exceed the overall bounds (in most cases, when this occurs it will be sufficient to reverse the sign of the increment).

- When $\chi^2\approx 0$, (4.50) obviously fails. It is therefore necessary to provide additional safety bounds also for the value of the function to be derived, for example in terms of the range of the function.

The principle guiding these choices is that it is always preferable to overestimate Δp_k rather than underestimate it, because the error given by (4.49) clearly grows much more rapidly when Δp_k is lower than the optimum. Moreover, the truncation error can be expected to become less and less as the

iterations progress towards the minimum, whereas the roundoff error is always waiting to happen as soon as the increment becomes too small. Therefore, this is the definition used for the increment Δp_k:

$$\Delta p_k = 2\sqrt{k_\varepsilon \frac{n}{2}\varepsilon_M \max\left(\left|\chi^2\right|, \left|\chi^2{}_{MAX} - \chi^2{}_{MIN}\right|\right)\left|\frac{\partial^2\chi^2}{\partial p_k^2}\right|^{-1}} \tag{4.54}$$

Of course, this formula implies that at the beginning of every iteration an estimate for the Hessian is already available, which in turn would require the increments to be already fixed. Two courses of action can be envisaged:

I) Starting from an initial guess for the $\{\Delta p_k\}$, for each new position in parameter space a nested cycle of iterations is started in which derivatives and increments are progressively updated and refined. This alternative is tremendously expensive and can hardly be justified.

II) An initial guess is used for the first step, while the increments for the next ones are calculated on the basis of the Hessian at the preceding step. The error committed in doing so tends to vanish when the iterations converge to the minimum and the distance between consecutive points becomes smaller and smaller. The initial guess has to be selected carefully, since unreasonable values may cause failure of the whole algorithm.

Alternative II) is the obvious choice, and the initial guesses can be taken as reasonably small fractions of the range of each parameter.

4.4.1.2 Centred differences

The well-known centred formula for finite differences can be written as:

$$\frac{\partial\chi^2}{\partial p_k} = \frac{\chi^2(p_j + \delta_{jk}\Delta p_k) - \chi^2(p_j - \delta_{jk}\Delta p_k)}{2\Delta p_k} \tag{4.55}$$

This provides, at the cost of doubling the number of evaluations of χ^2, a truncation error that scales as $1/\Delta p_k{}^2$ and, therefore, allows a larger Δp_k to be used near the minimum where the gradient vanishes and the roundoff error tends to dominate [83]. In most cases the minimisation procedure appears to work well with one-sided differences, although the option of using centred ones has been found to be essential to recover from badly behaved objective functions. The possibility to switch automatically to central differences towards the latest steps of the minimisation has also been included, so as to obtain better precision in the solution at a minimal cost. An approximate switching criterion has been used, based on the comparison between the absolute value of the difference and an appropriate multiple of the machine accuracy:

$$\max_{k}\left\{\left|\chi^2(p_j+\delta_{jk}\Delta p_k)-\chi^2(p_j)\right|\right\}\le k_{TOL}\varepsilon_{\chi^2} \quad \Rightarrow \quad \text{use centred differences at next step} \tag{4.56}$$

Here, the value $k_{TOL}>1$ has to be chosen empirically as a safeguard against letting the calculation being swamped by roundoff error. The maximum (in magnitude) of the components of the gradient has been considered as an indicator of the closeness of the solution, since as long as any one of them remains significantly greater than zero, the real minimum cannot have been reached.

4.4.1.3 Inclusion of the second-order derivatives

The possibility to include in the hessian the term containing the second derivatives has been included in the program, although the choice is left to user and no attempt at doing it automatically is considered[26]. The standard practice is to omit it [71], considering that:

— the calculation is computationally very expensive ($\propto M^{\text{order of derivation}+1}$);
— close enough to the best fit, the differences (x_{ki}-x_{Mki}) are random and tend to average out;
— the second derivative itself is often negligible respect to J^TJ;
— small variations in the hessian matrix do not affect the final minimum of χ^2, but only the path followed by the iterative algorithm to get there;
— this term can be even destabilising when the model fits badly or when significant outliers are present in the data (large residual case).

In the context of the models under investigation, characterised by rather noisy objective functions, the second order derivatives have been found indeed to introduce instabilities in the algorithm, as well as to impose a performance penalty which is barely acceptable for interactive work.

4.4.1.4 Parameter increments for second-order differentiation

The problem of selecting an optimal increment for the calculation of the finite-difference approximation to the second derivatives, following the simple one-sided formula:

$$\frac{\partial^2\chi^2}{\partial p_k\partial p_h}=\frac{\chi^2(p_j+\delta_{jk}\Delta p_k+\delta_{jh}\Delta p_h)-\chi^2(p_j+\delta_{jk}\Delta p_k)-\chi^2(p_j+\delta_{jh}\Delta p_h)+\chi^2(p_j)}{\Delta p_k\Delta p_h} \tag{4.57}$$

is substantially complicated by the fact that the Taylor expansion of $\chi^2(p_k)$, truncated at the third-order terms, now contains terms that couple the contributions to the error from two parameters at once. Even if

---

26 Note that in the case of objective functions which are not derived from least squares problems (like, for instance, functions defined analytically such as the Rosenbrock example in Appendix 2) the evaluation of the second-order derivatives is of course necessary.

most authors skip the problem and take the increments to be the same as the ones used for first-order derivatives, a simplified approach to a more accurate procedure will be outlined here.

First, the increments will be estimated in such a way as to minimise the overall error in the calculation of the principal derivatives $\partial^2\chi^2/\partial p_k^2$ only. The assumption that these increments will be also acceptable for the calculation of the mixed derivatives, if rather arbitrary, is necessary to keep the procedure simple. By applying similar arguments as the ones in 4.4.1.2, an upper bound for the total error in the calculation of $\partial^2\chi^2/\partial p_k^2$ can be written as:

$$\varepsilon_{\max} = \frac{2\varepsilon_{\chi^2}}{\Delta p_k^2}\left|\frac{\partial\chi^2}{\partial p_k}\right| + \frac{2}{3}\left|\frac{\partial^3\chi^2}{\partial p_k^3}\right|\Delta p_k \tag{4.58}$$

and the corresponding optimum is:

$$\Delta p_k = \left\{\frac{2\varepsilon_{\chi^2}}{3}\left|\frac{\partial\chi^2}{\partial p_k}\right|\left|\frac{\partial^3\chi^2}{\partial p_k^3}\right|^{-1}\right\}^{\frac{1}{3}} \tag{4.59}$$

The evaluation of this expression is made more difficult by the third derivative, for which two alternatives have been considered:

1. Drop the optimisation of Δp_k as an objective and simply choose it in such a way as to make the relative roundoff error no worse than it was for the calculation of the first derivative, that is:

$$\frac{2\varepsilon_{\chi^2}\left|\frac{\partial\chi^2}{\partial p_k}\right|}{\Delta p_k^2\left|\frac{\partial^2\chi^2}{\partial p_k^2}\right|} = \frac{2\varepsilon_{\chi^2}|\chi^2|}{\Delta p_k\left|\frac{\partial\chi^2}{\partial p_k}\right|} \quad\Rightarrow\quad \Delta p_k = \frac{\left|\frac{\partial\chi^2}{\partial p_k}\right|^2}{|\chi^2|\left|\frac{\partial^2\chi^2}{\partial p_k^2}\right|} \tag{4.60}$$

2. Estimate $\partial^3\chi^2/\partial p_k^3$ on the basis of the two previous iterations. This approximation is worse than in II) above, but it is cheaply implemented.

Since these alternatives are cheap in computational terms, they have both been implemented and the more conservative result (i.e. the largest Δp_k) is chosen at each step.

4.4.1.5 Alternative differentiation strategies

The problem of differentiating the objective function efficiently and accurately could also be approached with other strategies, such as for example:

- *Richardson extrapolation:* the idea (originally expressed in the context of variable-step integration algorithms, see [71]) is to build up a sequence of approximated values for each component of the gradient $\{\nabla\chi^2_{k,i}\}$, obtained with decreasing increments Δp_{ki}. The sequence is then fitted by a function such as, for example:

$$\nabla\chi_k{}^2(\Delta p_k) = \nabla\chi_{k,0}{}^2 + \text{const}\cdot\Delta p^n{}_k \qquad (4.61)$$

  where $\nabla\chi^2_{k0}$ represents the limit of the sequence for $\Delta p_k \to 0$. The value of the exponent n and the magnitude of the residual of the fit give some indication on the behaviour of the objective function and can be used to diagnose potential problems.

- *Analytic differentiation:* as the differential equation in the models are expressed analytically, the gradient and the Hessian could also be reformulated in closed-form. However, this would require the user to calculate and enter manually $N\cdot M$ first derivatives for the gradient and $N\cdot M^2$ for the Hessian, which can be very tedious for large models which are frequently modified, unless some sort of symbolic manipulation capability is built-in the program[27]. Moreover, cancellation problems can occur even with analytic derivatives in some cases.

Both these methods would be rather cumbersome to implement and have not been deemed essential for the present work.

27 Commercial codes such as Mathematica offer an interface to C and FORTRAN programs; also, stand-alone function libraries with symbolic capabilities are available.

4.4.2 Damping-undamping stagnation loops

In this section the special problem of the occurrence of stagnation loops in the Levenberg-Marquardt algorithm is considered. The applicability of the results obtained is quite general in the context of the possible applications of this method.

Most of the basic literature on the Levenberg-Marquardt method gives little attention to the choice of the values for the factors which respectively boost and drop the damping coefficient λ. In many cases equal values $\beta^+=\beta^-=\beta$ are recommended, typically with $\beta=10$ [71,76]. This choice has been found to lead occasionally to endless loops in which the iterations keep cycling between two points in parameter space and λ is alternatively increased and decreased by the factor β. Further investigation has showed these to be special cases of a more general kind of loop, which appear to be possible for arbitrary values of β^+ and β^- and is characterised by cycles through multiple points in parameter space. This possibility is barely mentioned in the references examined (e.g. in [73]), yet it is a serious problem because it obviously results in failure of the algorithm. A simplified theoretical explanation of this behaviour is attempted in the following, while some indications to overcome the problem are given in the next section.

4.4.2.1 Mono-dimensional stagnation loops

The mono-dimensional minimisation of $\chi^2=\chi^2(p)$ respect to the parameter p with $\beta^+=\beta^-=\beta$ will be addressed first. In this case the Levenberg-Marquardt formula to find the optimal parameter increment Δp at each step is simply:

$$\Delta p = -\frac{\dfrac{\partial \chi^2}{\partial p}}{(1+\lambda)\dfrac{\partial^2 \chi^2}{\partial p^2}} = -\frac{g(p)}{1+\lambda} \qquad \text{where } g(p) = \frac{\dfrac{\partial \chi^2}{\partial p}}{\dfrac{\partial^2 \chi^2}{\partial p^2}} \tag{4.62}$$

where, for the sake of simplicity, the standard formulation of the multiplicative damping is considered and the second derivative is assumed to be positive. As seen in section 4.2.2.3, a value $\lambda>>1$ corresponds to a (damped) steepest descent step, while $\lambda\approx 0$ gives the exact solution for a quadratic χ^2; λ gets respectively multiplied or divided by the damping factor $\beta>1$ depending on whether χ^2 did increase or decrease at the last step. Assuming that the step leading to A was a bad one (i.e. leading to an increase in χ^2), the necessary and sufficient conditions for a loop to arise between the points A and B (see Fig. 4.4.1) can be stated as follows:

$$\begin{cases} \Delta p = -\dfrac{g(p)}{1+\lambda} & \text{step } A \rightarrow B \\ \Delta p = +\dfrac{g(p+\Delta p)}{1+\beta\lambda} & \text{step } B \rightarrow A \\ \chi^2(p) < \chi^2(p+\Delta p) & \end{cases} \tag{4.63}$$

(a similar argument would apply to a bad latest step). In words, this means that the step from A to B must take χ^2 in the direction opposite to the previous one, while at the same time g(p) is required to have different signs at the two endpoints. Conditions (4.63) are relatively easy to satisfy: for any given values of λ and β the value of p that triggers the loop can be found by solving this equation:

$$\frac{g(p-\frac{g(p)}{1+\lambda})}{1+\beta\lambda}+\frac{g(p)}{1+\lambda}=0 \qquad (4.64)$$

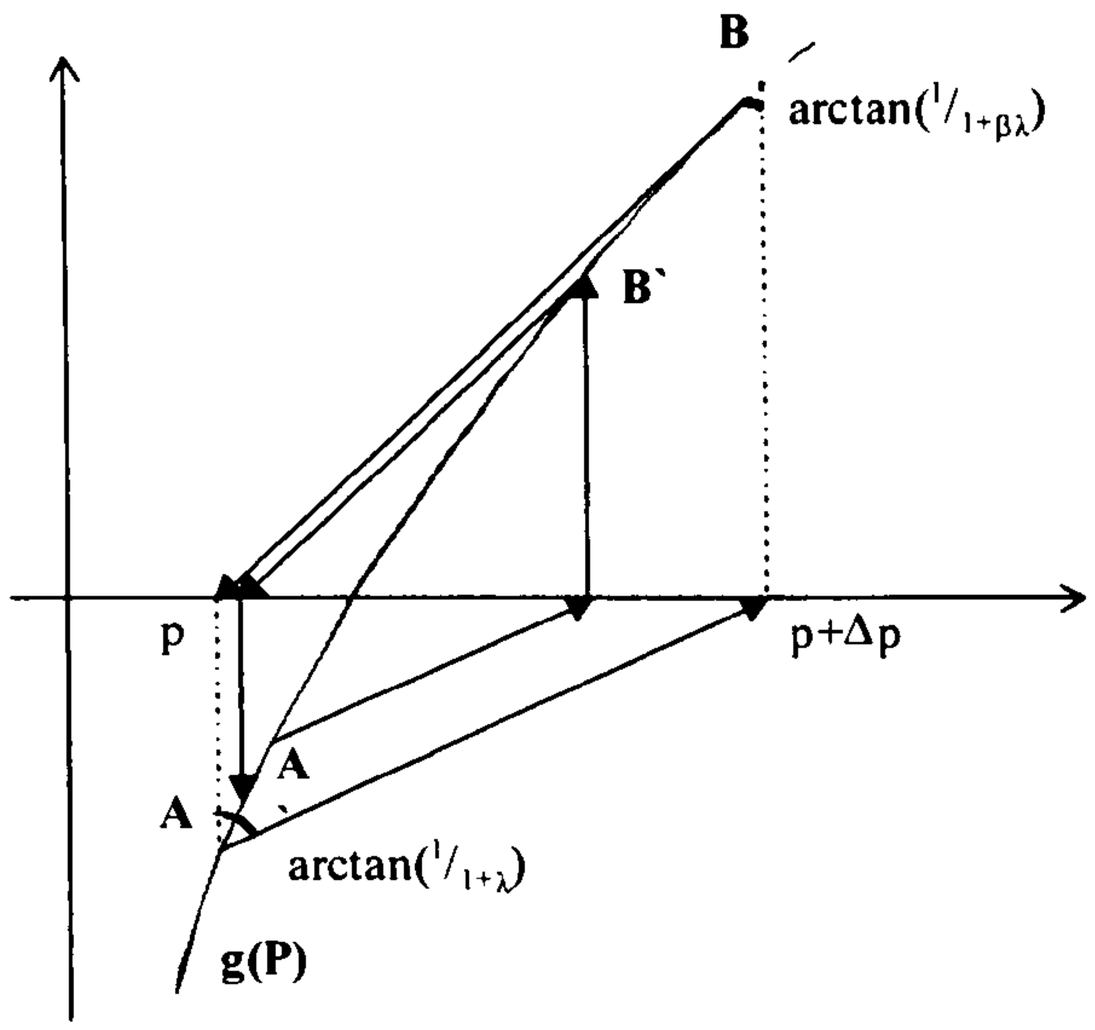


Figure 4.4 - Occurrence and stability of loops in Levenberg-Marquardt algorithm

while the corresponding value of Δp can be found from either of the (4.63). Graphically, solving the (4.64) can be done by shifting independently points A and B along the curve g(p), dragging along the angles shown in Fig. 4.4, until two common intersections on the p axis is found. Therefore, if g(p) changes sign at least once and if the curve has the right slope in the vicinity of the zero then at least one value of p suitable to start a loop can be found.

Conditions (4.63) have actually been met during the present investigation on JET disruption models. The topology of real-world objective functions is complicated not only by the higher dimensionality of the parameter space, but also by the presence of measurement noise and by artefacts of the Levenberg-Marquardt algorithm such as the absolute value in the formulation of the multiplicative damping (3.2). This implies that the range of pathological effects is much wider than what has been just outlined: for example, in some instances the occurrence of more complex loops involving three or more points in parameter space has been observed. In practice, the analyst must be always aware of the possibilities of stagnation to occur even if reasonable precautions (such as $\beta^+ \neq \beta^-$) have been taken.

4.4.2.2 Stagnation loop stability

Conditions (4.63) do not really explain how loops can occur in practice, since only an infinitesimally small probability to encounter precisely the right value $\bar{p}$ necessary to trigger the loop can be reasonably expected. The following analysis aims at showing that a loop may be indeed stable, that is, that it will respond to perturbations in such a way as to reduce them. When this happens the loop might be defined more properly as an attractor, which means that it is sufficient for the algorithm to produce a value of p close enough to the critical one in order to get sucked in the loop.

As a preliminary demonstration let us consider the Levenberg-Marquardt steps that would be taken if the initial point had been moved from $\bar{p}$ to $\bar{p}+\delta p$ (point A' in Fig. 4.4). Assuming the perturbation δp to be small, by using the first-order Taylor expansion of g(p) around $\bar{p}$ and $\bar{p}+\Delta p$ it is easy to show that the two first steps would be:

$$\begin{cases} \Delta p_1 = -\dfrac{g(\bar{p}+\delta p)}{1+\lambda} \approx \Delta p - \dfrac{g'(\bar{p})}{1+\lambda}\delta p \\ \Delta p_2 = -\dfrac{g(\bar{p}+\delta p+\Delta p_1)}{1+\beta\lambda} \approx -\Delta p - \dfrac{g'(\bar{p}+\Delta p)}{1+\beta\lambda}\left[1-\dfrac{g'(\bar{p})}{1+\lambda}\right]\delta p \end{cases} \tag{4.65}$$

The condition for stability is:

$$|\delta p+\Delta p_1+\Delta p_2|<|\delta p| \tag{4.66}$$

meaning that the distance from the unperturbed position must decrease after the first cycle. By substitution, this condition can be reformulated as:

$$\left|1-\frac{g'(p)}{1+\lambda}\right|\left|1-\frac{g'(p+\Delta p)}{1+\beta\lambda}\right|<1 \tag{4.67}$$

which shows more clearly that it can be satisfied only if g(p) is increasing at the end points of the loop and its derivative is small (or λ is large) enough, as shown in Fig. 4.4. In the hypothesis of small perturbations, therefore, the existence and stability of stagnation loops are influenced only by the values and the gradient of g(p) at the end points and not by the values it takes in between.

Example The phenomenon can be made clearer by examining an analytical example given by the minimisation of the function:

$$\chi^2=p^2+|p| \quad \Rightarrow \quad g(p)=p+\tfrac{1}{2}\mathrm{sgn}(p) \tag{4.68}$$

explicitly constructed to fool Hessian-based algorithms. As one can see in Fig. 4.1, the two branches of the graph ($p<0$ and $p>0$) belong to two different parabolae and therefore a naïve

Newton step, starting from any one of them, will always end up on the other missing the real minimum. Without damping, the symmetry would imply that any starting point would trigger a loop; if $\lambda \neq 0$, however, the starting point $\bar{p}$ has to be found according to (4.64):

$$\bar{p} = \frac{1}{2}\frac{\lambda(\beta - 1) - 1}{\lambda(\beta + 1) + 1} \tag{4.69}$$

The stability of this solution is guaranteed since g(p) certainly satisfies condition (4.67). It should be remarked that setting $\beta^+ \neq \beta^-$ does indeed prevent the loop to occur although, if $\beta' < \beta$, the iterations invariably lock into *another* loop. The nature of this second loop is fundamentally different, since the value of λ keeps changing. On the other hand, if $\beta' > \beta$ the loop disappears and the iterations converge to the solution p=0 at a rate increasing with the ratio between β^+ and β^-.

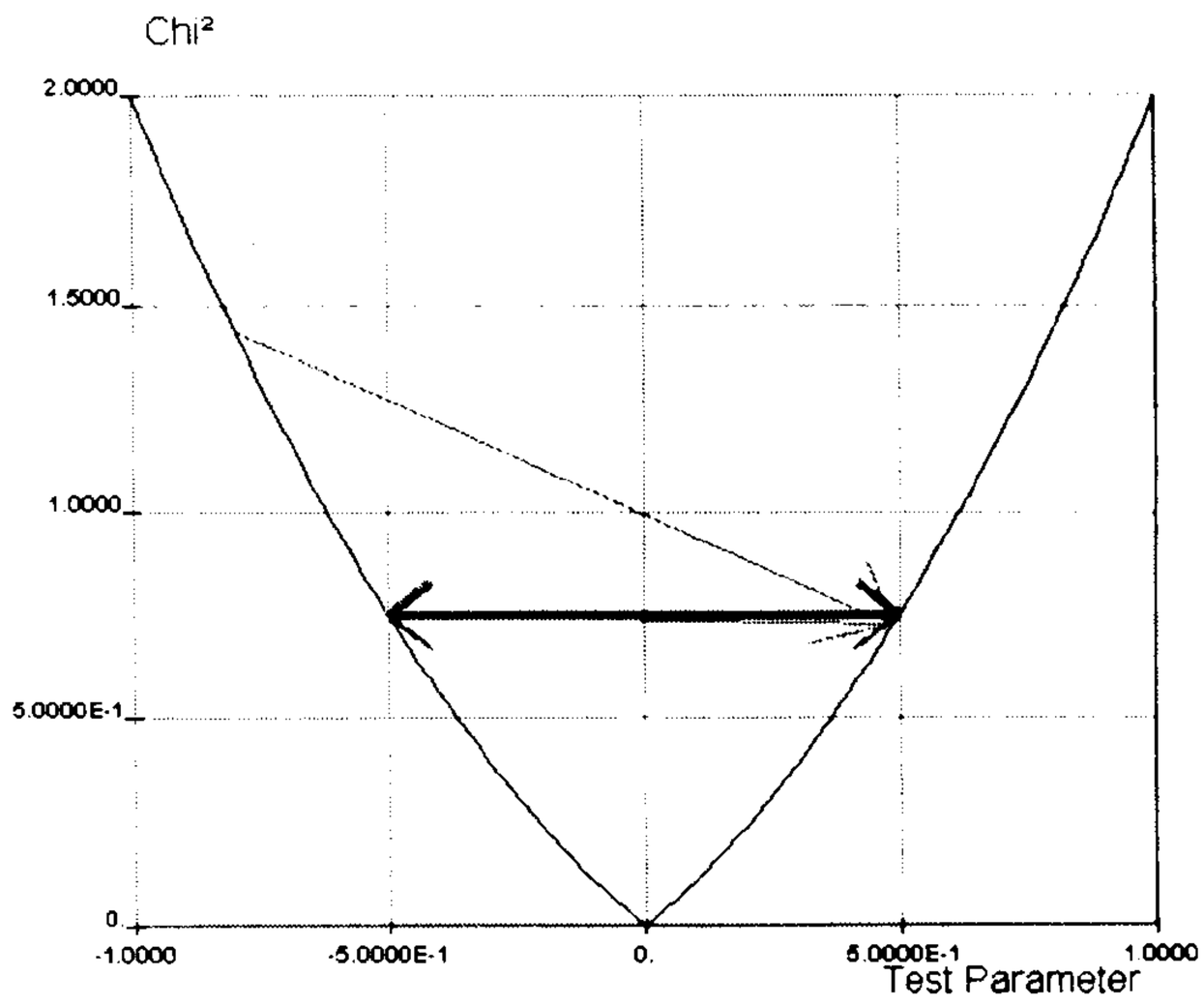


Fig. 4.1 - Pathological test function for Levenberg-Marquardt stagnation loops

The pathological nature of this example seems to justify the requirement of continuity of the first derivatives which is at the basis of many popular minimisation algorithms. However, behaviour similar to the one described has been encountered, on occasion, in the application of the Levenberg-Marquardt algorithm to JET models and the possibility of its occurrence should always be considered.

4.4.2.3 Multi-dimensional stagnation loops

The general case with an arbitrary number of parameters can be treated similarly, leading obviously to more complex equations. The conditions for the existence of the loop can be written as follows:

$$\begin{cases} \{\Delta p\} = -\left[\nabla^2\chi^2(p) + \lambda|\mathrm{diag}\{\nabla^2\chi^2(p)\}|\right]^{-1}\{\nabla\chi^2(p)\} & \text{step A} \rightarrow \text{B} \\ \{\Delta p\} = \left[\nabla^2\chi^2(p+\Delta p) + \lambda|\mathrm{diag}\{\nabla^2\chi^2(p+\Delta p)\}|\right]^{-1}\{\nabla\chi^2(p+\Delta p)\} & \text{step B} \rightarrow \text{A} \\ \chi^2(p) < \chi^2(p+\Delta p) \end{cases} \tag{4.70}$$

The analysis of this case has not been taken further.

4.4.3 Adaptive damping-undamping strategy

In this section the adaptive strategy followed to assign values to the damping coefficient λ is considered. Because of the discontinuous nature of the modulation effected an analytic convergence investigation would be very difficult and has not been attempted; rather, heuristic justifications are proposed and numerical tests have been carried out to assess the reliability of the algorithms proposed.

4.4.3.1 Choice of boost and drop factors

The problem of the optimal choice of the factors β^+ and β^- will be now discussed. The results of the previous section indicate that the possible occurrence of stagnation, for a given objective function and starting point, depends on these values. In most cases having $\beta^+ \neq \beta^-$ will be sufficient to avert endless loops; however, this is by no means a necessary nor a sufficient condition to guarantee convergence. Furthermore, the boost and drop factors affect the path followed to get to a minimum and thus the overall efficiency of the algorithm. As a full theoretical convergence analysis to clarify this issue would fall outside the scope of this work, some numerical tests have been carried out in order to get practical indications following suggestions found in the literature.

An extensive run of tests on the classical Rosenbrock problem (an analytical 2D function described in Appendix 2) is reported by Lampton in [73], including the effect of β^+, β^- and other parameters on the number of objective function evaluations necessary to get to the minimum. It is shown there that the choice $\beta^+=1.5$, $\beta^-=10$ is the best overall for the case of multiplicative damping. This test has been repeated here with an example more representative of the present problem, i.e. the fitting of the ideal waveform

$$x(t)=e^{-2\pi\xi f(t-t_0)}\sin[2\pi f(t-t_0)] \tag{4.71}$$

with t_0=.1 s, f=15 Hz, ξ=0.1 by means of the simplified model defined in (4.38), where the excitation has been taken as a very short impulse. For brevity, just one of the several cases that have been run will be discussed now. In this example, the oscillation frequency f and the starting time t_0 have been used as free parameters and the starting point has been fixed in f=5 Hz, t_0=.11 s (both the data and the simulated waveform are plotted in Fig. 4.2). The range to be fitted has been restricted to $0.095 \leq t \leq 0.13$ s so as to eliminate spurious maxima in the objective function corresponding to $2k\pi$ phase shifts of the simulated waveform. The results of the test are reported in Table 4.1 in terms of the number of Levenberg-Marquardt iterations to convergence (N_{LM}). The longest and one of the shortest minimisation runs are plotted in Fig. 4.3, overlaid to the objective function $\chi^2(f,t_0)$ where the values are color-mapped.

The results of the complete series of tests can be summarised in the following points:

— values $\beta^+<\beta^-$ give in this case slower convergence since the algorithm tends to use too early the inverse hessian method, where the local topology is not well approximated by a quadratic. Unfortunately, this behaviour depends very much on the topology of the objective functions and is not readily generalised.

— the addition of 10 to 20% of random noise to the data waveform does not affect significantly the speed of convergence.

The strategy $\beta^+=2.0$, $\beta^-=6.3$ will be taken provisionally as the default for the rest of this work. Of course, different values will be tested any time that a new kind of problem is considered. Further tests including the effects of dimension number, start position and different local topologies will be completed in the near future.

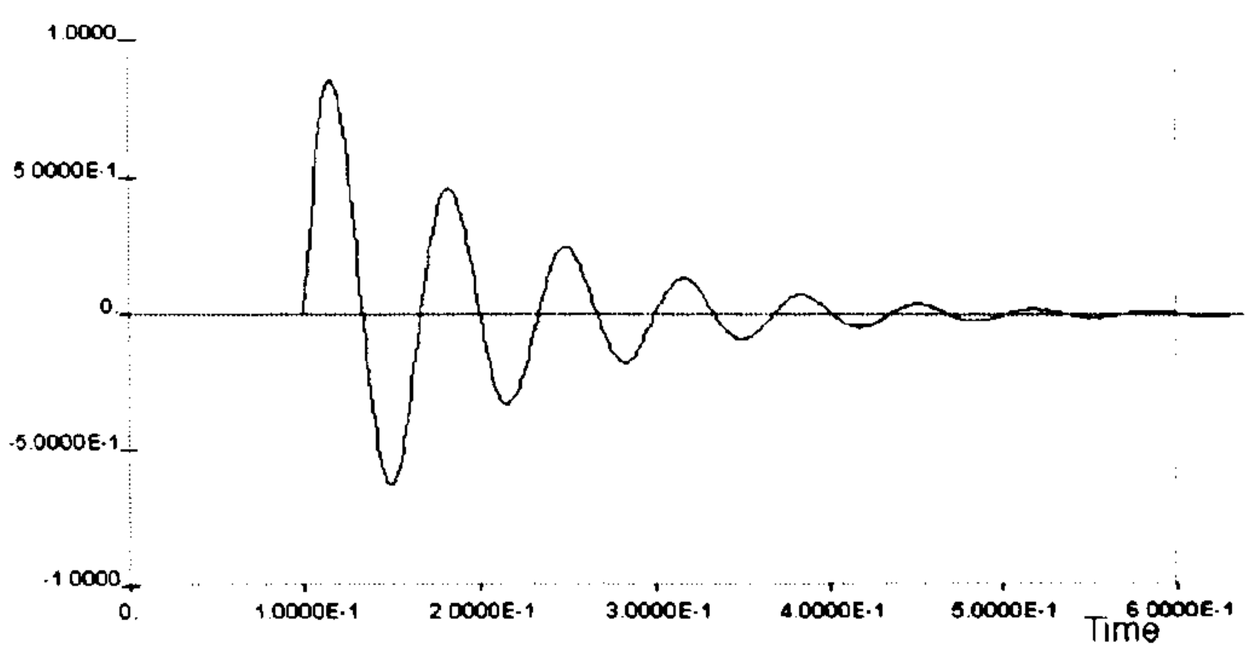


Fig. 4.2 - Test waveform for LM damping strategy study

Drop β^- / Boost β^+	**1.1**	**2.0**	**3.5**	**6.3**	**11.0**	**20.0**
1.1	10	10	10	13	14	11
2.0	10	10	12	9	17	9
3.5	15	15	13	10	9	11
6.3	11	11	17	9	9	11
11.0	13	10	12	10	11	10
20.0	13	11	12	14	14	10

Table 4.1 - N_{LM} vs. boost and drop factors for the ideal test.
Each iteration corresponds to 5 objective function evaluations using centred differences. The greyed area of the table represents the optimistic approach boost<drop.

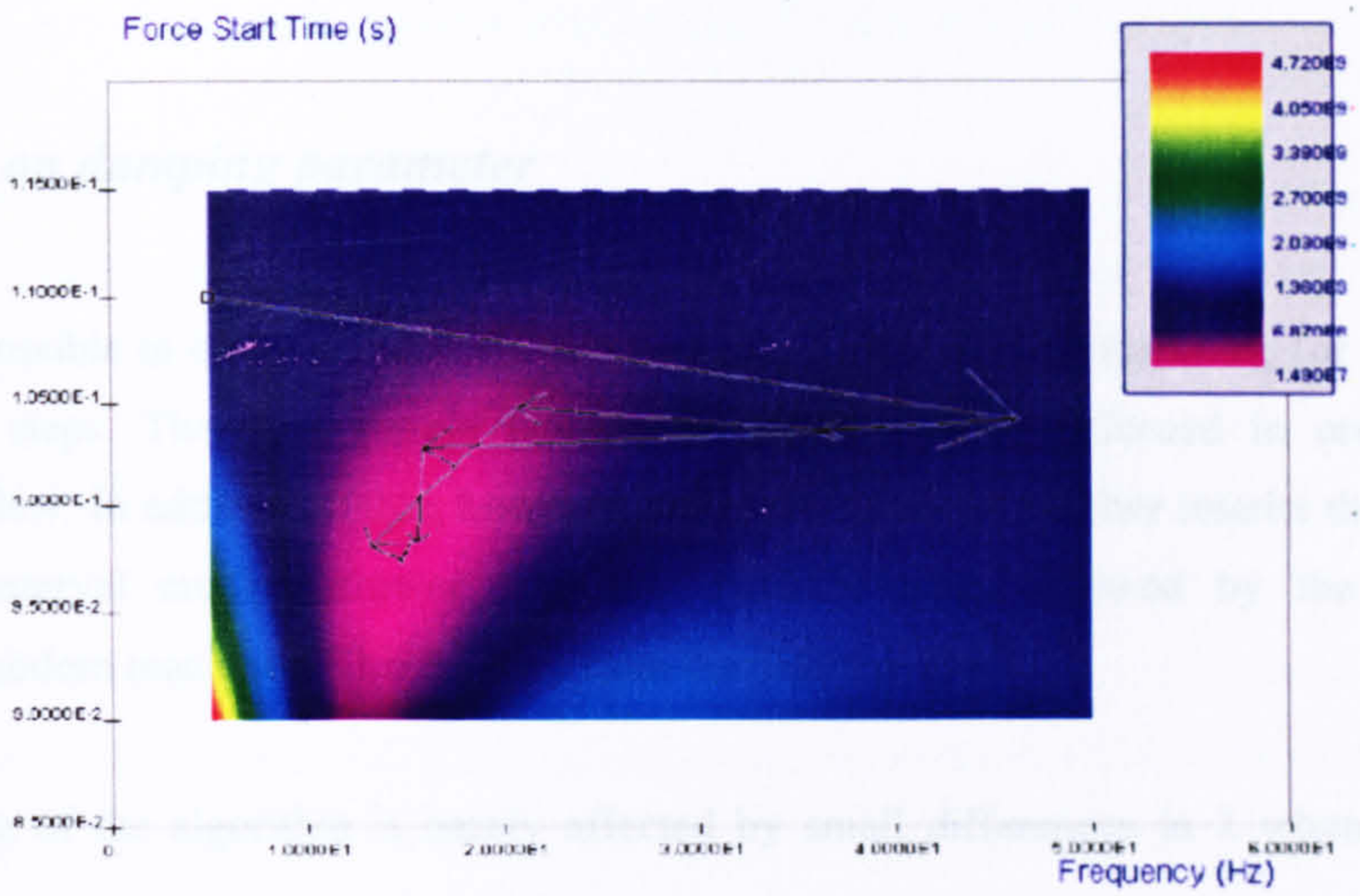


Fig. 4.3 - Minimisation paths corresponding to the runs with boost and drop factors equal to (6.3, 3.5) and (2, 6.3). The two paths are partially overlapped.

4.4.3.2 Effect of the local topology of the Hessian

As explained in 4.2.3.4, the damping/undamping strategy of the Levenberg-Marquardt algorithm aims at taking inverse Hessian steps, corresponding to values of $\lambda<<1$, whenever a minimum is believed to be near. On the other hand, in case [H] is not positive definite the absolute value appearing in (4.25) serves the purpose to move away from the maximum (or saddle point). However, this corrective action does not work automatically for all values of λ: if, for any reason, the current value of λ close to zero the steering effect will be negligible, while if $\lambda=1$ all diagonal elements $h_{jj}<0$ will be zeroed and the system may even become singular. This nasty pitfall could occur also in the case of additive damping although, in general, only one h_{jj} could be zeroed at a given step if $\lambda=-1/h_{jj}$.

Since these possibilities are not considered explicitly in the literature reviewed, a method to include information on the local topology of the objective function in the choice of λ has been devised and included in the present procedure. The strategy adopted is very simple:

$$\text{If}\{\ H\neq\text{positive definite},\ \lambda\leq 1\ \}\ \Rightarrow\quad \lambda=\lambda^{*} \tag{4.72}$$

where $\lambda^{*}>1$ is a function of the condition number ρ_C of the Hessian (i.e. the ratio between the largest and smallest eigenvalue), like for example:

$$\lambda^{*}=1+\rho_C \tag{4.73}$$

which gives at least $\lambda^{*}=2$ for a perfectly scaled problem, and a more and more damped step length as the conditioning of the problem gets worse. The necessary information on the definiteness of H and on its conditioning is obtained from its eigenvalues [81], which in turn are extracted by means of a standard QR routine taken from [71].

4.4.3.3 Bounds on damping parameter

In general, it is possible to imagine pathological cases in which λ keeps decreasing (or increasing) for many consecutive steps. Therefore simple bounds should always be enforced in order to prevent underflow or overflow. In addition to this, however, it may be useful to further restrict the actual values of λ within an interval much narrower than the dynamic range allowed by the floating-point representation on modern machines. This follows from considering that:

a) the performance of the algorithm is barely affected by small differences in λ when either $\lambda \approx 0$ or $\lambda >> 1$;
b) values of λ which are too extreme slow the response of the algorithm to sudden inversions of tendency;
c) high values of λ result in step lengths which may be too small compared with the resolution required in the solution.

Hence, the following bounds have been implemented:

$$\lambda_{MIN} \leq \lambda \leq \min\{\lambda_{MAX}, \lambda`_{MAX}\} \tag{4.74}$$

where λ_{MIN} and λ_{MAX} embody a) and b), and:

$$\lambda`_{MAX} = \min_j \left\{ \frac{\left|\frac{\partial \chi^2}{\partial p_j}\right|}{\Delta p_{j,\min} \left|\frac{\partial^2 \chi^2}{\partial p_j^2}\right|} \right\} \tag{4.75}$$

prevents c) by ensuring that λ is always small enough to make the smaller component of the step larger than the minimum acceptable length (defined by $\Delta p_{j,\,min}$). Reasonable values for the global bounds have been shown to be, respectively, $\lambda_{MIN}=10^{-8}$ and $\lambda_{MAX}=10^{4}$; the smaller order of magnitude of λ_{MIN} is consistent with the fact that $\beta^- < \beta^+$ (see c)) and, furthermore, with the necessity of perturbing the Hessian as little as possible when the minimum has been found.

4.4.4 Robust solution of the linearized equations

In this section the details of the solution of the linearized system (4.25) are considered. The objective, i.e. to get a robust solution in case of ill-conditioning of the damped Hessian matrix, is achieved by adapting the well-known singular value decomposition (SVD) technique, briefly reviewed in Appendix 3.

4.4.4.1 Model identification issues

When the number of parameters is large it can be very difficult to predict whether the estimation problem has or not a unique solution. In fact, as is commonly experienced in fitting problems, it is easy to define inadvertently two or more parameters having the same effect on the output, like for example two springs acting in parallel on the same mass: in this case, the parameter estimation procedure is able to infer information on their sum, but not on their individual values. It is therefore important to assess the identifiability of the system, i.e. the reversibility of the correspondence between points in parameter space and the output of the model's equations (see [85], for a detailed analysis to this concept in the broader context of identification theory). A simple identifiability criterion for problems like the present one, involving least squares objective functions, may be stated as follows [77]:

$$\left\| [X]^T [X] \right\| \neq 0 \quad \text{where } [\mathrm{X}] = \left[\frac{\partial x_k}{\partial p_j} \right] = \text{sensitivity matrix} \tag{4.76}$$

where the entries in [X] are called sensitivity coefficients and appear also in the Jacobian of the system, which however includes additional information related to the measured data and not just to the model. Condition (4.76), which is equivalent to impose that the sensitivity matrix has no null singular values, would ensure global identifiability in the linear case but has only a local meaning for non-linear models.

Unfortunately, it is easy to predict that the mechanical models defined in chapter 3 will not satisfy (4.76). Two major inherent kinds of dependency can be identified at a glance:

- multiple coefficients, representing springs or damper in parallel, which enter the equations only with their sum. This reflects the physical redundancy of the constraints which, of course, is a safety measure designed in purposefully.
- pairs of coefficients which enter the equations only with their ratios. Typically, in a second-order system the ratios mass/stiffness, mass/damping coefficient and mass/external load will be a function respectively of the frequency, of the logarithmic decrement and of the magnitude of the response. (in systems of strongly coupled equations, however, the eigenvalues are complicated functions of the parameters and this simplification is no longer valid).

As a result, in these two cases only the sums (or ratios) of the desired parameters can be estimated. Even if it would have been possible to reformulate the models eliminating some parameters so as to avoid

this problem, all the parameters have been retained instead for convenience in order to keep the equations as close to the physical situation as possible. This means that some of the parameters will have to be frozen somehow during the fitting procedure; although the choice may vary depending on the circumstances, generally the spring rates will be fixed since they are the parameters that can be determined with the least uncertainty (either from experimental data or from Finite Element calculations).

4.4.4.2 SVD solution of the linearized system

Even if the option to freeze redundant parameters is considered, a procedure to deal with singular or ill-conditioned system has to be included in the algorithm all the same as, in general, it is very difficult to actually predict all the possibilities for linear dependency in the parameters from a set of complicated non-linear equations. Moreover, while the identifiability criterion (4.76) reflects a specific mathematical property of the model, analysis of the conditioning of [H] is more complicated because of the following reasons:

1. the Hessian [H] includes a contribution from the actual data set being fitted (both in the first and in the optional second-order derivatives), which may bias either way the degree of correlation between different parameters;
2. the damped Hessian $[H_D]$ has modified diagonal elements which alter radically the nature of the matrix (in fact, the damping aims at making it always positive definite).

Therefore, ill-conditioning can occur in the problem even if the model seems to behave well on its own (and vice-versa). The conditioning of [H] and $[H_D]$ may be investigated at each step by eigendecomposing the matrices and looking for small eigenvalues. In the particular case of diagonal Hessian, for example, multiplicative damping would clearly leave small diagonal entries unaffected and, therefore, would not alter the singular character of [H]. On the other hand, if [H] is dense it is very difficult to predict the effect on the eigenvalues from knowledge on the alterations on the diagonal entries alone; thus, in the general case, it is advisable to eigendecompose both matrices in order to get the full picture.

The eigenvectors corresponding to vanishing eigenvalues give explicitly the linear combinations of parameters which are redundant. These, in turn, may be used to modify the models or to choose which parameters to freeze. Although very useful, this information is not sufficient to actually solve the system in a numerically stable way and to do so it is necessary to resort to the SVD approach, which gives:

$$\{dp_j\}=[H_D]^{\dagger}\{-J\} \tag{4.77}$$

Where $[H_D]^{\dagger}$ is the pseudo-inverse of $[H_D]$ (see Appendix 3). As stated above, the solution so obtained is optimal because the pseudoinverse automatically discards the effects of the linear dependence between parameters, which otherwise would result in some dp_j being assigned a very large value dominated by roundoff error [71]. For this reason, the SVD method is extensively used in the fields of curve fitting and

parameter estimation and, whenever the increase in computational load can be accepted, should be considered the recommended choice [74].

4.4.4.3 Null singular value detection

The SVD method has only one major drawback, i.e. it depends critically upon the choice of the tolerance ε_σ used to cut off the singular values. The length and the direction of a step corresponding to a given and ill-conditioned Hessian, in fact, will be characterised by sharp discontinuities as ε_σ is made to vary in the vicinity of the vanishing singular values. In the present analysis, the situation is further complicated by the fact that the entries in the Hessian have both different physical dimensions and orders of magnitude, making the choice of a reasonable tolerance quite difficult. To overcome these problems, the following actions have been taken:

Dynamic scaling - The linear system can be scaled so as to get the largest coefficient in all equations to be exactly one by pre-multiplying $[H_D]$ and $\{J\}$ by the following diagonal matrix[28]:

$$\operatorname{diag}\left\{\frac{1}{\max_j\left|[H_D]_{ij}\right|}\right\} \tag{4.78}$$

If the Hessian is diagonally dominant and the diagonal terms are all ones, it can be shown that also the singular values will be of order one and therefore the tolerance ε_σ clearly acquires a relative meaning. If the dominant term is not on the diagonal, the rigorous analysis is more difficult but the previous conclusion still approximately holds.

Cutoff smoothing - The abrupt variation in step length when a singular value falls below ε_σ can be avoided by simply smoothing the cutoff logic, assuming for example:

$$[\Sigma]_j = \begin{cases} \dfrac{1}{\sigma_j} & \sigma_j \geq \varepsilon_\sigma \\ \dfrac{\sigma_j}{\varepsilon_\sigma^2} & 0 \leq \sigma_j < \varepsilon_\sigma \end{cases} \tag{4.79}$$

This allows one to confidently set more conservative (i.e. larger) values of ε_σ without fear of discarding completely the possibility of long steps due to some small but not truly pathologic component of the Hessian.

---

28 In case the whole i^{th} row of $[H_D]$ is null the χ^3 does not depend on p_j, therefore also the corresponding entry in the gradient should be zero and the diagonal element $[H_D]_{jj}$ can be safely set to 1.

4.4.5 Termination criteria

In this section the termination criteria used to stop the iterative procedure are described. Since implementation details may be critical as far as performance and solution accuracy are concerned, particular care has been put in adapting the criteria suggested in the literature to the specific requirements of the present problem and in testing the effects of the choices made. In total, five independent conditions have been used to decide whether to stop at the end of each step. These are listed below in the same order by which they are included in the algorithm, i.e. the most certain indicator of a satisfactory minimum having been reached is evaluated first:

1. *Absolute minimum*

   Since $\chi^2 \geq 0$, the condition $\chi^2 = 0$ implies that the best possible fit has been achieved and iterations can be stopped (the possibility of this happening at more than one point in parameter space is neglected). Because of measurement errors, however, it will be generally impossible to reach the zero value: the statistically expected value of χ^2 at the minimum is χ^{2*}=n. of measurements – n. of parameters. Therefore, taking also into account the weights defined for the various observations in χ^2, the following criterion has been adopted:

   $$\chi^2 \leq \chi^2_{TOL} = k_{\chi^2}(\Sigma_k w_k n_k - M) \quad \Rightarrow \quad \text{absolute min. attained} \tag{4.80}$$

   where the coefficient $k_{\chi^2} \geq 1$ allows one to add some margin to this evaluation, as is reasonable in cases where a perfect fit is not expected.

2. *Local minimum*

   The well-known necessary and sufficient conditions for a multi-dimensional function to be minimum are null gradient and definite positive Hessian matrix. In the vicinity of a stationary point, however, the finite difference approximation to the gradient is going to be dominated by the roundoff error and one cannot realistically expect to get a precise value of zero for all its components. According to [75] a relative gradient should be defined and compared to a pre-set tolerance in order to avoid problems connected to the different order of magnitude the variables may have. The following criterion has been used here:

   $$\begin{cases} \max_j \left| \dfrac{\partial \chi^2}{\partial p_j} \dfrac{p_{j,MAX} - p_{j,MIN}}{\chi^2_0} \right| \leq \varepsilon_{grad} \\ [H] > 0 \end{cases} \quad \Leftrightarrow \text{ local minimum attained} \tag{4.81}$$

   where the gradient is made non-dimensional by means of the initial value χ^2_0 and the allowable range for each parameter. This is slightly different to what is suggested in [75], where the maximum between the current value and a typical value is used to normalise both the p_j and χ^2. The choice made here avoids any discontinuity in the values of the normalised gradient and

provides a fixed reference against which to define a reasonable value of the tolerance ε_{grad}. If the condition on the gradient only is satisfied, but the Hessian is not definite positive, of course this means that the algorithm has wrongly converged to a maximum or a saddle point and a warning is issued.

3. *Steady-state on χ^2*

If the iterations reach a steady-state in which the value of χ^2 changes little at each step then the algorithm should be stopped, as further progress is deemed unlikely. Considering the relative variation between the n_S steps previous to the current, it is possible to define the following criterion:

$$\begin{cases} \left|\dfrac{\chi_i^2}{\chi_{i-1}^2} - 1\right| \le \varepsilon_{SS}, \quad i = i_{current} - n_s + 1,\ldots i_{current} \\ j:\ \chi_j^2 = \min_i\left\{\chi_i^2\right\} \qquad \Rightarrow \text{ local minimum attained} \\ [H_j] > 0 \end{cases} \tag{4.82}$$

where i is the index for steps, j indicates the step with the minimum χ^2 among the last n_s and the tolerance ε_{SS} represents the relative variation allowed. High values of n_s mean, of course, a more conservative definition of steady-state. Also in this case, if the Hessian is not positive definite at the minimum some kind of pathological behaviour has occurred and the user is warned.

4. *Steady-state on {pj}*

A second kind of steady-state is related to the position in the parameter space which can occur, for instance, when the damping parameter λ becomes too large. In a similar way to what has been made at point 3, one can define the following criterion:

$$\begin{cases} \dfrac{\left|p_{j,i} - p_{j,i-1}\right|}{p_{k,TYPICAL}} \le \varepsilon_{SS} \quad \begin{cases} i = i_{current} - n_s + 1,\ldots i_{current} \\ j = 1..M \end{cases} \Rightarrow \text{ local minimum attained} \\ [H_j] > 0 \end{cases} \tag{4.83}$$

which could be simply modified in order to cope with stagnation loop situations.

5. *Maximum n. of iterations*

This condition, which can be simply written as:

$$i \le i_{MAX} \tag{4.84}$$

is a safeguard to prevent excessive running times in case of failure to find a minimum satisfying any of the conditions above. The solution returned by the procedure will correspond in this case to the lowest value of χ^2 attained during the run.

4.5 Incorporation of prior knowledge

In this section some issues related to incorporation of prior knowledge on the values of the parameters into the minimisation procedure are discussed. The ideas put forward are essentially extensions and modifications based on suggestions found in the literature.

4.5.1 Weighting of measurements and prior knowledge

In the following the question of the relative significance of multiple measurements in the same model is considered, along with the problem of the balance between measurements and prior knowledge in determining the solution. The method adopted is slightly more general than the common Bayesian approach and is based upon the subjective interpretation of the likelihood concept (see 4.2.2.1). in practical terms, it consists simply in the inclusion of additional non-dimensional weighting coefficients in the formulation of the χ^2, leading to the following generalised version of equation (4.19):

$$\chi^2 = \sum_k \frac{\omega_k w_k}{\sigma_{Mk}^2} \sum_i \left(x_{ki} - x_{Mki}\right)^2 + \sum_j \frac{\left(p_j - p_{j0}\right)^2}{\sigma_{Pj}^2} \qquad (4.85)$$

where $|\omega_k|$ and $|w_k| \leq 1$. Note that all previous considerations on the minimisation of χ^2 are not affected by this extension and all formulæ in this chapter may be trivially modified to accommodate these extra coefficients. The rationale for this choice can be explained in the two following points:

- *Relative weighting of different measurements (w_k)*

  In most of the statistical literature reviewed the observed data points are implicitly assumed to be the results of repeated instances of the same experiment, i.e. repeated measurements of the same variable in the same system. On the other hand, in the present case different measurements $x_k(t)$ refer to a different variables, possibly with different physical meanings and measured with independent apparatus (e.g. displacements measured with LVRs and stresses measured with strain gages). Therefore, it seems reasonable to allow each of the measurements to be valued differently in the parameter estimation procedure, by means of a weight w_k reflecting the subjective degree of confidence the analyst has in the specific part of the model which determines the measured quantity.

  For example, the vertical support force R_{MVP} (as discussed in section 3.1.1.2) is believed to be inherently simulated with lower precision than the displacement signal x_{RM} by the rolling motion model; the respective weights in the parameter estimation procedure have therefore been taken as $w_{Xrm}=1$, $w_{Rmvp}=0.67$. It should be emphasised that the degree of confidence in question is totally independent from the accuracy of the measurement in itself, which is accounted for separately by means of the variances σ_{Mk}.

- *Relative weighting of measurements and prior knowledge (ω_k)*

A somewhat more subtle problem arises if one thinks about the nature of the data points x_{ki}, which are obtained from sampling a measurement $x_k(t)$ that is a function of time. In fact, in the cases generally described in the literature, every data point is the result of an individual experiment and thus all the observations x_{ki} have the same relevance in the χ^2. Indeed, the more data points are available, the smaller the significance of the prior parameter distributions becomes. In the present situation, however, there appears to be an inconsistency: if the sampling rate is increased, say, from 1 kHz to 1 MHz, the weight of the prior distributions will clearly vanish, while at the same time the information contained in the waveform $x_k(t)$ is not necessarily changed. This means that making every data point count as if it was an independent observation leads to unreasonable results.

The opposite extreme, though, looks equally unsatisfactory. If all of the n_k data points are considered to count for just one observation (which is equivalent to assume $\omega_k=1/n_k$), then the goodness of the fit to a certain $x_{Mk}(t)$ is independent from the total duration of the sampling time T_k, which is also contrary to common sense: one would naturally expect that good agreement with a long stretch of data is more meaningful than the agreement with a measurement lasting, say, only a fraction of a second.

The central issue here appears to be the equivalence of the n_k sampled data points to a certain number n^*_k of "meaningful" observations, increasing with T_k and such as $1<n^*_k<n_k$, against which the prior information will be weighted[29]. A possible solution to the problem may come from considering only a few key points in $x_{Mk}(t)$ as meaningful from the viewpoint of the quality of the fit. If, for example, the estimation fits well the measured function at a peak and at the next valley, the agreement of the points on the slope in between can be expected to follow naturally; changing the density of such points will not affect the amount of information that can be inferred from the fit. If $x_{Mk}(t)$, for instance, includes significant spectral components up to a frequency $f_{Mk,MAX}$, the maximum number of meaningful features that can be reasonably expected in $x_{Mk}(t)$ will be given be the peaks and valleys of a sine wave at that frequency and one could thus define:

$$n^*_k = T_k f_{Mk,MAX} \tag{4.86}$$

from which it follows:

$$\omega_k = n^*_k / n_k \tag{4.87}$$

This is equivalent to assume that the available information is lumped in n^*_k equivalent data points. It should be remarked that the problem of the relative weights of prior information and measurement is indeed considered in the statistical literature [89], although no references could be found on this specific aspect linked to the time-varying nature of the data.

---

29 In case of no prior knowledge the minimisation procedure is unaffected by a scale factor in χ^2 and the question becomes irrelevant.

4.5.2 Parameter constraints

In this section the inclusion of additional constraints on the parameters is considered. This may seem redundant with respect to the Bayesian approach, which already makes use of the prior distributions in order to express the initial knowledge. However, further constraints may be very useful for a variety of practical reasons, like for example:

- to prevent parameters from taking physically unrealistic values, e.g. negative mass or damping coefficients which could make the system unstable and cause failure of the integration routine;
- to prevent parameter runaway, e.g. in the case when $\lim_{p_j \to \infty} \chi^2 = 0$

The simplest possibility is to define a permissible range $\{p_{j,MIN}, p_{j,MAX}\}$ for each parameter, resulting therefore in a rectangular region in the M-dimensional parameter space in which the algorithm will be confined. Other options, including modifications of the prior distribution, equality constraints etc. would be far more complicated to implement and have not been considered.

A strategy has to be devised in case one of the p_j is assigned an increment that would bring it beyond the bounds. In the literature the subject is treated extensively; for instance, penalty methods or projection methods are suggested to cope with the special cases when the minimum lies on the boundary, or the only downhill route to the minimum requires to exit and re-enter the allowable region [74].

A simpler but acceptable strategy has been found to be the following:

1) assign the parameter a "damped" incremented value, in accord with the direction requested by the algorithm but within acceptable limits (the average between the current value and the bound that would have been exceeded is a good compromise);

2) if this occurs more than a small number of times consecutively, it may mean that:
   — there actually is a meaningful minimum outside the bounds, which therefore have to be extended;
   — some pathological condition has occurred, in which case it is better to restart the iterations from a safe distance (either chosen at random or by the user) or with different algorithm parameters (e.g. with a different λ).

Full diagnostic information is vital in order to overcome this sort of problems. If the range is sufficiently wide, anyway, this occurrence is unlikely and the minimisation procedure will not be affected.

4.5.3 Parameter cluster estimation

This section is concerned with the adaptation of a method for dealing with large numbers of parameters also known in the literature as grid search algorithm [76]. The method consists essentially in dividing the parameters into separate clusters and solving the estimation problem in stages, cycling through the clusters until convergence is reached. In the limit case, a cluster may include only a single parameter.

Despite the fact that the minimisation procedure may be need to be iterated many times for each parameter group, a substantial improvement in speed is usually observed as the computational workload scales with M^2 (M being the number of coupled parameters to be estimated at the same time). More importantly, the subdivision in clusters proves often to be the only practical means to get a solution at all, since the complicated topology of higher-dimensional spaces makes it usually very difficult for the algorithm to converge to the global minimum when all the parameters are allowed to vary simultaneously.

The key to an efficient use of this technique is careful selection of the clusters, which should contain parameters highly correlated with each other but uncorrelated from the parameters in other clusters. Ideally, one should be able to identify which parameters affect any given feature of the data, targeting thus only one feature per run of the procedure. This approach grants a great flexibility to the analyst, since it is possible:

- to alter the minimisation path by changing the order in which the clusters are estimated;
- to tailor the internal parameters of the Levenberg-Marquardt algorithm (damping/undamping factors, tolerances and so on) differently for each cluster;
- to change the composition of the clusters between successive iterations, in order to test the degree of correlation among parameters.
- to increase gradually the size of the clusters as the quality of the fit gets better; one final estimation run, including all parameters, should be done once the global minimum is believed to be near.

The precise way in which to carry out this technique is clearly problem-dependent. Some suggestions, based on the analysis of specific JET models described in Chapter 3, can be summarised in the following points:

— the possibility of redundant parameters should be continuously checked by monitoring the eigenvalues and the singular values of the linearized system; only one in each group of linearly dependent parameters should be allowed to vary.

— for this reason, spring ratios should usually be kept fixed throughout the whole analysis (see also 4.4.4) together with geometrical constants. The spring ratios could be allowed to vary, within the narrow limits of their prior distributions, only towards the very last stages of the estimation in order to get as good as possible a fit for any particular experiment.

— mass coefficients influence mostly oscillation frequencies and peak-to-peak responses, therefore should be estimated at an early stage;
— damping and friction coefficients have little influence over the initial transient but affect heavily the decay of the following oscillations, therefore can be estimated at later stages.
— the start time and the duration of the load impulse influence strongly both the goodness of fit of the first transient and the phase of the subsequent oscillations, therefore should be estimated first and then kept fixed.
— force rise, hold and swing times determine the shape of the initial transient;
— the impulse $\int Fdt$ and, to a lesser extent, the magnitude of the forces determine the amplitude of the response.

As one can see, in some cases the effect of a parameter cluster is more apparent on a particular slice of the data rather than others. This feature has been exploited by adding to the algorithm the capability of fitting the model's output to a given time window in the measurement only. If used carefully, this gives the benefit of higher-curvature, higher-gradient χ^2 (leading in turn to faster and more precise convergence) as non-relevant data points are discarded. The notion of splitting the data to facilitate the estimation can be also found in [74] and, on a larger scale, constitutes the basis for the multi-stage method discussed in the next section.

The prior density of the estimated parameters should be kept fixed throughout the analysis, as the partial updates may fluctuate wildly and carry little meaning until convergence is achieved.

4.5.4 Multi-stage estimation

In this section the adaptation of a method for dealing with large amounts of data known either as multi-stage [74] or sequential estimation [77] is discussed. This method is related to the continuous update of parameter estimates and variances during an experimental campaign, which in the present case should be identified with the whole life span of the JET machine. The purpose of the method is twofold:

- to minimise the time and computer resources needed to estimate the parameters from a huge experimental database all at once;
- to obtain partial but useful estimates during long campaigns, or when the data cannot physically be collected together (e.g. in real time situations).

As a side advantage, repeated estimation runs allow the analyst to get a feel for the sensitivity of the model to the different parameters; if, for instance, the sensitivity changes too much between experiments, this may imply that the model is wrong [77].

4.5.4.1 Combination of prior distributions

At any given stage of the procedure, the prior knowledge available on a parameter p will be encapsulated in the prior density. Assuming that two such distributions exist (and that they are independent from each other, since they are generated in parallel from two sets of experimental data) it is possible to combine them into a single cumulative probability density proportional to their product:

$$\wp \propto \frac{1}{\sigma_1 \sigma_2} e^{-\frac{1}{2}\frac{(p-p_1)}{\sigma_1^2}-\frac{1}{2}\frac{(p-p_2)}{\sigma_2^2}} \tag{4.88}$$

where $\bar{p}_i$ and σ_i represent respectively the mean and standard deviation of the priors (with i=1,2) and the scaling factor will be determined so as to give unit total area. If the mean values and the deviations are not too dissimilar, it is possible to approximate the distribution (4.88) with another equivalent gaussian having:

$$\begin{cases} \bar{p}_{equivalent} = \dfrac{\bar{p}_1 + \bar{p}_2}{2} \\ \dfrac{1}{\sigma^2_{equivalent}} = \dfrac{1}{\sigma^2_1} + \dfrac{1}{\sigma^2_2} \end{cases} \tag{4.89}$$

as can be shown trivially by substituting and neglecting the second-order terms in the differences. Note that the resulting distribution is actually a gaussian and the second of the (4.89) is rigorously true when $\bar{p}_1 = \bar{p}_2$. If $\sigma_1=\sigma_2=\sigma$, then $\sigma_{equivalent}=\sigma/\sqrt{2}$, i.e. the familiar results stating that the uncertainty of an experiment decreases with the square of the number of measurements [66]. When $\bar{p}_1$ is significantly different from $\bar{p}_2$ (i.e. if $|\bar{p}_1-\bar{p}_2| >> \sigma_1$ or σ_2, which has proved to be the more frequent case), no mathematical shortcut exists because the distribution is truly bimodal, which is another way to say that the underlying model cannot reproduce satisfactorily the data. In this case, one might accept the inconsistency and take simply

$$\sigma_{equivalent} = \frac{|\bar{p}_1 - \bar{p}_2|}{2} \tag{4.90}$$

as a guess of the order of magnitude of the uncertainty.

4.5.4.2 Parameter estimate updating

Having a rule to combine together the estimates for the same parameter obtained from two experiments, it is possible now to focus onto the best way to apply it systematically and recursively to the multiplicity of parameters and JET pulses under investigation. JET models include two broad categories of parameters:

- geometrical and mechanical parameters (masses, spring ratios, damping coefficients) known to a moderate to good degree of precision, which can be considered as constants throughout ranges including hundreds or thousands of events;
- force and induced current parameters, estimated in advance only with large uncertainty, which are expected to be unique for each experiment.

Estimates for the parameters of the first group can be progressively refined by repeating the fitting procedure several times with different data, utilising the results of each run as prior knowledge which then gets incorporated into the next. Of course, also force parameters have to be estimated at the same time, but as long as the estimates of the mechanical properties are still fluctuating the forces obtained shall be considered as provisional. A further round of estimation runs, this time with the mechanical parameters being frozen, will be necessary to get force estimates with the maximum possible confidence.

In the end, the gain in knowledge on each of these parameters has to be evaluated by comparing its estimated variance at the end of the investigation to the estimated value at the beginning, neglecting the intermediate results.

4.5.4.3 Progressive modelling

The stage-wise subdivision of the parameter estimation procedure, which is the underlying theme of both this and the previous sections, can be applied on yet another level by letting the model itself evolve between stages, using the results of simpler versions as the initial guesses for the more complex ones. This is of course a perfectly natural and common approach: complex models are usually simplified in a variety of ways, for example by approximating the equations or by breaking them down into more manageable, independent parts. In this sense, the models presented in chapter 3 should be seen as an intermediate step between previous, rougher assessment and future models such as the one described in 1.2.3.

5

ANALYSIS OF AXISYMMETRIC DISRUPTIONS

This chapter describes the results of the parameter estimation procedure applied to the models representing the averaged axisymmetric response of the vacuum vessel, defined in section 3.1. The work on some of these models, namely the ones for the radial motion (3.1.3) and the halo currents (3.1.5) is still ongoing and results will not be presented here.

Although several JET VDEs have been analysed, the general pattern of the results tends to show many similarities and a detailed report will be given only for the some of the more representative events:

Pulse	Date	I_{PLA} (MA)	B_T (T)	t_{DISR} (s)	Notes:
Pre-divertor					
16297	7/5/88	4.0	3.45	55.500	An early disruption showing the response of the "bare" vessel structure, without the Inner Restraint Rings and MVP dampers.
20802	28/9/89	4.1	2.5	49.360	Largest occurrence of rolling motion ever (11.2 mm)
Divertor MkII					
37628	19/7/96	3.7	3.45	55.338	Most severe axisymmetric VDE in MkII divertor configuration
38690	18/9/96	2.6	2.73	55.036	Very small amount of non-axisymmetry

Some of these events also exhibit a small amount of toroidal asymmetry. This, however, is essentially decoupled from the axisymmetric component and therefore has not been considered in the present analysis.

5.1 Analysis of pre-divertor events

In this section two early JET disruptions are analysed. These events refer to the period when the divertor was not yet installed and the relative results can be found in Table 1.1. Pre-divertor disruptions can be modelled adequately by a cut down version of the rolling motion model, which includes a force history considerably simplified respect to the waveform described in 3.2.1.4. One has in fact that:

- $F_0=0$ no force during the steady-state phase
- $F_{max}=\tau_4=0$ no residual force after the disruption
- $\varepsilon_0=\varepsilon_1=\varepsilon$ the line of application of the force does not move
- $b_{MVP0}=b`_{MVP}=F_{damp,MAX}=0$s no radial MVP dampers were installed

Following the multi-stage parameter approach described in 4.5.4, these simplifications can be used to isolate and fix the values for some of the mechanical properties of the model such as the spring ratios, the masses and the damping coefficient of the vessel bulk (β_{VV}). These values will be used then as prior information in the next estimation stage.

5.1.1 JET Pulse 16297

This event is a 4MA disruption which shows clearly the dynamic properties of the vessel minus the effects of the MVP dampers and the inner restraint ring. The direction of the vertical plasma instability is downward, which explains the reversed oscillation pattern as the top MVPs move inwards first. The rolling motion model can be used to represent pre-divertor downward VDEs because then, as opposed to the current configuration, vessel and magnetic field were with good approximation top-bottom symmetric.

The only measurement considered here is the rolling motion (Fig. 5.1), which shows very clearly a free, exponentially damped sine oscillation starting from an initial state of rest. Following the preliminary analysis approach outlined in section 4.3, this signal has been fitted with the simplified model defined in (4.38). The following results have been obtained:

— critical damping ratio $\xi=0.084$ (in substantial accord with the ASME-recommended standard value $\xi=0.05\sim0.10$, valid for welded/bolted steel structures);

— frequency f=10.6 Hz, practically coincident with the peak of the Fourier spectrum of the signal at f=10.3 Hz. This relatively low value reflects the relative compliance of the original structure.

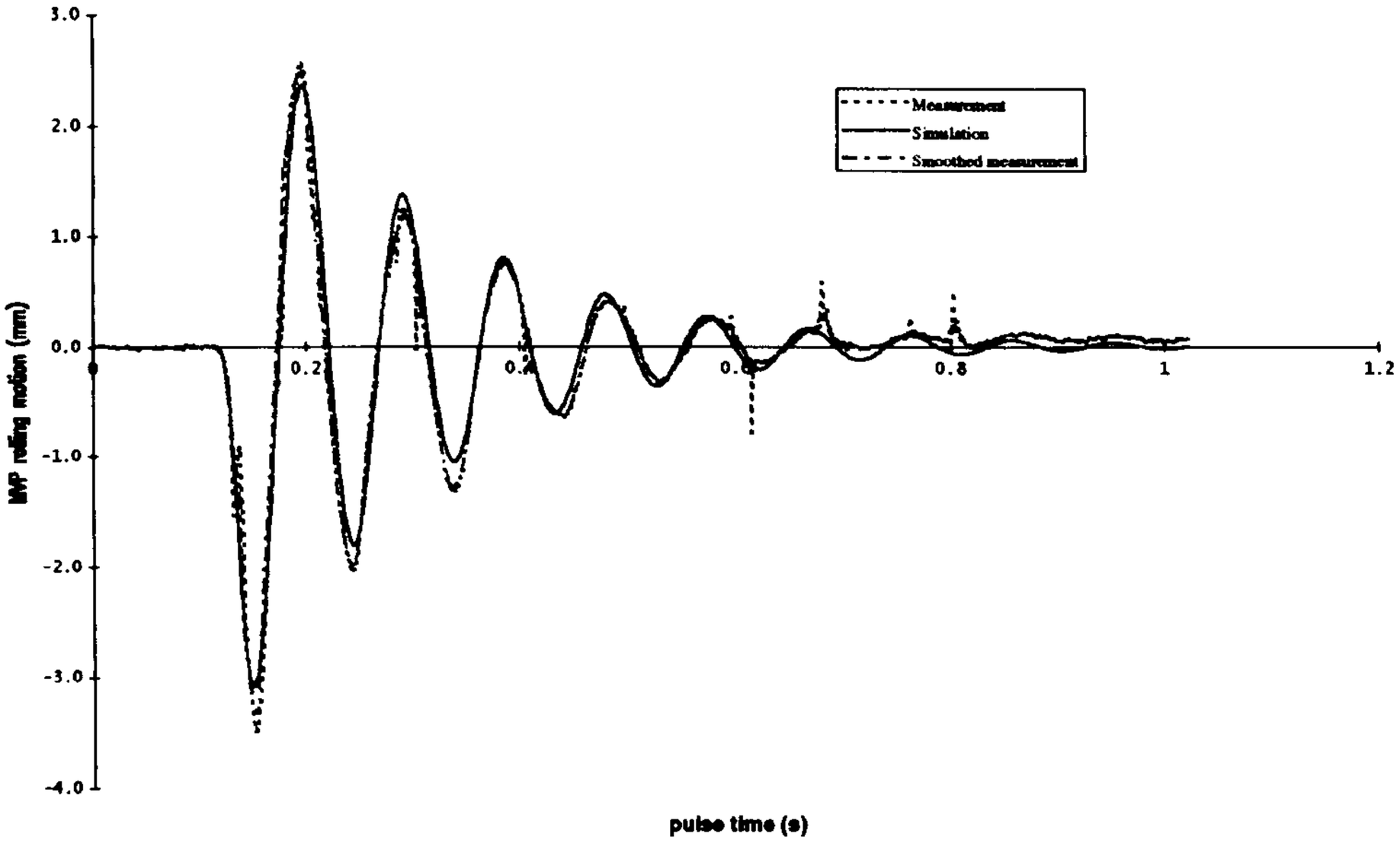


Fig. 5.1 - Rolling motion of pulse 16297

On the basis of these values, the bulk vessel damping coefficient β_{VV} has been worked out using (4.37), keeping into account the uncertainty on k_{VV} which derives from the fact that the position of the force is not known in advance.

The problem represented by the noise spikes clearly visible in the signal has also been considered. The spikes have been removed with the algorithm described in 4.3.3, setting a window width of 10 ms and a spike threshold of 15%. In Fig. 5.1 the smoothed signal is plotted superimposed to the original. The effect of the smoothing on the estimation procedure has been quantified by comparing, as an example, the profile of $\chi^2(\beta_{VV})$ obtained in the two cases (Fig. 5.2). The presence of the spikes can be clearly seen to affect adversely:

- the value of the minimum (χ^2_{min}), which is higher for the raw data;
- the curvature at the minimum, which is less pronounced for the raw data;
- the position of the minimum ($\beta_{VV,min}$)

This means that the minimisation algorithm will converge less easily if the data are not smoothed and, furthermore, that it will converge to a solution which is likely to be wrong. The fitting obtained for the smoothed data, also plotted in Fig. 5.1, appears to be very good with an error ε_{avg} less than 1.7% of the signal's range (see (4.27) for the definition of ε_{avg}).

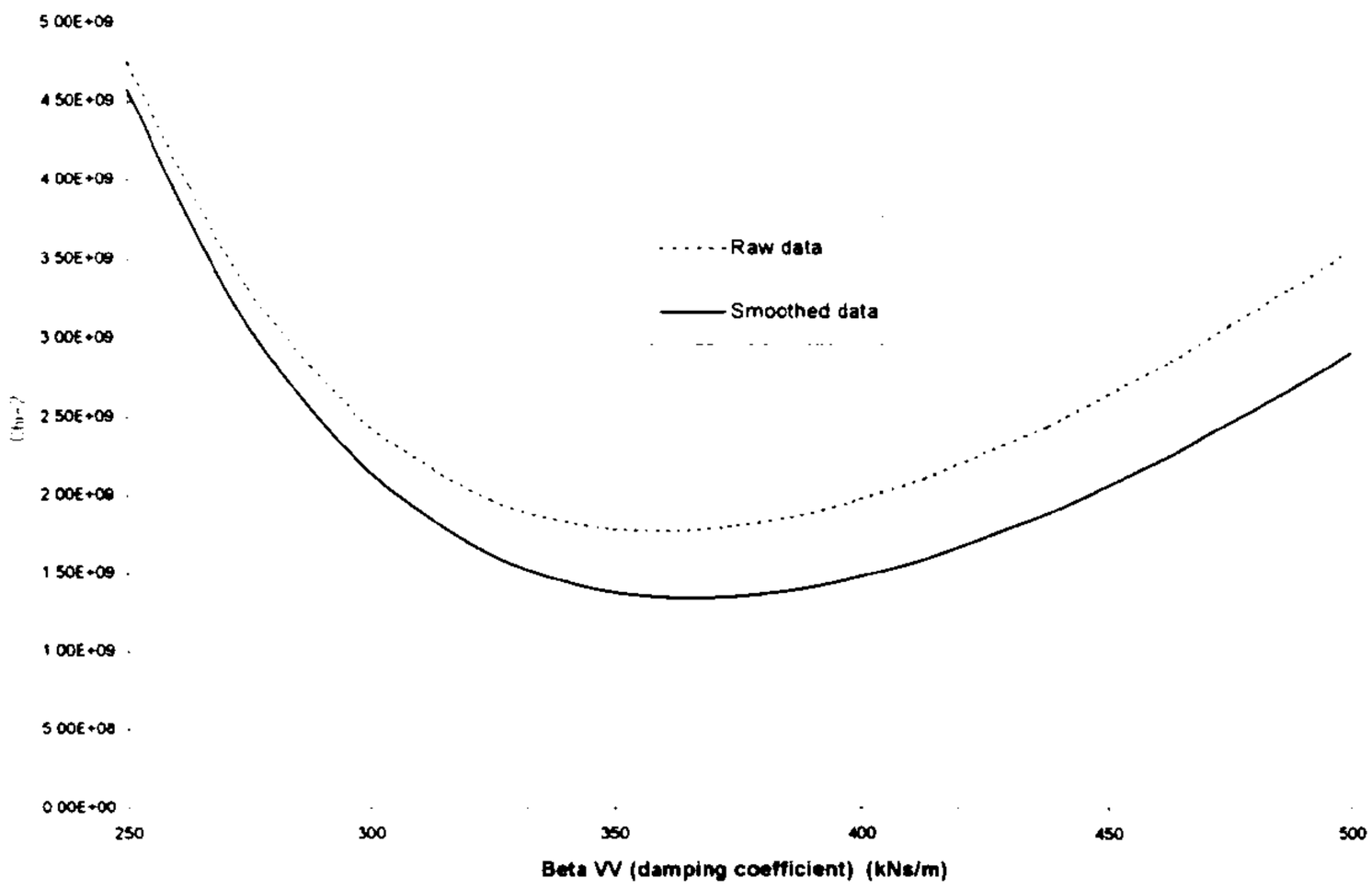


Fig. 5.2 - Effect of de-spiking on the fitting procedure, exemplified by the profile of χ^2 as a function of the parameter β_{VV} close to the minimum.

5.1.2 JET Pulse 20802

This 4MA, 2.5 T downward VDE gives the largest rolling motion ever recorded. The disruption was apparently due to a trip of the neutral beams and led to a vacuum leak (developed in a non-critical external connection).

Fitting the simplified model (4.38) provides the non-dimensional parameters ξ=0.056, f=13.6 Hz. In this case the frequency is higher, consistently with the presence of the Inner Restraint Ring. The measured and simulated rolling motion traces are plotted in Fig. 5.3, which shows a good quality fitting with ε_{avg}=1.1%. The estimated parameters are listed in Table 5.1, including a vertical force pulse of 2.7 MN $\times$ 44 ms.

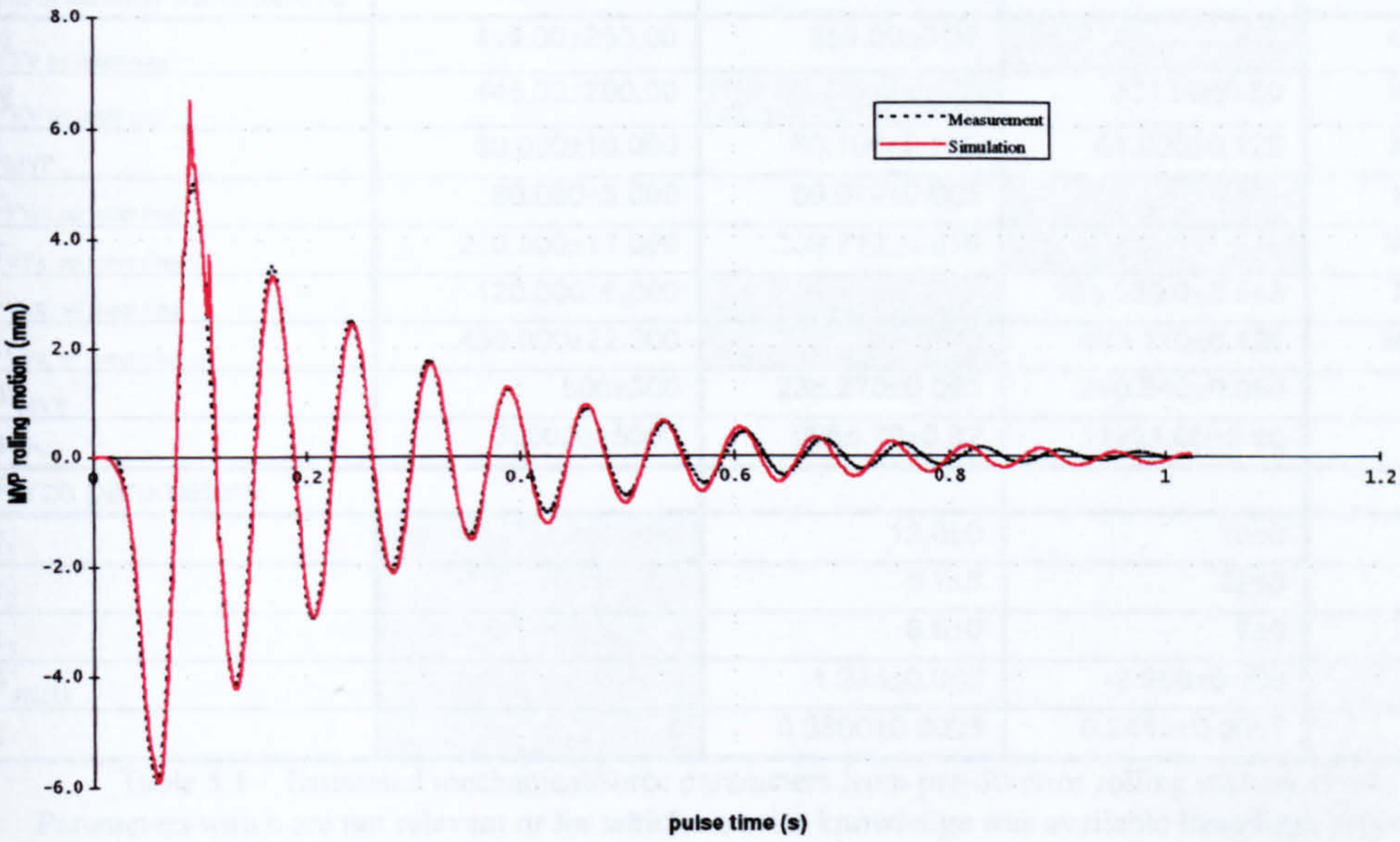


Fig. 5.3 - Rolling motion of pulse 20802

5.1.3 Summary of results

Results from the parameter estimation of pulses 16297 and 20802 indicate that the model is adequate to reproduce with very good accuracy the observed vessel displacements in the relatively simple pre-divertor cases. The estimated geometric parameters, stiffness ratios and masses, all listed in Table 5.1, are reasonably close to the initial guesses.

Geometry parameters	Prior knowledge	JPN 16297 (no Inner Ring)	JPN 20802 (with Inner Ring)	Unit
ρ	2.1000±0.2000	2.5005±0.0001	2.5173±0.0003	m
ε_{MHP}	2.0±0.1	2.0±0.0	2.0±0.0	m
h_{MVP}	3.7000±0.5000	3.4980±0.0008	3.6500±0.0046	m
Mechanical parameters				
$\beta_{VV\ no\ inner\ ring}$	416.00±265.00	359.00±0.07		kNs/m
$\beta_{VV\ w/\ inner\ ring}$	445.00±290.00		331.00±0.80	kNs/m
k_{MVP}	60.000±10.000	60.100±0.110	61.000±0.120	MN/m
$k_{VV0,\ no\ inner\ ring}$	60.000±3.000	59.972±0.005		MN/m
$k_{VV\varepsilon,\ no\ inner\ ring}$	210.000±11.000	209.712±0.016		MN/m^2
$k_{VV0,\ w/\ inner\ ring}$	120.000±6.000		120.039.0±0.048	MN/m
$k_{VV\varepsilon,\ w/\ inner\ ring}$	430.000±22.000		430.170±0.126	MN/m^2
m_{MVP}	500±300	235.270±0.023	250.340±0.080	kg
m_{VV}	30000±15000	9955.70±0.82	11231.00±5.60	kg
Force parameters				
τ_1		12.0±0	16±0	ms
τ_2		5.7±0	22±0	ms
τ_3		8.6±0	6±0	ms
F_{max}		-1.276±0.002	-2.958±0.003	MN
ε		0.3800±0.0003	0.2453±0.0007	m

Table 5.1 - Estimated mechanical/force parameters from pre-divertor rolling motion events. Parameters which are not relevant or for which no prior knowledge was available have been greyed out.

As can be seen, the variances of most parameters are extremely small compared with the initial uncertainties. This feature is discussed more in detail in 7.2.1.

The estimated value of the vessel damping coefficient, β_{VV}=345±15, has been obtained combining the previous estimates on the basis of (4.89). This estimate is important for the analysis of the pulses in the next section, where it will prove useful to discriminate more precisely the magnitude of the other damping sources (namely, the hydraulic dampers at the Main Vertical Ports).

5.2 Analysis of MkII divertor events

In this section the parameter estimation procedure is applied to JET disruptions which belong to the phase V and VI of Table 1.1, i.e. the MkII divertor configuration representative of the current status of the machine. In this stage the attention is focused on the estimation of the parameters related to the MVP hydraulic dampers and to the magnetic force. This requires also the support force measurements to be included in the estimation procedure.

5.2.1 JET Pulse 37628

This upwards VDE has been selected as one of the most violent events in the MkII campaign, with 3.6 mm of rolling motion (x_{RM}) swing and 3.4 MN of vertical MVP support force (R_{MVP}) swing (see Fig. 5.4 and 5.5). The disruption occurred when the plasma touched one of the limiters during a soft stop due to a divertor cooling alarm. This event, too, provoked an air leak which forced the session to be abandoned.

The first step of the analysis consists in identifying clearly the divide between the initial quasi-steady state ($t \le t_0$) and the disruption ($t > t_0$). Since this cannot be done unambiguously on the basis of the fast time traces represented in Fig. 5.4 and 5.5, one has to examine also their slow counterparts together with the plasma current and position (see Fig. 5.6). From these, one can roughly identify $t_0 \approx 55.39 \pm 0.01$ s as the start of the current quench and vertical displacement giving rise to vertical forces; the value $t_0 = 55.395$ s, quoted in Table 5.2 together with all other estimated parameters, is the one which gives the best match to the rising front of the mechanical measurements. Note that the nominal disruption time $t_{DISR} = 55.338$ s, stored in the JPF database, is related to the energy quench (associated with the small bump in I_{PLA} visible in Fig. 5.6) and, therefore, can only be used as a lower bound for t_0.

As the next step, the offset of x_{RM} and R_{MVP} has to be adjusted, making use again of the slow signals, so as to get $x_{RM}(0) = R_{MVP}(0) = 0$. This correction is necessary in order to compare correctly the measurements to the conditions at the beginning of the pulse, which are usually taken as reference. The initial force parameters F_0 and ε_0 are then determined as those that give the best match to both signals at $t = t_0$ precisely.

The estimation procedure has been applied only to the data points with $t \ge t_0$. The best fitting simulated traces are also plotted in Fig. 5.4 and 5.5, with average errors ε_{avg} respectively 2.1% for the rolling motion and 3.4% for the support force. As in all other disruptions examined a perfect fit cannot be obtained for both measurements simultaneously; a greater weight has been assigned to the displacement signal, which has a comparatively small error bar (±0.5%) respect to the force error (±2.5%). The following major inconsistencies can be noted:

— the damping of the oscillations is less pronounced in R_{MVP} than in x_{RM};
— the rate of decay of the support force in the tail of the signal is higher than the corresponding rate for the displacement

These differences are, to a certain extent, expected from the Finite Element results in Table 3.1, which indicate that a single d.o.f. model cannot simulate well the vertical support force.

The radial force on the Main Vertical Port (F_{MVP}), which is the mechanical quantity of ultimate interest in the rolling motion model, has also been analysed for this pulse. Fig. 5.7 and 5.8 show respectively the damping force

$$F^*_{damp}=b_0\dot{x}_{RM} + b`\dot{x}^2_{RM} \tag{5.1}$$

and the total force

$$F^*_{MVP}= F^*_{damp} + m\ddot{x} \tag{5.2}$$

obtained directly from the measurement on the basis of the input reversal approach described in section 4.1.2. As the numerical differentiation of the measured signal is inherently prone to noise, smoothing over a rectangular time window of width 10 ms (approximately corresponding to a 50 Hz LPF) has been applied at each stage. The figures show a substantial agreement between the direct estimation and the results of the simulation. This justifies the following conclusions:

- the MVP radial force swing is less than 15 kN, which is much smaller than previous estimates and represents a negligible fraction of the allowable limit.
- the hydraulic damper makes, as expected, the major contribution (corresponding to almost 75% of the total force).

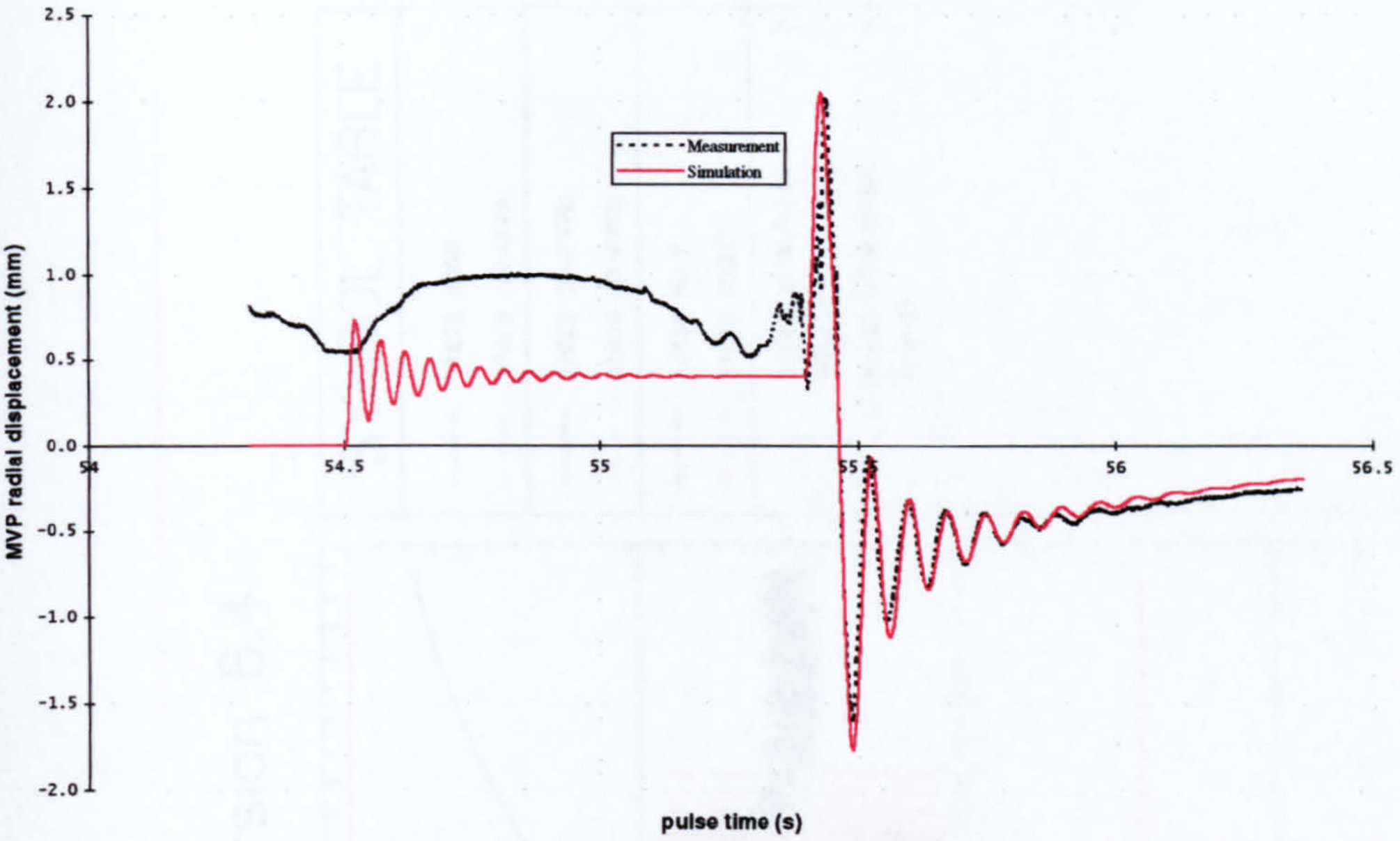


Fig. 5.4 - Rolling motion of pulse 37628

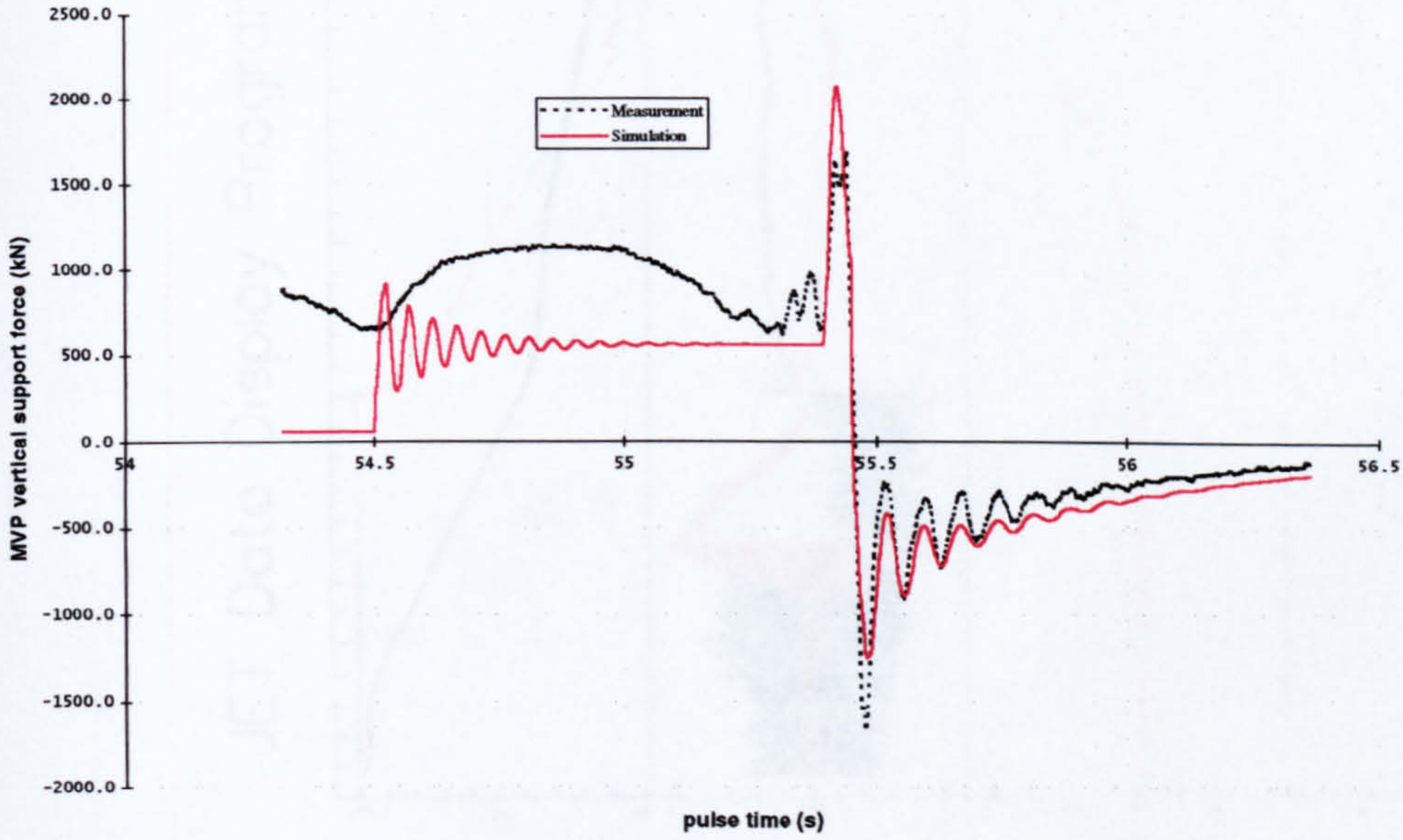


Fig. 5.5 - Vertical MVP support force pulse 37628

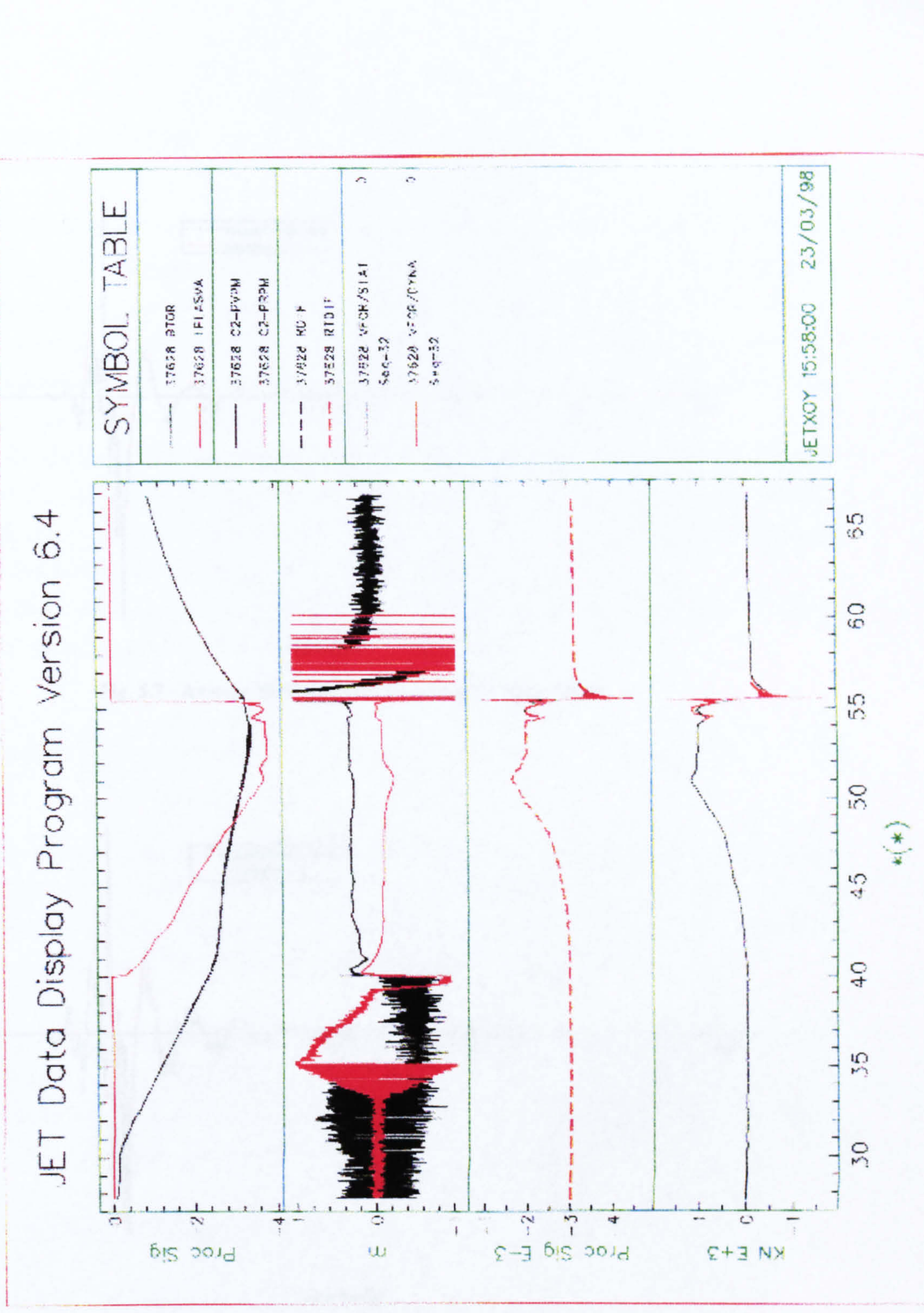


Fig. 5.6 - Mechanical and magnetic measurements for pulse 37628: from top to bottom, plasma current, toroidal field, vertical and radial plasma position, rolling motion (fast and slow signals), vertical support force (fast and slow)

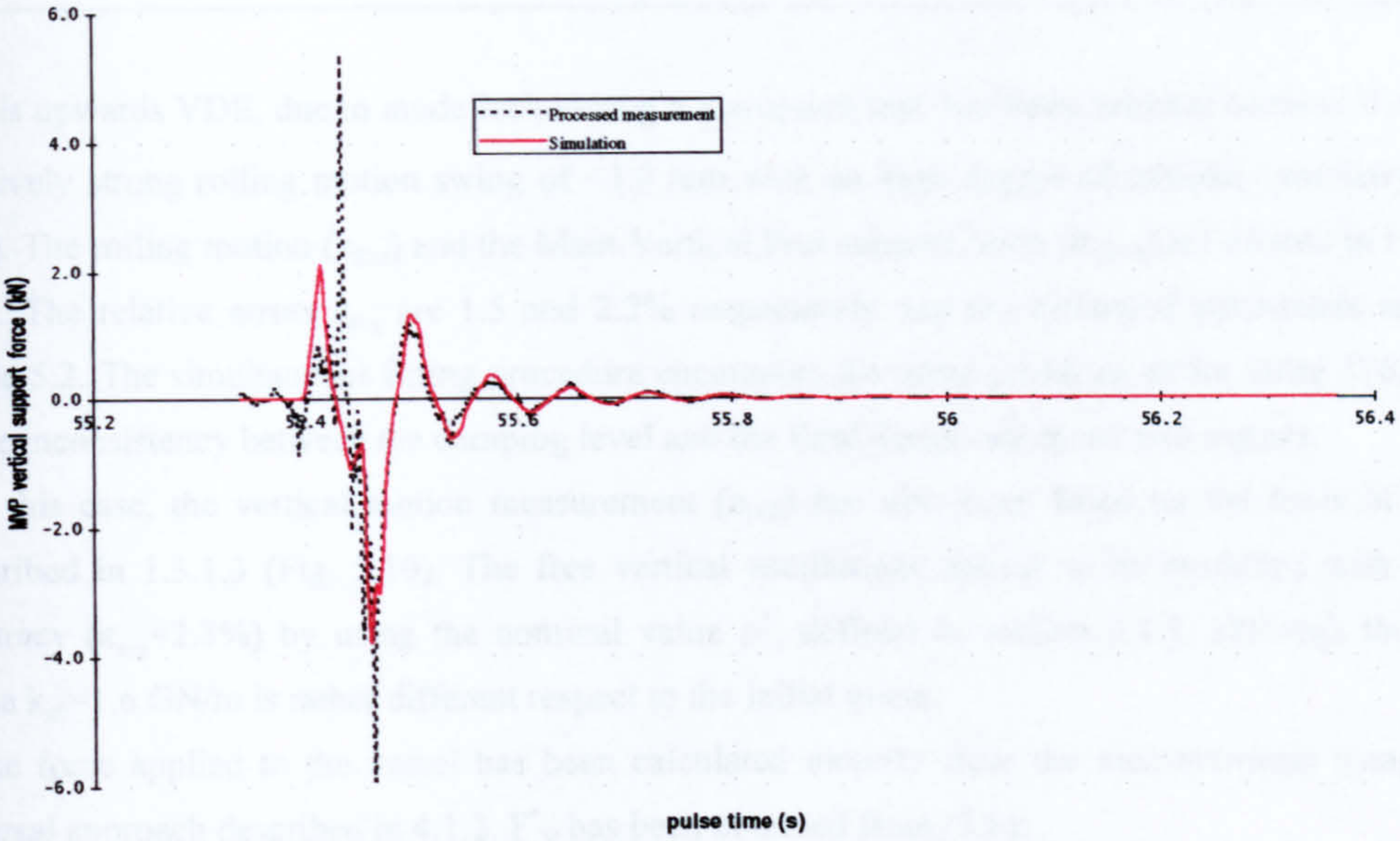


Fig. 5.7 - Average MVP damper radial force for pulse 37628

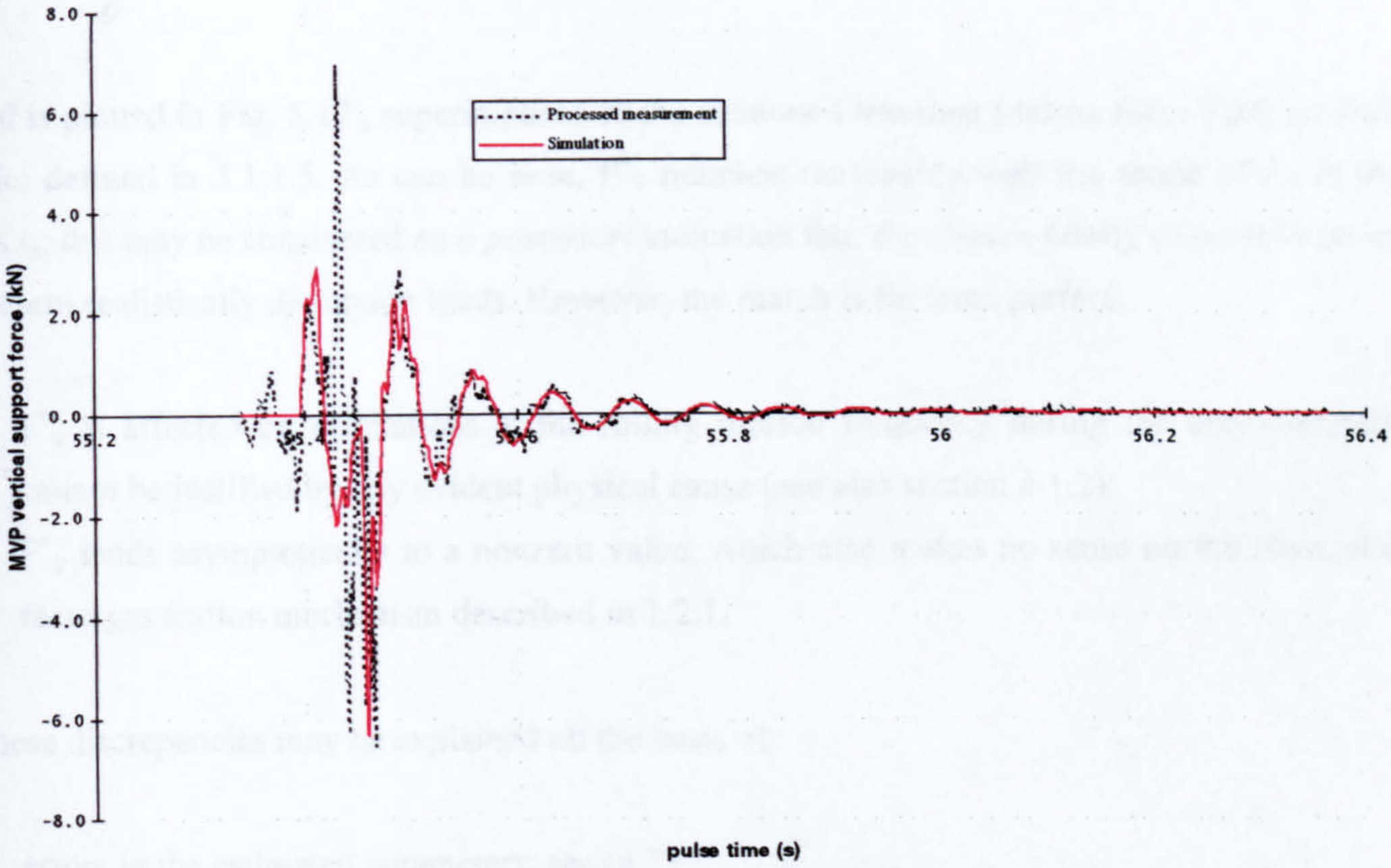


Fig. 5.8 - Average total MVP radial force for pulse 37628

5.2.2 JET Pulse 38690

This upwards VDE, due to mode lock during a disruption test, has been selected because it combines a relatively strong rolling motion swing of ~3.0 mm with an high degree of toroidal symmetry ($\delta_{SW} \leq 0.3$ mm). The rolling motion (x_{RM}) and the Main Vertical Port support force (R_{MVP}) are plotted in Fig. 5.9 and 5.11. The relative errors ε_{avg} are 1.5 and 2.2% respectively and the estimated parameters are listed in Table 5.2. The simultaneous fitting procedure encounters the same problems as for pulse 37628, namely some inconsistency between the damping level and the final decay rate in the two signals.

In this case, the vertical motion measurement (z_{IVP}) has also been fitted on the basis of the model described in 1.3.1.3 (Fig. 5.10). The free vertical oscillations appear to be modelled with reasonable accuracy (ε_{avg}=2.3%) by using the nominal value ρ^*_z defined in section 3.1.2, although the estimated value k_{z0}=1.6 GN/m is rather different respect to the initial guess.

The force applied to the vessel has been calculated directly from the measurements using the input reversal approach described in 4.1.2. F^*_V has been obtained from (3.6):

$$F_V^* = \frac{1}{1-\frac{\varepsilon}{\rho}}\left\{R_{MVP} - \ddot{x}\frac{\beta m_{MVP}}{\lambda k_{MVP}} - \ddot{x}\left[\frac{16h}{\rho}m_{MVP} + \frac{\beta b_{MVP} + k(\varepsilon)m_{MVP}}{\lambda k_{MVP}}\right] - \dot{x}\left[\frac{16h}{\rho}b_{MVP} + \frac{\beta k_{MVP} + k(\varepsilon)b_{MVP}}{\lambda k_{MVP}}\right] - x\frac{k(\varepsilon)}{\lambda}\right\} \tag{5.3}$$

and is plotted in Fig. 5.12., superimposed to the estimated transient plasma force $F_V(t)$ according to the model defined in 3.1.1.5. As can be seen, F^*_V matches reasonably well the shape of F_V in the interval $t_0 \leq t \leq t_3$; this may be considered an *a posteriori* indication that the chosen family of waveforms can indeed represent realistically disruption loads. However, the match is far from perfect:

— F^*_V is affected by oscillations at the rolling motion frequency during the decaying phase which cannot be justified by any evident physical cause (see also section 4.1.2).
— F^*_V tends asymptotically to a nonzero value, which also makes no sense on the basis of the vessel force generation mechanism described in 1.2.1.

These discrepancies may be explained on the basis of:

- errors in the estimated parameters: see (4.7)
- errors in the reversed input approach: it may be not possible to get consistent results from (5.3) since it also contains parameters which are not measured directly, like ε, but which have to be fixed arbitrarily
- errors in the model: a 2 d.o.f. model may not be sufficient to capture all the subtleties of the response of such a complex system (see also 3.1.1.2)

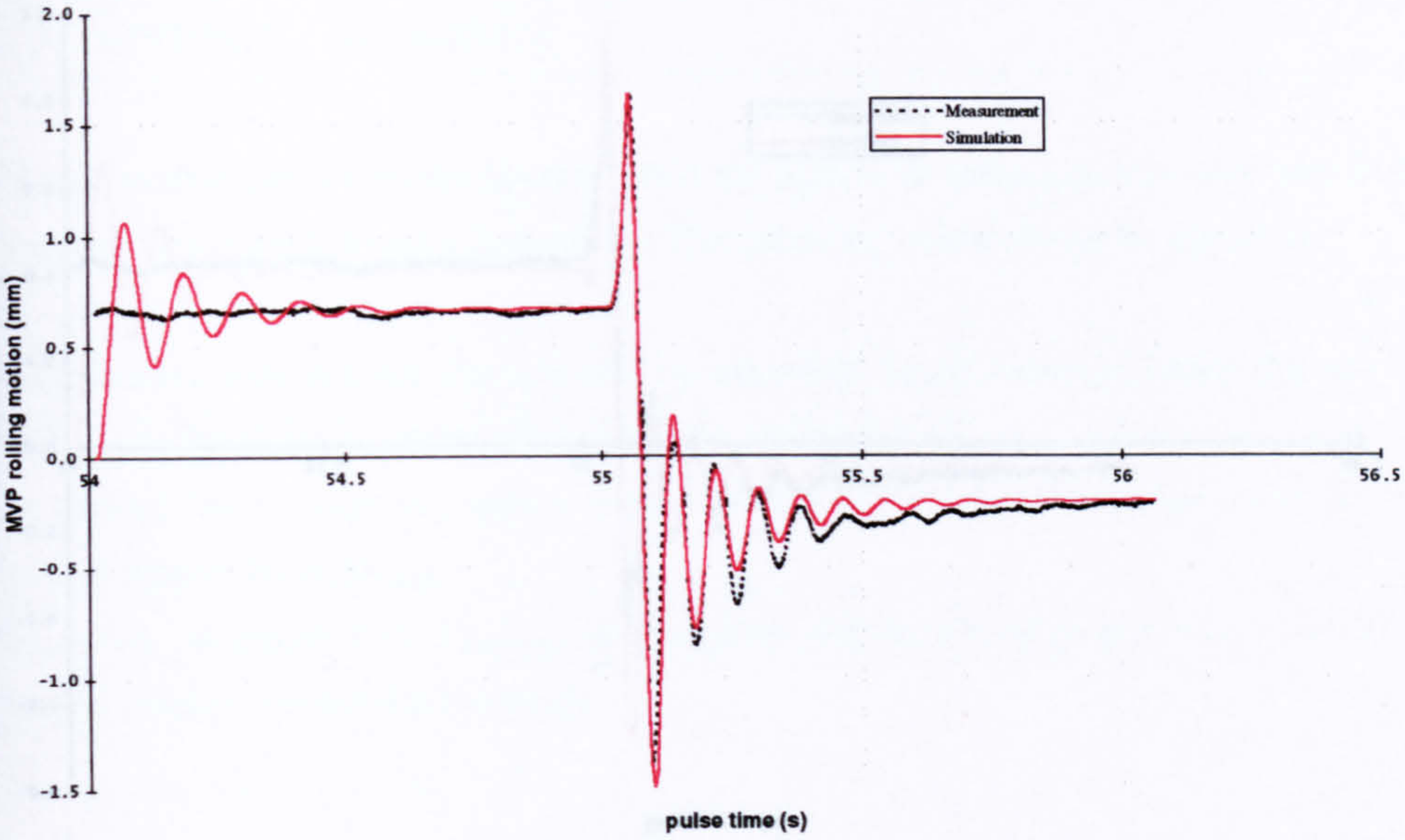


Fig. 5.9 - Rolling motion of pulse 38690

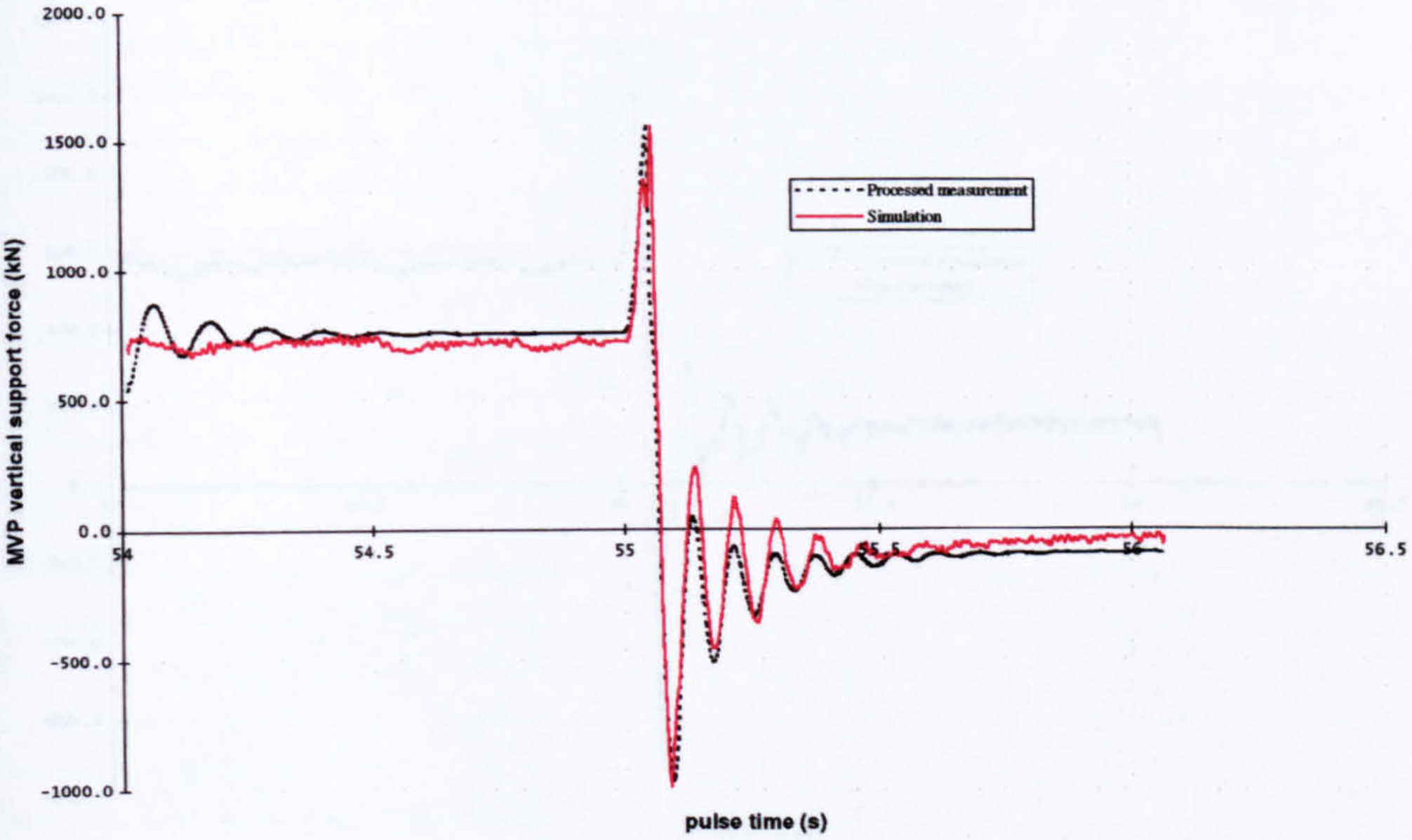


Fig. 5.10 - Vertical MVP support force pulse 38690

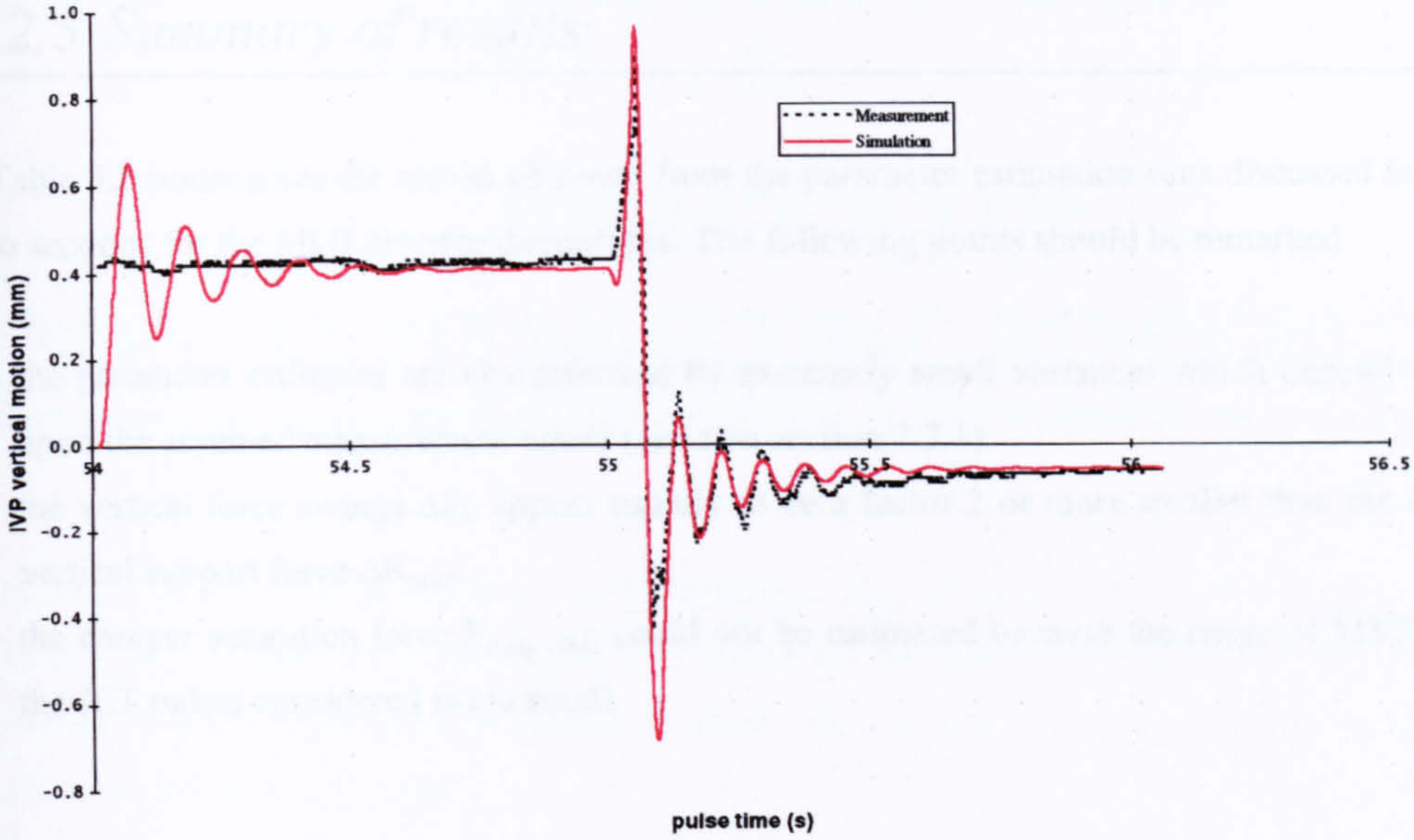


Fig. 5.11 - Vertical IVP motion pulse 38690

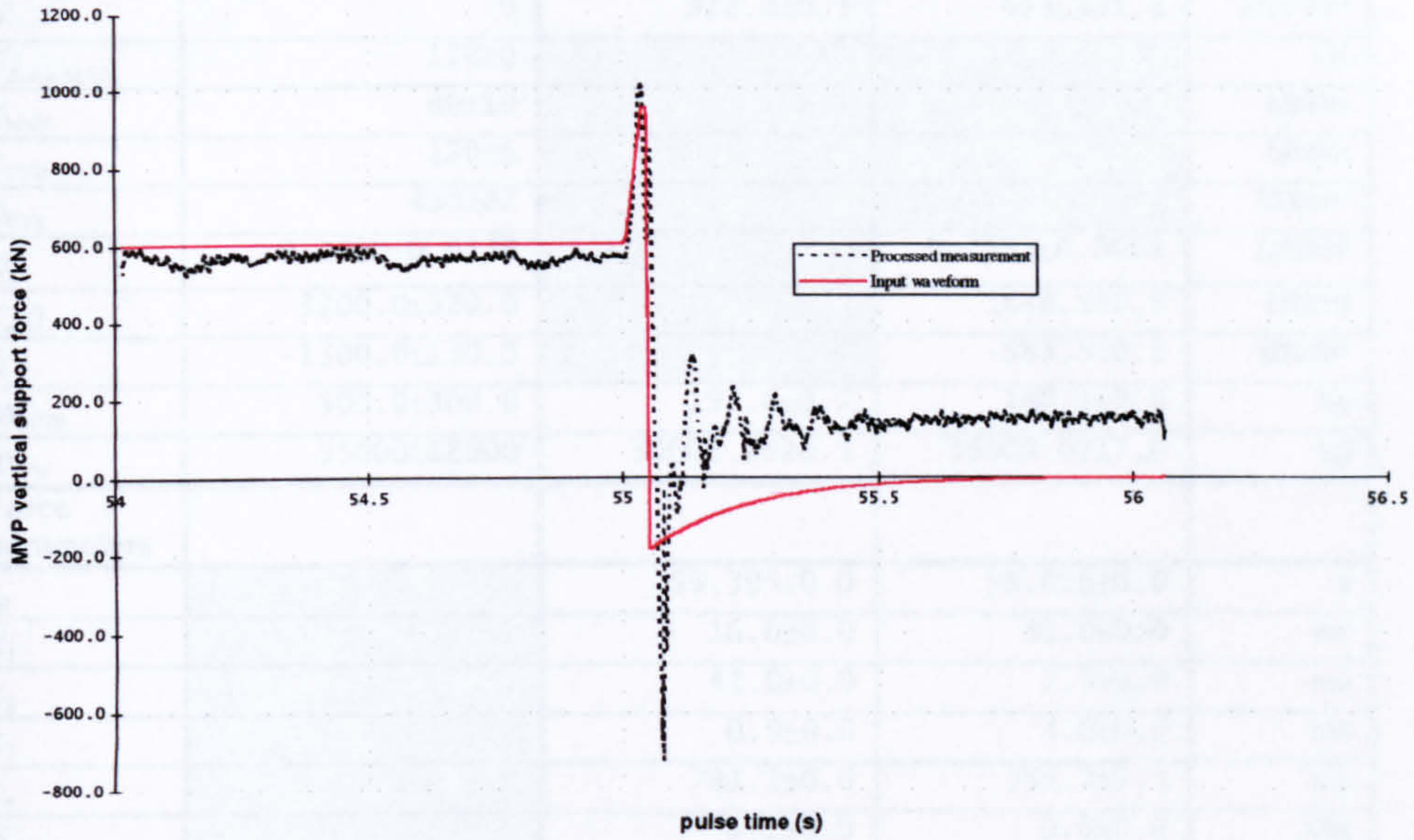


Fig. 5.12 - Vertical vessel force pulse 38690

5.2.3 Summary of results

Table 5.2 summarises the results obtained from the parameter estimation runs discussed in the previous two sections for the MkII divertor disruptions. The following points should be remarked:

- the parameter estimates are characterised by extremely small variances which depend very strongly upon the assumed measurement errors (see also section 7.2.1)
- the vertical force swings ΔF_V appear usually to be a factor 2 or more smaller than the swings of the vertical support force ΔR_{MVP}.
- the damper saturation force $F_{damp,MAX}$ could not be estimated because the range of MVP velocities in the JET pulses considered is too small.

Mechanical parameters	Prior knowledge	JPN 37628	JPN 38690	Unit
β	365±183	377.4±3.5	362.5±1.3	kNs/m
b_0	300±50	1.789±0.045	1.824±0.040	kNs/m
b`	0	322.6±0.5	473.4±1.1	kNs^2/m^2
$F_{damp,MAX}$	120±0			kN
k_{MVP}	60±10			MN/m
k_{VV0}	120±6			MN/m
$k_{VV\varepsilon}$	430±22			MN/m^2
ρ_z	0.2780±0.0139		0.2551±0.0001	MN/m^2
k_{Z0}	3200.0±320.0		1648.5±0.5	MN/m
k'_z	-1300.0±130.0		-883.5±0.1	MN/m^2
m_{MVP}	500.0±300.0	197.6±0.7	180.1±0.6	kg
m_{VV}	35000±18000	30602.2±26.1	36009.0±17.0	kg
Force parameters				
t_0		55.395±0.0	55.010±0.0	s
τ_1		16.0±0.0	31.0±0.0	ms
τ_2		41.0±0.0	7.5±0.0	ms
τ_3		0.9±0.0	4.0±0.0	ms
τ_4		791.1±0.0	355.7±2.5	ms
F_0		0.2±0.0	0.6±0.0	MN
F_{max}		0.729±0.0012	1.003±0.002	MN
F_{min}		-0.4997±0.0005	-0.191±0.001	MN
ε_0		1.0024±0.0055	0.2498±0.0006	m
ε_1		0.7749±0.0011	0.7513±0.0009	m

Table 5.2 - Estimated force parameters from MkII rolling motion events

6

ANALYSIS OF NON-AXISYMMETRIC DISRUPTIONS

This chapter presents the results of the application of the parameter estimation method to the sideways motion model, defined in section 3.2, which represents the major non-axisymmetric component of the vessel response to disruptions. Work on the global eight-octant vessel model is still ongoing and only preliminary results are presented.

Two particularly representative JET pulses have been analysed in detail:

Pulse	Date	I_{PLA} (MA)	B_T (T)	t_{DISR} (s)	Notes:
34078	24/2/95	3.6	2.40	53.417	First occurrence of sideways motion to be noticed
38705	19/9/96	4.0	3.20	56.791	Largest occurrence of sideways motion ever (7.1 mm)

6.1 Analysis of sideways events

In this section the parameter estimation procedure is applied to the mechanical model describing the sideways motion of the vessel as a whole in the horizontal plane (see section 3.2). This model is considerably more complex and uncertain than the one representing the rolling motion, considered in detail in the last chapter; this makes the analysis correspondingly more difficult. Some of the problems encountered are the following:

- the physical nature of the underlying plasma kink mode is not clear
- the geometry of the horizontal restraints and mass distribution is very complicated (see for example Fig. 1.10), which makes the single-d.o.f. lumped-parameter approximation inherently less accurate
- the large half-vessel Finite Element model is very time-consuming to run and, consequently, a limited range of load cases has been analysed in support of the model
- some critical spring ratios (as for example k_{NBI}) depend upon very complicated connections and could be estimated only to a large degree of uncertainty.

6.1.1 JET Pulse 34078

This pulse represents the first occurrence of sideways motion to be noticed in 1995 and, as such, is perhaps the one most thoroughly studied in the history of the Engineering Analysis Group at JET [24]. The disruption was due to a growing MHD mode which caused the radial field amplifier to drift and subsequently trip, leading to loss of vertical stability.

The dominant component of the sideways motion of this pulse, i.e. the projection in the direction from octant 5 to octant 1 has been analysed. The measurements of the sideways motion of the vessel and of the sideways reaction force given by the MVP supports, plotted in Fig. 6.13 and 6.14, have been fitted simultaneously. The results are listed in Table 6.3.

The vessel displacement exhibits a typical behaviour for this kind of events, i.e. a whiplash effect due to the NBI mass. The vessel mass is first accelerated forward, reaches the maximum displacement at $t \approx t_0+60$ ms and then is pulled back by the combined action of the MVP supports and the magnetic stiffness. The mass of the NBI follows the movement with some delay, as shown in Fig. 6.13. Around t=53.56 s the distance between vessel and NBI reaches a maximum of ~6 mm and the vessel is pulled forward again, inverting its motion. The total elastic force between vessel and NBI (plotted in Fig. 6.15) peaks then at about 400 kN (~20 tonnes per unit).

As one can see, the quality of the fit is generally worse than that achieved for the axisymmetric cases, the relative errors being ε_{avg}=8.8% for the displacement and 5.2% for the support force. The problems encountered in the parameter estimation procedure can be summarised as follows:

— oscillations in the final phase (t≥53.7 s) cannot be reproduced by whatever combination of masses and spring constants, when priority is given to a good fitting of the initial transients is imposed. This means likely that more d.o.f. are necessary for a correct simulation.

— Coulomb friction is not able to simulate the final average offset in the displacement signal x_{SW} without imposing a similar offset to the support force R^T_{MVP} (since $R^T_{MVP}=k^T_{MVP}x_{SW}$), which on the other hand appears to oscillate around zero. Therefore, one can either assume that R^T_{MVP} is wrong or use instead the additional friction mechanism described in 3.2.1.5 (see the analysis of pulse 38705 in the next section).

The applied sideways force F_{SW} is plotted in Fig. 6.15 together with the sideways force F^*_{SW} calculated on the basis of the input reversal approach (see section 4.1.2). For the sake of simplicity, given the high level of initial uncertainty that affects most parameters, this is simply taken to be the inertia force on the vessel mass $F^*_{SW} = m_{VV}\ddot{x}_{SW}$. The peak value and the duration of the load (approx. 2.6 MN×45 ms) show a remarkably good agreement between themselves and with the upper bound F_{SW}=2.7 MN calculated in 2.2.2.3 on the basis of the magnetic interaction between kinked plasma and TF coils; these values are also consistent with previous assessments [27].

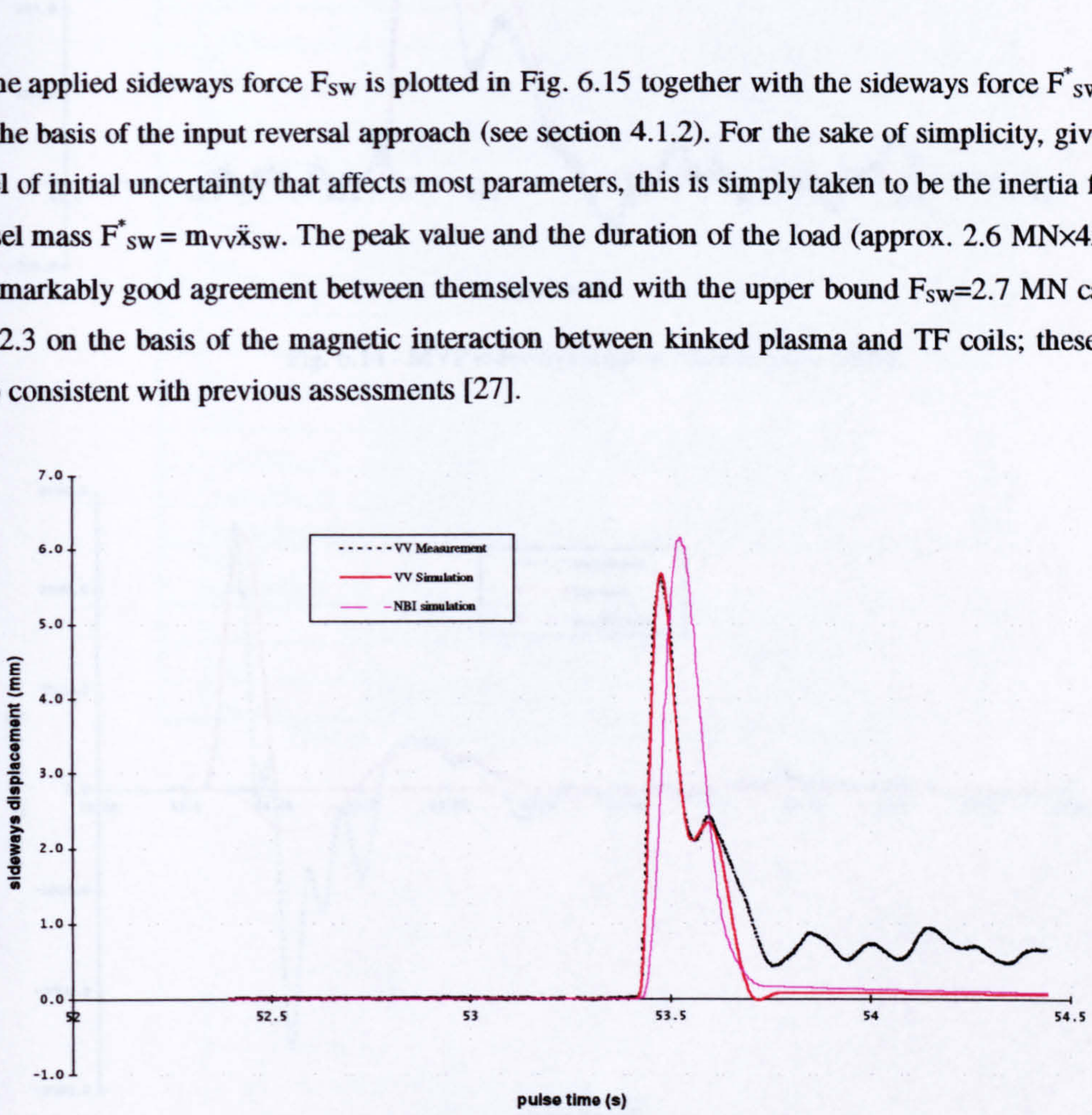


Fig. 6.13 - Sideways motion of pulse 34078

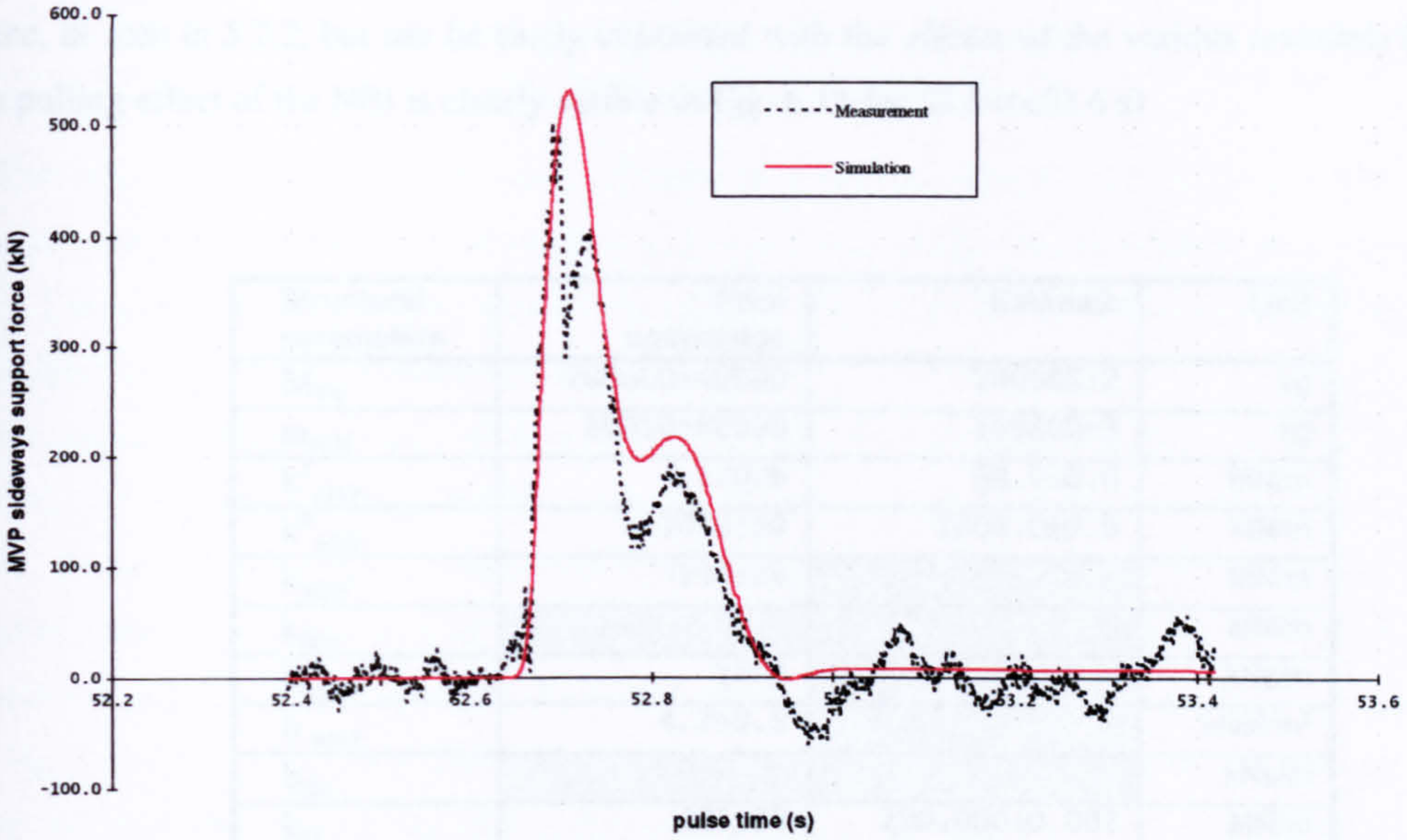


Fig. 6.14 - MVP sideways support force in pulse 34078

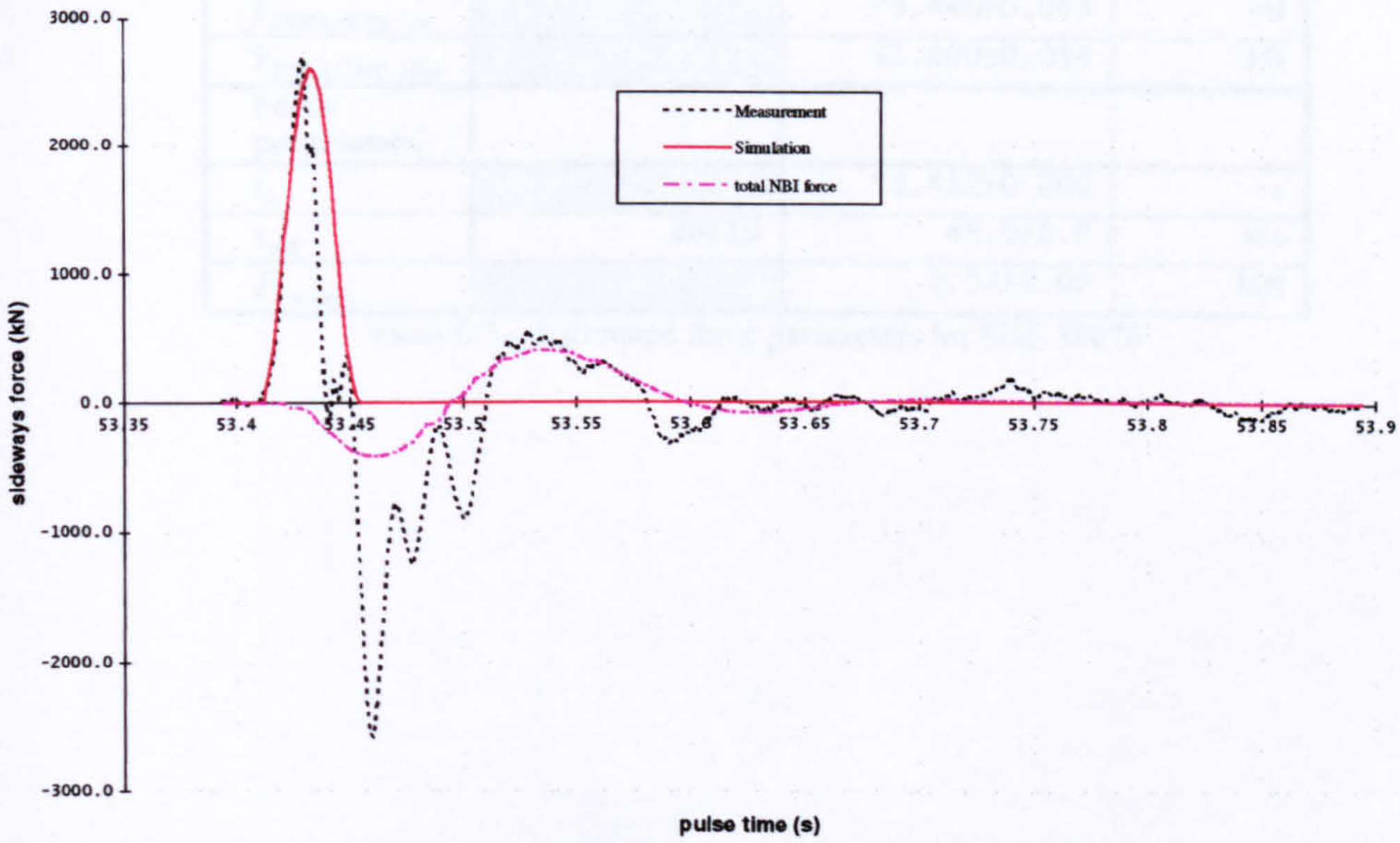


Fig. 6.15 - Sideways force in pulse 34078

Further oscillations in F^{*}_{SW} after the initial transient are not to be necessarily attributed to the magnetic force, as seen in 5.2.2, but can be easily explained with the effects of the various restraints (for instance, the pulling effect of the NBI is clearly visible in Fig. 6.15 for 53.5<t<53.6 s)

Structural parameters	Prior knowledge	Estimate	Unit
M_{VV}	200000±40000	240088±2	kg
m_{NBI}	80000±80000	159800±3	kg
k^{T}_{MVP}	120±6	94.0±0.0	MN/m
k^{R}_{MVP}	1000±50	1200.0±0.0	MN/m
k_{MHP}	533±26		MN/m
k_{HH}			MN/m
$b_{0,MVP}$	18±2		kNs/m
$b`_{MVP}$	4.7±0.5		kNs^2/m^2
b_{HH}			kNs/m
k_{M}	288±29	290.000±0.002	MN/m
k_{NBI}	120±80	112.0±0.0	MN/m
b_{M}	236±24	515.7±0.0	kNs/m
b_{NBI}		1.919±0.003	kNs/m
$F_{FRICTION, MVP}$			kN
$F_{COULOMB, VV}$		73.440±0.043	kN
$F_{COULOMB, NBI}$		51.800±0.054	kN
Force parameters			
t_0		53.412±0.000	s
τ_{SW}	20±10	45.0±0.0	ms
$F_{SW,max}$		2.57±0.00	MN

Table 6.3 - Estimated force parameters for SDE 34078

6.1.2 JET Pulse 38705

This pulse represents the most severe instance of sideways motion ever recorded. The disruption was due to a very large n=1 and n=2 mode lock in a high triangularity configuration and led to a displacement of 7.1 mm in the direction from octant 5 to octant 1. This event is often taken as reference to extrapolate the effect of disruptions to future configurations.

The vessel displacement and MVP support force signals, plotted in Fig. 6.16 and 6.18, have the same general behaviour as in pulse 34078, except for the nonzero offset in the tail of the signals which, in this case, characterises also R^T_{MVP}. The results of the parameter estimation procedure are listed in Table 6.4.

This pulse shows the effects of the tangential MHP dampers installed during the 1996 shutdown. The relative weight of these supports in the vessel response has been quantified by removing them as shown in Fig. 6.19 (where, for comparison, also a simulation without magnetic damping is plotted).

In this pulse the effect of the sliding friction mechanism at the level of the MVP (described in 3.2.1.5) has been applied. This gives a better agreement between the two final offsets than the Coulomb friction alone, although the oscillations in the tail still cannot be reproduced by the model.

Structural parameters	**Prior knowledge**	**Estimate**	Unit
M_{VV}	200000±40000	189110±0.1	kg
m_{NBI}	80000±80000	120630±0.1	tonne
k^T_{MVP}	120±6	97.4±0.0	MN/m
k^R_{MVP}	1000±50	1198±0	MN/m
k_{NBI}	112±6	155±0.000	MN/m
k_{MHP}	533±	533±0.000	MN/m
k_{HH}	184±	190.9±0.0	MN/m
$b_{0,MVP}$	18±2		kNs/m
$b`_{MVP}$	4.7±0.5		MNs^2/m^2
b_{HH}	0.0±0.0	10.1±0.0	MNs/m
k_M	512.0±51.2	477.500±0.003	MN/m
k_{NBI}	120±80	107.3±0.0	MN/m
b_M	4.2±0.4	4.056±0.000	MNs/m
b_{NBI}		1.706±0.005	MNs/m
$F_{FRICTION, MVP}$		-66.379±0.003	kN
$F_{COULOMB, VV}$			kN
$F_{COULOMB, NBI}$		110.250±0.002	kN
Force parameters			
t_0		56.817±0.000	s
τ_{SW}	20±10	35.8±0.0	ms
$F_{SW,max}$		4.1054±0.0015	MN

Table 6.4 - Estimated parameters for SDE 38705

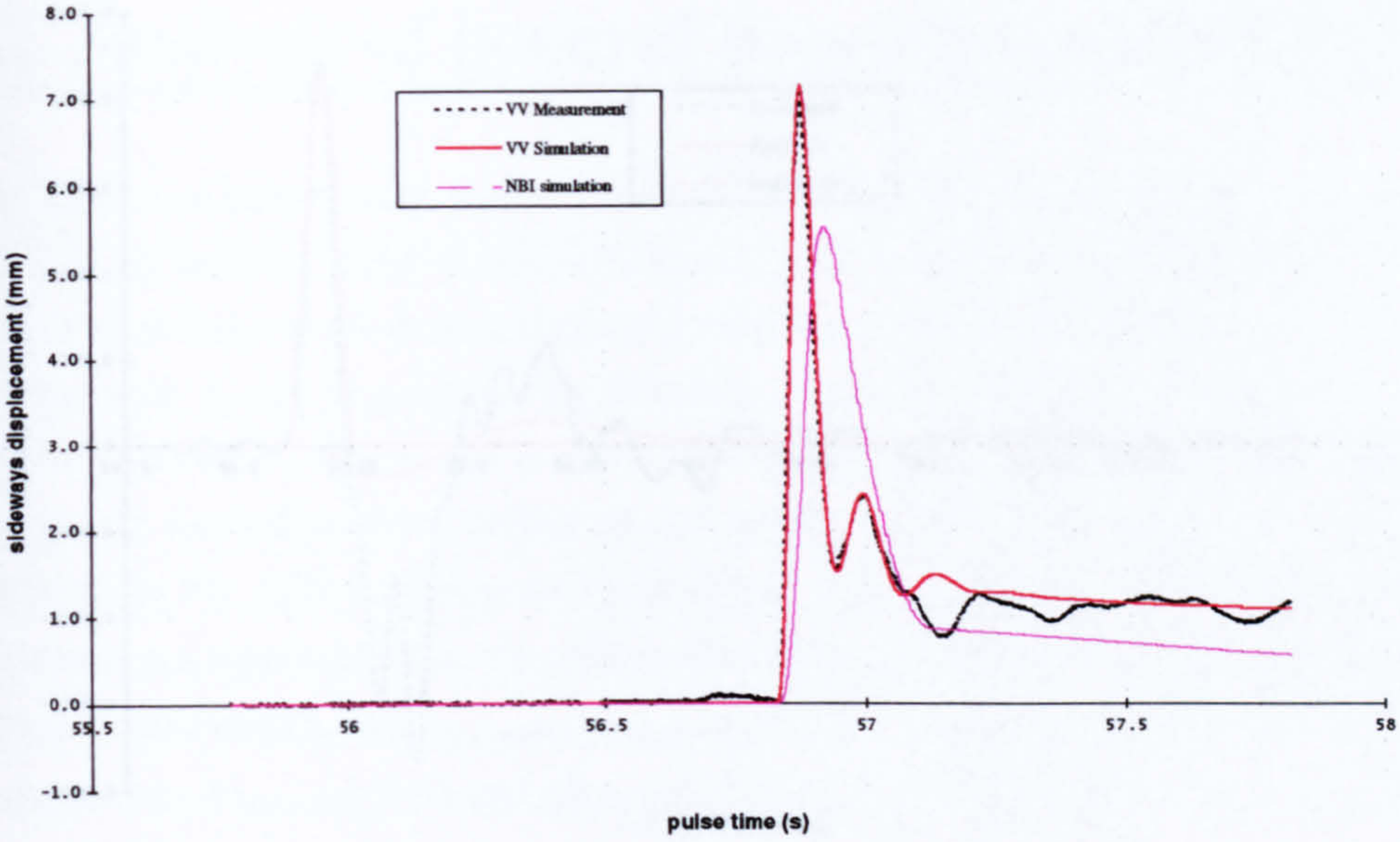


Fig. 6.16 - Sideways motion of pulse 38705

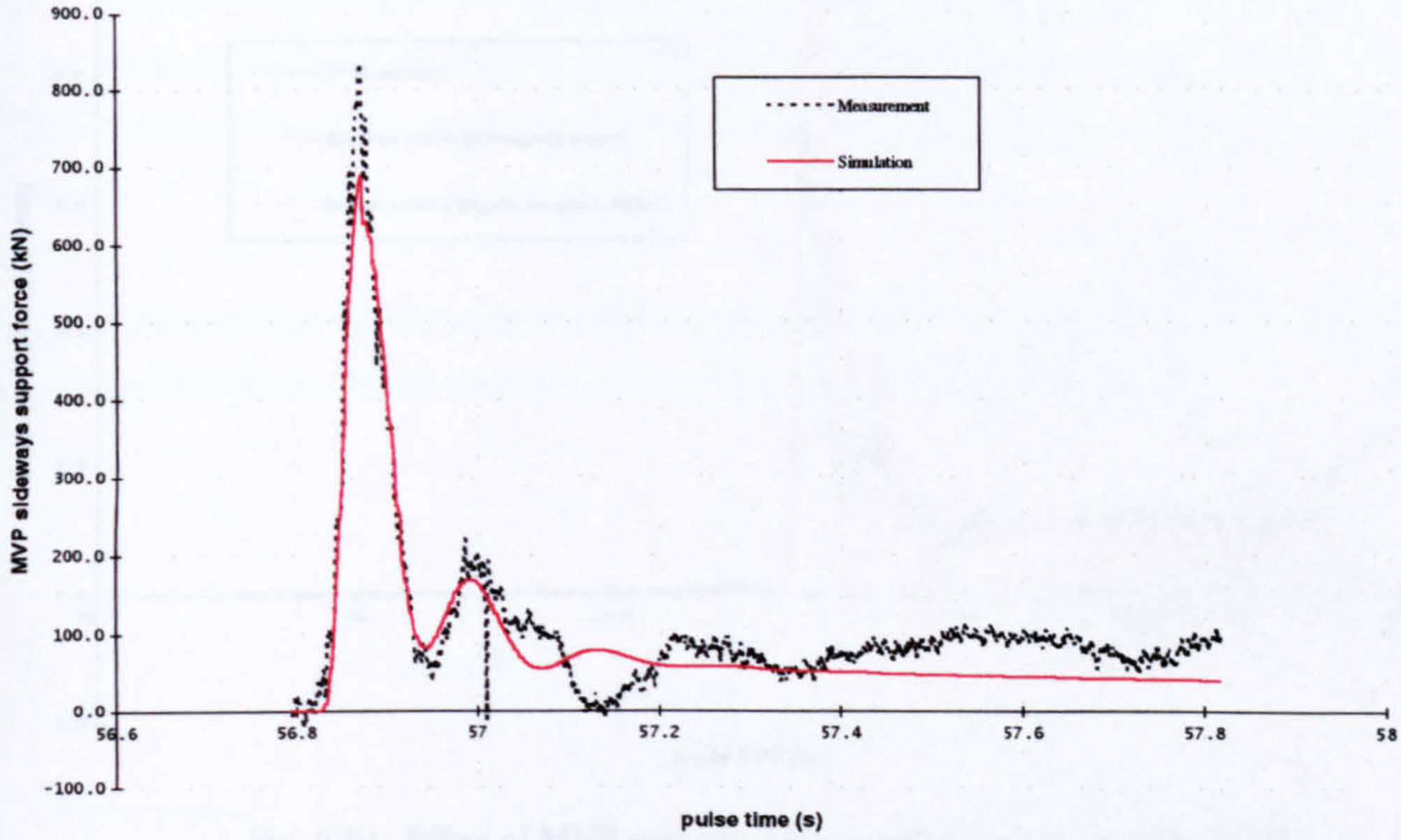


Fig. 6.17 - MVP sideways support force in pulse 38705

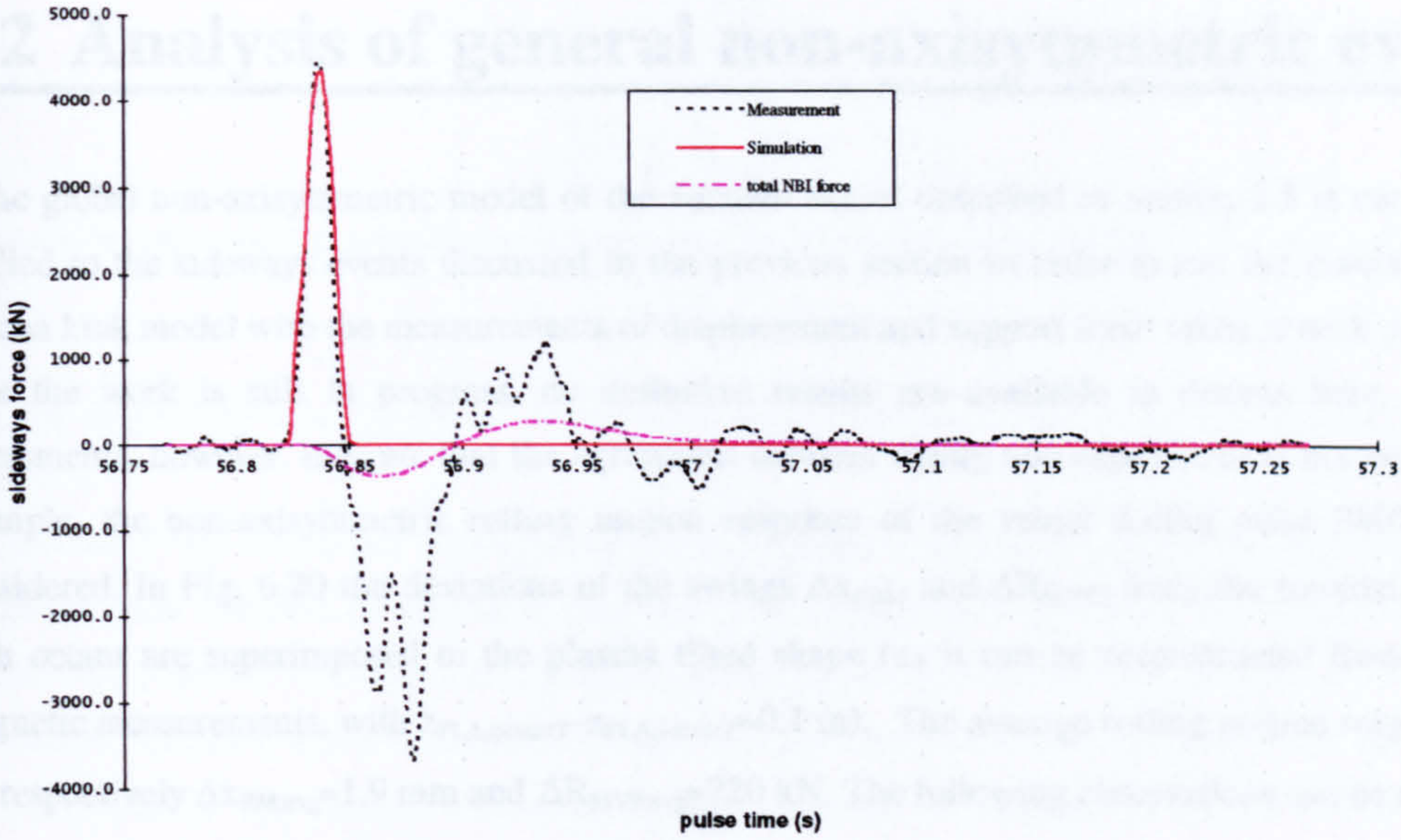


Fig. 6.18 - Sideways force in pulse 38705

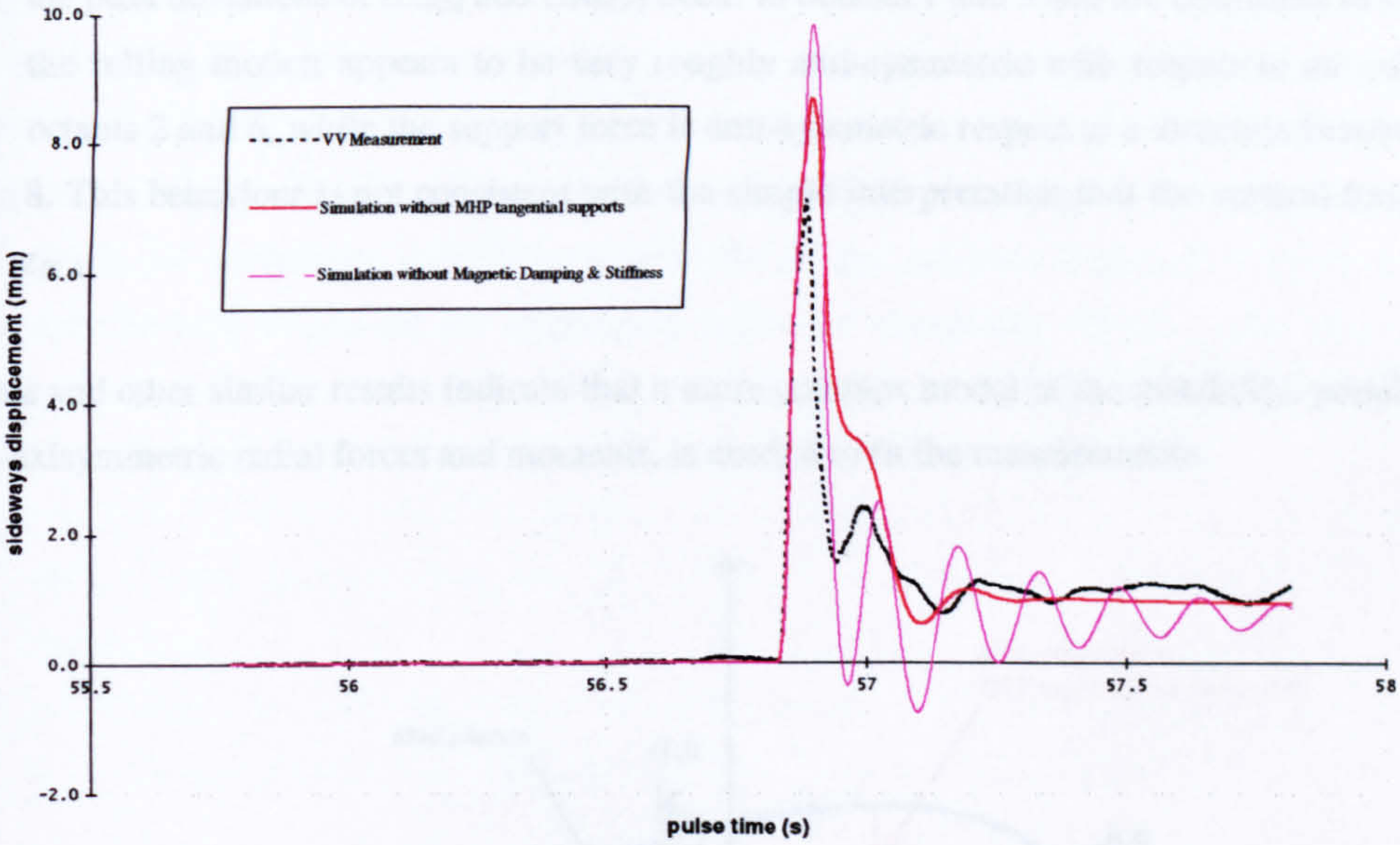


Fig. 6.19 - Effect of MHP supports and magnetic damping in pulse 38705

6.2 Analysis of general non-axisymmetric events

The global non-axisymmetric model of the vacuum vessel described in section 3.3 is currently being applied to the sideways events discussed in the previous section in order to test the consistency of the plasma kink model with the measurements of displacement and support force taken at each octant.

As the work is still in progress, no definitive results are available to discuss here. Preliminary assessments, however, indicate that the agreement between theory and experiment is not very good. For example, the non-axisymmetric rolling motion response of the vessel during pulse 34078 has been considered. In Fig. 6.20 the deviations of the swings $\Delta x_{RM,i}$ and $\Delta R_{MVP,i}$ from the toroidal averages in each octant are superimposed to the plasma tilted shape (as it can be reconstructed from the limited magnetic measurements, with $z_{PLA,octant3} - z_{PLA,octant7} \approx 0.1$ m). The average rolling motion response swings are respectively $\Delta x_{RM,avg} = 1.9$ mm and $\Delta R_{MVP,avg} = 720$ kN. The following observations can be made:

- the deviations from the toroidal symmetry are more than 50% for the rolling motion and 40% for the support force (inconsistently with the FE results shown in section 3.3).
- the peak deviations of Δx_{RM} and ΔR_{MVP} occur in octants 1 and 5 and are consistent in sign.
- the rolling motion appears to be very roughly anti-symmetric with respect to an axis passing by octants 2 and 6, while the support force is anti-symmetric respect to a direction between 3-7 and 4-8. This behaviour is not consistent with the simple interpretation that the vertical force scales with z_{PLA}.

This and other similar results indicate that a more complex model of the instability, possibly including non-axisymmetric radial forces and moments, is needed to fit the measurements.

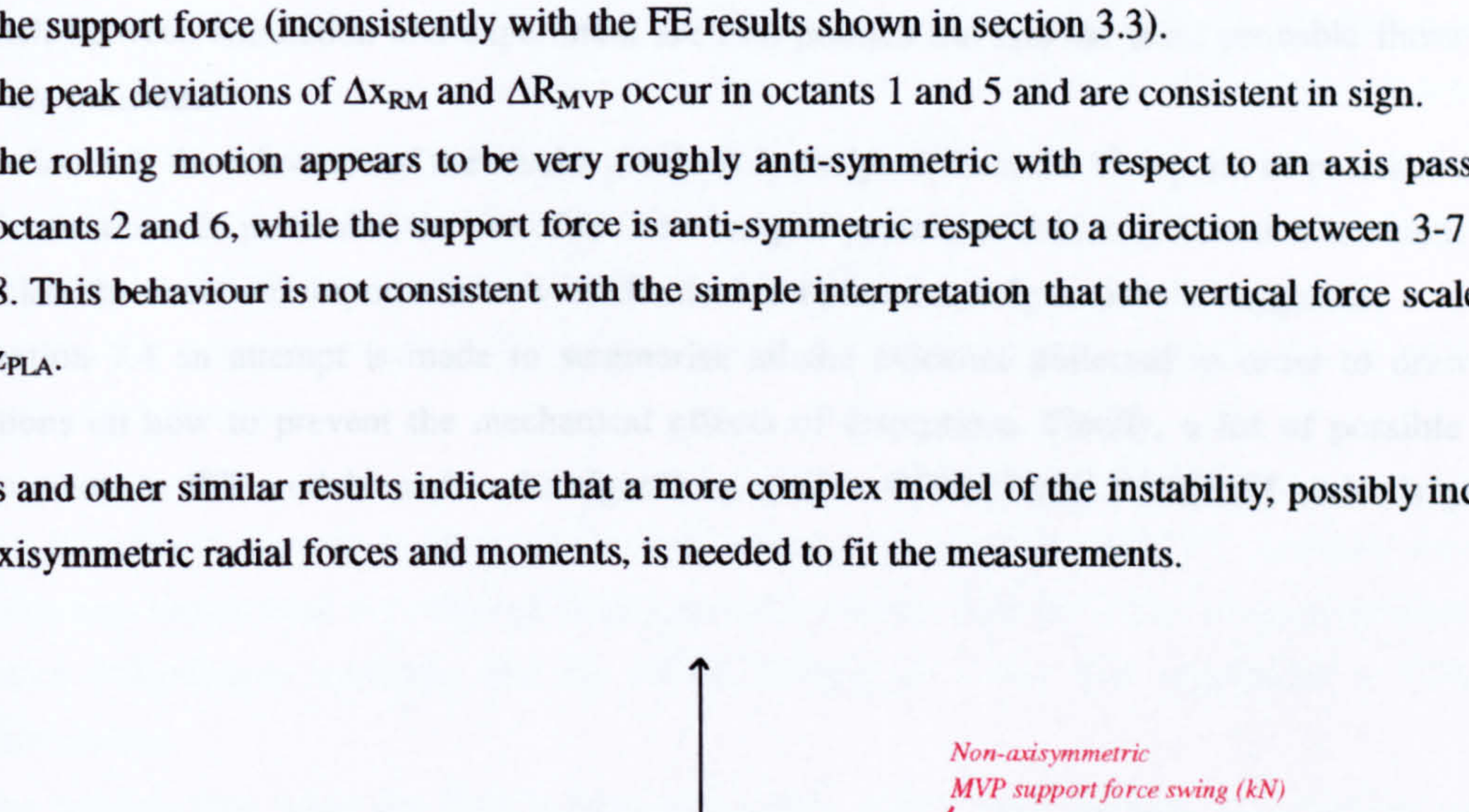


Fig. 6.20 - Deviations from the axisymmetry of rolling motion and vertical support force in pulse 34078

7

RESULTS

In this chapter the results achieved in this work are reviewed, discussed and compared with the initial objectives.

In section 7.1 the merits and drawbacks of the Biot-Savart integration procedure for the magnetic forces on the coils are analysed. In section 7.2 the results of the parameter estimation procedure are discussed. In particular, section 7.2.1 summarises some practical guidelines for the application of the Levenberg-Marquardt algorithm, while sections 7.2.2 and 7.2.3 are concerned with the parameters estimated from the axisymmetric and non-axisymmetric models reported respectively in chapter 5 and 6. Special emphasis is given to the estimated coefficients for the hydraulic MVP dampers and for the magnetic damping, which have a major role in determining vessel stresses. Some inconsistencies arising from the mismatch between simulation and experiment are also pointed out and the most probable flaws of the model are indicated.

In section 7.3, the relevance of the results obtained is analysed from the viewpoint of practical interest to JET operations. In particular, the use of the new lumped-parameter models for stress assessment and to extrapolate the structural response to new mechanical and plasma configurations is suggested.

In section 7.4 an attempt is made to summarise all the evidence collected in order to draw some indications on how to prevent the mechanical effects of disruptions. Finally, a list of possible future improvements to JET models and to the algorithms used in COMET and TEMPEST codes is given in 7.5.

7.1 Tokamak disruption load paths

This section describes briefly the conclusions that have been obtained from the work presented in chapter 2.

7.1.1 Magnetic coil force integration

The Biot-Savart field integration procedure described in section 2.1 has been incorporated into the general-purpose computer code COMET (see Appendix 1). This code, although still at an early stage of development, has been used extensively to run not only the cases of section 2.2.2, but also plasma kink assessments for ITER [28] and a variety of different load conditions for the JET TF and PF coils.

The code has proven to be able to fulfil the basic requirement that motivated its development, i.e. to set up and analyse magnetic systems including dozens of coils with an arbitrary degree of accuracy and spatial resolution, in a time (and at a cost) which is orders of magnitude less than what could be achieved using commercial Finite Element tools. The method chosen to pursue this goal, i.e. the semi-analytical integration of Biot-Savart's law over brick-shaped elements, has also been tested and validated; the formulation proposed, based on a geometry representation via Bézier curves and the adaptive algorithm of section 2.1.2.4, can be considered an extension and an improvement respect to the methods which could be found in the literature in terms of precision and efficiency.

Of course, the approach adopted is not ideal in all possible situations. In particular, the following drawbacks have emerged:

- the Biot-Savart formula to integrate the field cannot accommodate easily the boundary conditions necessary to represent the effect of ferromagnetic materials. This problem, which is common to all other integral-type methods, can be solved trivially in codes that implement a differential formulation.
- the solution time when the field is required at many points may compare unfavourably with the Finite Element method, where the field is solved for everywhere at once.

7.1.2 Non-axisymmetric disruption load paths

The distribution of forces analysed in section 2.2.2 should be realistically regarded only as a first approximation of the real path followed by non-axisymmetric disruption loads throughout the JET tokamak. These results give, on the one hand, a detailed quantitative picture of the loads expected on the magnetic coils, while on the other hand they provide only a qualitative indication of the other structural components that could be endangered. A comprehensive analysis would certainly require a Finite Element model coupling all the components at the same time, because of the strong hyperstaticity of their connections; such an analysis would be extremely computer-intensive and has not been attempted as yet.

A very good agreement has been achieved between the estimates of the sideways force for JET pulse 34078, i.e. $F_{SW}\approx 2.6$ MN from the kinked plasma/magnetic coils interaction (section 2.2.2.3) and $F_{SW}\approx 2.7$ from the parameter estimation procedure (section 6.1.1.1). This result seems to indicate that the magnetostatic force integration approach can be used with reasonable confidence to assess this kind of loads. However, this should be confirmed by a more systematic analysis of the various possible configurations ,including the shielding effects of eddy currents in the vessel and in the other conducting structures.

7.2 Estimates of mechanical and force parameters

In this section the results obtained from the application of the parameter estimation method are discussed both in general and for the specific examples presented in chapters 5 and 6.

7.2.1 Application of the parameter estimation procedure

The parameter estimation procedure described in chapter 4 and implemented within the code TEMPEST has been applied to the models of the vacuum vessel defined in chapter 3 in order to analyse a few representative disruptions. By comparison to the large database available, including thousands of JET pulses, the work carried out so far is preliminary; however, since disruptions tend to exhibit similar characteristics, some broad conclusions can be already drawn at this stage.

On a general note, it appears clearly that the parameter estimation problem cannot be approached blindly; feeding raw measurements and a random initial guess to a minimisation algorithm usually does not work. Real-world, large-scale problems like the ones investigated here, by contrast to analytical benchmarks, tend to have an unpredictable number of maxima, minima and saddle points amongst which even the most sophisticated methods are not able to navigate unaided. The analyst has to interact closely with the program putting together engineering judgement and rigorous mathematical techniques, switching between different tools and incorporating as much prior information as possible so as to steer the algorithm towards regions of the parameter space where a physically meaningful solution may be found.

In more practical terms, the specific features of the algorithms discussed in sections 4.3 to 4.5 have been tested on JET data and have been found to have different degrees of usefulness. The main conclusions reached are listed in the following points:

Global minimum search (4.3.1) The grid scan procedure has been found to be an invaluable aid in locating optimal regions of the parameter space, where a minimum can be isolated from other unwanted features of the χ^2 hypersurface. Once these regions have been individuated, the iterative Levenberg-Marquardt procedure can then be used as a sure-fire technique to converge on the minimum with the precision requested. In practice, grid scans have been performed preferentially over just one or two parameters at any one time. This is useful not only in order to save computer time, but also because it is possible to gain effective insight from the visual inspection of the function $\chi^2(p_j)$.

The random search procedure, on the other hand, has been found to have very limited use, apart from occasionally providing the algorithm an escape route out of pathological situations. In fact, resorting to random guesses goes exactly against the philosophy advocated in this work, i.e. to use all available

prior knowledge in order to better understand the physical behaviour of the models.

Frequency analysis

(4.3.2.1) Fourier frequency analysis has been used extensively to determine initial guesses for the mass parameters according to 3.3 and, moreover, to determine *a posteriori* whether the frequency content of the simulated time traces match those of the corresponding measurement. Analysis via the Hilbert transform, on the other hand, has been found to be prone to numerical errors[30] and has not been further pursued.

Noise analysis

(4.3.3) As a rule, smoothing and FFT filtering of the measured signals have been avoided in all but the more extreme cases so as not to tamper with the information contained therein. The Wiener filtering technique, in particular, could not be used successfully at all since the spectral content of the measurements usually falls off very rapidly above 20~30 Hz and remains almost zero up to the Nyquist frequency (usually 500 or 1000 Hz).

The experience gained, on the other hand, shows that clearing a signal from spikes may help in finding a better fit, as shown in section 5.1.1, as long as one can make sure that the spikes are an artefact of the measurement system.

Numerical differentiation

(4.4.1) The Levenberg-Marquardt minimisation algorithm has been found to be extremely sensitive to the choice of the parameter increments Δp_j used for the numerical calculation of the derivatives of the objective function. Good performance has been obtained by switching permanently on the centred difference feature and by setting an high value for the coefficient k_ε (defined in 4.4.1.1) which biases the algorithm towards relatively high values of Δp_j. Second-order derivatives have not usually been included in the Hessian, as they have been found to make the procedure not only extremely slow but, in some occasions, also unstable.

Stagnation loops

(4.4.2) Stagnation loops in the Levenberg-Marquardt algorithm, which had occurred in some early test cases, have not been detected in the analysis of JET pulses reported in chapter 5 and 6, even when using the unrecommended setting $\beta^- = \beta^+$. However, given the difficulty of predicting this kind of pathological situations, one should always be aware of the possibility of their occurrence.

---

30 Steady-state mono-component signal, for instance, have been found to cause fluctuations in the frequency calculated with the Hilbert transform depending on the total duration of the measurement and on the type of windowing employed in the FFT convolution.

Minimisation strategy

(4.4.3 to 4.4.5) The precise setting of the parameters affecting the minimisation strategy (including the damping drop and boost factors β^- and β^+, the bounds on the damping factor and the singular value tolerance) have been found not to affect significantly the ability of the algorithm to find or not to find a solution from any given starting point. Similarly, the tolerances specified in the termination tests have been found to affect the precision of the solution found and the number of iterations required to find it, but not the global convergence properties of the algorithm.

Prior knowledge

(4.5) The incorporation of prior probability densities and parameter bounds in the procedure has been found to be an extremely useful tool in order to get realistic results more quickly. Moreover, prior densities have been used as a means to enforce good conditioning of the Hessian matrix in those cases where linearly dependent parameters would have lead to rank deficiency.

It must be said that in some cases the prior estimates proved to be totally wrong, i.e. they had to be discarded in order to get a good match between simulation and experiment. In other cases the initial error bars, assigned subjectively on the basis of the available (usually scarce) information, proved to be too narrow and had to be considerably relaxed. For these reasons, the adaptive weighting techniques discussed in 4.5.1 could not be fully tested. These findings, anyway, indicate that the prior knowledge itself should always be subject to critical judgement (especially when it derives from sources outside one's control).

Cluster estimation

(4.5.3) Grouping the parameters to be estimated in small clusters of up to 4~5 has been found to be the best practical way to deal with large models. This allows typical running times of the order of the minute, which in turn permits an interactive use of the computer code. A careful selection of highly correlated parameters (such as, for instance, masses and damping coefficients from different subsystems of the same model) in the same cluster usually prevents matrix ill-conditioning and speeds up the search.

The capability to specify different time windows in the signal to be fitted as a function of the specific parameters being estimated has also proved to be extremely useful. This is due to fact that specific combinations of parameters usually affect certain features of the measured waveforms more than others (as an example, the maximum swing of the rolling motion displacement mainly depends upon the swing of the applied force, $F_{max}-F_{min}$, and the related swing time τ_3). Once such dependencies are identified, the analyst can target those features by fitting exclusively the time window in which they are contained. This method is in principle equivalent to attaching a different variance to each measured data point; in other words, one must be prepared

to accept a generally bad fit as the price to pay to have a near-perfect fit of one particular feature, like the force swing in the above example (which is of critical importance for fatigue life assessments). In general, the values of the parameters estimated in this way have been found to be very sensitive to the width and position of the windows, which is the analyst's responsibility to selected suitably.

Multi-stage estimation

(4.5.4) The multi-stage approach, consisting in analysing one JET pulse at a time and in combining together the estimates thus obtained, is the only practical way to proceed until a fully automated data retrieval and processing system will be implemented. Perhaps the most striking feature of the estimates obtained from individual JET pulses is the extremely small width of the associated confidence intervals (as seen in Tables 5.1 to 6.4), which are in most cases orders of magnitude smaller than the initial error bars. Unfortunately, this circumstance does not imply a correspondingly huge improvement of the knowledge, since the differences between pulses may be of the same order (or even larger) than the initial error bars. In other words, a small confidence interval simply means that a very good fit (i.e. a deep, well-defined minimum) has been found for that particular measurement: large discrepancies may be found with successive estimates because the measurement errors have been underestimated, or because modifications have occurred in the structure or, more simply, because the model is wrong. Future analysis of the full database will, hopefully, clarify this point.

To conclude, it has to be admitted that the techniques implemented are more complex and rigorous than what was strictly necessary to analyse the few cases of chapter 5 and 6; on the other hand, the product of this work is a powerful tool that will be able to analyse with precision and efficiency also future, more sophisticated models dealing with huge quantities of data.

7.2.2 Results for the axisymmetric models

The examples presented in chapter 5 show that the models for the axisymmetric motions of the vacuum vessel manage to reproduce experimental data with rather good accuracy, especially considering the rolling motion which, as seen in 1.3.3, is the single most important measurement as far as vessel stresses are concerned. The final conclusions of the analysis can be summarised in the following points:

7.2.2.1 Vertical vessel force

In the cases considered, the vertical force swing (ΔF_V) is more than a factor two smaller than the swing of the measured support force (ΔR_{MVP}). This is in agreement with the following considerations:

1. the static response of the vessel is such as to make $|R_{MVP}|>| F_V|$ because of the effect of the vertical support at the Main Horizontal Ports (see section 3.1.1).
2. the dynamic magnification factor is expected to be > 1 because the typical duration of the loads, which is of the order of 50 ms, is very close to the natural period of the oscillations [51]

This result should be considered with some attention since at JET, in many past occasions, the support force has been mistakenly considered to be a close approximation of the vessel force.

7.2.2.2 Coefficients for the Main Vertical Port dampers

Perhaps the most significant result obtained from the rolling motion model concerns the characteristic (i.e. the force/velocity curve) of the MVP dampers, which give the main contribution to the radial MVP force and thus to the stresses at the base of the port. According to the results of the analysis of pulse 38690 (see Table 5.2), the unsaturated (low- and medium-velocity) part of the force/velocity curve is given by:

$$F_{damper}=1.8\,\dot{x}+473\dot{x}^{2}\ \text{kN} \tag{7.30}$$

(with $\dot{x}$ in m/s). These figures may not be conclusive, since a large amount of data still remains to be analysed and some discrepancies are seen to arise between different pulses; however, judging by the other estimates obtained so far, they can reasonably be assumed to be conservative.

This result gives a strong indication that previous JET calculations have been rather pessimistic. In fact, the force calculated on the basis of the design value (b_0=300 kNs/m, b`=0) is at least a factor 3 larger than the one obtained from (7.30) in the range of maximum velocities typically observed ($\dot{x}\approx$0.1~0.2 m/s). This ratio is equivalent to one or two orders of magnitude in terms of fatigue life, which of course affects dramatically the predictions of the capability of JET to withstand disruptions.

The lack of agreement between the estimated coefficients and the test measurements reported in section 3.1.1.4 may be explained as follows:

— the test has been done at room temperature (kinematic viscosity of the oil $\nu=10^{-4}$ m^2s^{-1}), while data from the producer (CASTROL) indicate that the viscosity at the operating temperature, which could be as high as 60°C, would drop by a factor up to 5.

— because a testing rig capable of operating by the specifications (150 kN @ v=0.5 m/s) could not be found, reverse operating conditions were tested. This means that the force was applied on the piston from the inside using pressurised oil. This may have influenced the outcome of the test in various ways: for example, by retarding the transition of the flow in the gap to the laminar regime, or via non-reversible friction effects.

— the possibility of air infiltrations into the oil, which would have an effect equivalent to a soft spring in series with the damper, have not been considered. The occurrence of such a fault seems to be likely, as oil leaks have been routinely found on these devices.

7.2.2.3 Model limitations and possible improvements

Although the quality of the results obtained represents a definite improvement over what had been achieved in the past, the axisymmetric motion model has showed some limitations which need to be corrected. In fact, as seen in section 5.2, in most cases, a near-perfect match ($\varepsilon_{avg}\lesssim 1\%$) can be obtained for the rolling displacement or for the vertical support force, but not for the two at the same time. In order to get more realistic simulations, it may be necessary to remove some of the simplifying assumptions on which the model is based:

- the torque due to the radial component of the vessel force should be included in the balance of moments around O (see Fig. 3.1);
- additional masses should be included to represent the higher-frequency eigenmodes appearing in the spectrum of the support force (see 3.1.1.1)
- the compliance of the Mechanical Structure and of the Iron Core should be incorporated in the model (or, equivalently, displacement measurements should be corrected to allow for the fact that the reference is moving);
- the additional forces due to the Octant Joint and Main Horizontal Port supports springs should be taken into account;
- the various contributions to the vessel force F_V due to the divertor, eddy and halo currents should be modelled separately. In particular, one should take advantage of the fact that the position of the force acting on the divertor coils is known in advance in order to fix more precisely the position ε of the moving component due to the induced currents.

7.2.3 Results for the sideways model

The JET pulses analysed in chapter 6 show that the vacuum vessel sideways motion model manages, on the whole, to fit experimental results reasonably well. The quality of the fit is especially good for the initial transient of the vessel displacement signal (δ_{SW}), which carries most of the information content necessary to calculate stresses, while it degrades for the tail; in general, it is worse for the support force (R^T_{MVP}) than for the displacement. These results should be judged keeping in mind that the main objective of this analysis is not to reproduce perfectly every minute detail of the measurements but, rather, to identify and simulate the features that are relevant from the viewpoint of stress generation.

The main conclusions reached can be summarised in the following points:

7.2.3.1 Sideways vessel force

The estimated value of $F_{SW}\approx 2.6$ MN for pulse 34078 is in reasonable agreement not only with the value obtained in 2.2.2.3, but also with other independent calculations [49]. The values obtained for both sideways events examined are much larger than the corresponding vertical vessel forces, confirming the importance of this kind of disruptions.

7.2.3.2 Magnetic damping and stiffness

The magnetic stiffness coefficient (k_M) obtained with the parameter estimation procedure is in good agreement with the one obtained from magnetic calculations [49]. On the other hand, the magnetic damping coefficient (b_M) shows a good accord only for pulse 38705, while for pulse 34078 there is a factor ~2 of difference. At any rate, these results show unequivocally that the interaction between vessel and toroidal field is indeed the major source of damping in the model and that, in comparison, the effect of the MHP supports is much less important (see Fig. 6.16).

7.2.3.3 Neutral Beam Injectors forces

The incorporation in the model of a second d.o.f. equivalent to the combined masses of the Neutral Beam Injector boxes (m_{NBI}) has proved essential to reproduce an important feature of the vessel response, namely the second oscillation that can be seen in both the sideways displacement and support force measurements (Fig. 6.13, 6.14, 6.17, 6.18). The local quality of the fit depends critically upon the total stiffness of the vessel-NBI connection, which has been estimated at $k_{NBI}\approx 110$ MN/m with very good agreement between the two cases considered. In turn, this value allows one to calculate the elastic connection force (see Fig. 6.15 and 6.18), which can be seen to have a peak-to-peak range of ~700 kN in pulse 38705. Such force level is more than enough to explain the multiple failures which have affected this component.

7.2.3.4 Model limitations and possible improvements

As remarked above, also the sideways motion model is affected by problems of apparent inconsistency between the quality of the fit that can be obtained to displacement and to support measurements. The tails of both δ_{SW} and R^{T}_{MVP}, in particular, exhibit oscillations that cannot be reproduced by any combination of the parameters in the model. The following modifications could be made in order to overcome this problem:

- the measurement δ_{SW} may not represent the movement of the centre of mass of the vessel with sufficient accuracy because of the bending of the Main Vertical Ports. For recent pulses, a more complete and precise picture should be obtained by considering also the displacement measured at the MHP.
- more degrees of freedom should be added to represent the masses of each NBI box independently, as well as those of other heavy equipment attached to the MHP. The effects of the non-linearity and the proper alignment of the elastic connections respect to the direction of the sideways motion should be also included.
- as suggested for the rolling motion model, the compliance of the Mechanical Structure and of the Iron Core should be taken into account.

7.3 Impact on JET operations

This section illustrates briefly some of the ways in which the mechanical models analysed in this work could be used to benefit practically JET operations.

7.3.1 On-line stress assessment

The models put forward in sections 3.1 and 3.2 lend themselves naturally to implement a new generation of monitoring procedures in which the actual dynamics of the structure is integrated automatically, providing a level of precision far superior to what one can get from the approximated scaling laws used so far.

The functioning of JET involves both automatic and manual monitoring of critical mechanical quantities from the control room, resulting in a hierarchy of warnings and alarms corresponding to different levels of safety. These are usually expressed in the forms of simplified rules associating measured support forces and displacements to allowable stress levels; for instance, currently operations have to be stopped (and the Chief Engineer called) whenever $R_{MVP} \geq 500$ kN or $x_{MVP} \geq 3$ mm (at any one of the Main Vertical Ports).

The results obtained with the vessel model developed for this work could be first used to update these limits and make them less restrictive, for example, on the basis of the results obtained on the MVP damping coefficients. On a further level, the models could be directly incorporated in the on-line system in two basic ways (following the approaches outlined in section 4.1):

- the parameter estimation procedure could be carried out automatically at the end of each disruption in order to estimate the magnitude of the vessel force. Stress levels and the corresponding quota of fatigue life consumed could be then approximately calculated. This method could be difficult to automate fully, but it would guarantee the best possible results within the limits of the assumptions made.
- vessel and Main Vertical Port forces could be calculated directly from the r.h.s. of the dynamic equations, accepting suitable assumptions on the various parameters involved. This method, although potentially less accurate, is completely straightforward and is suitable for real-time implementation.

7.3.2 Predictive use of the models

In this section two possible ways in which the lumped parameter models (once validated by the parameter estimation procedure) can be used to make predictions are discussed. In both cases the usage of the models is reversed respect to what has been assumed so far in the analysis, which provides further proof of the flexibility inherent in the approach followed.

7.3.2.1 Extrapolation to future plasma configurations

The vessel models can be used to extrapolate quickly the structural response to future JET pulses, particularly in view of high-risk experiments such as the upcoming 4 T campaign and the final DT phase. In this case vessel forces, either scaled from empirical laws or simulated by MHD codes, represent an input into the dynamic equations which may then solved for displacements and support forces.

As an example, the effect of the increased sideways force on the vessel displacement has been calculated by scaling the simulation of pulse 38705 up to a B_T=4T, I_{PLA}=6MA configuration. Using the simple scaling law $F_{SW} \propto B_T I_{PLA}$ [26], the force has been varied in steps from 4 to 7 MN. The results, plotted in Fig. 7.1, show a maximum peak displacement of only ~12 mm, which can be accommodated without problems by the vessel, to be compared with the ~18 mm predicted by earlier models [29].

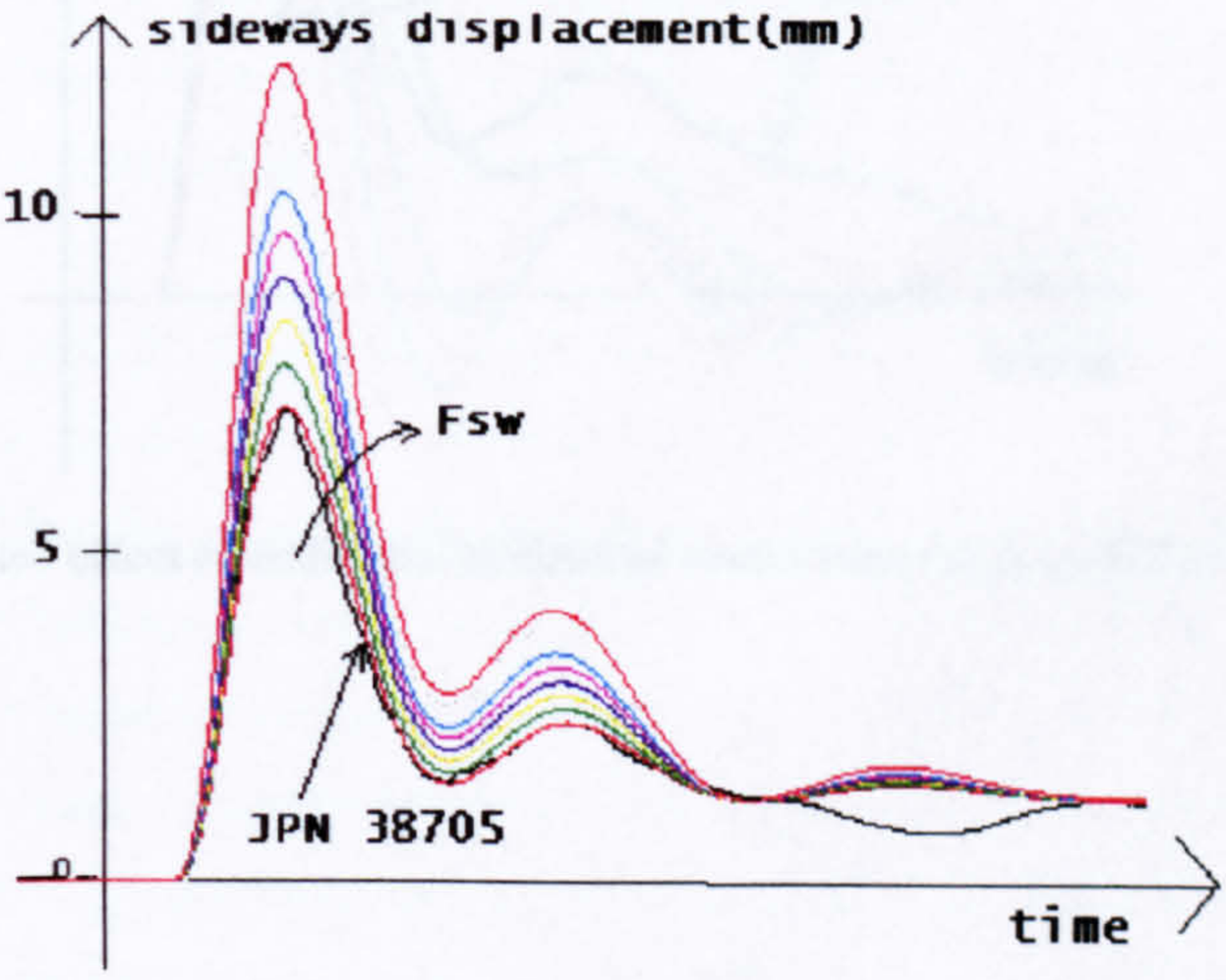


Fig. 7.1 - Effect of increasing sideways force up to the maximum expected at 4T, 6MA (F_{SW}=4 to 7 MN × 38 ms)

7.3.2.2 Support design optimisation

Another way of using lumped-parameter models consists in modifying existing parameters (typically support spring rates or damping coefficients) in order to assess their effect on displacement and stresses. For instance, this is usually done in order to upgrade the existing support system. A range can be specified for the selected coefficients and a simple grid scan, or the full Levenberg-Marquardt procedure, can be then run in order to optimise these parameters with respect to any predefined figure of merit. As an example, an analysis is currently under way to determine whether a new set of horizontal restraints should be added to limit vessel displacements due to sideways forces. Fig. 7.2, based on the response of pulse 38705, shows the effects of replacing the MHP supports with elastic struts having a total spring ratio (k_{SW}) in the range from 20 to 2000 MN/m.

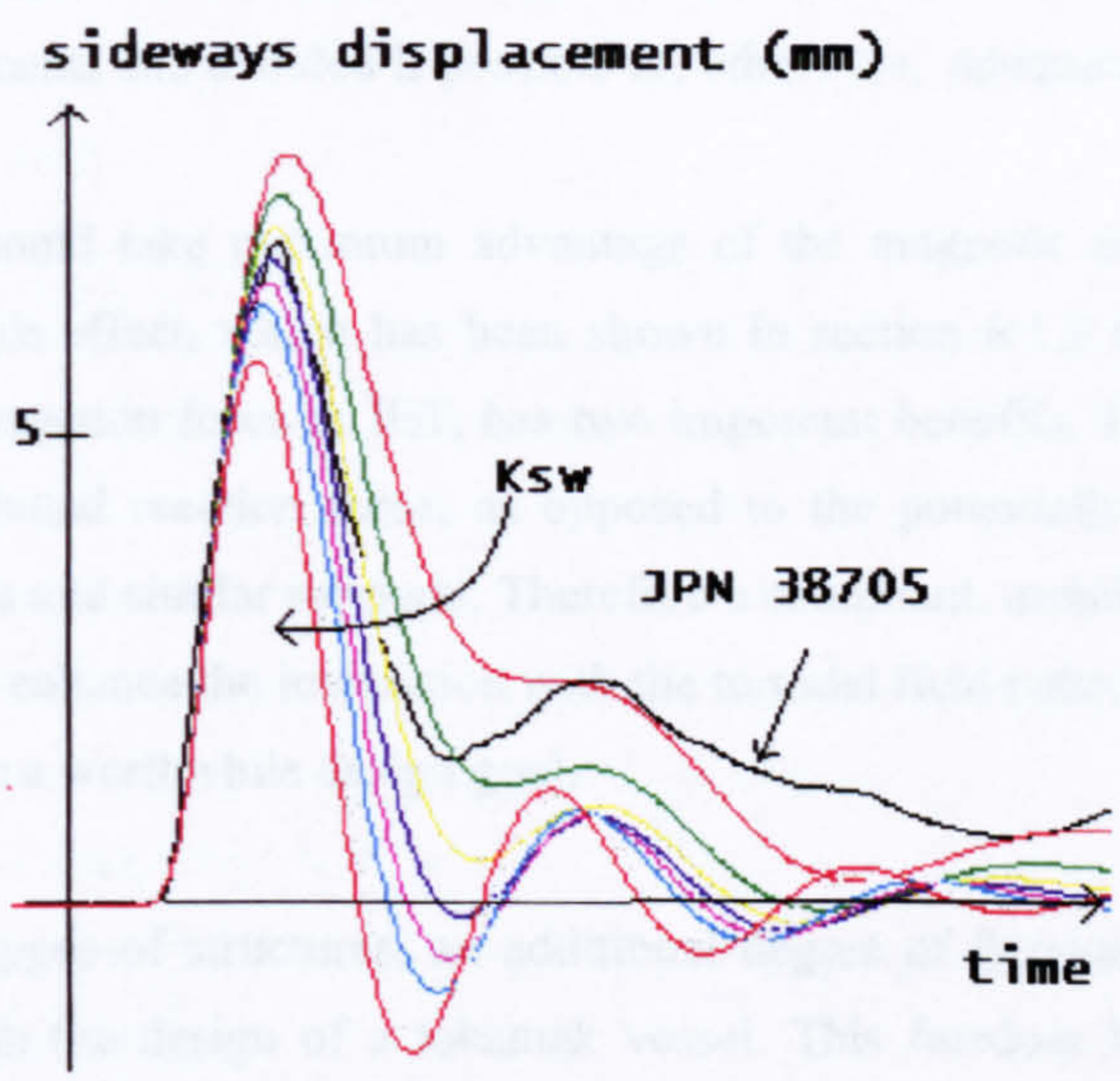


Fig. 7.2 - Extrapolated effect of additional horizontal vessel restraint (k_{SW}=20 to 2000 MN/m)

7.4 Design suggestions

Loads due to disruptions and, in particular, to non-axisymmetric events could not be fully predicted at the time when JET was being designed; as a consequence, today there is some concern about the structural integrity of the machine. Now that a better understanding is being reached, it is extremely important to incorporate it in any new project, such as ITER for example, at an early stage so as to integrate the necessary features into the design in the best possible way.

In spite of the preliminary and approximated character of the present work, a few simple suggestions can nevertheless be derived from what has been discussed so far:

- the main structural supports should avoid to load cantilevered parts in bending or in torsion; instead, supports should be placed as close as possible to the applied loads. Stress concentration areas (such as the re-entrant corner at the base of the Main Vertical Ports) should be predicted with Finite Element assessments and avoided if possible or, otherwise, adequately strengthened.

- an efficient design should take maximum advantage of the magnetic damping effect to restrain vessel movements. This effect, which has been shown in section 6.1.2 to account for more than 30% of the sideways reaction force in JET, has two important benefits: 1) it is free; 2) it provides automatically a distributed reaction force, as opposed to the potentially dangerous concentrated forces exerted by struts and similar supports. Therefore a compliant, mobile vessel with a resistivity distribution such as to enhance the interaction with the toroidal field (which, incidentally, is just the case of JET) should be a worthwhile design goal.

- by contrast to other types of structures, an additional degree of freedom to control the loads is potentially available in the design of a tokamak vessel. This freedom lies in the distribution of electrical resistivity which, for a given total resistance, could conceivably be optimised so as to get a favourable load distribution (i.e. one that minimises stresses). Such optimisation might involve, for example, setting up suitable low-resistance paths which could collect the induced currents and transfer the associated loads to nearby supports. This concept could be expanded further by trying to identify a distribution of resistivity able to steer the trajectory of the unstable plasma towards areas where, for example, halo currents can develop without risks for internal equipment.

7.5 Further work

The work presented in this thesis might of course be improved and extended along many possible lines. The following points represent some of the highest-priority aspects that will be addressed in the near future:

Biot-Savart magnetic field/force integration

- The symbolic integration formulæ will be extended to wedge-shaped volumes. This will enable conductors of a much wider class of shapes to be represented, with an arbitrarily small error, by means of a triangular decomposition of their cross-section.
- The adaptive coil subdivision algorithm described in 2.1.2.4 will be fully tested and extended to non-uniform subdivisions of each single coil segment.

Electromechanical JET models

- the numerical minimisation algorithm implemented in the TEMPEST code will be augmented with the possibility to add equality constraints on the parameters, as well as an interface module designed to communicate with external programs (e.g. FE codes) which performing the dynamic system integration and/or the evaluation of the objective function.
- Axisymmetric and non-axisymmetric models will be completed with additional degrees of freedom so as to include all relevant structural eigenmodes, in addition to a filament representation of the eddy and halo currents as described in 3.1.5.
- The whole array of available mechanical and magnetic measurements will be included in the parameter estimation procedure.
- The data retrieval and analysis procedures will be automated and applied on the whole database of JET disruptions
- The models will be incorporated within an integrated code called IMPROVE (Interactive Modelling of Plasma disRuptions with Object-oriented Visualisation Engine), currently being developed at JET, able to provide 3D animated visualisation of the vessel movements and of other measurements.

APPENDICES

A1 The COMET program

COMET (CO*il and* M*agnetic Field* E*ngineering* T*ool*) is a C++ program, running under the Microsoft Windows operating system, which implements the Biot-Savart integration procedure discussed in 2.1 in order to find the magnetic field and forces generated by the interaction between the JET coil system and the plasma in a kinked configuration. In this appendix the essential aspects of the architecture of COMET are outlined.

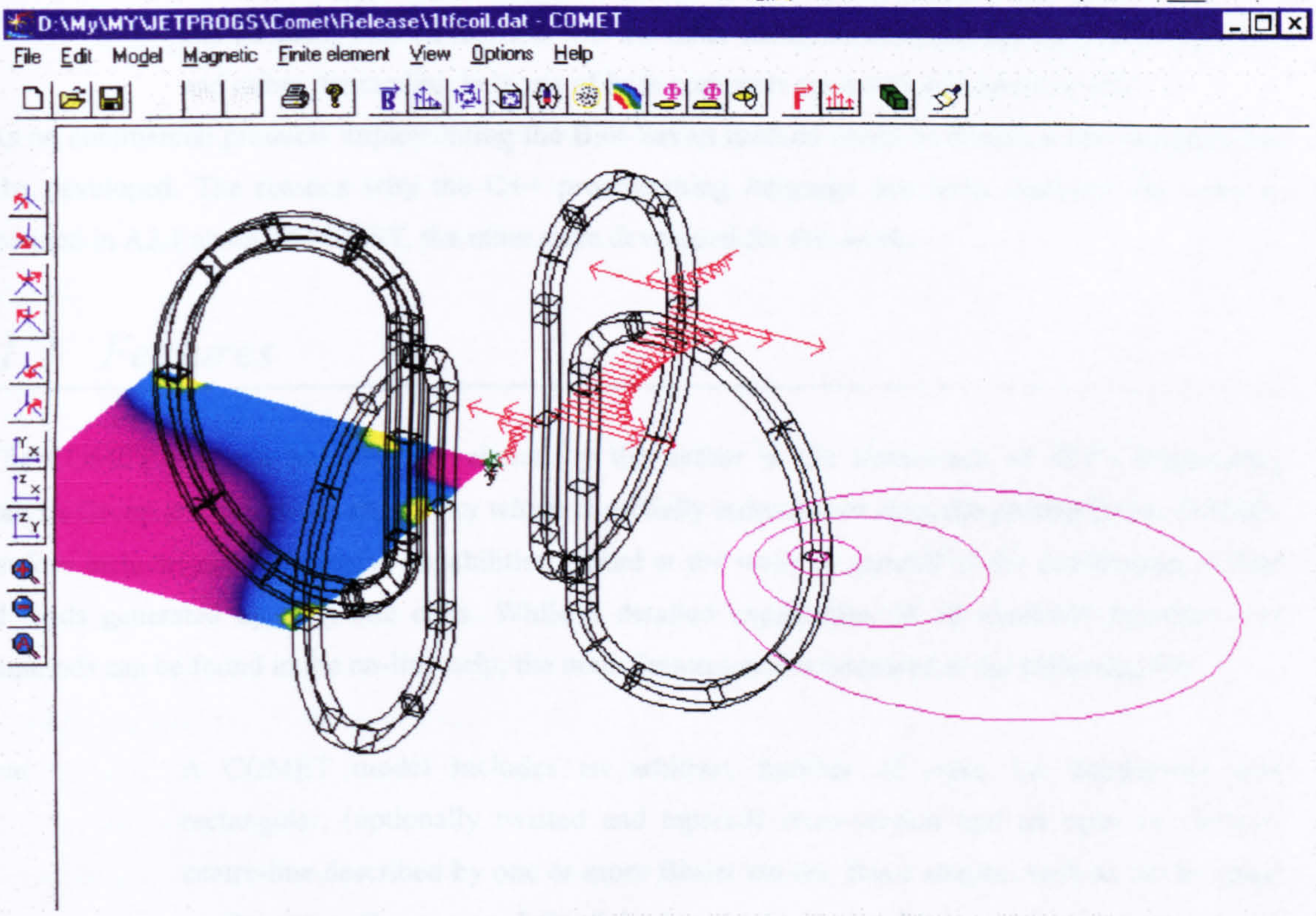


Fig. A.1 - COMET screenshot showing the main field visualisation methods: arrow plot, color map and field lines

A1.1 Rationale

This section briefly explains the reasons why a new computer program has been developed to carry out magnetic forces calculations and why, in particular, Biot-Savart's law has been used. In principle, sets of magnetic coils interacting statically can be modelled by many Finite Element packages such as for example NASTRAN, ANSYS (which implement a conventional differential formulation) or EMAS (using an integral formulation which does not require to mesh explicitly the empty space between the coils). The advantages of the Biot-Savart method over Finite Element can be summarised as follows:

Flexibility A filament coil model, such as the one required by the Biot-Savart method, requires only minimal input and can be modified with very little effort. On the other hand, FE meshes with volume elements are considerably more complex and usually need to be rebuilt completely if the geometry changes.

Speed Integral formulations like the Biot-Savart method are faster when the field is required only at a few locations, while the FE method yields simultaneously the field everywhere. However, FE codes require time-consuming model preparation and post-processing and the total analysis time may be very long.

Portability An *ad-hoc* implementation of Biot-Savart's law such as COMET is simple to use and can be easily run on any PC. On the other hand, commercial FE codes are expensive and rather demanding in terms of both computer resources and operator skill.

As no commercial products implementing the Biot-Savart method could be found, a new program had to be developed. The reasons why the C++ programming language has been used are the same as explained in A2.1 about TEMPEST, the other code developed for this work.

A1.2 Features

The COMET program has been developed by the author in the framework of JET's Engineering Analysis Group and represents an activity which is partially independent from the present thesis. COMET therefore includes rather extensive capabilities, aimed at the study in general of the distribution of field and loads generated by magnetic coils. While a detailed explanation of all available functions and commands can be found in the on-line help, the main features are summarised in the following list:

Input A COMET model includes an arbitrary number of *coils*, i.e. conductors with rectangular, (optionally twisted and tapered) cross-section and an open or closed[31] centre-line described by one or more Bèzier curves. Basic shapes, such as circle, spiral or Princeton D, are pre-defined in terms of simpler Bèzier components (arcs and straight segments). The coil set is input either interactively with mouse and keyboard or from a script file. External fields, defined by analytical formulæ, can also be added.

31 A current which does not form a closed loop (i.e. which does not satisfy $\nabla \cdot \mathbf{J}=0$) is physically unreasonable, unless a time-varying electrical charge exists at both ends of the conductor. The capability to model open current loops is useful, however, to study the effects of different parts of a magnetic circuit independently .

Calculations COMET is able to calculate the magnetic field at any given point and at multiple positions along lines, across surfaces or coil cross-sections. The accuracy of Biot-Savart's law integration, as discussed in 2.1.2, can be specified. Individual coils and external fields can be switched on or off for convenience. Field lines passing by given points can be integrated and Poincaré maps representing the intersection of a line with a given plane can be plotted[32]. The magnetic flux through an arbitrary surface can be integrated and, on the basis of this result, self- and mutual coil inductances can be computed. The distribution of magnetic forces and torques acting on any coil (or a part of it) can be computed and integrated to obtain resultants.

Output Coils and calculated results can be viewed on-screen or printed (with optional hidden line removal), rotated, panned, zoomed or scaled. The computed field and forces can be represented either as vectors or with colour-coding and can be optionally saved to a text file. The coils can be automatically meshed with different kinds of finite elements (beams, 8- or 20-noded bricks) and the appropriate magnetic load can be applied to these elements. The resulting FE model can be exported to an ASCII text file in NASTRAN or ABAQUS format for later structural analysis.

A1.3 Performance

On an Intel PentiumPro/150 PC the code is able to compute about 30 magnetic field vectors per second per coil in the model with a precision better than 0.5%. As a typical example of memory requirements, the program with a model including JET TF system (32 coils + plasma) loaded into memory occupies about 5 MB of RAM.

A1.4 Testing

The code has been carefully tested for consistency with independent magnetic field calculations. The following tests were performed successfully:

- comparison with the theoretical values for the field produced by straight wires and by a solenoid
- comparison with the theoretical values for the magnetic forces exerted between straight parallel wires and on a square coil inside a solenoid
- comparison with theoretical and tabulated results for the field, the self-inductance and the self-force of circular current loops
- comparison with numerical results obtained from MAXFEA on the self-forces acting on JET TF coils

32 This is useful, for instance, to visualise the topology of toroidal configurations where a single line may fill a 2D or 3D region.

Cases with multiple coils have been checked successfully for zero total resultant force and moment, so as to ensure that the divergence of the discretized current density is zero (within a small roundoff error).

A2 The TEMPEST program

TEMPEST (T*ool for* E*nhanced* M*odel-based* P*arameter* EST*imation*) is a program which implements the model-based parameter estimation method discussed in chapter 4. The program is written using the C++ object-oriented language and runs currently under the Microsoft Windows 95/NT operating systems. This appendix describes some details of the architecture and implementation of code.

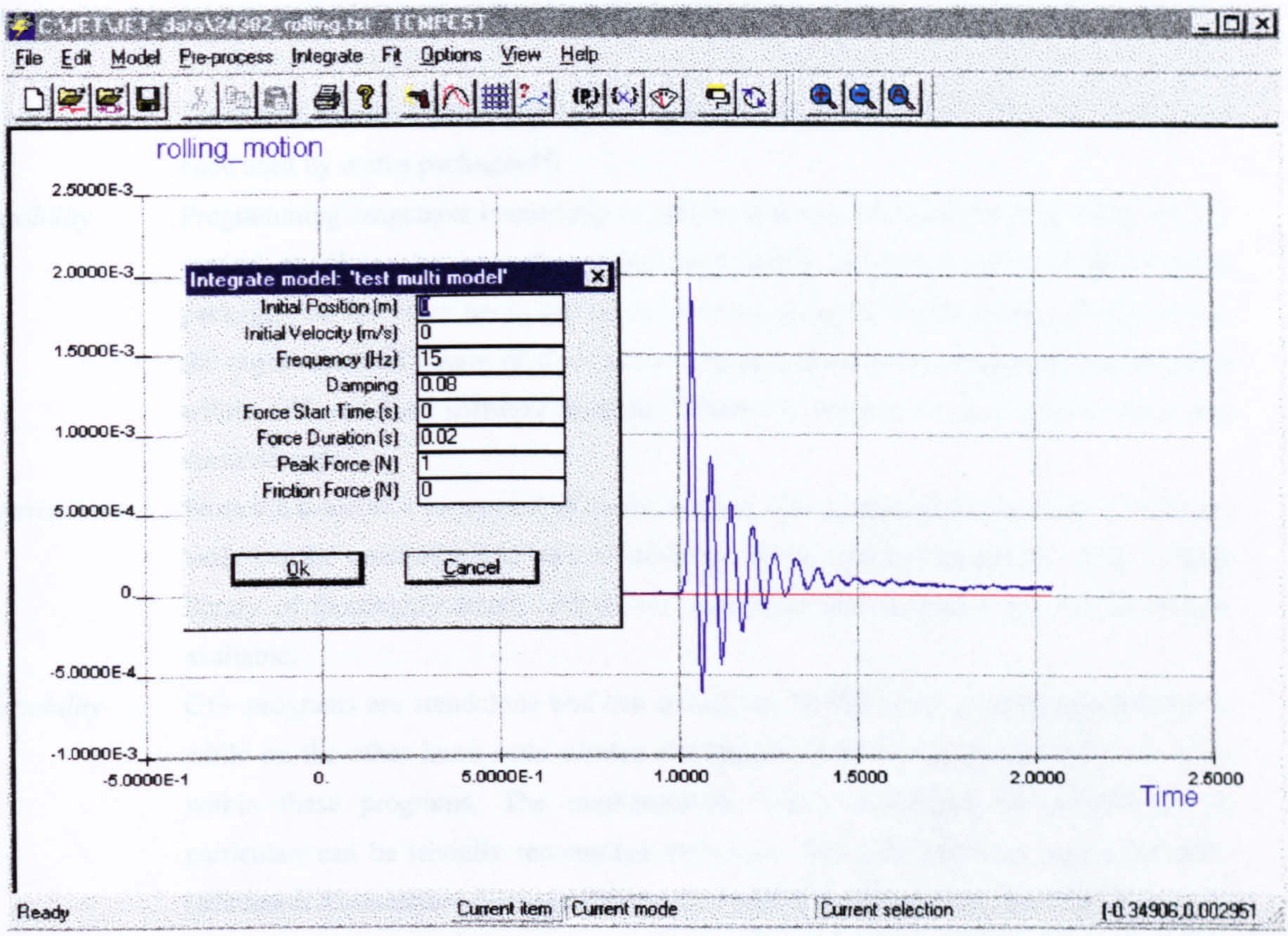


Fig. A.2- TEMPEST screenshot showing the main window and the dialog box to enter parameters values

A1.1 Rationale

This section briefly explains the reasons for the development of such a computer program from scratch. First, no ready-made commercial product exists capable to carry out the parameter estimation procedure in the way described in chapter 4. Although many packages incorporate some form of the Levenberg-Marquardt method, most are concerned with standard curve fitting problems and cannot deal with systems of differential equations of the type considered here. As no product could be found with the required flexibility, recourse to a programming environment was necessary. Two kinds of possibilities exist: maths packages such as Matlab or Mathematica, which also provide integrated graphics (and in some cases symbolic calculation capabilities[33]), and generic programming languages. Of these, the C++ language has been chosen considering the following advantages:

Speed Compiled/optimised programs can be orders of magnitude faster than the interpreted code used by maths packages[34].

Flexibility Programming languages (especially C and its derivatives) offer the possibility of fine control at all levels, from the global architecture to system level routines; maths packages, on the other hand, are much more constrained in this respect. Furthermore, the object-oriented nature of C++ allows the programmer to encapsulate functionality within self-contained software units (or "classes"), leading to inherently modular and reusable code.

Convenience From the subjective viewpoint of the author, the C++ language and the relative software tools are the most efficient way to develop, debug and test programs. Also, a large library of thoroughly tested self-written numerical and graphical routines is already available.

Portability C++ programs are standalone and can usually be ported to all computer architectures, while on the other hand code written for Matlab or Mathematica can only run from within these programs. The mathematical classes developed for TEMPEST, in particular, can be trivially recompiled anywhere. The user interface, based the MFC (Microsoft Foundation Classes) library, can also be simply recompiled on the Apple Mac and on all hardware platforms supporting Microsoft Windows; third-party software tools are available to port it under various flavours of UNIX.

---

33 This option, offered for example by Mathematica and by Maple, would allow the problems of numerical differentiation to be dropped altogether as described in 4.4.1. This solution, however, is much more difficult to implement in practice.

34 Matlab code, for instance, can be automatically translated in C and therefore compiled as a part of an external program, recovering to skip the speed disadvantage. This solution is somewhat cumbersome, however, as two separate programs have to be developed and maintained.

A1.2 Features

The TEMPEST program is designed to apply the model-based parameter estimation method to arbitrary user-defined dynamic models. In this section a brief description of the main features is included; a more detailed explanation, including the syntax for the input script files, is provided in the on-line help.

Input

The models are defined either interactively or from script files listing the variables and the parameters (along with their names, initial values, variances and bounds), the system of first-order differential equations plus the auxiliary functions used to compute the output quantities to be fitted to experimental data. A commented example input file for the rolling motion model is given below. Data waveforms are also loaded from simple ASCII files.

Capabilities

On the most basic level TEMPEST can work as a simple ODE system integrator, given the values of the model's parameters and the initial conditions (which are also treated as parameters). Optionally, arbitrary scalar functions of the parameters can be defined in symbolic form and added to the objective function. This allows the program to solve standard least-squares curve-fitting problems where the time is treated as an arbitrary independent variable, as well as analytic function minimisation when no data are loaded at all. All of the parameter estimation algorithms presented in chapter 4 are implemented and full interactive control over their features is offered. An extensive range of generic pre-processing functions can be applied to the experimental data including smoothing, de-spiking, band-pass filtering with different preconditioning options, optimal (Wiener) filtering, re-sampling, scaling, offsetting and de-trending. Advanced analysis functions such as the Fourier and Hilbert transforms, real cepstrum, autocorrelation and amplitude density (all based on the FFT) can also be applied to either experimental data or simulation results. Multiple time traces can be loaded and processed in batch by arbitrary mathematical expressions (e.g. to automate the calculation of weighted averages from JET data taken from all octants). In addition, arbitrary functions of the time, the experimental data and the parameters can be defined, allowing the use of the models in "reverse" to provide direct estimates (as explained in 4.1.2).

Output

The results of the parameter estimation procedure can be viewed on screen or saved to a text file. Comprehensive diagnostic messages are automatically logged and warnings are issued when numerical problems occur at any stage of the computations. The mapping of the χ^2 function in the parameter space can be visualised in the 1D and 2D cases, while the path followed by the fitting procedure can be plotted for up to three parameters at the same time. The waveforms representing experimental data, output of the models and results of the pre-processing analysis functions can be plotted on-screen, printed and saved to text files.

A1.3 Architecture

The structure of the program, which is physically reflected in the underlying hierarchy of C++ classes, is briefly explained in this section. The basic building block of TEMPEST is the *DynamicModel*, an object which encapsulates most of the required data and functionality. Each model contains an array of *Observation* objects, each including two versions of the same time trace (the *Measurement*, i.e. the data read as an input, and the *Estimate*, which is generated by the ODE system) together with timing information. A model also includes an array of *Parameters*, which are simply a set of floating point values representing the value of each parameter in the model, its allowable range, initial and current variances, optimal increments for differentiation and so on. Higher-order objects called *MultiDynamicModels* can also be defined by grouping together a number of DynamicModels, which are then fitted all at the same time with the advantage of keeping automatically in synch all the common parameters.

As far as the user interface is concerned, TEMPEST follows the typical rules for modern event-driven programs in windowing operating systems; the user decides the workflow by selection of the proper commands from menus. In this case, tight interaction between computer and analyst is not merely a matter of fashion and convenience but, rather, is an absolutely essential tool in order to approach effectively complex minimisation problems (see 7.2.1).

A1.4 Testing

The program has been tested on a wide range of JET pulses and analytical benchmarks. Perhaps the most commonly referenced of the artificial tests is represented by the "banana valley" Rosenbrock's function [73,82]:

$$f(x,y) = (1-x)^2+D^2(y-x^2)^2 \qquad (A.1)$$

This function has a minimum in (1,1) at the bottom of a flat, curved valley which is quite difficult to navigate efficiently. This test, which has a degree of difficulty scaling with the parameter D, gives overall a good indication of the performance of a minimisation algorithm when no pathological situations occur,

A1.5 Performance

Typically, disruption-related experimental data are available as arrays of N=2048 floating-point values sampled at 1 kHz; the 2 sec. time window is set by a pre-triggering algorithm in the data acquisition software and is usually centred around the beginning of the instability. The operation count for the most computationally intensive part of core algorithm (i.e. the calculation of the hessian matrix and the gradient vector) scales with $n_M n_I NM$, where n_M is the number of transient measurements considered

simultaneously, n_l is the number of iterations required to converge and M is the number of parameters to be estimated[35]. Considering that, on a relatively old Intel Pentium 90 PC, the time required for the program to run on a test case with n_l=20, n_l=1 and M=7 is about 20 sec. (including graphics), this means that the performance of the algorithm is more than adequate for interactive use. For future batch processing, even cases where each JET pulse requires n_l=100~200 time traces and M=50~100 parameters to be fully analysed will be well manageable.

The current version of the program requires the user to download the data files off the JET IBM mainframe, to prepare them in an acceptable format (which is simply an ASCII file with the list of the samples) and to analyse them one at a time. Future versions will make use of a remote access library which is being developed at JET and will be able to load data files directly across the network, giving the possibility to process batch of pulses in a completely automatic way. Of course, the ability to apply automatically the parameter estimation procedure will depend on the individuation of suitable algorithms to select reasonable initial conditions and to adapt to all-too-common faulty signals, which in turn will require a lot of careful preparatory analysis.

35 There are parts of the computation which require nNM^2 (the solution of the combined linear system) or even M^3 (the inversion of the hessian) FLOPs but, as long, as M is reasonably small (say, M<100), the time required for these is negligible.

A3 Singular Value Decomposition

The singular value decomposition of a m×n matrix A is defined by the factorisation:

$$[A]=[Q]^T[\Sigma][V] \tag{A.2}$$

where [Q] and [V] are unitary matrices (of order respectively m×n and n×n) and [Σ] is the diagonal matrix of the n singular values σ_j, which may be defined as the eigenvalues of $[A]^T[A]$. The SVD is used in the definition of the pseudoinverse of [A], that is the n×m matrix:

$$[A]^+=[V]^T[\Sigma]^+[Q] \tag{A.3}$$

where the pseudoinverse $[\Sigma]^+$ is formed characteristically by setting $1/\sigma_j=0$ if $|\sigma_j|<\varepsilon_\sigma$. If [A] is invertible, all singular values are nonzero and the pseudoinverse coincides with $[A]^{-1}$. The most useful property of the pseudoinverse is that it allows to solve any linear system $[A]\{x\}=\{y\}$, be it singular, ill conditioned, under- or over-determined, in terms of $\{x\}=[A]^+\{y\}$. The solution {x} is always optimal in the least-squares sense, i.e. it has the minimum norm (or leaves the minimum-norm residual) among all other solutions.

A4 Modelling of spring/damper series

The modelling of a moving mass linked to the a fixed support (the ground) by means of a spring and a damper connected in series is discussed here. This kind of arrangement arises frequently in lumped-parameter models and is used in most of the models for the JET vacuum vessel investigated in this work. While a simple parallel connection leads to the standard second-order oscillator scheme, the series connection needs the introduction of a further d.o.f. and leads to two different results depending on the order of the items (see Fig. A.3). As the difference between these two cases is not immediately apparent (and since this topic belongs to that class of hardly-referenced problems which are too simple for journal papers but too complex for textbooks), a brief summary is provided here.

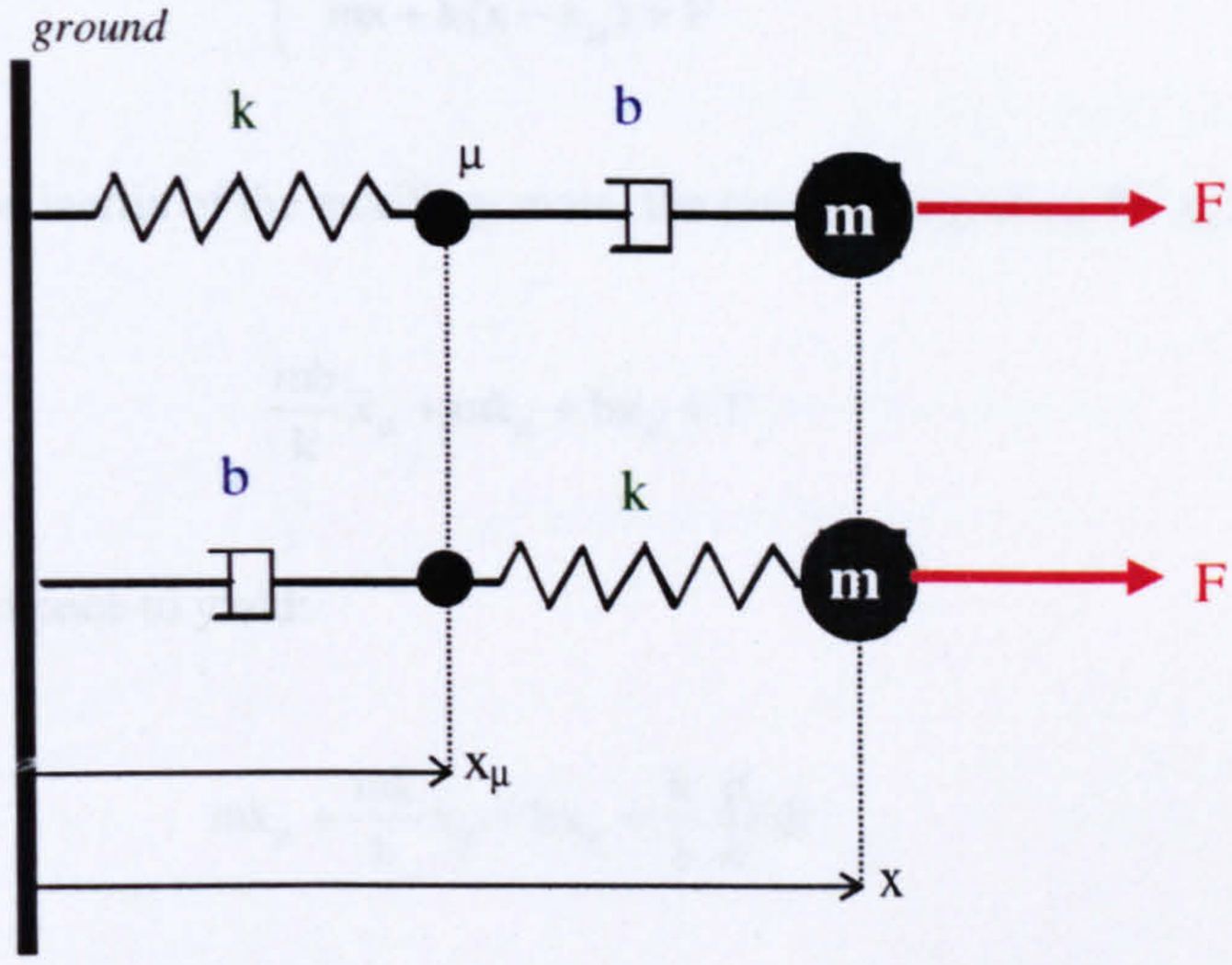


Fig A.3- Possible series connections of a mass/spring/damper system

A1.1 Ground/Spring/Damper/Mass connection

This connection (for brevity referred to as gSDm in the following) leads to the following system:

$$\begin{cases} \mu\ddot{x}_\mu + kx_\mu = b(\dot{x} - \dot{x}_\mu) \\ m\ddot{x} + b(\dot{x} - \dot{x}_\mu) = F \end{cases} \tag{A.3}$$

it is possible, by simple substitution, to transfer the dynamics of the system into a single equation for the auxiliary mass μ:

$$m\ddot{x}_\mu + \frac{mk}{b}\dot{x}_\mu + kx_\mu = F \tag{A.4}$$

where the inertia of μ has been neglected[36]. Once this equation is solved (starting from initial conditions $x_{\mu 0}=0$, $\dot{x}_{\mu 0}=\dot{x}_0$) x(t) follows from a single integration of the second of (A.4). This shows that the dynamics of the auxiliary mass is the same as that of the main d.o.f, except for the value of the damping coefficient (which is inversely proportional to the actual damping and scales linearly with the spring stiffness).

A1.2 Ground/Damper/Spring/Mass connection

This connection (gDSm) leads to the system:

$$\begin{cases} \mu\ddot{x}_\mu + b\dot{x}_\mu = k(x - x_\mu) \\ m\ddot{x} + k(x - x_\mu) = F \end{cases} \tag{A.6}$$

Neglecting as before the inertia of the auxiliary mass, the resulting equation for x_μ is:

$$\frac{mb}{k}\dddot{x}_\mu + m\ddot{x}_\mu + b\dot{x}_\mu = F \tag{A.7}$$

which can be integrated once to yield:

$$m\ddot{x}_\mu + \frac{mk}{b}\dot{x}_\mu + kx_\mu = \frac{k}{b}\int_0^t F dt \tag{A.8}$$

Qualitatively, the situation is very different from the previous case: the auxiliary mass follows the same equation as in the gDSm case, but now it feels the effects of the integral of the external force.

36 From the viewpoint of the numerical stability of the integration routine μ can be safely set to zero.

A1.3 Comparison

The difference between the two cases can be further clarified with an example. Considering a rectangular impulse load of magnitude and duration $F \times \tau$, the response is in both cases is a motion at an average speed $\dot{x}=F/b$ followed by oscillations which relax around the position reached at $t=\tau$ (equilibrium can be achieved at any position because no restoring force acts directly on the mass) (Fig. A.4). The auxiliary mass tends obviously to remain close to its original position in the gSDm case, while it will follow the main mass in the gDSm case. As a result, in the gSDm case, damping and stiffness coefficients being equal, oscillations of the main mass are usually much wider.

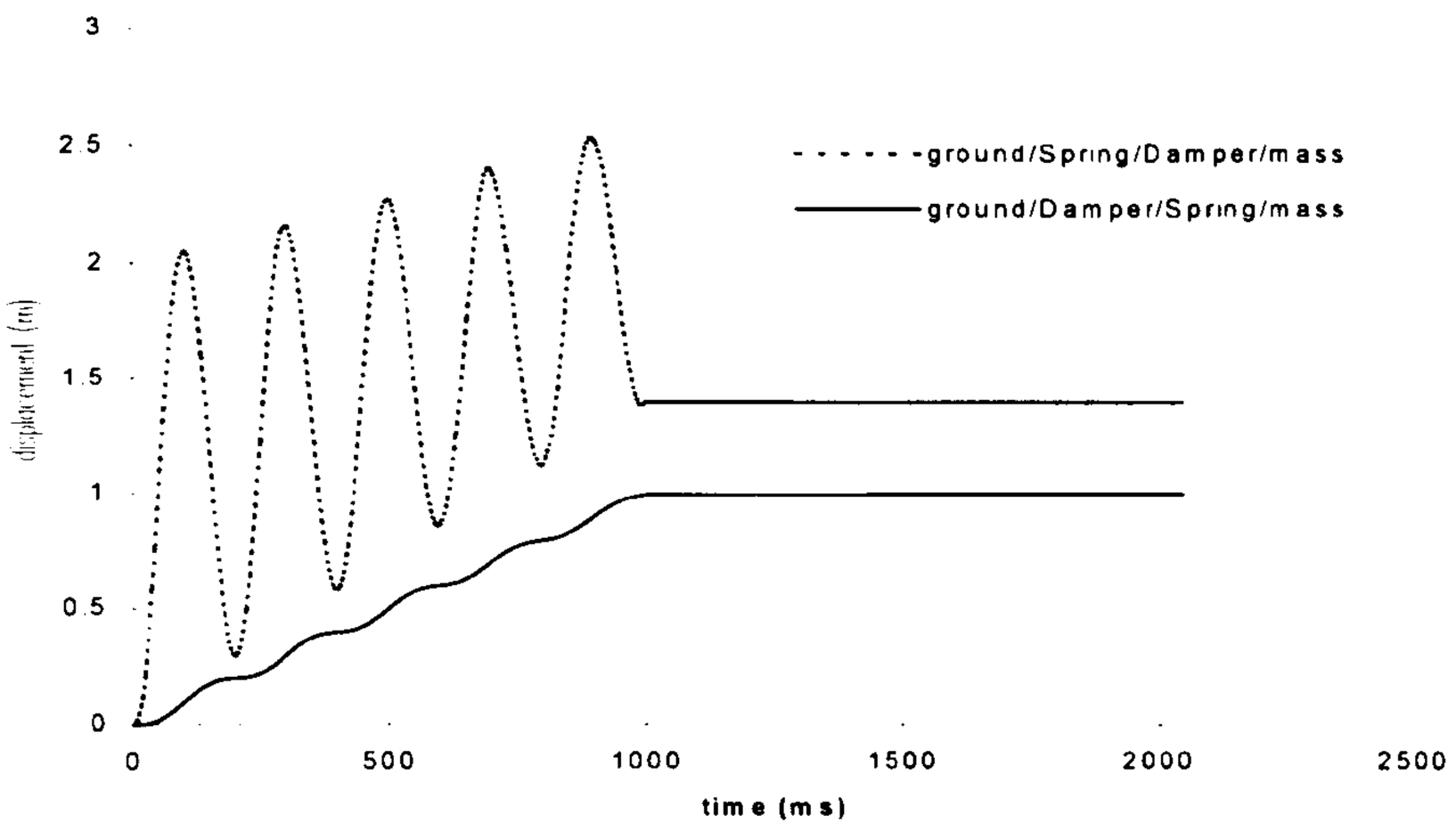


Fig. A.4 - Response of series spring/damper systems to a ($F=1$ kN)×($\tau=1$s) rectangular force pulse ($m=1$ kg, $k=1$ kN/m, $b=1$ kNs/m)

REFERENCES

Chapter 1

Tokamak devices and JET components

[1] FF CHEN, *Introduction to plasma physics and controlled fusion*, Plenum, 1984

[2] J WESSON, *Tokamaks*, Clarendon Press, Oxford, 1997

[3] DJ ROSE, M CLARK, *Plasmas and Controlled Fusion,* J.Wiley&Sons, New York, 1961

[4] IH HUTCHINSON, *Principles of plasma diagnostics*, Cambridge University Press, 1987

[5] M HUGUET ET AL., *The JET machine: design construction and operation of the major systems,* Fusion Technology, Vol. 11, Jan. 1987, p. 43

[6] *JET Annual Reports*, EUR-JET AR 1 to 20, 1983-1997

[7] Commission of the European Communities, *The JET project - scientific and technical developments 1976*, Report EUR 5791e, 1977

[8] WGF CORE, P NOLL, *Transverse magnetic field penetration trough the JET toroidal coil and support structure*, Report JET-R(88)03

[9] JR LAST, M BUZIO ET AL., *Analysis and tests in support of upgrading the JET toroidal Field to 4 Tesla*, Proc. of 15th International Conference of Magnet Technology, Peking, 1997

[10] V MARCHESE, T BUSINARO, M BUZIO ET AL., *Enhancement of JET machine instrumentation and coil protection systems*, Proc. Of 19th Symposium On Fusion Technology, Lisboa, 1996

Axisymmetric plasma instabilities

[11] AA GALEEV, RN SUDAN (ED.), *Handbook of Plasma Physics Vol. 1, Basic Plasma Physics,* North Holland, Amsterdam, 1983

[12] FB MARCUS, C JARDIN, P NOLL ET AL, *Simulations of control, perturbation, displacement and disruption in highly elongated tokamak plasmas,* Nuclear Fusion N. 8, Vol. 30 (1990), p. 1511

[13] R ALBANESE, E BERTOLINI, P NOLL ET AL., *Analysis of vertical instabilities in the JET Experiment,* Fusion Technology, 1988

[14] TH JENSEN, LL LAO, *MHD Equilibria of attached plasmas after loss of vertical stability in elongated Tokamaks,* Nuclear Fusion n. 10, Vol. 31, 1991, p. 1909

[15] A MAFFUCCI, V RICCARDO, *Influence on iron modelling on MAXFEA magnetic equilibrium computations for JET,* Report JET-IR(97)10, 1997

[16] MF JOHNSON, *Update of statistical analysis of JET disruptions,* Report JET-R(94)02, 1994

[17] M BUZIO, *Structural effects of disruptions on the Vacuum Vessel of the Joint European Torus Tokamak*, Laurea Thesis, Politecnico di Milano, 1993

[18] M BUZIO, *Halo currents and their mechanical effects in JET and other tokamaks,* JET Memorandum, 1995

[19] P NOLL, G SANNAZZARO, T RAIMONDI, M BUZIO, M VERRECCHIA ET AL, *Forces on the Vacuum Vessel and on the In-Vessel Components during disruptions,* Proceedings of 16th IEEE Symposium on Fusion Engineering, Champaigne, IL, 1995

[20] P NOLL ET AL., *Experience of Electromagnetic forces during JET Divertor Operations,* EMF Workshop, Capri, 29 Aug. 1994

[21] E BERTOLINI, M BUZIO, P NOLL, T RAIMONDI, G SANNAZZARO, M VERRECCHIA, *Engineering analysis of JET operation,* Proceedings of 16th IEEE Symposium on Fusion Engineering, Champaigne, IL, 1995

[22] P NOLL, P BARABASCHI ET AL., *Evidence of Halo Currents in JET,* Proceedings of 14th Symposium on Fusion Engineering, Lisbon, 1992

[23] M GARRIBBA, R LITUNOVSKI, S PUPPIN., *The plasma shape and current control system of JET,* Report JET-P(95)19

Non-axisymmetric plasma instabilities

[24] P NOLL, P ANDREW, M BUZIO, R LITUNOVSKY, T RAIMONDI, V RICCARDO, M VERRECCHIA., *Present understanding of electromagnetic behaviour during disruptions in JET,* Proceedings of 14th IEEE Symposium on Fusion Engineering, Champaigne, IL, 1995, Vol. 1, p. 187

[25] M BUZIO, P NOLL, T RAIMONDI, V RICCARDO, L SONNERUP. *Axisymmetric and non-axisymmetric structural effects of disruption-induced electromechanical forces on the JET Tokamak*, Proc. Of 19th Symposium On Fusion Technology, Lisboa, 1996

[26] V RICCARDO, P ANDREW, M BUZIO, A KAYE, P NOLL, T RAIMONDI, *Asymmetric vertical displacement events at JET,* Proceedings of 16th Symposium on Fusion Engineering, San Diego, CA, 1997

[27] P NOLL, V RICCARDO, P ANDREW, *Tentative interpretation of plasma behaviour leading to forces on structural components,* Proceedings of the Tripartite Exchange Agreement Workshop on the effects of plasma behaviour on tokamak structural components, JET, 1996 (internal document)

[28] S FANTECHI, *Three-dimensional modelling and electromagnetic analysis of plasma vertical displacement events in a Next Step tokamak fusion reactor*, PhD Thesis, École Polytechnique de l'Université Libre de Bruxelles, 1998

[29] A GIBSON, M BUZIO, A KAYE, P NOLL, T RAIMONDI, V RICCARDO, L SONNERUP, *Stresses on the JET vacuum vessel in operations up to 4T,* JET Report, 1997

[30] P NOLL, *Magnetic damping of vessel displacements,* JET Memorandum, October 1996

Plasma instabilities and Halo Currents in other tokamaks

[31] Y NEYATANI, *Recent progress in JT-60U experiments,* Fusion Engineering and Design, Vol. 30, 1995, p. 25-37

[32] M SAIDOH, *Effect of plasma behaviour on Tokamak components under JT-60 operation,* Proceedings of the Tripartite Exchange Agreement Workshop on the effects of plasma behaviour on tokamak structural components, JET, 1996 (internal document)

[33] MJ SCAHEFFER, D HUMPHREYS ET AL., *VDE halo Current Asymmetry forces and mitigation in DIII-D,* Proceedings of the Tripartite Exchange Agreement Workshop on the effects of plasma behaviour on tokamak structural components, JET, 1996 (internal document)

[34] O GRUBER ET AL, *Vertical Displacement Events and Halo Currents,* PPCF 35, 1993, p. B191

[35] TH JENSEN, EJ STRAIT ET AL., *Vertical Stability, High Elongation, and the Consequences of loss of Vertical Control on DIII-D,* FT 1990, p.1045

[36] EJ STRAIT, *Observation of Poloidal Current Flow to the Vacuum Vessel Wall during Vertical Instabilities in the DIII-D Tokamak,* NF 31, No.3, 1991

[37] GG CASTLE, AW MORRIS, DA GATES, CG GIMBLETT, M VALOVIC, *Halo Currents and VDE in Compass-D,* Proc. of the 16th IAEA Fusion Energy Conference, Montreal, 1996

Chapter 2

Bézier curves

[38] R SALMON, M SLATER, *Computer Graphics systems and concepts,* Addison-Wesley, Wokingham, UK, 1987.

[39] AR FORREST, *Interactive interpolation and approximation by Bézier polynomials,* Computer-aided design, Vol. 22, N. 9, Nov. 1990

[40] DJ WALTON, DS MEEK, *Approximation of a planar cubic Bézier spiral by circular arcs* , J. of Computational and Applied Mathematics 75 (1996) 47-56

[41] A HAMLER, B HRIBERNIK, M LIKAR, N GUID, *Torque calculation by Bernstein Bézier's surfaces,* IEEE Transactions on Magnetics, Vol. 31, N. 3, May 1995

Semi-analytical integration of Biot-Savart's law

[42] L LANDAU, E LIFSHITZ, *The classical theory of fields,* Pergamon Press,London, 1951
[43] M GYIMESI, D LAVERS, D OSTERGAARD, T PAWLAK, *Biot-Savart integration for bars and arcs,* IEEE Transactions on Magnetics, Vol. 29, N. 6, Nov. 1993
[44] LK URANKAR, *Vector Potential and Magnetic Field of Current-Carrying Finite Arc Segment in Analytical form, Part III: Exact Computation for Rectangular Cross-Subsection,* IEEE Transactions on Magnetics, Vol. MAG-18, N. 6, Nov. 1982
[45] LK FORBES, S CROZIER, DM DODDRELL, *Rapid computation of static fields produced by thick circular solenoids*, IEEE Transactions on Magnetics, Vol. 33, N. 5, Sept. 1997
[46] DR WILTON, AW GLISSON, DH SCHAUBERT, OM AL-BUNDAK, CM BUTLER, *Potential integrals for uniform and linear source distributions on polygonal and polyhedral domains,* IEEE Transactions on Antennas and Propagation, Vol. AP-32, N. 3, p. 276, March 1984
[47] Intel Pentium processor reference manual (*www.intel.com*)

Chapter 3

Magnetic modelling

[48] IS GRADSHTEIN, IM RYZHIK, *Tables of integrals, series and products,* Academic Press, New York, 1980
[49] V RICCARDO, *Asymmetries during Vertical Displacement Events in JET*, PhD Thesis, Imperial College, London, 1998
[50] WR SMYTHE, *Static and dynamic electricity,* McGraw-Hill, NY, 1969

Mechanical modelling

[51] RW CLOUGH, J PENZIEN , *Dynamics of structures,* McGraw-Hill, NY 1975
[52] S DIMOVA, *Comparison and experimental verification of two techniques for friction force representation*, Computers & Structures, Vol. 60, N. 1, 1996, p. 11-19
[53] L SONNERUP, *Mechanical design assessment of structural component and auxiliaries of the Joint European Torus,* Nuclear Engineering and Design/Fusion, Vol. 3, 1986, p. 233-247
[54] H HEMMERICH, *Impact test of MVP dampers,* JET Memorandum, Sept. 1997
[55] AF VAKAKIS, *Non-linear normal modes (NNMs) and their applications in vibration theory: an overview,* Mechanical Systems and Signal Processing, Vol. 11(1), Academic Press, New York, 1997, p. 3-22
[56] *ASME Boiler and Pressure Vessel Code, Section III, Rules for construction of nuclear power plant components,* New York, 1995
[57] MSC/NASTRAN *Handbook for dynamic analysis* Version 63, The MacNeal-Schwendler Corporation, Los Angeles, CA, 1983
[58] T RAIMONDI, *Preliminary modelling of asymmetries*, JET Memorandum, May 1996

Chapter 4

Force estimation

[59] CW GROETSCH, *Inverse problems in the mathematical sciences,* Vieweg, Braunschweig/Wiesbaden, 1993
[60] H LEE, YS PARK, *Error analysis of indirect force determination and a regularisation method to reduce force determination error*, Mechanical Systems and Signal Processing, Vol. 9, N. 6, 1995, p. 615-633
[61] KK STEVENS, *Force identification: an overview,* in Proceedings of SEM spring conference on experimental mechanics, 1987, p. 838-844

[62] JC BRIGGS, *Impact force identification using extracted modal parameters and pattern matching*, International Journal of Impact Engineering, Vol. 12, 1992, p. 361-372
[63] SS LAW, T CHAN, QH ZENG, *Moving force identification: a time domain method*, Journal of Sound and Vibration, Vol. 201, N. 1, 1997, p. 1-22
[64] SS JO, D BEALE, *Parameter estimation to improve accuracy of mechanical system simulation using rigid body codes*, Computers and Structures, Vol. 65, N. 5, 1997, p. 679-686
[65] F MILANI, *Disruption force estimation in JET*, PhD Thesis, Aston University, 1998

Statistical parameter estimation and the Levenberg-Marquardt method

[66] MG BULMER, *Principles of statistics*, Dover, New York, 1979
[67] G STRANG, *Linear algebra and its applications*, Academic Press, London, 1976
[68] GEP BOX, GC TIAO, *Bayesian inference in statistical analysis*, J Wiley and Sons, New York, 1992
[69] K LEVENBERG, *A method for the solution of certain non-linear methods in least squares*, Quartely Journal of Applied Mathematics, Vol. 2, 1944, p. 164
[70] DW MARQUARDT, *An algorithm for least-squares estimation of non-linear parameters*, Journal of the Society of Industrial and Applied Mathematics, Vol. 11, 1963, p. 431
[71] WH PRESS et al., *Numerical Recipes: the art of scientific computing*, Cambridge University Press, New York, 1989
[72] FA LOOTSMA (editor), *Numerical methods for non-linear optimisation*, Academic Press, London, 1972
[73] M LAMPTON, *Damping-undamping strategies for the Levenberg-Marquardt non-linear least-squares method*, Computers in Physics, Vol. 11, N. 1, Jan/Feb 1997, p. 110
[74] Y BARD, *Non-linear parameter estimation*, Academic Press, New York 1974
[75] JE DENNIS, RB SCHNABEL, *Numerical methods for unconstrained optimisation and nonlinear equations*, Prentice-Hall, Englewood Cliffs, NJ, 1983
[76] PR BEVINGTON, DK ROBINSON, *Data reduction and error analysis for the physical sciences*, McGraw-Hill, New York, 1992
[77] JV BECK, KJ ARNOLD, *Parameter estimation in engineering and science* , John Wiley and Sons, New York, 1977
[78] RP BRENT, *Algorithms for minimisation without derivatives*, Prentice-Hall, Englewood Cliffs, NJ, 1973
[79] JE DENNIS, DM GAY, RE WELSCH, *An adaptive nonlinear least squares algorithm*, ACM Transactions on Mathematical Software, Vol. 7, N. 3, Sept. 1981, p. 348-368
[80] PT BOGGS, JR DONALDSON, RH BYRD, RB SCHNABEL, *ODRPACK: software for weighted orthogonal distance regression*, ACM Transactions on Mathematical Software, Vol. 15, N. 4, Dec. 1989, p. 348-364
[81] WE BAYLIS, A PRADHAN, *Locating minima of a hypersurface: a modification of the Levenberg-Marquardt method*, Computer Physics communications, Vol 31., 1984, p. 297-301
[82] JJ MORÉ, BS GARBOW, KE HILLSTROM, *Testing unconstrained optimisation software*, ACM Transactions on Mathematical Software, Vol. 7, N. 1, Mar. 1981, p. 17-41
[83] PE GILL, W MURRAY, MH WRIGHT, *Practical optimisation*, Academic Press, London, 1981
[84] RC DAVIDSON, *Kinetic waves and instabilities in a uniform plasma*, in AA Galeev, RN Sudan (editors) *Handbook of plasma physics*, Vol. I, North Holland, Amsterdam, 1983, p. 521
[85] L LJUNG, *system identification: theory for the user*, Prentice-Hall, Englewood Cliffs, NJ, 1987
[86] J QUIANG, CE SINGER, *Parameter estimation in a tokamak transport model and application to L- and H-model simulations*, IEEE Transactions on Plasma Science, Vol. 24, N. 4, Aug. 1996
[87] V DOSE, W VON DER LINDEN, A GARRETT, *Bayesian parameter estimation of nuclear fusion confinement time scaling laws*, in KM Hanson (ed.), Maximum Entropy and Bayesian Methods, Kluwer Academic Publishers, NL, 1996
[88] DA SPONG, *J* Optimisation of small aspect ratio stellarator/tokamak hybrid devices*, Proc. Of the 39th Meeting of the APS Division of Plasma Physics, Pittsburgh, PA, 1997
[89] J BEYERER, *A method for assessing the worth of prior knowledge about the measurand*, Measurement, Vol. 18, No. 4, 1996, p. 225-235

Signal processing

[90] EO BRIGHAM, *The Fast Fourier Transform*, Prentice-Hall, Englewood Cliffs, NJ, 1974
[91] RW HAMMING, *Digital Filters*, Prentice-Hall, Englewood Cliffs, NJ, 1983
[92] RB RANDALL, *Frequency analysis*, Brüel & Kjær, 1987
[93] S BRAUN, M FELDMAN, *Time-frequency characteristics of non-linear systems*, Mechanical Systems and Signal Processing Vol. 11, N. 4, 1997, p.611-620
[94] CT HUANG, CJ CHOU, *Estimation of the underdamped second-order parameters from the system transient*, Journal of the Industrial Engineering and Chemical Research, Vol. 33, 1994, p. 174-176
[95] JT BROCH, *Effects of spectrum non-linearities upon the peak distribution of random signals*, Technical Review, N. 3, Brüel & Kjær, 1963

BIBL LONDON UNIV